On the Tailoring of Magnetic Properties of Fe-Based Alloy Thin Films by Swift Heavy Ion Irradiation and Thermal Annealing

Thesis submitted to
Cochin University of Science and Technology
in partial fulfillment of the requirements
for the award of the degree of
Doctor of Philosophy

by

Hysen Thomas

COCHIN UNIVERSITY OF
SCIENCE AND TECHNOLOGY

Department of Physics
Cochin University of Science & Technology
Cochin- 682 022, India.

June 2013

On the Tailoring of Magnetic Properties of Fe-Based Alloy Thin Films by Swift Heavy Ion Irradiation and Thermal Annealing

Author

Hysen Thomas
Thazhathekuttu House
Kumbanadu PO
Kumbanadu 689 547
Emai: hysenthomas@gmail.com
Phone: 9446974398

Supervising Guide

Prof. M. R. Anantharaman
Department of Physics
Cochin University of Science & Technology
Cochin- 682 022, India.

June 2013

Cover page illustration

Front Cover: 3D AFM image of Co-Fe-Si thin film deposited by oblique angle deposition using thermal evaporation.

Back Cover: VSM hysteresis loops recorded from in-plane direction to out of plane directions (0 to 90^0) at intervals of 10^0 for Co-Fe-Si thin film.

I was born not knowing and have had only a little time to change that here and there.

Richard P. Feynman

Department of Physics
Cochin University of Science and Technology
Cochin 682 022, Kerala

Dr. M. R. Anantharaman
Professor

25th June, 2013

Certificate

Certified that the thesis entitled **"On the Tailoring of Magnetic Properties of Fe-Based Alloy Thin Films by Swift Heavy Ion Irradiation and Thermal Annealing"** is an authentic record of the bonafide research work done by Mr. Hysen Thomas under my guidance and supervision in the Department of Physics, Cochin University of Science and Technology, Cochin-682 022 and no part of it has been included in any other thesis submitted previously for the award of any degree.

Dr. M. R. Anantharaman
Supervising Guide

Declaration

I hereby declare that the work presented in this thesis entitled **"*On the Tailoring of Magnetic Properties of Fe-Based Alloy Thin Films by Swift Heavy Ion Irradiation and Thermal Annealing*"** is based on the original research work carried out by me under the guidance and supervision of Prof. M R Anantharaman, Department of Physics , Cochin University of Science and Technology, Cochin-682 022 and no part of the work reported in this thesis has been presented for the award of any other degree from any other institution.

Hysen Thomas

Cochin-22
25-06-2013

Publications in Peer Reviewed Journals

1. R. Lisha, **T. Hysen** , P. Geetha , O. Sunil , S. Indra, R. C. Choudhary, D. K. Avasthi., M R Anantharaman, Structural and magnetic behaviour of zinc ferrite thin films with annealing Under Review in *Physica B*

2. **T. Hysen**, P. Geetha, I. A. Al-Omari, R. Lisha, and M. R. Anantharaman "Oblique angle deposition of Co-Fe-Si thin films for designing nanostructures for tailoring coercivity" Under review in *Physica B.*

3. **T. Hysen**, P. Geetha, I. A. Al-Omari, R. Lisha, and M. R. Anantharaman "Evaluation of Kinetic triplets and the evolution of magnetic properties with micro-structural transformations in and Fe based metallic glass" Under review in *Journal of Materials Science* (2013).

4. G. Pookat, **H. Thomas**, S. Thomas, S. H. Al-Harthi, L. Raghavan, I. A. Al-Omari, D. Sakthikumar, R.V. Ramanujan, M.R. Anantharaman, Evolution of structural and magnetic properties of Co–Fe based metallic glass thin films with thermal annealing, *Surface Coatings and Technology*, In Press

5. G. Pookat, **T. Hysen**, S. H. Al-Harthi, I.A. Al-Omari, R. Lisha, D. K. Avasthi, M. R. Anantharaman, Magnetic and topographical modifications of amorphous Co–Fe thin films induced by high energy Ag7+ ion irradiation, *Nuclear Instruments and Methods in Physics Research* Section B: Beam Interactions with Materials and Atoms, 310 (2013) 81–86

6. **T. Hysen**, P. Geetha, Salim Al-Harthi, I. A. Al-Omari, R. Lisha, R. V. Ramanujan, D. Sakthikumar, D. K. Avasthi and M. R. Anantharaman "On the Evolution of Surface Roughness induced Magnetic Properties by Swift Heavy ion Irradiation on Co-Fe-Si Thin films" Under Minor Revision in *Journal of Magnetism and Magnetic Materials* (2013).

7. **T. Hysen**, Salim Al-Harthi, I. A. Al-Omari, P. Geetha, R. Lisha, R. V. Ramanujan, D. Sakthikumar and M. R. Anantharaman "Annealing induced low coercivity, nanocrystalline Co-Fe-Si thin films exhibiting inverse cosine angular variation" *Journal of Magnetism and Magnetic Materials* 341 (2013) 165–172.

8. **T. Hysen**, T. Senoy, R. V. Ramanujan, D. K. Avasthi, I. A. Al- Omari, Salim Al-Harthi and M. R. Anantharaman "Swift heavy ion induced surface and microstructural evolution in metallic glass thin films" *Nuclear Instruments and Methods in Physics* Research B 287 (2012) 85–90.

9. S. H. Al-Harthi, M. Elzain, M. Al-Barwani, A. Kora'a, **T. Hysen**, M. T. .Z. Myint "Unusual surface and edge morphologies, sp2 to sp3 hybridized transformation and electronic damage after Ar+ ion irradiation of few-layer graphene surfaces" *Nanoscale Research Letters* 7 (2012) 466.

10. S. H. Al-Harthi A. Kara'a **T. Hysen**, M. Elzain, A. T. Al-Hinai and M. T. Z. Myint "Evolution of surface morphology and electronic structure of few layer graphene after low energy Ar1 ion irradiation" *Applied Physics Letters* 101 (2012) 213107.

11. S. H. Al-Harthi, M. Al-Barwani, M. Elzain, Ashraf T. Al-Hinai, N. Al-Naamani, Issa Al-Amri and **T. Hysen** "Self-assembly of $CuSO_4$ nanoparticles and bending multi-wall carbon nanotubes on few-layer graphene surfaces" *Applied Physics A* 105 (2011) 469–477.

12. S. H. Al-Harthi, M. Al-Barwani, M. Elzain, N. Al-Naamani, and **T. Hysen** "Nanobubbles stability and multiwall carbon nanotubes straightening on few-layer graphene surfaces" *Journal of Applied Physics* 110 (2011) 044319.

13. T. Senoy, T. **Hysen**, D. K. Avasthi, A. Tripathi, R. V. Ramanujan and M. R. Anantharaman "Swift heavy ion induced surface modification for tailoring coercivity in Fe–Ni based amorphous thin films" *Journal of Applied Physics* 105 (2009) 033910.

14. **T. Hysen**, V. Thomas, R. V. Ramanujan and M. R. Anantharaman "Thermal and structural analysis of the crystallization dynamics of metallic glass - $Fe_{40}Ni_{38}B_{18}Mo_4$" *Journal of Optoelectronics and Advanced Materials* 11 (2009) 1094–1099.

15. **T. Hysen**, T. Senoy, R. V. Ramanujan and M. R. Anantharaman "On the crystallization kinetics and micro-structural transformations of $Fe_{40}Ni_{38}B_{18}Mo_4$ alloys" *Journal of Materials Science* 43 (2008) 635–640.

16. **T. Hysen**, S. Deepa, S. Saravanan, R. V. Ramanujan, D. K. Avasthi, P. A. Joy, S. D. Kulkarni and M. R. Anantharaman 'Modified Herzer model for magnetic evolution of ultra-thin $Fe_{48}Ni_{38}B_{18}Mo_4$ films' *Journal of Physics D: Applied Physics.* 39 (2006) 1993–2000.

17. V. Thomas, Anit Elizebeth, **H. Thomas**, G. Jose, N. V. Unnikrishnan, Cyriac Joseph and M. A. Ittyachen "Studies on the growth and optical characterization of dysprosium praseodymium oxalate single crystals" *Journal of Optoelectronics and Advanced Materials* 7 (2005) 2687 – 2692.

Papers in Conferences

1) Investigations on CoFe Thin Films for Possible MEMS Applications, **IUMRS-ICYRAM**-July 1-6 2012, Singapore

2) 'Magnetic evolution of Ultra-Thin Nano Structural $Fe_{40}Ni_{38}B_{18}Mo_4$ films with Thermal Annealing', ***XIX Kerala Science Congress,*** January 29-31 2007, Kannur. Kerala, India

3) 'Initial Investigations on The Influence of SHI on the Structural Magnetic and Microstructural Properties of Thin Films of $Fe_{48}Ni_{38}B_{18}Mo_4$', **ICMAT**-July *2005,* Singapore

4) 'Magnetic and Structural properties of METGLAS with Swift Heavy Ion Irradiation', ***Proceedings of Indo German Workshop on Nanostructuring by Ion Beams***, 20-24 February 2005, held at Nuclear Science Centre, New Delhi, India

Acknowledgements

It is with profound joy that I present this thesis and I take this opportunity to express my sincere thanks and gratitude to those who have helped me to accomplish this work.

The works reported in this thesis have been carried out under the supervision of Dr. M. R. Anantharaman, Professor, Department of Physics, Cochin University of Science and Technology. I express my deep sense of gratitude for his excellent guidance, competent advice, keen observations and persistent encouragement as well as the concern shown to me during the entire course of my investigation, without which the successful completion of this work would not have been possible.

My thankful acknowledgements are due to University Grants Commission, Government of India for the award of a teacher fellowship, which enabled me to carry out this work. I am also thankful to the Government of Kerala for granting me deputation for the study.

I acknowledge METGLAS® Inc. for providing amorphous ribbon samples for this research.

I wish to acknowledge all former Heads of the Department of Physics, CUSAT, Prof. K. P. Vijayakumar, Prof. V. C. Kuriakose, Prof. Ramesh Babu T., Prof. Godfrey Louis, Prof. M. R. Anantharaman and the present HOD Prof. B. Pradeep for providing the laboratory and library facilities during my research program. I am also thankful to the other faculty members of the department of physics, Prof. S. Jayalekshmi, Prof. Sudha Kartha, Prof. M. K. Jayaraj, Prof. V. C Kuriakose, Prof. M. Sabir, Dr. Junaid Bushiri and Dr, Titus K Mathew.

I am greatly indebted to Dr. Salim Al-Harthi who gave me the opportunity to work with him in the Department of Physics, Sultan Qaboos University, Sultanate of Oman and gave me untiring help and support. I cannot forget the helping hands extended by Prof. A. K. George and Dr. Imad Al-Omari during my stay at Oman.

Contents

On the Tailoring of Magnetic Properties of Fe-Based Alloy Thin Films by Swift Heavy Ion Irradiation and Thermal Annealing

The development of new materials has been the hall mark of human civilization. The quest for making new devices and new materials has prompted humanity to pursue new methods and techniques that eventually has given birth to modern science and technology. With the advent of nanoscience and nanotechnology, scientists are trying hard to tailor materials by varying their size and shape rather than playing with the composition of the material. This, along with the discovery of new and sophisticated imaging tools, has led to the discovery of several new classes of materials like (3D) Graphite, (2D) graphene, (1D) carbon nanotubes, (0D) fullerenes etc. It is in this context that the world renowned material scientist Eiji Kobayashi remarked: "Those who control materials control technology". This adage reflects the enormous importance of material science in the development of technology and thereby progress of a country. Also in order to keep pace with the Moore's law, semiconductor industry is pushing the limits of technology from micro to nanoscale where a whole new set of problems needs to be solved. Thus the study of materials is synonymous with technology and progress.

Magnetic materials are in the forefront of applications and have been contributing their share to remove obsolescence and bring in new devices based on magnetism and magnetic materials. They find applications in various devices such as electromagnets, read heads, sensors, antennas, lubricants etc. Ferromagnetic as well as ferrimagnetic materials have been in use in the form of various devices. Among the ferromagnetic materials iron, cobalt and nickel occupy an important position while various ferrites finds applications in devices ranging from magnetic cores to sensors.

Right from the beginning of metallurgy metallurgists were trying to improve upon the properties of metals and their alloys by various treatments and alloying. Most metals are crystalline in the solid state which means that their

atoms are arranged in an ordered manner. Most of the conventional processing routes to synthesise metals and alloys from the melt have very small cooling rates facilitating the formation of crystalline microstructure.

Metallic glasses or amorphous metal alloys were first synthesized by Klement, Willens and Duwez of California Institute of Technology in 1959 in an $Au_{75}Si_{25}$ alloy system by rapid cooling from the melt. Since then several experimental and theoretical investigations were carried out on a variety of systems and as a result, several new alloy systems were reported in scientific literature. The absence of long range order and random structure make them suitable for a variety of applications. For example iron based metallic glasses can be made extremely soft magnetic by judicious choice of alloying elements and post processing. Magneto-elastic sensors made up of amorphous metallic glass ribbons or wires, were used to detect a variety of physical parameters including stress, pressure, temperature, flow velocity, liquid viscosity, magnetic field, and mass loading. Metallic glasses are also very tough, light weight and elastic; even though they can be very brittle once they crystallise. They can be classified into various groups based on any of the properties discussed above. Based on the magnetic properties they can be classified into ferrous and nonferrous.

Metallic glasses are also light weight, tough and cheaper than high-quality steels or titanium alloys, and hence they make very good implants. They can be also made biodegradable. Mg-Zn-Ca metallic glasses are biocompatible as well as biodegradable. When such glasses are used as bone implants in the body, they are absorbed at a rate of about a microgram a day until they are completely absorbed by the body which makes them excellent candidates for implants

Among the variety of properties exhibited by metallic glasses, soft magnetic properties are of particular importance owing to their possible applications in transformers, motors, sensors, power electronics, electrical energy control/management systems, telecommunication equipments and pulse power devices.

The desirable properties for a soft magnetic material in high-end applications include, (1) higher magnetic induction and permeability and (2) capability of working at higher temperatures, along with desirable mechanical strength, and corrosion resistance power. In realising these properties, the major factors to be considered include alloy chemistry, structure and importantly the ability to tailor microstructural features. The materials used in soft magnetic applications must be optimized in terms of their intrinsic and extrinsic magnetic properties as well as their morphology. The intrinsic magnetic properties like the saturation magnetic induction (M_s), and Curie temperatures (T_c), are dictated by alloy composition and crystal structure. The extrinsic magnetic properties like coercivity (H_c) and remanence (M_r) are controlled by the morphology, crystal structure and anisotropies in the system. Technically a good soft magnetic material should have high permeability, low hysteresis loss, large saturation, remnant magnetizations and high Curie temperature.

Before the advent of rapid quenching techniques and realisation of metallic glasses, soft magnetic properties of conventional crystalline materials are fine tuned by tailoring the composition and optimizing the microstructure. It was the general observation that measure of the magnetic hardness (the coercivity, H_c) is roughly inversely proportional to the grain size (D) for grain sizes exceeding 0.1-1 mm. Recent developments in the study of magnetic coercivity mechanisms have led to the further understanding that for very small grain sizes D < 100 nm, where H_c decreases rapidly with decreasing grain size. All the above discussed properties make metallic glasses highly desirable for applications in soft magnetic cores. The desire for large magnetic inductions limits choices to alloys of Fe and Co possessing the largest magnetic moments among the elements. Curie temperatures are also largest for elemental Fe (778°C) and Co (1108°C), suggesting the use of Fe or Co (or Fe-Co) alloys especially in high temperature applications.

Due to the remarkable magnetic and structural properties, the magnetic amorphous alloys have replaced many conventional crystalline soft magnetic

materials in applications ranging from DC to high frequencies. A spinoff of this technology is nanocrystalline materials offering much more desirable soft magnetic properties than their amorphous counterparts. Nanocrystalline alloys obtained by the devitrification of metallic glasses have been the subject matter of intense research ever since their discovery. Since then much attention had been focused on the structural and magnetic features of the bulk amorphous alloys and their changes resulting from various thermal treatments. They usually possess a biphasic structure with soft magnetic nanocrystalline grains surrounded by a magnetic/non magnetic phase. These alloys are often synthesized by melt quenching techniques with cooling rates often exceeding 10^6 K/s which are subsequently subjected to heat treatment to induce nanocrystallization. Amorphous alloys which are precursors for nano-crystalline alloys can be synthesized by several methods viz, melt quenching, splat cooling, laser glazing, electro-deposition, ion implantation, sand blasting, swift heavy ion irradiation, and vapour quenching.

In 1988, Yoshizawa *et. al.* first reported that excellent magnetic softness and permeability can be obtained from Fe-Si-B-Nb-Cu amorphous alloys (commercially known as FINEMET), when they are thermally annealed above the first crystallisation temperature (these materials generally have more than one crystallization events as the temperature is increased from room temperature to a higher temperature) to precipitate nanocrystallites in the amorphous matrix. After annealing, the FINEMET alloy is composed of an ultrafine grain structure composed of bcc FeSi solid solution with grain diameter of 10 nm. Since the grain size of the nanocrystalline phase is much smaller than the magnetic exchange correlation length, the magneto-crystalline anisotropies are averaged out over several grains leading to excellent soft magnetic properties. In FINEMET alloy Cu acts as a nucleating agent and Nb inhibits grain growth. An alloy with a nominal composition $Fe_{40}Ni_{40}P_{14}B_6$ under the trade name METGLAS 2826A is also reported in the literature. Because of their attractive properties and relative scarcity in the number of reported glassy metals at that time, this material was

thoroughly studied by many investigators. It was found that phosphorous atoms tend to migrate out of the material, resulting in the brittle nature of the ribbon. A glassy alloy with the composition $Fe_{40}Ni_{38}Mo_4B_{18}$ (METGLAS 2826MB®) was then introduced to replace the phosphorous containing alloy. The material in the nanocrystalline state is reported to have a very low magnetostriction and excellent soft magnetic properties. In all these materials nanocrystallization can be induced by thermal annealing, current annealing, swift heavy ion irradiation, mechanical milling etc.

By the time the first glassy alloys were reported by Duwez *et. al.*, the existence of ferromagnetic ordering in amorphous structures had already been predicted by Gubanov [1]. He made this prediction considering only the exchange interactions among neighbouring atoms and the radial distribution function for the atoms. Before Gubanov's prediction became known, some thin films were reported to have amorphous structure with ferromagnetic properties. These include Ni-P and Co-P films by electro-deposition [2]. Experimental evidence for the existence of ferromagnetism in amorphous solids was provided by the observation of magnetic domains in Fe, Ni-P and Co-Au films obtained by vapour-evaporation. Some of the metastable amorphous structures obtained by vapour evaporation on cold substrates were stabilized by introducing some impurities.

Magnetic properties, such as magnetostriction, anisotropy field, and the coercive force, of the FCC phase Co–Fe–Ni films have been studied and reported by various researchers [3]. Senoy Thomas and others of Magnetics laboratory of Cochin University have done the annealing and SHI irradiation induced magnetic evolution of Fe-Ni thin films of composition $Fe_{55}Ni_{45}$ prepared using thermal evaporation. They reported the films to have a thin native oxide layer on top. The magnetic evolution with annealing is explained based on the random anisotropy model for two dimensional cases. The SHI induced variations were correlated to the surface evolution with irradiation fluence [4,5].

Co-Fe thin films are usually prepared on different seed layers like CoO, Au/MgO etc. to further reduce their coercivity. From a literature survey it is found that research on Fe and Co based thin films are still going on and there is ample scope for fabrication and tailoring of properties of thin films based on them. More recently, thin film soft/hard magnetic materials has been recognized as a promising and high performance material in the field of micro/nano-electro-mechanical system (MEMS/NEMS) applications, since it can be patterned with standard lithography techniques and fabricated in batch process.

Attempts to fabricate thin film forms of metglas2826MB were reported in the literature by many researchers [6,7]. If Fe and Ni are thermally evaporated onto a substrate at room temperature, one generally ends up with a crystalline thin film. However the film can be made amorphous by the addition of small amount of boron. This is demonstrated in the case of metallic alloys. Lin *et. al.* reported that Fe-B can be made amorphous with boron concentrations as low as 5% [8]. Vapour deposition at high vacuum can be utilised to deposit Fe-Ni-B on suitable substrates. This method can be used as a cost effective way of realising Fe-Ni-B thin films using thermal evaporation. Thermal evaporation being a cheap technique will allow scaling up the process for industrial applications.

The magnetic behaviour of metallic glasses is well explained by the Herzer model applicable to bulk materials. The model predicts that when the average separations between the crystals as well as their sizes are smaller than the ferromagnetic exchange correlation length, the magnetic anisotropies are averaged out due to the random fluctuation of anisotropies over several grains and leads to low values of coercivity. When one of the dimensions of the system is reduced to sizes less than the exchange correlation length, the system should behave like 2D systems. It is interesting to investigate whether it obeys the Herzer Model extended to 2D.

Magnetic properties of amorphous alloy ribbons can be tailored by nanocrystallisation. This can be achieved by annealing (current/thermal) as well as low/very high energy ion irradiation. Ion irradiation has been used for

material modification since a long time. The ion beams penetrating through a material loses energy to the target atoms via a number of process leading to various physical phenomenon like 1) latent tracks, 2) phase transitions, 3) amorphisation, 4) damage creation, 5) annealing effects, 6) dimensional changes, and 9) nanostructures. Since the magnetic properties of films are sensitively dependent on the surface as well as interface roughness – they can induce various surface morphologies in metallic films. Hence the magnetic evolution with surface morphology evolution resulting from SHI irradiation is yet another motivation for this investigation. Further this can serve as a test to check whether tracks can be induced in metallic glass thin films by SHI.

The magnetic properties of thin films are dependent on various factors like nature of the film, crystallinity, crystal structure, anisotropies, stress, thickness, composition and surface as well as interface roughness. A detailed investigation on the effect of substrate roughness on the soft magnetic properties of films is not only important from the fundamental perspective but also assumes significance from the application point of view.

The anisotropies in a magnetic film can be fine tuned by playing with the factors that give rise to these effects. In thin films the easy axis usually tends to lie along the direction where film has larger dimensions. Subsequently the anisotropy can be controlled by depositing nanostructures in the film. Oblique angle deposition can be used to deposit nanostructures on substrates. Oblique angle deposition yield nanostructures and the slanting of the nanostructures with respect to the surface normal can be fine-tuned to some extent by changing the angle of impingement of ions with respect to the beam direction during deposition.

In this perspective the main focus of the present research are:

i. *Fabrication of thin films of Fe-Ni and evaluation of the evolution of magnetic properties with thermal annealing.*

ii. *Swift heavy ion induced surface and micro structural evolution in Fe-Ni thin films*

iii.   *Fabrication of thin films of Co-Fe-Si and evaluation of the evolution of magnetic properties with thermal annealing.*

iv.   *Evolution of surface roughness induced magnetic properties by swift heavy ion Irradiation on Co-Fe-Si thin films deposited on glass and silicon substrates.*

v.   *Fabrication of nanostructures based of Co-Fe-Si and their morphology and magnetic characterisation.*

vi.   *Evaluation of the kinetic triplets for the bulk amorphous alloys Fe-Ni-Mo-B and investigation of the evolution of their magnetic properties with thermal annealing.*

vii.   *Correlation of results*

The proposed thesis is entitled "*On the Tailoring of Magnetic Properties of Fe-Based Alloy Thin Films by Swift Heavy Ion Irradiation and Thermal Annealing*" and consists of ten chapters.

Chapter I gives a general introduction and touch upon the basic properties of metallic glasses, nanocrystallization, amorphous thin films. Origin of magnetism in metallic glasses is also discussed in detail.

Chapter II deals with the theoretical concepts related to the estimation of kinetic triplets of metallic glasses. The isoconversional and isokinetic methods are discussed in detail. The process of physical vapour deposition for thin film fabrication is discussed. The evolution of surface morphology during film growth is discussed in the light of the Kader, Parisi, Zhang model. The two main magnetisation reversal mechanisms viz, the Stoner Wohlfarth model and the Kondorsky models are detailed. The sources of anisotropies in a metallic glass are explained and the origin of random anisotropy is elaborated. The Random anisotropy model explaining the dependence between grain size and coercivity in metallic glasses is discussed. The variation in surface roughness with SHI and the effect of SHI on the magnetic properties of metallic glasses and thin films is discussed. The evolution of surface morphology with thin film deposition at oblique angle deposition is also discussed.

Chapter III deals with the various experimental techniques used for characterising the samples prepared during this investigation. The techniques

involve atomic absorption spectroscopy, energy dispersive X-ray spectroscopy, X-ray photo electron spectroscopy, x-ray diffraction, Glancing angle X-ray diffraction, transmission electron microscopy, atomic force microscopy/magnetic force microscopy, scanning electron microscopy, thickness profiler, secondary ion mass spectroscopy, vibrating sample magnetometry and magneto optic Kerr effect.

Chapter IV discusses the evolution of magnetic properties of Fe-Ni-B with microstructural properties brought about by thermal annealing. The evolution of coercivity with thermal annealing is correlated with the change in grain size. The modified Herzer model is used to correlate the variation of coercivity with grain size.

Chapter V deals with the fabrication of Co-Fe-Si thin films with thermal evaporation. The films were subjected to thermal annealing and the variation in magnetic properties with thermal annealing is investigated. The angular variation of coercivity from in plane to out of plane direction is investigated using VSM and the observed variation is explained using the modified Kondorsky model.

Chapter VI deals with the effect of SHI irradiation on the surface morphology of Fe-Ni-B thin films. The variation in surface roughness is correlated to the variation in coercivity. On irradiation with SHI at fluence $3X10^{11}$ ions/cm^2 the coercivity decreases compared to the pristine sample. As the irradiation fluence is further increased to $3x10^{12}$ ions/cm^2 and $3x10^{13}$ ions/cm^2 the coercivity progressively increases.

Chapter VII reports the effects of SHI on the surface morphological properties of thin films of Co-Fe-Si deposited on glass and silicon substrates. The films deposited on silicon substrates show roughness smaller than those deposited on glass. The variation in coercivity with annealing is correlated with the change in surface roughness.

Chapter VIII discusses oblique angle deposition as a technique for forming nanostructures. The effect of deposition angle on the morphology of

thin films is investigated. The effect of deposition angle on the magnetic properties of resulting thin films is also investigated.

Chapter IX is the concluding chapter of the thesis and in this chapter the salient observations and the inferences out of these investigations and the summary of results are presented in a nutshell. The scope for future work is also proposed here.

Appendix A deals with evaluation of kinetic triplets (activation energy of crystallization, Avarami exponents and frequency factor) for the bulk amorphous alloy Fe-Ni-Mo-B using the various mathematical models available in literature to investigate which model is most suited for estimating each of the kinetic triplets

References

[1]   A.I. Gubanov, Soviet Phys. Solid State 2 (1960) 468.

[2]   A. Brenner, D.E. Couch, E.K. Williams, J. Res. Natl. Bur. Std. 44 (1950) 109.

[3]   R. Lampert, J. Gorres, M. Hanson, IEEE Transactions on Magnetics 4 (1968) 525.

[4]   S. Thomas, S. H. Al-Harthi, D. Sakthikumar, I. Al-Omari, R. V. Ramanujan, Y. Yoshida, M. R. Anantharaman, Journal of Physics D: Applied Physics 41 (2008) 155009.

[5]   S. Thomas, H. Thomas, D. K. Avasthi, A. Tripathi, R. V. Ramanujan, M. R. Anantharaman, Journal of Applied Physics 105 (2009) 033910.

[6]   M. Jyothi, C. Suryanarayana, Zeitschrift Für Metallkunde 76 (1985) 801.

[7]   C. Liang, C. Gooneratne, D. Cha, L. Chen, Y. Gianchandani, J. Kosel, Journal of Applied Physics 112 (2012) 113912.

[8]   C. J. Lin, Applied Physics Letters 41 (1982) 721.

Chapter 1

Introduction

1.1	Magnetism in Amorphous alloys
1.2	Amorphous and Nano-crystalline Soft Magnetic Materials
1.3	Metallic Glasses
1.4	Nanocrystallisation of metallic glasses
1.5	Amorphous and Nanocrystalline Thin Films
1.6	Motivation of the Present Work
1.7	Objectives

Magnetism and magnetic materials have been playing a lead role in our daily life ever since the discovery of lodestone. It is history that the discovery of lodestone paved way to the discovery of continents and gave birth to various civilisations. From time immemorial magnetic materials have been playing a key role in the day to day life of human beings. In modern times magnetic materials are synonymous with technologies.

In recent times studies in magnetic materials have been on the rise and have lead to new fields/disciplines like spintronics, multiferroics, giant magneto resistance (GMR), magnetic refrigeration and carbon magnetism. The influence of magnetic materials is so great that the magnetic industry has almost surpassed the semiconductor industry. Though magnetism is an age old subject, it is a rich area in physics especially materials science where a lot more is to be understood. Quantum mechanics has been playing a lead role in explaining some of the new phenomenon and will continue to play a seminal role in the years to come. With the advances in quantum mechanics and condensed matter physics, physicists were able to provide theoretical explanations for the occurrence of magnetism in metals and alloys.

Most metals are crystalline in the solid state, which means their atoms are arranged in an ordered manner. They are crystalline because they bond via metallic bonding which does not impose any restrictions as to the number and position of nearest neighbouring atoms, and have dense atomic packing. Most of the conventional processing routes to synthesise metals and alloys from the melt have very small cooling rates, facilitating the formation of crystalline microstructure. However by employing sufficiently large cooling rates, alloys could be rendered amorphous bypassing the amorphous state resulting in a metastable amorphous alloy.

Metallic glasses were first synthesized by Klement, Willens and Duwez of California Institute of Technology in 1959 in an $Au_{75}Si_{25}$ alloy system by rapid

cooling from the melt [1]. In his book chapter entitled "Metallic glasses-historical background", Duwez reminiscence the first experiment, based on "the gun technique" as "a success combined with a failure". His technique consists of shooting a fine stream of melted liquid at high velocities into a water cooled copper drum. He was able to obtain sufficient quantity of metallic glass to do x-ray diffraction studies. The failure was the destruction of experimental apparatus. In Duwez's own words: "the shock pressure was too high and about half of the apparatus disintegrated, sending hot broken pieces into the laboratory"[2].

Since then several experimental and theoretical investigations were carried out on a variety of systems and as a result several new alloy systems were discovered [3,4]. The absence of long range order and random structure make them suitable for a variety of applications. For example iron based metallic glasses can be made extremely soft magnetic by judicious choice of alloying elements and post processing. Magneto-elastic sensors made up of amorphous metallic glass ribbons or wires, were used to remotely detect a variety of physical parameters including stress, pressure, temperature, flow velocity, liquid viscosity, magnetic field, and mass loading [5]. Metallic glasses are very tough, light-weight and elastic; even though they can be very brittle once they crystallise. Metallic glasses can be classified into various groups based on any of the properties discussed above. A general classification is based on their magnetic properties and based on that they can be classified as ferrous and nonferrous. Since 1990, a number of glass-forming systems with excellent glass forming ability (GFA) in the La [6], Zr [7–11], Pd [12], Ti [13], Co [14], Ni [15] and Fe [16–18] systems have been discovered, which enabled the synthesis of bulk specimens with dimensions in the millimetre range by conventional metallurgical casting methods. The maximum diameter of the bulk amorphous alloys tends to increase in the order of Pd-Cu >Zr> Ln = Mg > Fe > Ni > Co = Ti systems [19]. Fe-based bulk metallic glasses with critical cooling rates below 10^3K/s have been often found in Fe-based alloy systems containing metalloids (B, C, Si, and P) and

early transition elements (Zr, Nb, Hf). The first Fe-based bulk glassy alloys were prepared in 1995 and since then, a variety of Fe-based bulk glassy alloys have been prepared with good soft magnetic properties. Those properties are attractive compared with conventional crystalline alloys and they are very useful in a wide range of technical applications.

Metallic glasses, being lightweight, tough and cheaper than high-quality steels or titanium alloys make good candidates for implants. They can also be made biodegradable. Mg-Zn-Ca metallic glasses are biocompatible as well as biodegradable. When Mg-Zn-Ca glasses are used as bone implants in the body, they are absorbed at the rate of about a microgram a day until they are completely absorbed by the body which makes them excellent candidates for implants [20,21].

Among the variety of properties exhibited by metallic glasses, soft magnetic properties are of particular importance owing to their possible applications in transformers, motors, and a wide variety of magnetic components in sensors, power electronics, electrical energy control/management systems, telecommunication equipment and pulse power devices [22].

The desirable properties for a soft magnetic material in high-end applications include, (1) higher magnetic induction and permeability and (2) capability of working at higher temperatures, along with desirable mechanical strength and corrosion resistance. In realising these properties the major factors to be considered include alloy chemistry, structure and, importantly the ability to tailor micro-structural features. The materials used in soft magnetic applications must be optimized in terms of their intrinsic and extrinsic magnetic properties as well as their morphology. The intrinsic magnetic properties, the saturation magnetic induction (M_s), and Curie temperatures (T_c), are determined by alloy composition and crystal structure [19].The extrinsic magnetic properties like coercivity (H_c) and remanence(M_r) are dictated by the morphology, crystal structure and anisotropies in the system. Technically a good soft magnetic

material should have high permeability, low hysteresis loss and coercivity, large saturation and remnant magnetizations and high Curie temperature.

Amorphous metallic glasses possess random arrangement of atoms and hence don't possess magneto-crystalline anisotropy. They possess very low anisotropies (stress/field induced) and hence can have extremely low coercivities and high permeabilities compared with their bulk crystalline counterparts. They exhibit increased strength/hardness, enhanced diffusivity, improved ductility/toughness, reduced density, reduced elastic modulus, higher electrical resistivity, increased specific heat, higher thermal expansion coefficient, lower thermal conductivity, and superior soft magnetic properties in comparison with conventional coarse grained materials [22].

Before the advent of rapid quenching techniques and realisation of metallic glasses, soft magnetic properties of conventional crystalline materials were fine-tuned by tailoring the composition and optimizing the microstructure. It was the general observation that measure of the magnetic hardness (H_c) is roughly inversely proportional to the grain size (D) for grain sizes exceeding 0.1-1 μm. However, recent developments in the understanding of magnetic coercivity mechanisms have led to the inference that for grain sizes of D < 100 nm, H_c decreases rapidly with decreasing grain size [23]. All the above discussed properties make metallic glasses highly desirable for applications in soft magnetic cores. The desire for large magnetic inductions limits choices to alloys of Fe and Co having the largest magnetic moments among the elements. Curie temperatures are also largest for elemental Fe (1051 K) and Co (1381 K), suggesting the use of Fe or Co (or Fe-Co) alloys especially in high temperature applications.

1.1 Magnetism in Amorphous Alloys

Out of all the metallic elements, ferromagnetism is exhibited by three of the *3d* transition metals (Fe, Co, and Ni), and heavy rare-earth metals such as Gd, Tb, Dy etc. The *3d* transition metals have high Curie temperatures and exhibit

ferromagnetism with large spontaneous magnetizations at room temperature. The *3d* electrons which are the carriers of magnetism exist relatively screened from the atomic core, and are considered to be moving freely among the atoms (or itinerant) and they form a band structure. On the other hand, the carriers of magnetism in rare-earth metals are 4f electrons, which are located deep inside the atoms so that their magnetic moments are well localized at individual atoms [24]. The magnetic dipole moments exhibited by metals and alloys can be explained based on the band theory of solids. The band theory is based on the notion that when N atoms are brought together to form a solid, the individual energy levels are split into N closely spaced levels to form a continuum/band [25]. The band theory could successfully predict the non-integral or half integral atomic dipole moments and resulting ground state magnetizations in metals and alloys as well as the dependence of band widths and exchange splitting on magnetic coordination number and atomic volume [25]. Figure 1.1 shows the Slater-Pauling curve that illustrates the variation of the mean atomic magnetic dipole moment as a function of outer electron number in transition metal alloy systems. Slater-Pauling curve is an important starting point in deciding the alloy composition for a particular application. Applications requiring large induction limit choices of alloys to those rich in Fe or Co and therefore near the top of the Slater-Pauling curve. As evident from the Slater-Pauling curve, Fe-Co alloys exhibit the largest magnetic inductions among any material, which possess large Curie temperatures also, making them desirable for high temperature applications. The ferromagnetic elements Fe (Z=26), Co (Z=27), and Ni (Z=28) have 4, 3, and 2 vacancies respectively in the *3d* shell. According to Hund's rule of maximum multiplicity, if two or more levels of equal energy are available, electrons will occupy them singly before filling them in pairs. Consider the case of Fe, Co and Ni with partially filled orbital $3d^6$, $3d^7$ and $3d^8$; we expect spin magnetic moments of 4, 3, and 2 Bohr magnetons (μ_B), respectively. Actually, these elements exhibit saturation magnetic moments of only 2.2, 1.7, and 0.6 Bohr magnetons per atom,

respectively, at 0K. In the Slater- Pauling curve, the non-integral Bohr magneton numbers of 2.2, 1.7, and 0.6 for Fe, Co, and Ni are smoothly connected by two straight lines. The experimental points for Ni-Co alloys fall on the straight line connecting the points (9, 1.7) for Co and (8, 0.6) for Ni. It is possible to interpret this behaviour by considering that Co atoms with 1.7 μ_B and Ni atoms with 0.6 μ_B are mixed in the alloys, with each atom keeping its individual moment.
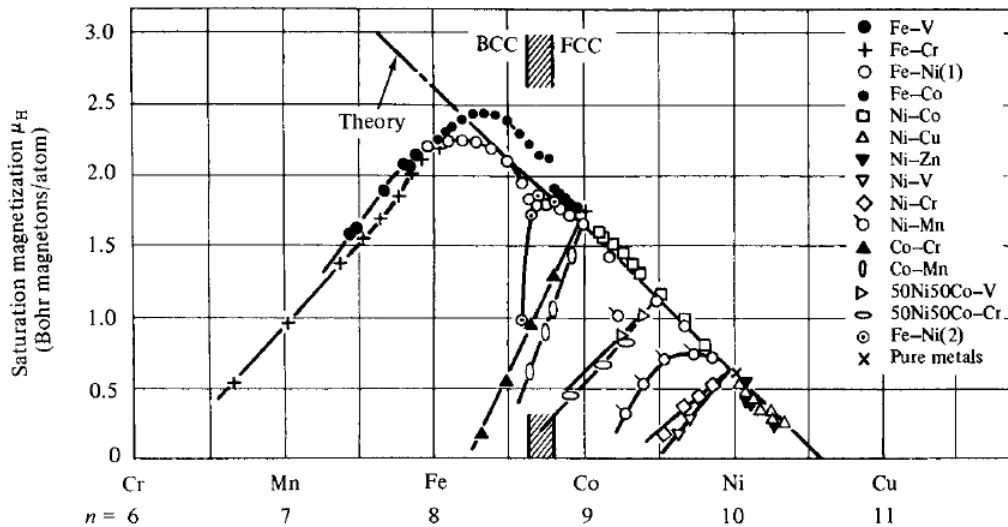
Figure 1.1: Slater-Pauling curve for transition metal alloys. Reproduced from reference [26]

The Slater Pauling curve has the shape of an inverted 'V' with right hand side and left hand side lines forming the inverted V shape. Similar to Ni-Co systems, there are many branches from the right-hand straight line of the Slater-Pauling curve. Each branch shows a decrease in saturation magnetic moment produced by the addition of impurity atoms with fewer positive nuclear charges, i.e. Mn, Cr, V, or Ti. This was attributed to the fact that the magnetic moments of these impurity atoms are coupled anti-ferromagnetically with the ferromagnetic matrix moment, which results in a decrease in the average magnetic moment [27].

In general, the following observations can be made when magnetic elements like Fe, Co and Ni are alloyed to each other and along with other nonmagnetic elements.

- When two elements form a solid solution, the variation of the M_s and T_c with composition is unpredictable.

- In an alloy consisting of two phases, the change in overall composition modifies only the relative amounts of the two phases, while the composition of each phase remains constant. Hence if one phase is ferromagnetic, the M_s of the alloy varies linearly with the weight percentage of the added element in the alloy, and T_c will remain constant.
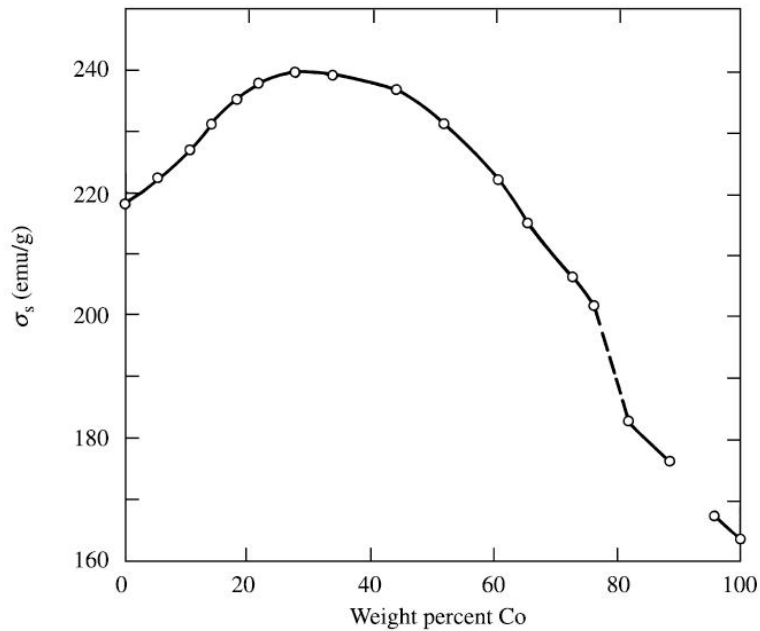
Figure 1.2: Variation of saturation magnetisation in Fe-Co binary alloy with composition. Reproduced from [25].

For example Fe-Co alloy forms solid solution over a wide range of compositions and figure 1.2 shows the variation of saturation magnetization with Co addition. The addition of cobalt, which has less magnetic moment per atom than iron, increases the magnetization, and the 30% Co alloy has a higher value of magnetisation at room temperature than Fe or Co itself.

When a non-transition element (e.g., Cu, Zn, Al, Si, etc.) is added to Fe, Co, or Ni, to form an alloy, the magnetization decreases, and the rate of decrease per added atom is not the same for all solutes. When a metal is alloyed to Ni the magnetization of the alloy decreases at a rate proportional to the valency of the solute [25]. 60 atom% of Cu (valence 1) can reduce the magnetization of the alloy to zero, but only 30 atom% of Zn (valence 2) is required for the same. The added atoms appear to contribute all its valence electrons to the 3d band of the alloy. Hence the larger the valency, the more rapidly the band fills up and more rapid the decrease in magnetization. This behaviour is in agreement with the band theory, whereas in the case of Fe and Co rich alloys the rate of decrease of magnetization, at least initially, is independent of the added atom. The added atoms appear to be acting as simple dilutants. For example, the magnetization decreases as though iron atoms, of moment 2.22 μ_B were being replaced by atoms of zero moment. This behaviour is not in terms of the simple band theory.

1.2 Amorphous and Nano-Crystalline Soft Magnetic Materials

Magnetic materials are generally classified as soft and hard magnetic materials [24]. Soft magnetic materials are easy to magnetise and demagnetise. In these types of materials the domain wall motion is easy, leading to very low coercivity. They also possess large magnetic susceptibility and permeability. On the other hand, hard magnetic materials are very difficult to demagnetise due to their large remanence and coercivity. Hence these classes of materials are conventionally used for making permanent magnets.

Another classification of magnetic materials is based on the crystallinity of the samples viz., crystalline and amorphous magnetic materials. In the earlier days of magnetic materials the studies on ferromagnetic materials were mainly concentrated on crystalline iron, cobalt, nickel and their alloys with other elements.

During the past few decades, considerable progress has been obtained in the field of rapid solidification of molten melts that allowed the realisation of materials with new compositions and amorphous structure [28]. Due to their remarkable properties, the magnetic amorphous alloys have replaced many conventional crystalline soft magnetic materials in applications ranging from DC to high frequencies. A spinoff of this technology is the nanocrystalline materials offering much more outstanding desirable soft magnetic properties than their amorphous counterparts. Nanocrystalline alloys obtained by the devitrification of metallic glasses have been the subject matter of intense research ever since their discovery. Since then much attention has been focused on the structural and magnetic features of the bulk amorphous alloys and their changes resulting from various thermal treatments. They usually possess a biphasic structure with soft magnetic nanocrystalline grains surrounded by a magnetic/non magnetic phase [9–12]. These alloys are often synthesized by melt quenching techniques with cooling rates often exceeding 10^6 K/s which are subsequently subjected to heat treatment to induce nanocrystallization [29]. Amorphous alloys which are precursors for nano-crystalline alloys can be synthesized by several methods viz., melt quenching, splat cooling, laser glazing, electro-deposition, ion implantation, sand blasting, swift heavy ion irradiation and vapour quenching [30].

1.3 Metallic Glasses

Metallurgy is one of the oldest of sciences whose history can be traced back to 6000 BCE [31]. Metals were known to many of the oldest civilisations. Metals generally exist in close packed structures leading to the crystalline state. On the other hand metallic glasses are alloys having a random atomic arrangement possessing amorphous structure. They are materials having a short

range order of atoms that were frozen in a liquid configuration because of the clever choice of alloying elements and rapid quenching from melt. For proper glass formation, these elements should have large negative heats of mixing and near eutectic compositions. The alloying elements required to have different atomic sizes to impede crystal formation in the system. But unlike glasses, which are insulating in nature, these materials possess electrical conductivity.

Klement (Jr.), Willens and Duwez of California Institute of Technology were the first to have successfully synthesised $Au_{75}Si_{25}$ alloy in amorphous form in 1959 [1]. They achieved this remarkable feat of bypassing the nucleation and growth of crystals by cooling down the sample with cooling rates of 10^6 K/s. In order to facilitate these large amounts of cooling rates, the material needs to have very low thickness and this limited the size and shape of metallic glasses that could be produced those days. The obtained materials are usually in the form of thin foils or wires. Today the techniques of melt quenching has been extensively developed and elaborated for the purpose of producing a wide variety of metallic glasses [32].

Even though metallic glasses were discovered in 1960s, the research on metallic glasses gained momentum in early 70s and 80s when commercial manufacturing methods of metallic glass ribbons, wires, and sheets [33] were developed. Following this renewed interest, the academic as well as industries involved in research came up with newer and newer metallic glasses of different compositions suitable for a wide variety of applications [34].

The research work of Turnbull and group provided further impetus to the development of these materials [19]. They proposed that glass transition exhibited by conventional glasses and polymers could also be observed in metallic glasses [35–37]. Turnbull predicted that a quantity called the reduced glass transition temperature, which is the ratio of glass transition temperature to the melting point of the alloy, can be used as a criterion to establish the glass forming

ability (GFA) of the material [37]. Turnbull showed that a material with GFA of 2/3 will be very slow in crystallizing within the ordinary time scales and can only crystallise within a narrow temperature range [38]. This criterion is generally used as a rule of thumb for finding the glass forming ability of an alloy [32].

In 1969, Chen and Turnbull reported formation of amorphous alloys based on Pd-Si by quenching melts to room temperature at various cooling rates. Certain ternary alloys such as Pd-Au-Si, Pd-Ag-Si and Pd-Cu-Si were reported to form glasses with thicknesses greater than 1 mm at cooling rates as low as 10^2 K/s [37]. Ternary amorphous alloys were also reported in the literature during the same period in Au-Si-Ge [36] and Fe-P-C systems [39]. Chen in 1974 developed Pd-Cu-Si in millimetre range thereby increasing the size of metallic glasses that can be synthesised in the laboratory. They used simple suction-casting methods to fabricate millimetre diameter rods of Pd–Cu–Si metallic glass at a significantly lower cooling rate of 10^3 K/s [40,41]. From the late 80's Inoue's group from Japan reported the synthesis of large number of multi-component alloy systems exhibiting amorphous structure fuelling the growth in the field of multi-component alloy systems [42]. Along with the experimental synthesis of these materials, theoretical aspects were also investigated in detail by several groups. The important aspect that stimulated these investigations is finding a successful theory or set of rules to predict the glass forming ability of an alloy. The most widely accepted empirical rules for the formation of glasses as put forward by Inoue [43] are atomic size mismatch, high negative heat of mixing, and multi-component alloy system. Since these preliminary investigations and reports, a large number of metallic glasses with varied compositions and physical properties were reported by various groups around the globe. The developments in the field of metallic glasses is well documented by the reviews of [44–48] and several conference proceedings [47,49,50]. As extensive studies on metallic glasses progressed through years, magnetic amorphous alloys gained importance due to their applications in fields like transformer cores, shielding, sensors and thin

films. It may be noted here that for soft magnetic applications the materials should have high saturation magnetic induction, and Curie temperatures, which are determined by alloy composition and crystal structure. Among the magnetic alloys the commercially produced FINEMET^{TM}, NANOPERM^{TM} and HITPERM^{TM} alloys assume importance owing to their interesting properties and diverse applications resulting primarily from their nanocrystalline grain structure.

1.4 Nanocrystallisation of Metallic Glasses

Metallic glasses generally have more than one crystallization events as the temperature is increased from room temperature to a higher temperature. In 1988, Yoshizawa *et. al.* first reported that excellent magnetic softness and permeability can be obtained in Fe-Si-B-Nb-Cu amorphous alloys, when they are thermally annealed above the first crystallisation temperature to precipitate nanocrystallites in the amorphous matrix [51]. They studied the magnetic properties of Fe-Si-B-Nb-Cu (FINEMET) alloys prepared by annealing amorphous ribbons. Excellent soft magnetic properties were exhibited by additions of Cu and Nb, Mo, W, Ta, etc., which have the effect of raising the crystallization temperature. The Cu addition to the Fe-Si-B-Nb alloy has the effect of nucleating body centered cubic (bcc) Fe-Si solid solution and suppressing the formation of Fe-metalloid compounds. After annealing, the "FINEMET" alloy is found to be composed of an ultrafine grain structure composed of bcc Fe-Si solid solution with grain diameter of 10 nm. Since the grain size of the nanocrystalline phase is much smaller than the exchange correlation length, the magneto-crystalline anisotropies are washed out over several grains leading to excellent soft magnetic properties [52]. In Fe-Si-B alloy copper acts as a nucleating agent thereby providing large number of nuclei for crystallites to form and Nb inhibits grain growth [51,53]. FINEMET is reported to have very high relative permeability in the low and high-frequency range and an almost equivalent frequency dependence of relative permeability as the Co-

based amorphous alloys. Hence, since its discovery these materials are widely used as transformer cores [51,54].

Generally nanocrystalline alloys can be represented by the formulae TL_{1-x} $(TE-M-NM.)_x$ where TL denotes a late (ferromagnetic) transition metal element, TE is an early transition metal element, M is a metalloid, and NM is a noble metal. This composition usually has $x < 0.2$. The remaining early transition metals (TE = Zr, Nb, Hf, Ta etc.) and metalloids (M = B, P, Si etc.) are added to promote glass formation in the precursor. The noble metal elements (TN = Cu, Ag, Au etc.) serve as nucleating agents for the ferromagnetic nanocrystalline phase. These alloys may be single phase (Type I) or two phase materials with a nanocrystalline ferromagnetic phase embedded in a residual amorphous phase (Type II) [19].

Soft magnetic alloys, based on Fe-M-B-Cu, have been patented under the trade name NANOPERM [55]. These nanocrystalline alloys have been optimized to achieve small magnetostriction coefficients and large permeabilities. (Fe-Co)-M-B-Cu (M = Nb, Hf, or Zr) nanocrystalline alloys, called HITPERM have been shown to have large magnetic inductions (1.6 to 2.1 T) combined with high permeabilities and high Curie temperatures. In FINEMET α-Fe-Si nanoparticles with a DO_3 structure is observed while in NANOPERM α-Fe particles with a bcc structure are formed. In HITPERM alloys [56–58] nanocrystalline α and α' bcc and B_2-Fe-Si and B_2- Fe-Co are formed with significantly improved high temperature magnetic properties than in the former two. An alloy with composition $Fe_{40}Ni_{4o}P_{14}B_6$ under the trade name METGLAS 2826A is also reported in the literature [59]. Because of their attractive properties and relative scarcity in the number of reported glassy metals at that time, this material was studied by many investigators. It was found that phosphorous atoms tend to migrate out of the material, resulting in the brittle nature of the ribbon. A glassy alloy with the composition $Fe_{40}Ni_{38}Mo_4B_{18}$ [(METGLAS 2826MB$^®$) [60] was then introduced by replacing P with Mo in METGLAS 2826A. The material in the

nanocrystalline state is reported to have a very low magnetostriction and excellent soft magnetic properties. In all these materials nanocrystallisation can be induced by thermal annealing, current annealing, swift heavy ion irradiation, mechanical milling etc. [61–63].

1.5 Amorphous and Nanocrystalline Thin Films

During the time the first glassy alloys were reported by Duwez *et. al.*, the existence of ferromagnetic ordering in amorphous structures had already been predicted by Gubanov [64]. He made this prediction considering only the exchange interactions among neighbouring atoms and the radial distribution function for the atoms. Before Gubanov's prediction became known, some thin films were reported to have amorphous structures with ferromagnetic properties. These include Ni-P and Co-P films prepared by electro-deposition [65]. Experimental evidence for the existence of ferromagnetism in amorphous solids was provided by the observation of magnetic domains in Fe [66], Ni-P [67], and Co-Au [68] films obtained by vapour-evaporation. Some of the metastable amorphous structures obtained by vapour evaporation on cold substrates were stabilized by introducing some impurities [69].

Ever since these observations, a large number of amorphous and nanocrystalline systems were reported in the literature [3,22,32,70,71]. Dietz gave an elaborate account of the reports of magnetic amorphous thin films prepared using vapour deposition and sputtering in a review published in 1977. He suggested that short range atomic ordering is the main cause of the observed uniaxial anisotropy in many amorphous thin film systems [72]. In the late eighties, Grundy reported that pure iron and cobalt can be evaporated to obtain amorphous films [73–75]. He reported that interesting variations in magnetic properties can be brought about by playing with the compositions and microstructures of deposited amorphous alloy phases. Bulk and thin film amorphous metallic glasses, specifically permalloys (Fe-Ni), prepared by rapid quenching and vapour deposition/sputtering were found to have excellent soft magnetic properties which attracted the attention

of magnetic recording industry, thereby fuelling intensive research on these materials [76]. By this time the desirable properties of amorphous alloys like high tensile strength, high resistivity and thin shape along with their high permeability with small induced anisotropy made them hot candidates for sensor fabrication. They were successfully used in magnetometers using zero-magnetostrictive alloys and in stress sensors using high-magnetostrictive alloys [77].

By the beginning of eighties, a novel way of transforming a material to a metastable energy state emerged. This is achieved by reducing its grain size to orders of a few nanometres so that the proportion of atoms in the grain boundaries is equivalent to or higher than those inside the grains. According to Turnbull, this metastability is named as morphological metastability [78]. These materials were subsequently referred to as nanocrystalline materials and since then shown to have properties much improved over their coarse grained cousins. By the end of eighties Herzer [79] put forward the random anisotropy model which is a modified version of the Alben, Becker, Chi [80] model for the evolution of magnetic properties of nanocrystalline materials. This theory was successfully applied for the evolution of magnetic properties of nanocrystalline materials with annealing and subsequent grain growth [52,81–85]. After the discovery of FINEMET ribbon [51], iron based nanocrystalline soft magnetic materials were investigated in thin-film forms also. Thin-film nanocrystalline materials in the Fe-M-C (M = Zr, Hf, Ta, etc.) system have been studied by Hasegava [86].

In the late 90′s thin film metallic glasses received even wider attention because of reports on several new multi-component bulk metallic glasses with good GFA in Mg, Ln, Zr, Fe, Pd, Cu, Ti and Ni based systems by Inoue and his group [42,43,46,87]. Yoon *et. al.* prepared Co-Fe-Si-B films using a six-target dc magnetron sputtering system. They observed that by increasing Co composition in the sputtering target the film structure was changed from an amorphous Co-Fe-Si-B phase to a nanocrystalline Co phase surrounded by an amorphous matrix [88].

Chou *et. al.* reported formation of Fe-Ta-C-N films on quartz substrates by co-sputtering of Fe and Ta-C targets at room temperature and the effect of annealing on the magnetic properties. X-ray diffraction and transmission electron microscopy analysis showed that the as-deposited Fe-Ta-C-N film has a nanocrystalline structure or mixed phase of nanocrystalline and amorphous phases. Jyothi and Suryanarayana in 1985 reported flash deposition of METGLAS 2826MB films from amorphous ribbons [89]. They obtained a metastable solid solution of fcc and simple cubic nanocrystalline phases embedded in an amorphous matrix.   However they have not reported any compositional or magnetic studies.

In 1999 and 2000, Zr\Cu\Al and Pd\Cu\Si ternary thin film metallic glasses produced by sputtering were reported in the literature [90,91]. Because of their excellent castability, good corrosion resistance and mechanical properties, compared to conventional crystalline films, Zr and Pd based thin film metallic glasses (TFMGs) are appropriate choices for MEMS applications. Zr\Al\Cu\Ni TFMGs prepared by sputter deposition and focused ion beam patterning are reported for nano device applications [92].

Cao *et. al.* reported the effects of high magnetic field on the evolution of structural, magnetic and electrical properties of molecular beam evaporated (MBE) Fe_xNi_{1-x} ($0.3 \leq x < 0.8$) thin films. Their results indicated that the crystallinity of the Fe_xNi_{1-x}($x = 0.74, 0.6$) thin films is enhanced, and the γ <111> orientation of the Fe_xNi_{1-x}($x = 0.55, 0.3$) thin films increase with deposition under a 6 T magnetic field [93].

Jung *et. al.* reported magnetic properties of sputtered soft magnetic Fe–Ni films with uniaxial anisotropy. They analysed the microstructure and magnetic properties of polycrystalline $Fe_{100-x}Ni_x$. They deposited films with varying thickness with and without a bias magnetic field to investigate the effect of bias field on magnetic anisotropy. The coercivity versus thickness, analysed using Neel's formula showed that the magnetic parameters for the films with the bias

field follow Neel's formula within the thickness range of 40–100 nm, except the range of 10–40 nm. This result indicated that there is a change in domain wall type at the thickness of 40 nm [94].

Shim *et. al.* reported good high-frequency characteristics for Fe–Co–B and Fe–Co–Ni–B thin films fabricated by RF magnetron sputtering. On adding Ni to Fe–Co–B system, the soft magnetic properties of Fe–Co–Ni–B films improved due to the microstructural changes brought about by Ni [95].

Kin *et. al.* reports that Co–Ni–Fe and Co–Ni–Fe–N soft magnetic thin films prepared using RF sputtering have a tendency to form amorphous phase during the initial growth stage and it gradually changes to crystalline structure as the film thickness increases [96].

Magnetic properties, such as the saturation magnetostriction, anisotropy field, and the coercive force, of the fcc phase of Co–Fe–Ni films have been studied and reported by other groups also [97–99].

Thomas *et. al.* reported thermal annealing and Swift Heavy Ion (SHI) irradiation induced magnetic evolution of Fe-Ni thin films prepared using thermal evaporation. He reported the films to have a thin native oxide layer on top. The magnetic evolution with annealing is explained based on the random anisotropy model for two dimensional cases. The SHI induced variations were correlated to the surface morphology evolution with irradiation fluence [100,101].

Co-Fe thin films are usually prepared on different seed layers to further reduce their coercivity. Thompson *et. al.* reported coercivity of 16 Oe for Co-Fe films grown on Au/MgO seed layers [102]. Platt *et. al.* reported coercivity of 12 Oe for Co-Fe film deposited on CoO. They showed that domain walls in the soft films have relatively large mobility in response to changing magnetic fields below the nominal H_c. They also attributed the observed low coercivity values to the averaging of the anisotropy energy [103]. Vopsaroiua reported the dependence of coercivity on grain size for 20 nm Co-Fe thin films prepared by sputtering. They observed a reduction in the coercivity from 120 Oe for samples with a mean grain size larger than 17 nm down to 12 Oe for a sample with a mean grain size

of 7.2 nm [104]. Ji *et. al.* reported growth and physical property of epitaxial $Co_{70}Fe_{30}$ thin film on Si substrate with a Ti-N buffer layer. They also reported that the films prepared at 450 ^{o}C exhibit a biaxial stress up to 0.52 %. The films were reported to have a small in plane biaxial anisotropy and a very low coercivity of 23 Oe for film thickness greater than 30 nm [105].

1.6 Motivation of the Present Work

A survey of literature reveals that research on Fe and Co based thin films are diverse and still pursued worldwide by scientists and engineers because they are ideal templates for studying magnetism at the alloy level. From an application point of view they are potential candidates for a horde of applications like transformer cores, sensors, magnetic shielding etc. More recently, thin films of soft/hard magnetic materials have been recognized as a promising and high performance material in the field of MEMS applications, since it can be patterned with standard lithography techniques and fabricated in batch process. In thin film devices subjected to ac magnetic fields, only a small amount of material undergoes magnetic cycling and hence the heat generated is less and thus the performance is unaffected over long time use.

$Fe_{40}Ni_{38}B_{18}Mo_4$ is a soft magnetic alloy that exhibits superior magnetic properties suitable for applications in many devices requiring soft materials. Boron aids the amorphous phase formation whereas molybdenum improves the thermal properties of the material [106]. Its magnetic softness after nanocrystallization can be ascribed to its two phase nature consisting of an ultra-fine grained Fe-Ni phase embedded in the remaining boron rich amorphous matrix [107]. The two phases have Curie temperatures of $\approx$ 760 K and $\approx$ 485 K respectively and their contributions to the total saturation magnetisations are $\approx$46 emu/g and $\approx$ 49 emu/g respectively. Its increased curie temperature of 626 K and low saturation magnetostriction of 12×10^{-6} accounts for the good soft magnetic properties exhibited by this material. The material can be tailored by

field annealing for superior soft magnetic properties such as H_c = 7 mOe and a dc permeability of about 45000 [108]. These superlative properties have been exploited for various technological applications namely sensors, actuators, shielding, high frequency transformer cores, magneto-optic sensors, and magnetic recording.

Nanocrystallization is a thermodynamic event which can be characterized by kinetic triplets viz. activation energy of crystallization (E), Avarami exponent (n) and the frequency factor (k_0) [109]. Thermal annealing of metallic glasses can trigger crystallization in the material by providing sufficient energy to the atoms to overcome the energy barrier for crystallization. Upon annealing the metallic glasses the amorphous phase generally devitrifies into a supersaturated solid solution which consequently decays into a mixture of solid solution and crystalline phase or phases. Crystallization proceeds through nucleation, subsequent growth and Ostwald ripening. The kinetics of crystallization of materials can be studied using differential scanning calorimetry techniques carried out in isothermal or non-isothermal mode. There have been diverse reports on the crystallization dynamics of $Fe_{40}Ni_{38}B_{18}Mo_4$ and they all mostly differ in their estimation of kinetic triplets. Hence a thorough investigation to estimate the kinetic triplets of this material based on the various models available in the literature will provide valuable information and shed light to the evolution of crystallization/ amorphisation in such systems.

Attempts to fabricate thin film forms of METGLAS 2826MB were reported earlier by many researchers [89,110]. For example Jyothi [89] *et. al.* used flash evaporation, whereas Cai *et. al.* used sputtering [110]. The latter paper discusses the compositional variations in thin films with variations in the quantity of alloying elements in the target material used for sputtering. If one thermally evaporates Fe and Ni onto a substrate at room temperature one generally ends up with a crystalline thin film. However, the film can be made amorphous by the addition of small amount of boron. This is demonstrated in the case of metallic

alloys. Lin *et. al.* reported that Fe-B can be made amorphous with boron concentrations as low as 5% [111]. Vapour deposition at high vacuum can be utilised to deposit Fe-Ni-B on suitable substrates. This method can be used as a cost effective way of realising Fe-Ni-B thin films using thermal evaporation. During thermal evaporation there are several parameters viz., difference in vapour pressures of elements, evaporation temperature, chamber pressure, deposition rate etc that affect the composition and morphology of thin films. Hence an accurate estimation of the sample composition is very essential to correlate the various physical properties of the films. X-ray photoelectron spectroscopy is used to obtain quantitative estimate of the film composition. Thermal evaporation being an inexpensive technique will allow scaling up the process for industrial applications.

Magnetic properties of amorphous alloy ribbons can be tailored by nanocrystallisation. This can be achieved by annealing (current/thermal) as well as low/very high energy ion irradiation. Both these methods were frequently reported in the scientific literature for inducing crystallization in amorphous materials. Fe-Ni-Mo-B is a well studied material and have well defined crystallization temperatures. The magnetic behaviour of amorphous magnetic materials is explained by the Herzer model applicable to bulk materials. The model predicts that when the average separation between the crystals as well as the crystallite size are smaller than the ferromagnetic exchange correlation length the magnetic anisotropies are averaged out due to the random fluctuation of anisotropies. This in turn reduces the coercivity. When one of the dimensions of the system is reduced to sizes less than the exchange correlation length the system should behave like a two dimensional system. Therefore it is interesting to investigate whether it obeys the Herzer model approximated to the two dimensional case.

Swift ion irradiation has been used for material modification since a long time. The ion beams penetrating through a material loses energy to the target

atoms via a number of process leading to various physical phenomenon like 1) latent tracks, 2) phase transitions, 3) amorphisation, 4) damage creation, 5) annealing effects, 6) dimensional changes and 9) nanostructures. Since the magnetic properties of films are sensitively dependent on the surface as well as interface roughness, ion irradiation can alter the magnetic properties by modifying the surface morphology. Hence a detailed investigation-regarding magnetic evolution with surface morphology changes resulting from SHI irradiation-can give insights about the correlation between surface morphology and thin film magnetism. Further this can serve as a test to check whether tracks can be induced in metallic glass thin films by SHI.

Thin film deposition is a dynamic process and several factors affect the growth of films and thereby influence the final film morphology. Atomic Force Microscope (AFM) is a powerful tool to investigate the surface morphology on nm scales. The morphology can be altered by thermal annealing as well as ion irradiation. The variation in surface morphology will be qualitatively visible in the AFM images. Quantitative information regarding the surface morphology evolution can be extracted from the AFM images by subjecting them to power spectral density (PSD) analysis. The slope of the PSD curve give valuable information regarding the surface roughening/smoothening mechanism operating during thermal annealing/ion irradiation. Hence in this investigation PSD analysis is used to gain information regarding the morphology evolution with thermal annealing and ion irradiation.

The magnetic properties of thin films are dependent on various factors like nature of the film, crystallinity, crystal structure, anisotropies, stress, thickness, composition and surface as well as interface roughness. A detailed investigation on the effect of substrate roughness on the soft magnetic properties of films is not only important from the fundamental perspective but also assumes significance from an application point of view. The magnetic films deposited on substrates (glass, silicon) having various roughness and the magnetic property

variation as a function of substrate roughness is also a promising area for research.

The anisotropies in a magnetic film can be fine tuned by playing with the factors that give rise to these effects. In thin films the easy axis usually tends to lie along the direction where films have larger dimension. Consequently, the anisotropy can be controlled by depositing nanostructures in the film. Oblique angle deposition can be used to deposit nanostructures on substrates. Oblique angle deposition yield nanostructures and the slanting of the nanostructures with respect to the surface normal can be fine-tuned to some extent by changing the angle of impingement of atoms with respect to the surface normal, during deposition. Thus oblique angle deposition is a simple inexpensive technique for designing thin films with desirable magnetic properties.

1.7 Objectives

In this perspective the main focus of the present research are the following:

- Evaluation of kinetic triplets for alloy $Fe_{40}Ni_{38}B_{18}Mo_4$ alloy using various isoconversional and isokinetic methods.
- Fabrication of thin films of Fe-Ni and evaluation of the evolution of magnetic properties with thermal annealing.
- Fabrication of thin films of Co-Fe-Si and evaluation of the evolution of magnetic properties with thermal annealing
- Investigation of the angular variation of coercivity from in plane to out of plane direction in the case of Co-Fe-Si thin films.
- Swift heavy ion induced surface and microstructural evolution in Fe-Ni thin films.
- Evolution of surface roughness induced magnetic properties by swift heavy ion irradiation on Co-Fe-Si thin films deposited on glass and silicon substrates.

- Fabrication of nanostructures based on Co-Fe-Si and their morphology and magnetic characterisation using oblique angle deposition.

- Investigate the influence of substrate characteristics on the magnetic properties of thin films of Fe-Ni and Co-Fe-Ni.

- Correlation of results.

References

[1]   W. Klement, R. H. Willens, P. Duwez, Nature 187 (1960) 869.

[2]   P. Duwez, Glassy Metals-I 46 (1981) 19.

[3]   T. R. Anantharaman, C. Suryanarayana, Journal of Materials Science 6 (1971) 1111.

[4]   A. Inoue, A. Takeuchi, Acta Materialia 59 (2011) 2243.

[5]   A. G. Craig, S. M. Casey, Z. Kefeng, K. J. Mahaveer, R. D. William, P. Maggie, G. O. Keat, Sensors 2 (2002) 294.

[6]   Z. P. Lu, X. Hu, Y. Li, S. C. Ng, Materials Science and Engineering A 304-306 (2001) 679.

[7]   L. Liu, K. C. Chan, G. K. H. Pang, Journal of Crystal Growth 265 (2004) 642.

[8]   Y. Zhang, Y. F. Ji, D. Q. Zhao, Y. X. Zhuang, R. J. Wang, M. X. Pan, Y. D. Dong, W. H. Wang, Scripta Materialia 44 (2001) 1107.

[9]   Z. Bian, G. L. Chen, G. He, X. D. Hui, Materials Science and Engineering A 316 (2001) 135.

[10]   L. Liu, C. L. Qiu, H. Zou, K. C. Chan, Journal of Alloys and Compounds 399 (2005) 144.

[11]   W. Chen, Y. Wang, J. Qian, G. C. Dong, Acta Materialia 51 (2003) 1899.

[12]   F. M. Alamgir, H. Jain, R.B. Schwarz, O. Jin, D. B. Williams, Journal of Non-Crystalline Solids 274 (2000) 289.

[13]   V. V. Molokanov, M. I. Petrzhik, T. N. Mikhailova, T. A. Sviridova, N. P. Djakonova, Journal of Non-Crystalline Solids 250-252 (1999) 560.

[14]   T. Itoi, T. Takamizawa, Y. Kawamura, A. Inoue, Scripta Materialia 45 (2001) 1131.

[15]   D. Xu, G. Duan, W. L. Johnson, C. Garland, Acta Materialia 52 (2004) 3493.

[16]   Q. Li, Materials Letters 60 (2006) 3113.

[17]   M. Shapaan, J. Lábár, J. Lendvai, L. K. Varga, Materials Science and Engineering A 375-377 (2004) 789.

[18]   Q. J. Chen, H.. B. Fan, L. Ye, S. Ringer, J. F. Sun, J. Shen, D. G. McCartney, Materials Science and Engineering A 402 (2005) 188.

[19]   M. E. McHenry, M. A. Willard, D. E. Laughlin, Progress in Materials Science 44 (1999) 291.

[20]   J. Heber, All That Matters, ttp://allthatmatters.heber.org/2010/11/30/50-years-of-metallic-glasses/]: Accessed on 12-06-2013 (2000).

[21]   L. Xu, G. Yu, E. Zhang, F. Pan, K. Yang, Journal of Biomedical Materials Research Part A 83 (2007) 703.

[22]   R. Hasegawa, Journal of Magnetism and Magnetic Materials 100 (1991) 1.

[23]   G. Herzer, Journal of Magnetism and Magnetic Materials 294 (2005) 99.

[24]   S. Chikazumi, S. H. Charap, Physics of Magnetism, Krieger Pub Co, New York, 1978.

[25]   B. D. Cullity, C. D. Graham, Introduction to Magnetic Materials, 2nd ed., John Wiley and Sons Inc., 2008.

[26]   R. M. Bozorth, Ferromagnetism, Van Nostrand, Prinston, New Jersey, 1951.

[27]   J. Friedel, Nuovo Cimento 7 (1958) 287.

[28]   S. K. Das, L. A. Davis, Materials Science and Engineering 98 (1988) 1.

[29]   S. Saiseng, P. Winotai, S. Nilpairuch, P. Limsuwan, I. M. Tang, Journal of Magnetism and Magnetic Materials 278 (2004) 172.

[30]   Z. A. Chaudhury, C. Suryanarayana, Metallography 17 (1984) 231.

[31]   L. Aicheson, A History of Metals, 2nd ed., Interscience, New York, 1960.

[32]   W.H. Wang, C. Dong, C. H. Shek, Materials Science and Engineering: R: 44 (2004) 45.

[33]   S. Kavesh, Metallic Glasses, ASM International, Metals Park, Ohio, 1978.

[34]   J. Basu, S. Ranganathan, Sadhana 28 (2003) 783.

[35]   D. Turnbull, Trans. Metall. Soc. AIME 221 (1961) 422.

[36]   H. S. Chen, D. Turnbull, Journal of Chemical Physics 48 (1968) 2560.

[37]   H. S. Chen, D. Turnbull, Acta Metallurgica 17 (1969) 1021.

[38]   D. Turnbull, J. C. Fisher, Journal of Chemical Physics 17 (1949) 71.

[39]   P. Duwez, S. C. H. Lin, Journal of Applied Physics 38 (1967) 4096.

[40]   H. S. Chen, Acat Metallurgica 22 (1974) 1505.

[41]   T. Kosaka, S. Suzuki, H. Inoue, M. Saito, Y. Waseda, E. Matsubara, Applied Surface Science 103 (1996) 55.

[42]   A. Inoue, X.M. Wang, W. Zhang, Reviews on Advanced Materials Science 18 (2008) 1.

[43]   A. Inoue, Materials Transactions Online - The Japan Institute of Metals 36 (1995) 866.

[44]   A. Inoue, Bulk Amorphous Alloys – Preparation and Fundamental Characteristics, Trans Tech Publications, Switzerland, 1998.

[45]   A. Inoue, Bulk Amorphous Alloys – Practical Characteristics and Applications, Trans Tech Publications, Switzerland, 1999.

[46]   A. Inoue, Acta Materialia 48 (2000) 279.

[47]   W. L. Johnson, Materials Research Society Bullettin. 24 (1999) 42.

[48]   W. L. Johnson, Journal of Materials 54 (2002) 40.

[49]   A. Inoue, A. R. Yavari, W. L. Johnson, R. H. Dauskardt, in:, Materials Research Society Symposium Proceedings, Materials Research Society, Warrendale, PA:USA, 2001, p. 520.

[50]   T. Egami, A. L. Greer, A. Inoue, S. Ranganathan, in:, Materials Research Society Symposium Proceedings, Materials Research Society, Warrendale, PA:USA, 2003, pp. 47–52.

[51]   Y. Yoshizawa, S. Oguma, K. Yamauchi, Journal of Applied Physics 64 (1988) 6044.

[52]   G. Herzer, IEEE Transactions on Magnetics 26 (1990) 1397.

[53]   M. Manivel Raja, K. Chattopadhyay, B. Majumdar, A. Narayanasamy, Journal of Alloys and Compounds 297 (2000) 199.

[54]   Y. Yoshizawa, K. Yamauchi, IEEE Transactions on Magnetics 25 (1989) 3324.

[55]   A. Kojima, H. Horikiri, Y. Kawamura, A. Makino, A. Inoue, T. Masumoto, Magnetic Properties of Extruded Nanocrystalline Fe-Nb-B Alloys, 1994.

[56]   H. Iwanabe, B. Lu, M.E. McHenry, D. E. Laughlin, Journal of Applied Physics 85 (1999) 4424.

[57]   M. A. Willard, D. E. Laughlin, M. E. McHenry, D. Thoma, K. Sickafus, J.O. Cross, V.G. Harris, Journal of Applied Physics 84 (1998) 6773.

[58]   M. A. Willard, M. Q. Huang, D. E. Laughlin, M. E. McHenry, J. O. Cross, V. G. Harris, C. Franchetti, Journal of Applied Physics 85 (1999) 4421.

[59] T. Egami, P.J. Flanders, C. D. Grahams, in:, G. H. L. and C. D. Grahams, Jr. (Ed.), AIP Conf. Proc. No. 24, 1979, pp. 697–701.

[60] R. Hasegawa, C. P. Chou, Metallic Glasses Having a Combination of High Permeability, Low Magnetostriction, Low Ac Core Loss and High Thermal Stability, U.S. Patent 4152144, 1979.

[61] C. F. Conde, A. Conde, Materials Letters 21 (1994) 409.

[62] T. Kulik, Journal of Noncrystalline Solids 287 (2001) 145.

[63] A. Dunlop, G. Jaskierowicz, G. Rizza, M. Kopcewicz, Physical Review Letters 90 (2003) 15503.

[64] A. I. Gubanov, Soviet Phys. Solid State 2 (1960) 468.

[65] A. Brenner, D. E. Couch, E. K. Williams, J. Res. Natl. Bur. Std. 44 (1950) 109.

[66] C. W. B. Grigson, D. B. Dove, G. R. Stilwell, Nature 205 (1965) 1198.

[67] B. G. Bagley, D. Turnbull, Journal of Applied Physics 39 (1968) 5681.

[68] A.S. Nowick, S. Mader, Applied Physics Letters 7 (1965) 57.

[69] W. Felsch, Zeitschrift Für Physik 195 (1966) 201.

[70] J.P. Chu, J.S.C. Jang, J.C. Huang, H.S. Chou, Y. Yang, J.C. Ye, Y.C. Wang, J.W. Lee, F.X. Liu, P.K. Liaw, Y.C. Chen, C.M. Lee, C.L. Li, C. Rullyani, Thin Solid Films 520 (2012) 5097.

[71] C. Suryanarayana, C.C. Koch, Hyperfine Interactions 130 (2000) 5.

[72] G. Dietz, Journal of Magnetism and Magnetic Materials 6 (1977) 47.

[73] P.J. Grundy, Journal of Magnetism and Magnetic Materials 21 (1980) 1.

[74] P.K. Leung, J.G. Wright, Philosophical Magazine 30 (1974) 995.

[75] P.K. Leung, J.G. Wright, Philosophical Magazine 30 (1974) 185.

[76] J.K. Howard, Journal of Vacuum Science & Technology A: Vacuum, Surfaces, and Films 4 (1986) 1.

[77] K. Mohri, Magnetics, IEEE Transactions on Magnetism 20 (1984) 942.

[78] D. Turnbull, Metallurgical Transactions B 12 (1981) 695.

[79] G. Herzer, in:, M.M. B. Idzikowski, P. Švec (Ed.), Properties and Application of Nanocrystalline Alloys from Amorphous Precursors, Kluwer Academic Publishers, Dordrecht, Budmerice, Slovakia, 2003, p. 15.

[80] R. Alben, J.J. Becker, M.C. Chi, Journal of Applied Physics 49 (1978) 1653.

[81] G. Herzer, in:, K.H.J. Buschow (Ed.), Handbook of Magnetic Materials Vol 10, Elsevier, 1997, pp. 415–462.

[82]   G. Herzer, L.K. Varga, Journal of Magnetism and Magnetic Materials 215-216 (2000) 506.

[83]   A. Hernando, P. Marín, M. Vázquez, J.M. Barandiarán, G. Herzer, Physical Review B 58 (1998) 366.

[84]   R. Schäfer, A. Hubert, G. Herzer, Journal of Applied Physics 69 (1991) 5325.

[85]   G. Herzer, Physica Scripta 307 (1993) 307.

[86]   N. Hasegawa, M. Saito, Journal of Magnetism and Magnetic Materials 103 (1992).

[87]   A. Inoue, Materials Science and Engineering A 304-306 (2001) 1.

[88]   J. Yoon, S. Park, Y. Jo, M. Jung, C. You, T. Kim, J. Youn, H.I. Yim, J.R. Rhee, B.S. Chun, Y.S. Kim, Y.K. Kim, IEEE Transactions on Nanotechnology 7 (2008) 409.

[89]   M. Jyothi, C. Suryanarayana, Zeitschrift Für Metallkunde 76 (1985) 801.

[90]   H. Seiichi, S. Kaiji, S. Akira, in:, C. Kevin, D. Sima (Eds.), Proc. SPIE 3892: Device and Process Technologies for MEMS and Microelectronics, Gold Coast, Australia, 1999, pp. 97–108.

[91]   L. Yongdong, H. Seiichi, W. Kouichi, S. Akira, Japanese Journal of Applied Physics 40 (2001) 5382.

[92]   P. Sharma, Z. Wei, A. Kenji, K. Hisamichi, A. Inoue, Journal of Nanoscience and Nanotechnology 5 (2005) 416.

[93]   C. Yongze, W. Qiang, L. Guojian, D. Jiaojiao, W. Chun, H. Jicheng, Journal of Magnetism and Magnetic Materials 332 (2013) 38.

[94]   J. Gi, K. Hunn, S. Ho, A. Reilly, Thin Solid Films 440 (2003) 54.

[95]   J. Shim, J. Kim, S.H. Han, H.J. Kim, K. Hyeon Kim, M. Yamaguchi, Journal of Magnetism and Magnetic Materials 290-291 (2005) 205.

[96]   Y.M. Kim, D. Choi, K.H. Kim, J. Kim, S.H. Han, H.J. Kim, Journal of Magnetism and Magnetic Materials 239 (2002) 498.

[97]   C.H. Tolman, Journal of Applied Physics 38 (1967) 3409.

[98]   R. Lampert, J. Gorres, M. Hanson, IEEE Transactions on Magnetics 4 (1968) 525.

[99]   S.U. Jen, H.P. Chiang, C.M. Chung, M.N. Kao, Journal of Magnetism and Magnetic Materials 236 (2001) 312.

[100] S. Thomas, S.H. Al-Harthi, D. Sakthikumar, I. Al-Omari, R. V Ramanujan, Y. Yoshida, M.R. Anantharaman, Journal of Physics D: Applied Physics 41 (2008) 155009.

[101] S. Thomas, H. Thomas, D.K. Avasthi, A. Tripathi, R. V. Ramanujan, M.R. Anantharaman, Journal of Applied Physics 105 (2009) 033910.

[102] T. Thomson, P.C. Reidi, C.L. Platt, A.E. Berkowits, IEEE Transactions on Magnetics 34 (1998) 1045.

[103] C.L. Platt, A.E. Berkowitz, D.J. Smith, M.R. McCartney, Journal of Applied Physics 88 (2000) 2058.

[104] M. Vopsaroiu, M. Georgieva, P.J. Grundy, G. Vallejo Fernandez, S. Manzoor, M.J. Thwaites, K. O'Grady, Journal of Applied Physics 97 (2005) 10N303.

[105] C.X. Ji, F. Lu, Y.A. Chang, J.J. Yang, M.S. Rzchowski, Applied Physics Letters 92 (2008) 022504.

[106] K. Shirae, Journal of Applied Physics 50 (1979) 7618.

[107] R.V. Ramanujan, S.W. Du, Journal of Alloys and Compounds 425 (2006) 251.

[108] R. Hasegawa, M.C. Narasimhan, N. DeCristofaro, Journal of Applied Physics 49 (1978) 1712.

[109] K.N. Lad, R.T. Savalia, A. Pratap, G.K. Dey, S. Banerjee, Thermochimica Acta 473 (2008) 74.

[110] C. Liang, C. Gooneratne, D. Cha, L. Chen, Y. Gianchandani, J. Kosel, Journal of Applied Physics 112 (2012) 113912.

[111] C.J. Lin, Applied Physics Letters 41 (1982) 721.

2.1 Theory of Nucleation and Growth of Crystals

The formation of crystals in an amorphous alloy is a thermodynamic event and is governed by many factors like composition, crystal structure, activation energy of crystallization, frequency factor, thermal history of the material, presence of nucleating factors etc. In order to have a detailed understanding regarding the formation of amorphous alloys, it is important to know how metals crystallise when they are cooled from the molten state.
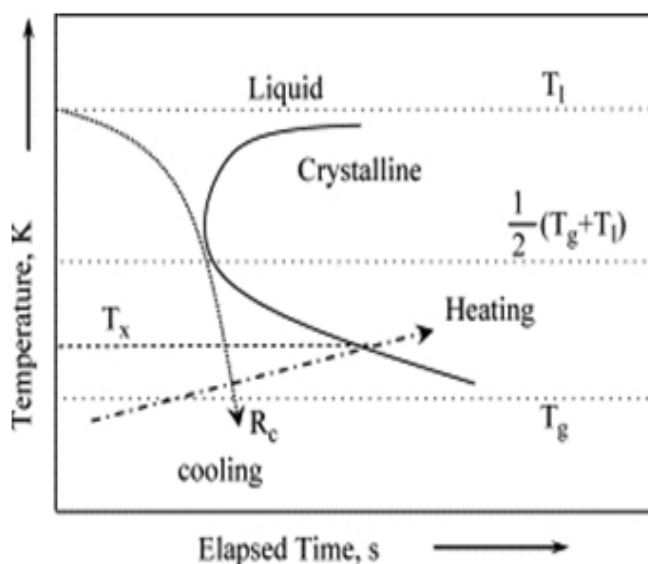
Figure 2.1 Time–Temperature-Transformation (TTT) diagram.

Metals and metallic alloys usually exist in nature in crystalline form. The secret of the same can be explained using the Time Temperature Transformation (TTT) diagram of an alloy cooled from the liquid state. In the typical cooling rates ordinarily existing in nature one would generally cross the nose region in the TTT diagram (figure 2.1) leading to crystalline state in the material. This opened up a new possibility that if the liquid can be cooled fast enough along the critical cooling curve "R_c" the material could be made amorphous. These large cooling

32

rates were realised with the advent of rapid solidification cooling and melt quenching. Recent reports indicate that in metallic glasses the arrangement of atoms are not entirely random and rather groups of seven to 15 atoms tend to arrange themselves around a central atom, forming three-dimensional shapes called Kasper polyhedra. Similar shapes were previously reported in crystalline metals, but in metallic glass, these polyhedra are distorted. In metallic glass, the polyhedra join together in unique ways as small nanometer-scale clusters [1].

Crystallization occurs between the liquidus temperature T_l and the glass transition temperature T_g, and can be avoided by sufficient cooling of the liquid . When the amorphous solids are isochronally heated at a constant heating rate, the sample starts to crystallize at an onset temperature denoted as T_x [2].

When a metallic glass is heated from room temperature to a higher temperature, different thermodynamic events may happen to the system. A differential scanning calorimetry study can elucidate these thermodynamic events. In most systems, a glass transition temperature (T_g)[3] is visible which is the temperature at which there is a drastic change in viscosity. The DSC study could also give information regarding the crystallisation temperatures (T_x) as well as the melting temperature (T_m). Turnbull established the importance of the reduced glass temperature T_g/T_m of an alloy in its GFA. As the value of reduced glass transition temperature increases from 0.5 to higher values, the required cooling rate for glass formation decreases, making it possible to synthesise thicker glasses at slower cooling rates [4]. Another important parameter namely ΔT_x which is the temperature interval between T_g and T_x is also used in evaluating the extend of super-cooled liquid region, the greater the super-cooled region the greater the glass forming ability of the alloy.

Since glasses are metastable and fabricated by processes which are far from equilibrium, they devitrifies upon heating to stable crystalline phases.

Crystallisation reactions have been broadly classified [5] into three categories; namely primary, polymorphous and eutectic crystallisation. In primary crystallisation, a crystal different in composition from that of the matrix precipitates out and in polymorphous crystallisation a precipitate of the same composition as that of the matrix precipitates out. In eutectic crystallisation, the glassy matrix separates into two crystalline phases according to the eutectic reaction [6].

The finer aspects regarding the thermodynamics of nucleation and growth of crystals in bulk as well as thin film form were explained based on the so called kinetic triplets and the same will be discussed in the next session.

2.2 Kinetics of Crystallization- Evaluation of Kinetic Triplets

The kinetics of crystallization of materials can be studied using differential scanning calorimetry techniques carried out in isothermal or non-isothermal mode. To extract the kinetic parameters, several models are available in the literature to simulate the process of crystallization. In the isokinetic methods the rate constant is assumed to be the same during the entire temperature range of crystallization, whereas the isoconversional methods assume that the reaction rate at a constant degree of transformation depends only on the temperature [7].

Metallic glasses are considered to exhibit structural and chemical disorder because of the high quenching rate involved in the fabrication process. In devitrification of metallic glasses, the nucleation rate sigmoidally increases from zero to a steady state value. Kolmogorow-Johnsen-Mehl-Avarami (KJMA) model replicate the nucleation rate with a sigmoidal curve and the model was widely used for evaluating Avarami exponent which signifies the dimensionality of crystal growth [8]. KJMA kinetic equation is formulated based on certain assumptions and is assumed to be valid when the growth rate of new randomly distributed nuclei is controlled by temperature, independent of time and linear [7]. Deviations from predictions of KJMA model happens if one or more of

these conditions are not satisfied. Phase transformations in glassy materials are modelled using the KJMA transformation rate equation derived for isothermal heating experiments.

The equation is

$$\frac{d\alpha}{dt} = nk(1-\alpha)[-\ln(1-\alpha)]^{\frac{n-1}{n}} \qquad\qquad 2.1$$

Where α is the degree of crystallite volume fraction transformed at time t $\alpha = \frac{A}{A_0}$, here A_0 is the total area under the crystallization curve i.e. the area under the curve between the temperature at the beginning of crystallization and the end temperature where the crystallization is completed. A is the area at any temperature between beginning of crystallisation and the temperature T at which the fractional crystallization is required to be known, n the avarami exponent and k the rate constant obeying an Arrhenius type relation

$$k(T) = k_0 \exp\left(-\frac{E}{RT}\right) \qquad\qquad 2.2$$

where k_0 is the pre exponential factor , E the activation energy and R the universal gas constant.

The iso-conversional techniques are based on the kinetic equation

$$\frac{d\alpha}{dt} = k(T)f(\alpha) \qquad\qquad 2.3$$

where k(T) is the rate constant given by equation 2.2 and f(α) is the model used to simulate the reaction. The integral form of the above equation can be obtained by substituting equation 2.2 in 2.3 and integrating by separation of variables

$$\int_0^\alpha \frac{d\alpha}{f(\alpha)} = \frac{k_0}{\beta}\int_0^{T_f}\exp\left(-\frac{E}{RT}\right)dT = \frac{k_0 E}{\beta R}\int_{y_f}^\infty \frac{\exp(-y)}{y^2}dy \qquad\qquad 2.4$$

Where, $y_f = \frac{E}{RT_f}$ and T_f is the temperature at a particular equivalent stage of crystalline transformation fraction (α) for different constant heating rates β. The integral in the above equation is called the temperature integral or Arrhenius

integral. The equation can be extended to non isothermal conditions by scaling using the equation $T = T_0 + \beta t$. However according to Henderson this is valid in certain special circumstances in which, the growth proceeds from a system saturated with nuclei [9]. He also argued that the conversion factor α depends on the thermal history of the material. Model free isoconversional methods or methods which do not incorporate an approximation to the temperature integral were widely used to give accurate values of activation energies. Isoconversion methods are generally categorized into two. One set of methods obtain kinetic parameters by approximating the temperature integral [10] using various approximations. This method includes the Kissinger-Akahira-Sunose method, Flyn-Wall-Ozawa method and Starink models [7,11–14]. The other set of models, though does not use any approximations, rely on the determination of reaction rate at an equivalent stage of the crystallization process for various heating rates. Friedman method falls into this category. Starink has provided an in depth discussion about the various isoconversional methods and their accuracy in estimating the kinetic triplets (α, k_0 and E).

2.3 Thin Film Deposition-Physical Vapour Deposition

Over the last century research on materials reduced (1-100nm) to one or more dimensions assumed importance due to the advent of nanotechnology as well as sophisticated characterization tools capable of probing materials at these dimensions. Thin films are one such form that is widely investigated owing to their various technological applications.

By the turn of last century thin films have become an intrinsic part of everyday life. The visible applications are wideranging from electronics to automobile parts and from solar cells to the metallic coatings inside bags to store food items. The properties of thin films differ from their bulk counterparts. For example, the optical properties of thin dielectric film layers can be tuned by adjusting their thicknesses to transmit or absorb light at very specific wavelengths. Duwez in 1976 reported that the technique of depositing thin

metallic films on a substrate by evaporation in high vacuum may lead to an amorphous structure especially if the film is very thin[15]. Since then there are several reports in the literature about the realization of amorphous metallic thin films by vapour deposition as well as sputtering[16–21].

Physical Vapour Deposition (PVD) is the process of depositing thin films from a bulk material on to a substrate. PVD techniques falls into two categories namely, sputtering (DC/RF, pulsed laser) and evaporation (thermal, electron beam, arc). Nowadays PVD techniques have wide variety of applications ranging from decorative to high temperature superconducting films [22].

PVD processes involve individual atoms or perhaps small clusters of atoms which are not normally found in the gas phase. The process proceeds through three different stages. First, these atoms are separated or removed from a solid or liquid source, secondly, they are transited from the source to the substrate and finally, allowed to fall on a solid surface at which point the atoms stick and form a film. The atoms can be removed from the original source by thermal heating of the source or by energetic particle bombardment by electrons, atoms, ions, molecules, or photons. The removal process can be thermodynamic, as is the case typically with evaporation, or may be the result of a sequence of energetic collisions resulting in the kinetic ejection of atoms from the source.

Evaporative sources can be classified into two; quasi-equilibrium and non-equilibrium, both of which are used widely for different applications. In quasi-equilibrium source, the evaporation process occurs in a nearly steady state equilibrium with its vapour For example, in Knudson cell which is an externally heated closed container with a fairly small hole on top. Since this hole is small compared to the total interior surface area of the cell, losses through the aperture can be considered as a perturbation on the dynamics of the liquid-vapour equilibrium in the cell. The non-equilibrium evaporation source can be characterized as an open source, where a small amount of liquid material evaporates off into a large, low pressure volume. Examples of this type of open source are the boat, crucible and filaments.

Deposition occurs by placing a sample in the direct line of sight of the source with a typical source substrate distance of ~10–100 cm. The flux is emitted from the source with roughly a cosine distribution and the deposition rate at the sample scales as roughly the inverse of the distance squared and hence evaporative systems are often configured with a parabolic dome onto which many samples are attached. The greater the vacuum in the chamber, greater will be the quality of the deposited films. This is because it is desirable to have the mean free path of the evaporant flux exceed the distance between source to the substrate. Also reduced pressure will reduce the contamination of the films with residual gas as well as carbon [22].

The ideal condition of thin film formation involves the deposition of the material as atom by atom (or molecule by molecule) and layer by layer, and there should be a sufficient time interval between the two successive depositions of atoms and also layers so that they can occupy the minimum potential energy configuration with respect to the substrate and subsequently with the previously deposited layers. In a thermodynamically stable film, all atoms (or molecules) will take up positions and orientations energetically compatible with the neighbouring atoms of the substrate or the previously deposited layers. However, in practice, the deposition will be taking place far away from the ideal scenario. The deposition will be proceeding in a way such that neither the successive atomic (or molecule) layers have sufficient interval of time for achieving the thermodynamic equilibrium condition nor a layer is completed before the formation of the second or even the third or other layer starts. Because of the deviation from the ideal conditions, the deposition results in the formation of metastable films. In general, atoms or molecules might get deposited preferentially on certain sites in the initial stages, leading to assemblages of atoms (or molecules) known as nuclei or clusters. The gap between the nuclei decrease gradually, eventually a continuous film will be formed at certain average thickness.

The thin film formation mechanism can be divided into three main stages:

- nucleation

38

- growth of nuclei
- coalescence

Nucleation is the birth stage of film formation. During this stage atoms impinging on the substrate are attracted to the substrate surface by dipole or quadrapole moment developing over the substrate surface. Because of this attraction vapour particles lose their kinetic energy perpendicular to the substrate surface and become an adatom. The atoms which are physically adhered may or may not be in thermal equilibrium. They may have a non zero kinetic energy in the parallel direction of the substrate surface. With this kinetic energy, they may jump or hope over the substrate surface until it meets with another adatom. Therefore, adatoms have certain stay time or time of residence over the substrate surface. After migration, the adatoms collide to form sub critical nuclei or critical nuclei or clusters which will involve the release of heat of condensation of vapour atoms. Impinging atom can also reflect back to vapour state without condensation, if the temperature of the substrate is of the order of melting point of the material. The vapour source provides a constant flux of incident atoms to the surface. The adsorbed atoms or adatoms, will diffuse over the substrate surface until they are consumed by a variety of microscopic process: Such as two adatoms can join together forming a nucleus, single adatoms can attach to existing nuclei or an adatom can re-evaporate from the substrate surface or even an adatom constituting a nucleus may also diffuse along the nuclear boundary or detach from the nucleus altogether. Each of these individual processes occurs over a range of characteristic time scales, meaning that the importance of each process governed by its perspective energetics and kinetics. Continued deposition will follow one of the three following growth mechanisms depending on the surface and interfacial energetics of the substrate and condensing atoms.

The growth of films is a thermodynamic event and basically there are three different modes of film growth which is schematically shown in the figure 2.2.
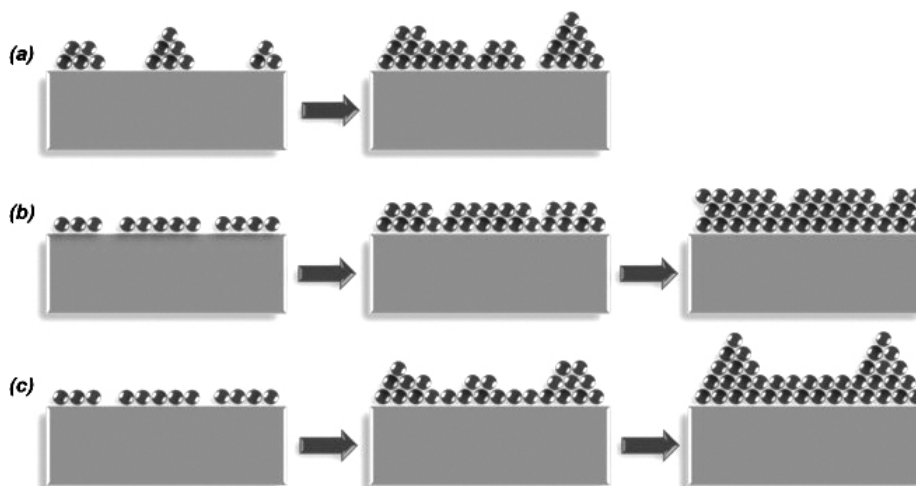
Figure 2.2: Illustrations of the basic growth modes including (a) Volmer–Weber (island), (b) Frank–Van der Merwe (layer-by-layer), and (c) Stranski–Krastanov growth. Schematics is adapted from ref [23]

If the deposited particles have a strong affinity to the substrate surface, the nucleation density will be high and islands grow around nuclei in a two-dimensional fashion until complete monolayer coverage of the substrate is attained. Subsequent growth occurs layer-by-layer. This growth mode is often referred to as the Frank-Van-der-Merwe mode(figure 2.2b) [24]. If the affinity of the substrate for the deposited particles is weak, islands will grow three-dimensionally to minimize the particle-substrate contact area and interaction. The resulting island growth mode is referred to as Volmer-Weber growth mode (figure 2.2a). An intermediate mode, referred to as Stranski-Krastinov mode (figure 2.2c) [24], occurs when the substrate-particle affinity is initially strong, but a lattice mismatch between the film and substrate introduces a strain into the growing film. After a few monolayers have covered the substrate, the film growth reverts to three-dimensional island formation to minimize the strain energy.

40

The three modes of growth can be explained using the Young's equation $\cos\theta = \frac{\gamma_{sv}-\gamma_{sl}}{\gamma_{lv}}$. For layer-by-layer growth, $\theta \approx 0$ or undefined. RHS of the equation can be≥ 1. Hence $\gamma_{sv} \geq \gamma_{sl} - \gamma_{lv}$.

When the film and substrate are identical materials, the interfacial energy, γ_{sl} approaches zero. Materials with low surface energies will "wet" substrates with high surface energies, promoting Frank-Van-der-Merwe growth. If there is lattice mismatch between the initial deposited layers and the substrate, Stranski-Krastanov growth will occur to minimize the strain energy.
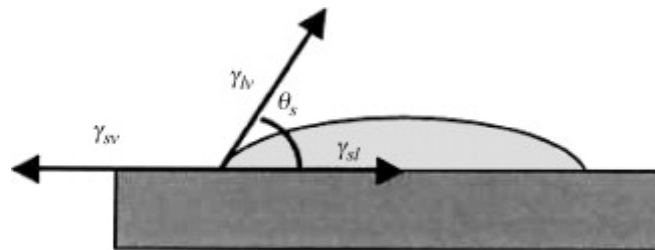
Figure 2.3: Graphical interpretation of the Young's equation. Adapted from ref [25].

For island growth, $\theta > 0$, and therefore $\gamma_{sv} < \gamma_{sl} - \gamma_{lv}$.

The surface energy between the film and the substrate is usually much smaller than that between a solid and the vapour. Thus, neglecting γ_{sl} suggests that if the surface tension of the film is greater than that of the substrate, Volmer-Weber growth will happen.

2.4 Surface Morphology Evolution During Deposition and Thermal Annealing.

Many important physical and chemical properties of films are related to its surface morphology. Hence it is of great importance to investigate, understand and control the evolution of the surface morphology during film growth. The formation of a growth front is a complicated phenomenon and very often occurs far from equilibrium. When atoms are deposited on to a surface, they do not arrive at the surface at the same instant uniformly across the surface area. The random fluctuation, or noise, which is inherent in the process, may create surface

growth front irregularities leading to surface roughness. The noise competes with surface smoothing processes, such as surface diffusion, to form a rough morphology if the experiment is performed at either at a sufficiently low temperature or at a high growth rate.

One of the earliest models to simulate the evolution of a growing interface was due to Kader Parisi and Zhang (KPZ) [26]. Scaling approaches are generally used by them to describe the morphological evolution of a growth front. There are two main scaling approaches to describe the mounded surface formation namely self-affine scaling and dynamic scaling.

2.4.1. Self-Affine Scaling

Consider a surface represented by the height profile h(r). This surface is said to be self-affine if, for an arbitrary scale factor $\epsilon > 0$, $h(r) \sim \varepsilon^{-\alpha} h(\varepsilon r)$ [27]

The roughness exponent α characterizes the short-range roughness of a self-affine surface. Larger values of α represents a smoother local surface profile. The power spectral density function (PSD) of a surface profile is a Fourier transform of the surface heights. A suitable model for the PSD of a self-affine surface is given by

$$P(k_{\parallel}) = \frac{4\pi\alpha w^2 \xi^2}{\left(1+k_{\parallel}^2 \xi^2\right)^{1+\alpha}} \qquad\qquad 2.5$$

Where, k is the parallel component of the wave vector k, ξ is the lateral correlation length and ω is the interface width or root mean square roughness. Note that this PSD has no characteristic peak, which allows for the scaling definition of a self-affine surface [27]. A characteristic peak in the PSD implies that there is a characteristic length scale on the surface that will change on rescaling, breaking the scaling behaviour of the surface.

2.4.2. Dynamic Scaling

A surface profile is said to exhibit dynamic scaling if the surface height profile can be scaled in time also.

For a self-affine surface, this gives [27]

$$h(r,t) \sim \varepsilon^{-\alpha} h(\varepsilon r, \varepsilon^z t) \qquad\qquad 2.6$$

Where, z is the dynamic exponent. Under dynamic scaling, an increase in the time by a factor ε increases the horizontal length scale by a factor $\varepsilon^{1/z}$. Thus, the lateral correlation length ξ, which is a function of the horizontal correlations on the surface, must evolve as

$$\xi(t) = t^{1/z} \qquad\qquad 2.7$$

Similarly, increasing the time by a factor ε changes the vertical length scale by a factor $\varepsilon^{\alpha/z}$. Since the interface width ω or rms roughness is a function of the vertical height profile of the surface, the interface width must evolve as function of the vertical height profile of the surface, as

$$w(t) = t^{\alpha/z} \qquad\qquad 2.8$$

The interface width is commonly defined as evolving with an exponent, which, when compared to above equation, gives the well-known relationship between the scaling exponents under dynamic scaling, $z = \alpha/\beta$.

Dynamic scaling predicts that all parameters that measure the surface are related to one another because the surface profile scales with time. Thus, one consequence of dynamic scaling is the time-dependent scaling of surface correlation functions. Time-dependent scaling implies that any surface correlation function profile measured at different deposition times can be collapsed onto one another by a suitable rescaling of the axes of the plots. For example, for the PSD of a self-affine surface scaling the horizontal wave number axis k by a factor $[\xi(t)]^{-1}$ and the vertical PSD axis by a factor $[w(t)\xi(t)]^{-2}$ gives a time-independent scaling form $Q(k_{ll})$ for the PSD of a self-affine surface,

$$Q(k_{\parallel}) = \frac{4\pi\alpha}{\left(1 + k_{\parallel}^2\right)^{1+\alpha}} \qquad\qquad 2.9$$

Hence, if the PSD of a surface does not obey time dependent scaling, it would imply that the surface does not obey dynamic scaling.

2.4.3. KPZ- Model

The KPZ universality class was introduced in the context of studying the motion of growing interfaces in a paper of Kardar, Parisi and Zhangb[26]. The KPZ equation $\frac{\partial h}{\partial t} = \upsilon\nabla^2 h + \frac{\lambda}{2}|\nabla h|^2 + \eta(r,t)$, where υ is the surface tension, λ represents the excess velocity (due e.g. to lateral growth) $\eta(r,t)$ is a Gaussian noise $\langle\eta(r,t)\,\eta(\acute{r},\acute{t})\rangle = 2D\,\delta(r,t)\delta(\acute{r},\acute{t})$. D is the strength of the noise. Employing dynamical renormalization group techniques (highly non-rigorous from a mathematical perspective) Forster, Nelson and Stephen's [28] in 1977 predicted estimates for the scaling exponents α and β. Since then several researchers tried to estimate the values of scaling exponents and for growth in two-dimensional substrates but no exact solution is still not available, and the best known estimates of KPZ exponents, α = 0.39 and β = 0.23 which were obtained by numerical simulations [29]. However other values of roughness exponents ranging from 1-4 were also reported by other researchers. The value of roughness exponents of a film can give indications about the mode of film growth and the dominant surface smoothening/roughening process involved in the film growth. Earlier works by Herring and Mullins [30–32] established α values of 1, 2, 3, and 4 to four different surface transport mechanisms,i.e., plastic flow driven by surface tension, evaporation and recondensation of particles, volume diffusion, and surface diffusion respectively. The roughness exponents of a thin film could be extracted from the PSD analysis carried out on the AFM images. Thermal annealing as well as SHI irradiation will alter the surface morphologies of thin films. Hence by analysing the roughness exponents of the films subjected to thermal annealing as well as SHI irradiation the surface evolution can be investigated in detail.

2.5 Thin Film Magnetism

2.5.1. Direct-Exchange Interaction

Direct exchange interaction is a quantum mechanical phenomenon between the adjacent atoms/ions leading to ferromagnetic or antiferromagnetic coupling. In metallic glasses this is the dominant mechanism leading to exchange averaging in the system leading to soft magnetic properties. The total energy of the system can be evaluated using perturbation techniques (in the case of two hydrogen atoms situated near to each other) to be $E_{\pm} = 2E_0 + \frac{E_c \pm E_{ex}}{1 \pm S^2}$, where the E_+ state represents symmetric state corresponding to anti-parallel spins where as E_- state represents anti-symmetric state corresponding to parallel spins. $2E_O$ is the total energy of the isolated atoms, E_C the Coulomb interaction between electrons, nuclei and electrons-nuclei, E_{ex} the exchange energy associated with the process of exchanging electrons. The magnitude of exchange energy E_{ex} is always much larger than that of E_C and therefore, the stability of the symmetric / anti-symmetric states depends on the term E_{ex}. The exchange energy E_{ex} depends on the dot product, S_i and S_j, where S_i and S_j are the total spin angular moment of the adjacent atoms and J_{ex} is the exchange integral, which represents the probabilities of exchange of   electrons.

$$E_{ex} = -2J_{ex}S_i \cdot S_j \qquad\qquad 2.10$$

J_{ex} is obviously a sensitive function of overlap of electronic wave functions and its sign can be either positive or negative. If $J_{ex}>0$, parallel alignment of the neighbouring spins is favoured and this corresponds to the ferromagnetic case. If $J_{ex}<0$, neighbouring spins will align themselves anti-parallel, corresponding to antiferromagnetic behaviour.

2.5.2. Coercivity at Nanoregime

Figure 2.4 shows the variation of coercivity with particle size. As the particle size of a system is reduced from a higher value (micron) it is found that the coercivity goes through a maximum before again falling to lower values at

small particle sizes. But it should be noted that this is based on the assumption that the particles are non-interacting. The variation of coercivitywith particle size (from a larger value to D_c) is experimentally found to be given by [34].

$$H_{ci} = a + \frac{b}{D} \qquad\qquad 2.11$$

where a and b are constants and D is the particle diameter.

Below a critical particle size D_c, the particles become single domain and in this range the coercivity reaches a maximum. The particles with size D_c and smaller change their magnetisation by spin rotation.
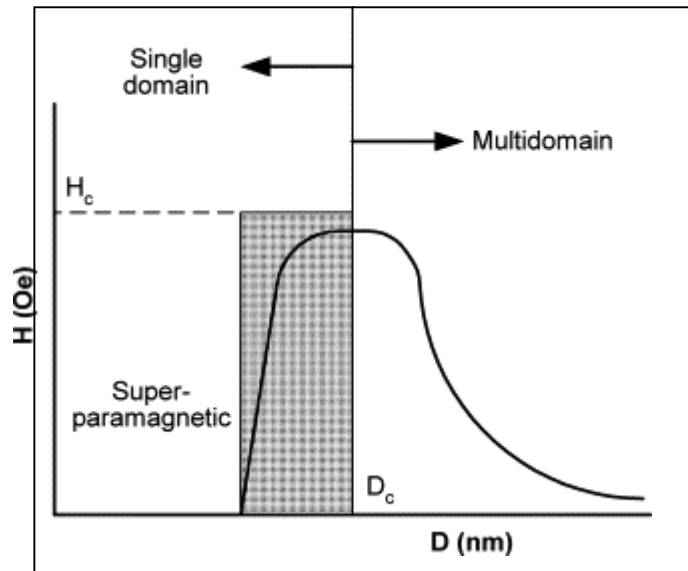
Figure 2.4: Qualitative illustration of the behaviour of the coercivity in ultrafine systems as the particle size changes, where *H* is the magnetic field amplitude (Oe) and *D* is the particle diameter (nm). Adapted from reference [33].

As the particle size decreases below D_c the coercivity decreases, because of thermal effects, according to

$$H_{ci} = g - \frac{h}{D^{3/2}} \qquad\qquad 2.12$$

where g and h are constants.

Below a critical diameter D_p the coercivity is zero, again because of thermal effects, which are now strong enough to spontaneously demagnetize a

previously saturated assembly of particles. Such particles are called super-paramagnetic.

2.6 Magnetisation Reversal Mechanisms- Stoner Wohlfarth and Kondorsky Models for Magnetisation Reversal

If exchange energy is the only energy acting on a atomic magnet the result would have been that the material would be magnetised to saturation (in case of a positive value of exchange integral). However there are other competing mechanisms opposing the exchange energy viz. magnetostatic energy which is the principal driving force for domain formation, and the magneto crystalline and magnetostrictive energies. A possible domain configuration in a material is the lower energy state resulting from the competition of these forces. In the case of a ferromagnetic material these forces result in a domain arrangement such that the magnetisation of the sample as a whole is zero. The magnetization process involves the growth of domains that are favourably oriented with the applied magnetic field at the expense of those that are not, and as well as by the rotation of domains [35]. The division of a domain to more than one requires the creation of a new interfacial layer where the magnetisation gradually turns from one orientation to another. As is the case of the creation of any new interface [36], the creation of a domain wall requires positive energy. Consider the case where a domain is divided into two and if the division is sharp the atoms on the two sides of the wall will have very large exchange energy. To minimise this, the exchange energy tries to make the wall thick. However if the wall is thick there will be large number of atoms pointing away from the easy axis (the spins on either side of the domain are along the easy axis) thereby increasing their magneto-crystalline anisotropy. Hence the anisotropy will try to make the wall thin enough to reduce the anisotropy energy. To obtain an approximate estimate of the domain wall width, consider the exchange energy acting on two adjacent spins (S) in a lattice [34].

$E_{ex} = -2JS^2 \cos \varphi$, Where J is the exchange integral and φ is the angle between the two spins.

47

But $cos\varphi = 1 - \frac{\varphi^2}{2} + \frac{\varphi^4}{4} + \cdots$ truncating the series at $\frac{\varphi^2}{2}$, since φ is small and substituting these value of $cos\varphi$ in the equation for

$$E_{ex} = -2JS^2\left(1 - \frac{\varphi^2}{2}\right) = JS^2\varphi^2 - 2JS^2 \qquad\qquad 2.13$$

Since the second term is independent of the angle it will have the same value inside the domain as well as the wall and hence it can be omitted. To evaluate extra energy per unit area of the domain let us assume a simple cubic structure with each atom along the corner of the cell of lattice parameter 'a' and the plane of the wall parallel to the cube face {100}. The wall is N atoms thick and for each unit area of the wall there will be $\frac{1}{a^2}$ rows of N atoms. Therefore the extra energy per unit area of the wall is $\gamma_{ex} = JS^2\varphi^2 \frac{1}{a^2}N$. For a 180° wall $\varphi = \frac{\pi}{N}$ and hence, $\gamma_{ex} = \frac{JS^2\pi^2}{a^2N}$. The anisotropy energy is the anisotropy constant K times the volume of the wall. The anisotropy energy per unit area is $\gamma_{an} = KNa$. The energy per unit area in the wall of thickness $\delta = Na$ can be expressed as a sum of exchange and anisotropy energy terms:

$$\gamma_d = \gamma_{ex} + \gamma_{an} = \frac{J_{ex}S^2\pi^2}{\delta a} + K\delta \qquad\qquad 2.14$$

This energy has a minimum for a particular value of δ.

This minimum is given by

$$\frac{d\gamma_d}{d\delta} = -\frac{J_{ex}S^2\pi^2}{\delta^2 a} + K = 0$$

$$\qquad\qquad 2.15$$

or

$$\delta = \sqrt{\frac{J_{ex}S^2\pi^2}{Ka}}$$

$$\qquad\qquad 2.16$$

The exchange integral J_{ex} is proportional to the Curie temperature T_C and there fore $\delta \sim \sqrt{\frac{T_C}{K}}$

The smaller the anisotropy constant, the thicker the domain wall. Therefore, wall thickness increases with temperature, because K almost always decreases with rising temperature [34]. The response of a domain as well as

domain walls to an applied magnetic field depends on various factors like the magnitude of competing energies leading to domain wall formation, pinning sites for domains etc. The Stoner-Wohlfarth model [37] is the simplest model describing magnetisation reversal. In this model it is assumed that magnetisation reversal occurs in a particle of an ideal magnetic material where exchange energy holds all spins parallel to each other. Hence the exchange energy is constant, and it plays no role in the energy minimisation. Consequently, it is the anisotropy of the particle which dictates the magnetic behaviour of the particle. The original model of Stoner and Wohlfarth assumed only uniaxial shape anisotropy with one anisotropy constant which is sufficient to describe highly symmetric cases like a prolate spheroid of revolution or an infinite cylinder. However, real systems are often quite complex, and the anisotropy is a sum of mainly shape (magnetostatic), magneto-crystalline, magnetoelastic, and surface anisotropy [38].

It is possible to elucidate the magnetization reversal mechanisms from the angular plot of coercivity. The plot is particularly usual in identifying the magnetization reversal mechanism prominent in the film. Generally there are two kinds of magnetization reversal mechanisms (1) coherent rotation modeled by the Stoner- Wohlfarth (S-W) relation[39] and (2) domain wall motion modeled by the Kondorsky relation [40]. The angular dependence can also give information about the isolation of grains since SW relation assumes that the particles are well isolated. When the magnetic field is along the easy axis, the magnetization reversal is primarily caused by domain wall motion and hence the coercivity follows more or less the Kondorsky model.

$$\frac{H_c(\theta)}{H_c(0)} = \sec(\theta) \text{for} 0^o \leq \theta \leq 90^o \qquad\qquad 2.16$$

Here $H_c(0)$ is the intrinsic coercivity along the easy axis.Contrary to it, when the field is along the hard axis, the magnetization reversal is dominated by coherent rotation as per the SW equation

$$.\frac{H_c(\theta)}{H_c(0)} = (\cos^{2/3}\theta + \sin^{2/3}\theta)^{-3/2} \text{For} 0^o \leq \theta \leq 45^o \qquad 2.17$$

$$\frac{H_c(\theta)}{H_c(0)} = \sin(\theta)\cos(\theta) \text{ for } 45^o \leq \theta \leq 90^o \qquad 2.18$$

Where $\frac{H_c(\theta)}{H_c(0)}$ is the coercivity scaled with the coercivity along the easy axis.

2.7 Anisotropies

One of the factors which strongly affect the shape of MH curve is magnetic anisotropy. Anisotropy simply means that magnetic properties depend on the direction in which they are measured. In the case of metallic glasses in which the basic microstructure consists of a nanocrystalline phase embedded in an amorphous matrix the relevant anisotropies in the decreasing order of their magnitude are (i) magneto-crystalline anisotropy, (ii) magneto-elastic anisotropies (iii) uniaxial anisotropies induced by annealing and (iv) random anisotropies.

2.7.1. Magneto-Crystalline Anisotropy

When it is required to rotate the spin system in a domain, away from the easy direction, the actual energy needed is the energy required to overcome the spin orbit coupling. When an applied field tries to orient the spin, the orbit also needs to be reoriented because of the spin orbit coupling. The strong coupling of the orbit with the lattice appears as resistance to the rotation of the spin. The symmetry of magneto-crystalline anisotropy is the same as that of the crystal structure. In the case of iron which crystallises in the cubic structure the anisotropy energy can be written in terms of the direction cosines as $E = K_1(\alpha_1^2\alpha_2^2 + \alpha_2^2\alpha_3^2 + \alpha_3^2\alpha_1^2) + K_2(\alpha_1^2\alpha_2^2\alpha_3^2) + \cdots$ where K_1 and K_2 are called anisotropy constants. Typical values for iron at room temperature are $K_1 = 4.2$ x 10^4 J/m^3 and $K_2 = 1.5$ x 10^4 J/m^3. Cobalt is hexagonal with easy axis along the hexagonal c axis. The anisotropy energy in such a case is a function of the angle between magnetisation vector and c axis. The anisotropy energy assumes the form $E = K_1 sin^2\theta + K_2 sin^4\theta + \cdots$. Typical values of anisotropy constants for cobalt are $K_1 = 4.1$ x 10^5 J/m^3 and $K_2 = 1$ x 10^5 J/m^3. For all materials the anisotropy decreases with temperature. For good soft magnetic properties, the magneto-crystalline anisotropy should be low. In amorphous and nanocrystalline

materials this is realized by exchange averaging of anisotropies between grains [35]. Although most materials show some magneto-crystalline anisotropy, a polycrystalline sample with no preferred orientation of its grains will have very negligible crystalline anisotropy. However this is valid only if the sample is exactly spherical. If the sample shape deviates from spherical, then it will be easier to magnetize it along a long axis than along the short axis and this phenomenon is called shape anisotropy.

2.7.2. Shape Anisotropy

Shape anisotropy can be explained using the concept of demagnetization field. If a magnetic material is placed in a magnetic field applied from right to left the lines of field radiate from the material in the same direction outside the samples and in opposite direction inside it creating an internal field which tends to demagnetize the material. This field is called demagnetizing field H_d. The magnitude of the demagnetizing field is directly proportional to the magnetization.

$$H_d = N_d M,$$ 2.19

Where, N_d is called the demagnetizing factor and depends only on the geometric shape of the sample. The results of calculations of N_d for different shapes reported in the literature shows that for elongated samples, N_d is smallest along the long axis and largest along short axis. The anisotropy increases as the aspect ratio increases.

$N_d \rightarrow 0$ as the distance between the poles$\rightarrow$ Infinity. Thus the effective field

$$H_{eff} = H_{applied} - H_d$$ 2.20

As N_d is small along the long axis,

$$H_{eff} = H_{applied} - N_d M \sim H_{applied}$$ 2.21

So, most of the applied field goes into magnetizing the sample, whereas along the short axis N_d is large. Then

$$H_{eff} = H_{applied} - N_d M << H_{applied}$$ 2.22

where, most of the applied field is used to overcome the demagnetizing field. As a consequence, it is easier to magnetize the sample along the long axis.

For a spherical sample there is no anisotropy. The magnetostatic energy density can be written as

$$E = \frac{1}{2}\mu_0 N_d M^2 \qquad\qquad 2.23$$

Where N_d is the tensor and represents the demagnetisation factor (which is calculated from the ratio of the axis lengths). M is the saturation magnetisation of the sample. For example the shape anisotropy energy of a uniform magnetised ellipsoid is

$$E = \frac{1}{2}\mu_0 V(N_x M_x^2 + N_y M_y^2 + N_z M_z^2) \qquad\qquad 2.24$$

where the tensors satisfied the relation: $N_x + N_y + N_z = 1$

2.7.3. Magneto- Elastic Anisotropy

When a magnetic material is subjected to stress its magnetic properties may change depending on the magnetostriction coefficient (λ_s) of the material. The effect of stress on magnetization is called inverse magnetostrictive effect or generally known as magneto mechanical effect. Consider a material having positive λ_s, it will elongate when it is magnetized. On the other hand, if a tensile stress is appilied to it, which will elongate it, the magnetisation along direction of stress will increase where a compressive stress would decrease it. But the stress applied to a demagnetized specimen will not produce any change in magnetisation.

Figure 2.5 shows the remarkable effect of applied stress (σ) on the magnetisation behaviour of polycrystalline nickel. At 10 Oe a compressive stress of 6×10^7 N/m^2 almost doubles the permeability while the same amount of tensile stress reduces permeability to one tenth of its zero stress value.
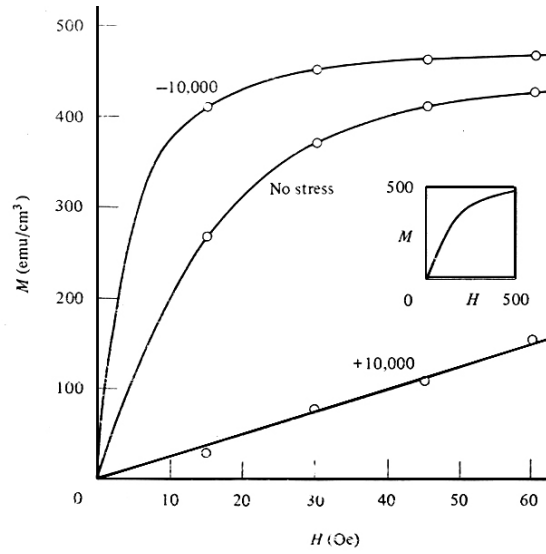
Figure 2.5: Effect of applied stress on MH curve of polycrystalline nickel.
Adapted from reference [34].

The magnetostriction coefficient of nickel is negative. In the demagnetized state, stress can cause domain wall motion. The motion will always take place ensuring that the net magnetisation of the sample is zero. Stress can create an easy axis for magnetisation. It is uniaxial in nature and hence the magneto elastic energy can be expressed as

$$E = K_\sigma sin^2\theta \qquad\qquad 2.25$$

where K_σ is the anisotropy induced due to stress and θ the angle between magnetisation vector and the easy axis. Excellent soft magnetic properties further require that the material should have low or vanishing magnetostriction λ_s which reduces the magneto elastic anisotropies arising from the internal or external mechanical stress [34,41].

$$K_\sigma = -\frac{3}{2}\lambda_s\sigma \qquad\qquad 2.26$$

The stresses in thin films as well as metallic glass ribbons can be relieved by subjecting them to thermal annealing. Once the magneto-crystalline (polycrystalline sample) and magneto elastic anisotropies (annealing) are minimized the magnetic properties will be dictated primarily by uniaxial

53

anisotropies induced during the heat treatment either by a magnetic field or by mechanical creep. The field induced anisotropies are of huge practical relevance and allow one to tailor the hysteresis loop according to the demands of application.

2.7.4. Random Anisotropy and Random Anisotropy Model

The magnetic properties of materials are governed by the anisotropies in the material and the most important among them is the magneto-crystalline anisotropy. The magneto crystalline anisotropy is determined by the symmetry axis of the crystal. The actual microstructure of the material leads to a distribution of easy axes directions over the scale of the structural correlation length (grain size) D. In conventional polycrystalline materials, where these distributions occur on a large scale, the magnetization process is determined by the local magneto-crystalline anisotropy constant K_1 of the grains. For small structural correlation lengths, however, ferromagnetic exchange interaction forces the magnetic moments to align parallel, (if the particle sizes are smaller than the range of ferromagnetic exchange interaction) thus hindering the magnetization to follow the easy axis of each individual structural unit. As a consequence the effective anisotropy for the magnetisation process will be an average over several structural units and thus reduced in magnitude. This is the cornerstone of the random anisotropy model (RAM) originally suggested by Alben *et.al.* and modified by Herzer [42,43]. The ferromagnetic exchange length L_{ex} characterizes the critical length scale where the exchange energy balances the anisotropy energy.

$$L_{ex} = \varphi_0 \sqrt{\frac{A}{K_1}} \qquad\qquad 2.27$$

Here A representsthe exchange stiffness constant, which is a characteristic parameter in magnetism and K_1 the uniaxial anisotropy and L_{ex} represents the exchange correlation length, φ is a parameter which reflects both the symmetry of the effective anisotropy constant K_1 and the total spin rotation

angle over the exchange-correlated coupling chain. (Herzer assumed φ=1 where as it was $\frac{4}{3}$ in the model of Alben *et. al.* [42,44]. The significance of φ is not generally discussed by any authors. The stress by most authors, is on the relation between coercivity and grain size. When the exchange correlation length overwhelms the structural correlation length the anisotropies are averaged over several domains.
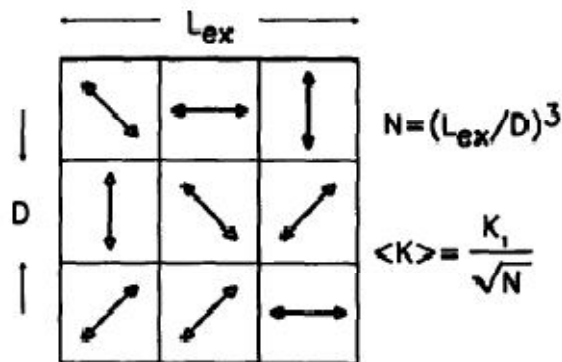
Figure 2.6: Schematic representation of the random anisotropy model. The arrows indicate the randomly fluctuating magneto-crystalline anisotropies. Adapted from reference [43].

The effective anisotropy affecting the magnetization process results from averaging over the N= (L_{ex}/D) grains within the volume $V = L_{ex}^3$, then it follows that

$$\langle K \rangle = \frac{K_1}{\sqrt{N}} = K_1 \left(\frac{D}{L_{ex}}\right)^{\frac{3}{2}}$$ 2.28

$\langle K \rangle$ is the mean fluctuation amplitudes of the anisotropies and D the average grain size. Combination of equations 2.27 & 2.28 gives

$$\langle K \rangle = \frac{K_1^4}{A^3} D^6$$ 2.29

which suggest that the mean anisotropy is scaled by the sixth cube root of the average grain size.

The coercivity is found to be related to the sixth power of grain size as

$$H_c = p_c \frac{\langle K \rangle}{M_s} = p_c \frac{K_1^4 D^6}{M_s A^3} \qquad 2.30$$

In equation 2.30, p_c serves as a fitting parameter and M_s is the saturation magnetization. The above equation suggests that the coercivity is directly proportional to $\frac{D^6}{M_s}$. The above equation is derived based on coherent rotation of domains. In the case of domain wall pinning contributing to coercivity, then $H_c = \frac{1}{2J_s}\left(\frac{d\gamma}{dx}\right)_{max} \sim \frac{\sqrt{A.K}}{J_s.L}$ where L denotes the typical wavelength of the effective anisotropy fluctuations and γ the domain wall energy. If one considers domain wall pinning or wall motion as the dominant mechanism that dictates the magnetization reversal, the final expression will be the same as equation 2.30.

2.7.5. Random Anisotropy Model Extended to Two Dimensional Systems (Thin Films)

When one of the dimensions are restricted to very low values, the system can very well be approximated to a two dimensional system. In such a case the averaging effect is confined to two dimensions and the above equations can be modified as [45,46].

$$\langle K \rangle = \frac{K_1}{\sqrt{N}} = K_1 \left(\frac{D}{L_{ex}}\right) \qquad 2.31$$

Substituting (2.15) in (2.20) we get

$$\langle K \rangle = \frac{K_1^2}{A} D^2 \qquad 2.32$$

Therefore

$$H_C = p_c \frac{\langle K \rangle}{M_s} \approx p_C \frac{K_1^2 D^2}{M_s A} \qquad 2.33$$

Where all the parameters in the equations have their usual meaning except they are the two dimensional counter parts of the corresponding three

dimensional values. This equation suggests that for ultra-thin films the Herzer's D^6 law for bulk magnetic films has to be replaced with a D^2 law. The coercivity H_c is directly proportional to (D^2/M_s).

2.8 Effect of Surface Roughness on the Magnetic Properties of Thin Films

The magnetic properties of thin films depends on a number of factors like composition, crystallinity, crystal structure, anisotropies (magneto-crystalline, magnetostrictive, magnetoelastic, shape, induced), surface and interface roughness etc. of which, surface roughness is an important parameter that can have a profound influence over the magnetic properties of thin films. The roughness in turn depends on the preparation techniques and processing conditions carried out during film deposition and post processing. For example during thermal evaporation, deposition pressure, target material composition, substrate roughness, shape of heat source, source substrate distance and substrate temperature influence the film homogeneity and surface roughness [47]. Also processing conditions like annealing, ion irradiation, etching etc. can influence the substrate roughness [48–50]. If a sample is thin and comparable to the size of a domain wall then the roughness of the surfaces can affect domain wall motion. The wall will always seek to minimize its energy, and so will stick in valleys where the sample is thinnest. The fact that domain walls tend to form as plane surfaces will act to average out this effect if the surface roughness is random, but not if there are more or less continuous hills and valleys running parallel to the primary domain walls [34]. The surface morphology of thin films could be altered by thermal annealing, ion irradiation, sputtering and chemical etching. SHI irradiation is a versatile tool to alter the surface morphology since each ion changes the morphology at a local region. As the beam is raster scanned over the surface the morphology of the surface changes leading to changes in surface magnetic properties.

2.8.1. Swift heavy Ion Irradiation-Coulomb Explosion and Thermal Spike Model

The advantages of using an energetic ion beam to modify surfaces with a view to enhancing their electrochemical, optical magneticand electrical properties have been known for some time [51–55]. An energetic ion that penetrates a solid loses energy mainly in collisions with the target nuclei or target electrons. The ion energy loss per unit path length, *dE/dx*, is termed stopping power and depends strongly on the ion velocity '*v*'. For ions having a velocity much lower than the velocity of the orbiting target electrons the energy loss will be dominated by the Coulomb interactions with the target nuclei screened by electrons. When the velocity of the incoming ion is much higher than the velocities of the target electrons, the electrons cannot adjust their orbitals adiabatically and hence they acquire momentum in direct collisions with the incident ion. The momentum transfer from the ion to the electrons is more effective than to the nuclei due to the lower mass of the electrons.

Heavy ions with high energies so that the electronic energy loss process dominates are referred to as swift heavy ions. The electronic energy loss, $\left(\frac{dE}{dx}\right)_{Elect}$ for ion-solid interaction was first derived semi classically by Bohr as;

$$\left(\frac{dE}{dx}\right)_{Elect} = \frac{Z_1^2 e^4 n_e}{4\pi m_e v^2 \varepsilon^2} \ln\left(\frac{2m_e v^2}{I}\right) \qquad 2.34$$

Where e and m_e are the charge and mass of electron respectively and Z_1 and v are the atomic number and the velocity of the ion respectively. The target is characterized by the dielectric constant 'ε', the number density of electron n_e and ionization potential 'I', that is proportional to Z_2. The expression indicates the influence of v andbZ_1on energy loss.

Total energy spent by the ions in the sample during their passage is:

$$\left(\frac{dE}{dx}\right)_{loss} = \left(\frac{dE}{dx}\right)_{elec} + \left(\frac{dE}{dx}\right)_{nucl} + \left(\frac{dE}{dx}\right)_{charge\ exchange} \qquad 2.35$$

Where $\left(\frac{dE}{dx}\right)_{elec}$ is electronic energy loss, $\left(\frac{dE}{dx}\right)_{nucl}$ is nuclear energy loss and $\left(\frac{dE}{dx}\right)_{charge\ exchange}$ the energy loss due to charge exchange process between ion and the atoms of the sample. Charge exchange loss is negligibly small compared to the other two losses.

Swift heavy ions can produce a variety of modifications in a material. These include Frenkel pairs (vacancy-interstitial pair) creation and their separation, sputtering, macroscopic effects like "Klaumünzer effect (widening and flattening of amorphous solids in a direction perpendicular to the ion beam), lateral mass transport at the surface of the solid, ditch and dike formation, track formation, modification in surface morphology and irradiation induced amorphisation/crystallization [49,52,56–61]. Seitz and Koehler in 1956 [62] proposed the Thermal spike model to explain the energy loss mechanism of swift heavy ions in a solid by suggesting the possibility of the existence of high energy electrons along the ion track in the wake of ion passage. The incoming ions is assumed to transfer energy to the electron clouds in a time scale less than 10^{-17}s, resulting in a region of hot electrons surrounded by a relatively unaffected cold lattice. The excited electrons achieve thermodynamic equilibrium in a short time span and transfer energy to the lattice via electron-phonon coupling. The temperature along the ion path can sometimes exceed the melting temperature of the material (depending on the energy of the ion and the type of target atom) thereby creating ion tracks in the target [55,63]. This process is the main mechanism of material modification in metals and metallic alloys where the electron density is quite high.

Instead of trying to change the surface morphology and magnetic properties after deposition one could try to tailor make films with desired properties by changing the deposition parameters. One of the important

59

parameter that can influence the magnetic anisotropies as well as magnetic properties is the deposition angle. By suitable choice of deposition angles and deposition parameters films with obliquely oriented (with respect to surface normal) nanostructures can be realised.

2.9 Oblique Angle Deposition for Fabrication of Nano Structures

Oblique angle deposition (OAD) is a physical vapour deposition method that can produce nanostructured thin films by changing the deposition angle. The main growth mechanism for OAD is the shadowing effect which tends to produce long nanostructures and the surface diffusion of adatoms which tries to compete that process. By varying the vapour incident angle, one could change the shadowing length thereby changing the particle size distribution on the substrate.

The growth of thin film is mainly governed by three mechanisms:

i.   Geometrical shadowing (the limited ability of a collinear flux to reach all parts of a rough surface)

ii.   Surface diffusion (movement of adatoms along the substrate, film surface and grain boundaries)

iii. Bulk diffusion (leading to oriented crystallization)

The importance of these mechanisms depend on the temperature of the film and substrate during growth. In low temperature thin film deposition, the geometrical effects dominate and gives a porous film structure, whereas at higher deposition temperatures diffusion dominates, yielding increasingly ordered and dense crystalline films.

Oblique angle flux of incoming ions cause atomic shadowing creating an inclined columnar microstructure. By controlling the orientation of the substrate relative to the impinging vapour flux the columnar structures can be tailored for

specific applications. The atomic-scale shadowing or self shadowing has an important role in deposition at oblique angles. The principle of this mechanism is that as the evaporant nucleates on the substrate, the region behind the nucleus does not receive any further vapour flux because this region falls in the shadow of the nucleus. Therefore, vapour will only be deposited onto the nucleus and the columnar structure develops[64].
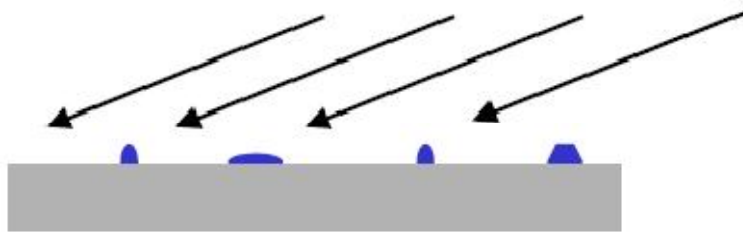

Figure 2.7: Initial nucleation to form shadowing centres during oblique angle deposition. Adapted from reference [65].

The mode of film growth during OAD is usually Volmer-Weber growth mode. The ballistic shadowing is the major factor leading to the formation of microscopic topologies in OAD. The size of the nuclei formed is greatly influenced by the arbitrary fluctuations in the local deposition rate combined with the random nature of adatom diffusion. Defects on the substrate such as impurities, point defects, edge defects etc. leads to sites for nuclei to form initially. As the nuclei are formed, the shadowing effect will quickly become a dominant factor in the film growth. A greater amount of material will be deposited onto the nuclei along the incident flux direction than in the shadowed area. Only those nuclei along the incident flux direction will develop into columns which are tilted in the direction of the incident flux [66].

An important requirement for this to happen is the linear vapour trajectory from the source to substrate. This could be achieved if the deposition in carried out in high or ultra high vacuum. The films prepared are generally porous, possessing nano-columnar structures [67]. The size and density of the nanocolumns change as a function of incident angle, i.e., the angle between the incident flux and substrate normal. The angle made by the columns with the substrate normal is called the column tilt angle β.
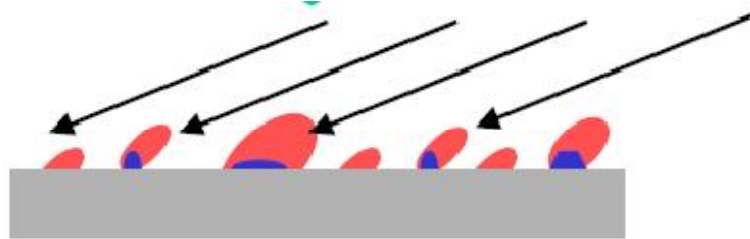
Figure 2.8: Columnar structures formed due to the shadowing effect during the oblique angle deposition. Adapted from reference [65].

In OAD the column tilt angle is always less than the deposition angle α. Nieuwenhuizen and Haanstra [68] proposed a relation between column tilt angle and deposition angle and is given by [64]

$$\tan \alpha = 2 \tan \beta \qquad\qquad 2.36$$

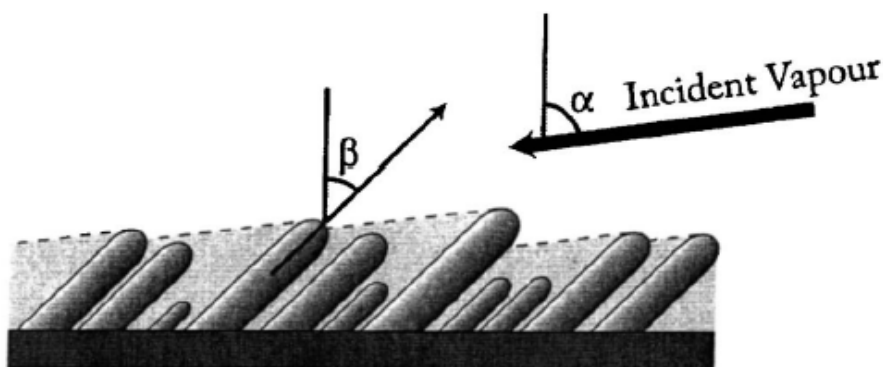**Figure 2.9: Column growth forming an angle β with the substrate during oblique angle deposition. Adapted from reference [65].**

Glancing angle deposition (GLAD) is a modified version of oblique angle deposition. In oblique angle deposition the substrate is held stationary at an angle to the incident vapour flux. But in GLAD, the substrate is no longer stationary during deposition. Substrate rotation alters the apparent location of the vapour source from the perspective of the growing columns. This changes the shadowing dynamics and the column growth will follow the perceived change in source location. The column growth can therefore be sculpted during deposition by dynamic rotation of the substrate.

References

[1]   H.W. Sheng, W.K. Luo, F.M. Alamgir, J. M. Bai, M. E, Nature 439 (2006) 419.

[2]   Z.P. Lu, C.T. Liu, Intermetallics 12 (2004) 1035.

[3]   S.H. Chen, D. Turnbull, Journal of Applied Physics 38 (1967) 3646.

[4]   D. Turnbull, Contemporary Physics 10 (1969) 473.

[5]   U. Herold, U. Koster, B. Cantor (Ed.), Rapidly Quenched Metals III, Metals Society, London, 1978, p. 281.

[6]   J. Basu, S. Ranganathan, Sadhana 28 (2003) 783.

[7]   M. Starink, Thermochimica Acta 404 (2003) 163.

[8]   S. Kurajica, J. Schmauch, E. Tkal, Croatica Chemica Acta 75 (2002) 693.

[9]   D.W. Henderson, Journal of Non-Crystalline Solids 30 (1979) 301.

[10]   G.R. Heal, Thermochmica Acta 340-341 (1999) 69.

[11]   H.E. Kissinger, Journal of Research of the National Bureau of Standards 57 (1956) 217.

[12]   A.T. Sunose, Report Chiba Inst Technol. 16 (1971) 22.

[13]   T. Ozawa, Bulletin of the Chemical Society of Japan 38 (1965) 1881.

[14]   J.H. Flynn, L.A. Wall, Journal of Research of the National Bureau of Standards. A Phys. Chem. 70A (1966) 487.

[15]   P. Duwez, Annual Review of Materials Science 6 (1976) 83.

[16] Z.Y. Lee, D.W. Dai, N.F. Shen, Y.S. Hu, Y.Y. Bao, IEEE Transactions on Magnetics Mag-23 (1987) 2599.

[17] K. Onishi, Y. Shibata, S. Matsushita, Y. Sakurai, IEEE Transactions on Magnetics Mag-17 (1981) 1981.

[18] H. Kobayashi, T. Ono, A. Tsushima, T. Suzuki, Applied Physics Letters 43 (1983) 389.

[19] J.K. Howard, Journal of Vacuum Science & Technology A: Vacuum, Surfaces, and Films 4 (1986) 1.

[20] N. Anuniwat, M. Ding, S.J. Poon, S.A. Wolf, J. Lu, Journal of Applied Physics 113 (2013) 043905.

[21] S. Thomas, H. Thomas, D.K. Avasthi, A. Tripathi, R. V. Ramanujan, M.R. Anantharaman, Journal of Applied Physics 105 (2009) 033910.

[22] S.M. Rossnagel, Journal of Vacuum Science & Technology A: Vacuum, Surfaces, and Films 21 (2003) S74.

[23] L.W. Martin, Y.-H. Chu, R. Ramesh, Materials Science and Engineering: R: Reports 68 (2010) 4.

[24] M. Ohring, Materials Science of Thin Films, 2nd ed., Academic press, San Diego, CA, USA, 2002.

[25] A. Dobrak, B. Verrecht, H. Van den Dungen, A. Buekenhoudt, I.F.J. Vankelecom, B. Van der Bruggen, Journal of Membrane Science 346 (2) (2010) 344.

[26] M. Kader, G. Parisi, Y. Zhang, Physical Review Letters 56 (1986) 889.

[27] M. Pelliccione, T. Karabacak, C. Gaire, G.-C. Wang, T.-M. Lu, Physical Review B 74 (2006) 125420.

[28] D. Forster, D.R. Nelson, M.J. Stephen, Physical Review A 16 (1977) 732.

[29] E. Marinari, A. Pagnani, P. G, Journal of Physics A: Mathematical and General 33 (2000) 8181.

[30] C. Herring, Journal of Applied Physics 21 (1950) 301.

[31] W.W. Mullins, Journal of Applied Physics 30 (1959) 77.

[32] W.M. Tong, R.S. Williams, Annual Review of Physical Chemistry 45 (1994) 401.

[33] S.M. Daliya, S.J. Ruey, Chemical Engineering Journal 129 (2007) 51.

[34]   B.D. Cullity, C.D. Graham, Introduction to Magnetic Materials, 2nd ed., John Wiley and Sons Inc., 2008.

[35]   N.A. Spaldin, Magnetic Materials: Fundamentals and Applications, Second, Cambridge University Press, 2011.

[36]   S.E. Offerman, N.H. Van Dijk, J. Sietsma, S. Grigull, E.M. Lauridsen, L. Margulies, H.F. Poulsen, M.T. Rekveldt, S. Van der Zwaag, Science 298 (2002) 1003.

[37]   E.C. Stoner, E.P. Wohlfarth, Philosophical Transactions of the Royal Society of London. Series A, Mathematical and Physical Sciences 240 (1948) 599.

[38]   W. Wernsdorfer, C. Thirion, N. Demoncy, H. Pascard, D. Mailly, Journal of Magnetism and Magnetic Materials 242-245 (2002) 132.

[39]   L. Zhang, Preparation and Characterization of Sputtered SmCo Thin Films for Magnetic Recording Media, National University of Singapore, 2010.

[40]   R.A. Mccurrie, S. Jackson, Journal of Applied Physics 61 (1987) 4858.

[41]   G. Herzer, G.C. Hadjipanayis (Ed.), Proceedings of the NATO Advanced Study Insititute on Magnetic Hysteresis in Novel Materials, Mykonos, Greece, 1997, pp. 1–12.

[42]   R. Alben, J.J. Becker, M.C. Chi, Journal of Applied Physics 49 (1978) 1653.

[43]   G. Herzer, IEEE Transactions on Magnetics 26 (1990) 1397.

[44]   G. Herzer, M.M. B. Idzikowski, P. Švec (Ed.), Properties and Application of Nanocrystalline Alloys from Amorphous Precursors, Kluwer Academic Publishers, Dordrecht, Budmerice, Slovakia, 2003, p. 15.

[45]   T. Hysen, S. Deepa, S. Saravanan, R. V. Ramanujan, D.K. Avasthi, P. A. Joy, S.D. Kulkarni, M.R. Anantharaman, Journal of Physics D: Applied Physics 39 (2006) 1993.

[46]   S. Thomas, S.H. Al-Harthi, D. Sakthikumar, I. Al-Omari, R. V. Ramanujan, Y. Yoshida, M.R. Anantharaman, Journal of Physics D: Applied Physics 41 (2008) 155009.

[47]   G. Joy, Preperation of Thin Films, Marcel Dekker Inc., New York, USA, 1992.

[48]   M.L. Munford, M.L. Sartorelli, L. Seligman, A.A. Pasa, Journal of The Electrochemical Society 149 (2002) C274.

[49]   H. Thomas, S. Thomas, R. V. Ramanujan, D.K. Avasthi, I. Al- Omari, S. Al-Harthi, M.R. Anantharaman, Nuclear Instruments and Methods in Physics Research Section B: Beam Interactions with Materials and Atoms 287 (2012) 85.

[50]   S. Thomas, S. H. Al-Harthi, I.A. Al-Omari, R. V. Ramanujan, V. Swaminathan, M.R. Anantharaman, Journal of Physics D: Applied Physics 42 (2009) 215005.

[51]   E.E.B. John, C.B. Robert, J.D. Demaree, E. Cattaruzza, S.E. Donnelly, B.F. David, L.F. Robert, G. Daniel, F. Gonella, K.H. James, H.K. Charles, G. Mattei, M. Koji, C. Maurizio, M. Paolo, A. Misra, N. Michael, K. Nordlund, P.J.T. Nunn, T. Masayasu, P.D. Townsend, Engineering Thin Films and Nanostructures with Ion Beams, Taylor & Francis Group, LLC, US, 2005.

[52]   S. Bagchi, S. Anwar, N.P. Lalla, Applied Surface Science 256 (2009) 541.

[53]   H. Narayan, H.M. Agrawal, R.P.S. Kushwaha, D. Kanjilal, S.K. Sharma, Nuclear Instruments and Methods in Physics Research Section B: Beam Interactions with Materials and Atoms 156 (1999) 217.

[54]   R. Kumar, M.W. Khan, J.P. Srivastava, S.K. Arora, R.G.S. Sofin, R.J. Choudhary, I. V. Shvets, Journal of Applied Physics 100 (2006) 033703.

[55]   A. Meftah, J.M. Costantini, M. Djebara, N. Khalfaoui, J.P. Stoquert, F. Studer, M. Toulemonde, Nuclear Instruments and Methods in Physics Research Section B: Beam Interactions with Materials and Atoms 122 (1997) 470.

[56]   S. Kavita, V.R. Reddy, A. Gupta, D.K. Avasthi, Nuclear Instruments and Methods in Physics Research Section B: Beam Interactions with Materials and Atoms 244 (2006) 19.

[57]   J.K. Tripathi, P.C. Srivastava, Applied Surface Science 253 (2007) 8689.

[58]   P. Mallick, R. Biswal, C. Rath, D.C. Agarwal, A. Tripathi, D.K. Avasthi, D. Kanjilal, P.V. Satyam, N.C. Mishra, Nuclear Instruments and Methods in Physics Research Section B: Beam Interactions with Materials and Atoms 268 (2010) 470.

[59]   R. Kumar, K.M. Wasi, J.P. Srivastava, S.K. Arora, S.R.G. S., R.J. Choudary, I. V. Shvets, Journal of Applied Physics 100 (2006) 33703.

[60]   J.K. Tripathi, P.C. Srivastava, Applied Surface Science 253 (2007) 8689.

[61] P. Dash, P. Mallick, H. Rath, A. Tripathi, J. Prakash, D.K. Avasthi, S. Mazumder, S. Varma, P.V. Satyam, N.C. Mishra, Applied Surface Science 256 (2009) 558.

[62] F. Seitz, J.S. Koehler, D. Turnbull, Solid State Physics 2 (1956) 307.

[63] E. Kuzmann, S. Stichleutner, K. Havancsák, M.R. El-Sharif, C.U. Chisholm, O. Doyle, V. Skuratov, K. Kellner, G. Dóra, Z. Homonnay, A. Vértes, Radiation Physics and Chemistry 75 (2006) 741.

[64] M.M. Hawkeye, M.J. Brett, Journal of Vacuum Science & Technology A Vacuum Surfaces and Films 25 (2007) 1317.

[65] Y. Zhao, D. Ye, G. Wang, T. Lu, L. Akhlesh, M. Sergey (Eds.), Proceedings of SPIE "Nanotubes and Nanowires" Vol:5219, SPIE, Bellingham, WA, 2003, pp. 59–73.

[66] F. Tang, D.L. Liu, D.X. Ye, Y.P. Zhao, T.M. Lu, G.C. Wang, A. Vijayaraghavan, Journal of Applied Physics 93 (2003) 4194.

[67] S. Thomas, S.H. Al-Harthi, R. V. Ramanujan, Z. Bangchuan, L. Yan, W. Lan, M.R. Anantharaman, Applied Physics Letters 94 (2009) 063110.

[68] J.M. Nieuwenhuizen, H.B. Haanstra, Philips Technical Review 27 (1966) 87.

Chapter 3

Analytical Techniques Used for Characterisation

3.1   Swift Heavy Ion (SHI) irradiation for materials modification

3.2   Thickness measurement

3.3   Compositional Analysis

3.4   Thermal Analysis

3.5   Structural Analysis

3.6   Surface Morphology Analysis

3.7   Magnetic Studies

3.8   Surface Magnetic Properties

Research in the realm of experimental physics and materials science complement each other and elaborate material preparation is a necessary condition. Materials are to be prepared using suitable techniques and adoption of appropriate techniques for characterisation of material is mandatory. A thorough knowledge on the history of preparation and also on the purity is also inexplicable in this regard. This only will lead to right interpretation of the results. It is in this context that the employment of sophisticated analytical techniques becomes all the more important. With the advent of modern technology various instruments like scanning probe microscopes, field emission scanning electron microscopes and high resolution transmission electron microscopes, superconducting quantum interference devices etc are available for characterisation of the sample at various stages. This chapter takes a look at the various experimental techniques used for the preparation of Fe-based magnetic thin film samples. A detailed description of the various analytical techniques is also provided here with appropriate first principles.

Swift Heavy Ion (SHI) irradiation is a fine technique to impart structural and morphological changes in the sample. A short discussion regarding the various aspects of SHI is provided in the next section.

3.1 Swift Heavy Ion Irradiation for Materials Modification
Accelerator Facility at Nuclear Science Centre

The ion beam irradiation experiment in the present study is carried out in the 15 UD Pelletron of Inter University Accelerator Centre, New Delhi, India. This accelerator can generate ions of the required elements with energy of few hundred million electron volts (MeV). Negative ions are generated in the SNICS (source of negative ions by caesium sputtering) ion source. The sputter source uses accelerated caesium ions, striking a cold cathode, to produce a negative ion beam of cathode material. These ions are extracted from the ion source by applying a positive injection voltage.

The negative ions are then injected into a strong electrical field inside an accelerator tank filled with sulphur hexafluoride insulating gas. At the centre of

the tank there is a terminal shell, which is maintained at a high voltage (~ 15 MV). The negative ions, on traversing through the accelerating tubes from the top of the tank to the positive terminal get accelerated. On reaching the terminal, they pass through a stripper, which removes some electrons from the negative ions, thus transforming the negative ions into positive ions.
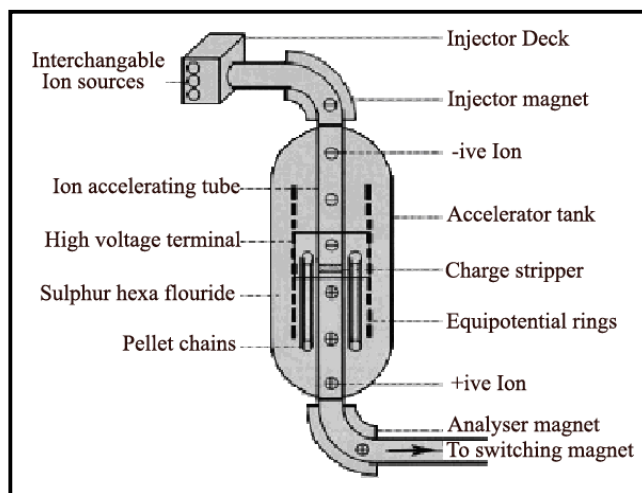

Figure 3.1: Schematic showing the principle of acceleration of ions in Pelletron. Adapted from IUAC website www.iuac.res.in.

These positive ions are then repelled away from the positively charged terminal and are accelerated to ground potential to the bottom of the tank. In this manner, same terminal potential is used twice to accelerate the ions. After coming out from the tank, the ions are bend into horizontal plane by an analyzing magnet, which also selects a particular beam of ion. The switching magnet diverts the high energy ion beams into various beam lines for the different experimental areas of the beam hall. The entire machine is computer controlled and is operated from the control room. These accelerated ions are fed into the materials science beam hall, where the samples are loaded in the sample holder, made of thick block of copper. The pressure in the chamber is maintained at 1×10^{-6} Torr during the irradiation. A schematic of the Pelletron accelerator at IUAC, New Delhi is shown in figure 3.1.

71

3.2 Thickness measurement

The film thickness is also calculated using Dektak 6M Thickness Profiler. The block diagram of the instrument is shown in figure 3.2.
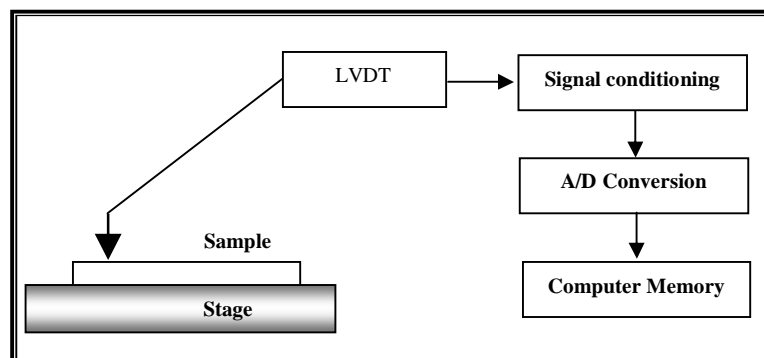

Figure 3.2: Schematics of thickness profiler.

Using this instrument, thickness and the surface roughness of the films can be evaluated. The measurements are taken electromechanically by moving the diamond tipped stylus horizontally over the sample according to a user programmed scan length, speed and stylus force. The stylus is mechanically coupled to the core of an LVDT (Linear Variable Differential Transformer.)

As the stage moves the stylus, it rides over the sample surface. Sample height variation causes the stylus to be transformed vertically. Electrical signals corresponding to stylus movements are produced as core position of the LVDT changes. The LVDT changes the stylus reference signal proportional to the position change, which is conditioned and converted to a digital format, through a high precession, integrating, analog-to-digital converter. The digitized signals obtained from a single scan are stored in a computer memory for display, manipulation and measurement.

3.3 Compositional Analysis

3.3.1   Energy Dispersive X-Ray Spectroscopy (EDS)

In electron microscope, on irradiation with high energy electrons elements in the specimen usually emit photons of x-radiation with wavelength and energy characteristic of the elements in the specimen. The spectrum of radiation can thus be used for elemental identification, using forms of x-ray

spectroscopy based on either wavelength or energy (known as wavelength dispersive or energy dispersive x-ray spectroscopy) [1].

An inelastic collision between a K shell electron and a primary electron with energy greater than the binding energy of the K shell electron can result in the ejection of core electron from the atom. The resulting vacancy in the K shell can be filled by an electron from one of the higher energy shells, L, M, etc. The excess energy of this electron, that is the difference between the energy states in the two shells, is emitted during the transition as an x-ray photon. Thus the energy of the K x-radiation equals E_L-E_K if the transition is between L, K shells and E_M-E_K if it is between M, K shells. The former is designated as $K(\alpha)$ radiation and later as $K(\beta)$.
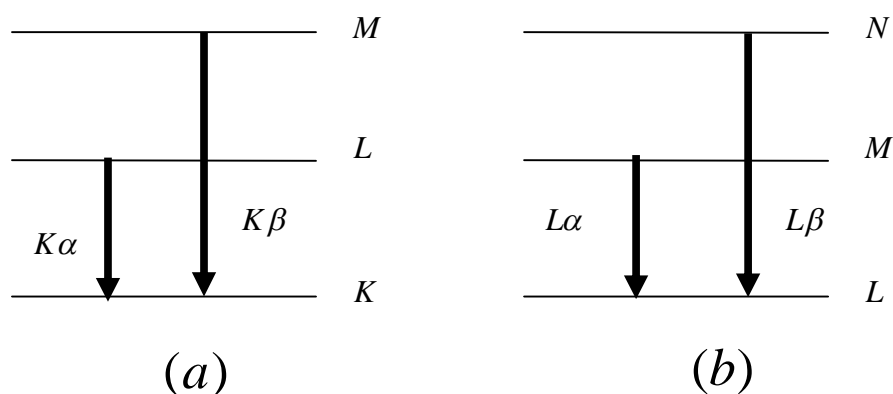

Figure 3.3: Schematic of electron transitions responsible for the production of (a)$K(\alpha)$and $K(\beta)$ (b) $L(\alpha)$ and $L(\beta)$ x-rays

A similar situation exists with respect to electrons in the L shell. The energy of the L x-radiation equals E_M-E_L if the transition is between M, L shells and E_N-E_L if it is between N, L shells. The former is designated as $L(\alpha)$ radiation and later as $L(\beta)$. Figure 3.3 shows a schematic of the electron transitions responsible for the production of $K(\alpha)$, $K(\beta)$, $L(\alpha)$ and $L(\beta)$ x-rays. Every atom species has, therefore, a characteristic x-ray emission spectrum which can be excited by supplying energy equal to or in excess of the appropriate binding energy, by electron bombardment. The characteristic line spectrum forms the

'fingerprint' of the different atomic species. Since the actual energy levels depend on the atomic number of the elements, it follows, therefore, that the elements present in a specimen can be identified by analysis of the emission spectrum. The characteristic lines are superimposed on a background continuum (Bremsstrahlung continuum).

When an incident x-ray strikes the detector, it creates a charge pulse that is proportional to the energy of the x-ray. The charge pulse is converted to a voltage pulse (which remains proportional to the x-ray energy) by a charge-sensitive preamplifier. The signal is then sent to a multichannel analyzer where the pulses are sorted by voltage. Thus ED spectrometer is able to analyze a whole spectrum simultaneously. The spectrum of x-ray energy versus counts is evaluated to determine the elemental composition of the sampled volume.

3.3.2   X ray Photoemission Spectroscopy (XPS)

The detection and energy analysis of photoelectrons produced by x-ray irradiation whose energy exceeds their binding energies is the subject of an extensively used technique known as x-ray photoelectron spectroscopy (XPS).

Figure 3.4 (a & b) shows a schematic of the process involved in the emission of a photo/auger electron. XPS involves the removal of a single core electron, while Auger electron spectroscopy (AES) is a two electron process. Auger electrons are produced in XPS along with photoelectrons.

In XPS the sample is irradiated with x-rays of known energy, $h\nu$ and electrons of binding energy (BE) E_b are ejected, where, $E_b < h\nu$. These electrons have a kinetic energy (KE) E_k which can be measured in the spectrometer, and is given by $E_k = h\nu - E_b - \phi_{sp}$ where ϕ_{sp} is the spectrometer work function, and is the combination of sample work function, ϕ_s, and the work function induced by the analyser [2,3].

Since we can compensate for the work function term electronically, it can be eliminated, leaving $E_k = h\nu - E_b$ or $E_b = h\nu - E_k$

Thus by measuring the KE of the photoelectrons we can determine the BE of the electrons. An XP spectrum is generated by plotting the measured photoelectron intensity as a function of BE. The BEs of these lines is characteristic for each element, and is a direct representation of the atomic orbital energies.
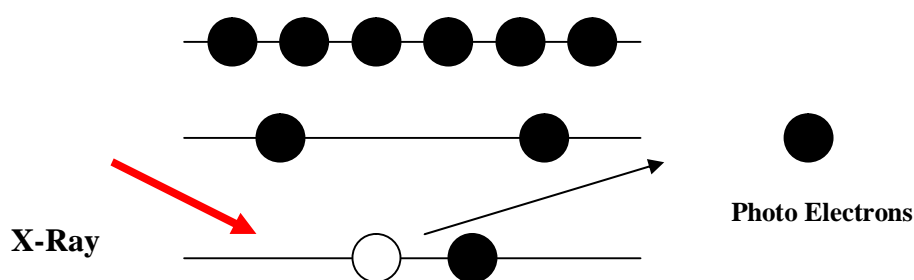
X-Ray

Photo Electrons

Figure 3.4 (a): Process involved in photoelectron emission

The exact binding energy of an electron depends not only upon the level from which photoemission is occurring, but also upon the formal oxidation state of the atom and the local chemical and physical environment. Changes in either of the above will give rise to small shifts in the peak positions in the spectrum - so-called chemical shifts. Atoms of a higher positive oxidation state exhibit a higher binding energy due to the extra coulomb interaction between the photo-emitted electron and the ion core. This ability to discriminate between different oxidation states and chemical environments is one of the major strengths of the XPS technique.
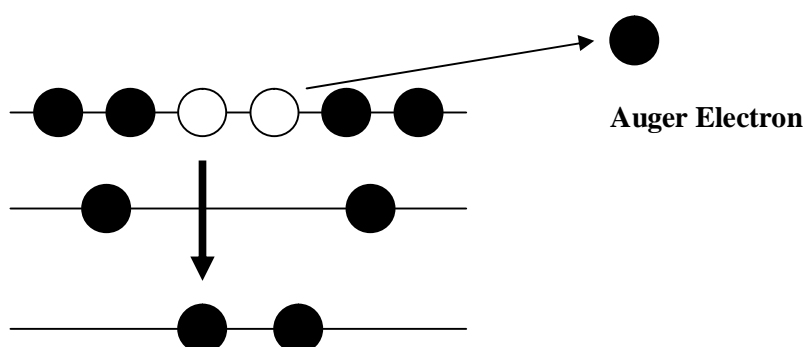
Auger Electron

Figure 3.4 (b) Process involved in Auger electron emission

75

XPS is a surface sensitive technique and the surface sensitivity of XPS is due to the low inelastic mean-free path, λ_m of the electrons within the sample. The actual escape depth λ of the photoelectrons depends on the direction in which they are travelling within the sample, such that $\lambda = \lambda_m \cos\theta$, where θ is the angle of emission with respect to the surface normal.

The basic requirements for a photoemission experiment are:

1. A source of fixed-energy radiation (an x-ray source).

2. An electron energy analyzer (which can disperse the emitted electrons according to their kinetic energy, and thereby measure the flux of emitted electrons of a particular energy).

3. A high vacuum environment (to enable the emitted photoelectrons to be analyzed without interference from gas phase collisions).
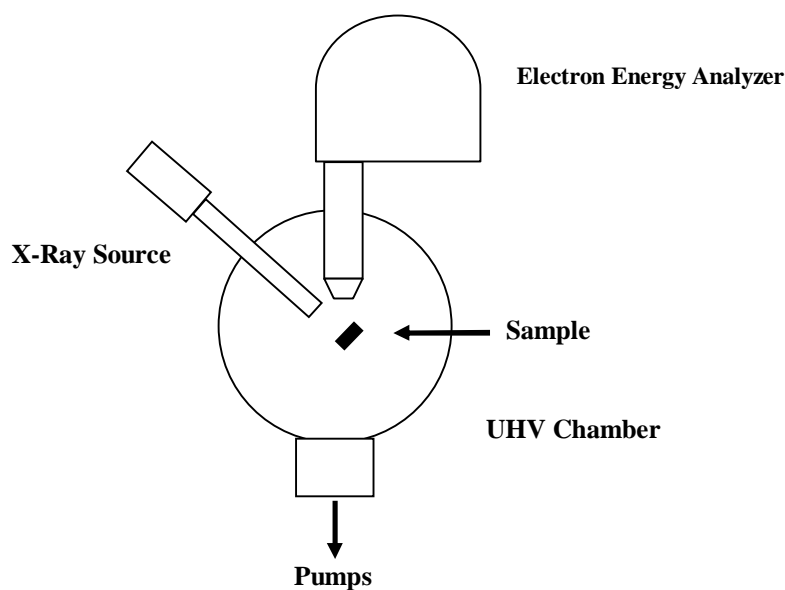

Figure 3.5 Schematic of XPS system

As the photons of X-ray strike the sample, photoelectrons will be ejected. A lens system focuses the photoelectrons into an energy analyzer. The analyzer is hemispherical. It filters the photoelectrons depending on their kinetic energy. The photoelectrons enter the analyzer in straight line. They will be exposed to an

electrostatic field and their paths will be bended with different radius for different kinetic energy. The curved paths will reach a detector. The electrons arriving at the detector will be converted to a signal.

To estimate at% of elements from XPS wide scan

1. After ascribing a suitable background function to represent the background the peak area for each element is integrated and is divided by the relative sensitivity factor for that element to obtain the weighted area.

2. The atom percent of each element is obtained by dividing the weighted area of the curve for the element by the sum of the areas for all the elements in the sample (there are provisions in the software for adding or removing elements).

To estimate wt% of elements from XPS wide scan

3. First the at % is calculated from the wide scan spectrum

4. Then the at % is multiplied with the atomic mass of the corresponding element to obtain the weighted atom percentage

5. The weight percent of each element is obtained by dividing the weighted atom percentage for each element by the sum of the weighted atom percentage for all the elements in the sample

3.3.3 Secondary Ion Mass Spectroscopy (SIMS) & Secondary Neutral Mass Spectroscopy (SNMS)

Secondary Ion Mass Spectrometry (SIMS) and Secondary Neutral Mass Spectrometry (SNMS) are both surface analysis techniques in which the specimen is bombarded by an ion beam and sputtered particles are detected by a mass spectrometer. The critical difference between the techniques is that the SIMS ions are generated directly by the sputtering process, whereas those detected in SNMS are produced by ionisation of neutral particles sometime after leaving the surface. The separation of the sputtering and ionisation events in SNMS results in a near-constant ionisation probability for each element, irrespective of the

material from which it originated. This is in contrast to the well-known matrix effect of SIMS where the ionisation probability during sputtering can vary by orders of magnitude, depending on the surface chemistry. The compositions obtained from both techniques are quantified in different ways and are complimentary in the concentrations that they measure. SIMS is a high sensitivity surface analysis technique for the determination of surface composition, contaminant analysis and depth profiling in a sample's uppermost surface layers.

The important points are,

SIMS

- SIMS signals vary non-linearly with the matrix composition (matrix effect), often over orders of magnitude.

- Accurate quantification is possible when the impurity (dopant) is dilute within a uniform matrix (<3%).

- Quantification requires matrix matched reference material to provide a relative sensitivity factor (RSF).

SNMS

- Ionisation is separated from sputtering – minimal matrix effects.

- RSF is constant so specialist reference materials are not required, easily available alloys will suffice.

- SNMS signals vary linearly with composition and quantification methods are essentially simple.

- Detection range is typically 100% to 0.1%.

3.4 Thermal Analysis

3.4.1 Differential Scanning Calorimetric Studies (DSC)

Whenever a material undergoes a change in its physical state, such as melting or transition from one crystalline state to another or whenever it reacts chemically, heat is either absorbed or liberated. Thus these thermal changes are either due to endothermic or exothermic reactions or transitions. Generally phase

transitions are endothermic processes where crystallization, oxidation etc are exothermic processes. DSC is an effective tool to detect such thermal changes in a material. In DSC, the thermal behaviour of a sample is studied by measuring the differential heat flow required to maintain the sample material and an inert reference material at the same temperature. The curve obtained in DSC is a recording of the heat flow dH/dt in mcal/s as a function of temperature T. Area enclosed by the DSC curve is proportional to enthalpy change.

There are two modes used in DSC. One is the power compensated DSC and the other is heat flux DSC. In the former case separate heaters heat the sample and the reference and their temperature is increased or decreased linearly. In heat flux DSC the difference in heat flow into the sample and reference are noted as the sample and reference are heated linearly.

DSC 7 (Perkin- Elmer) operates in power compensated mode and gives direct calorimetric measurements, characterization and analyses of thermal properties of the sample. The adjustment of heater power necessary to keep the sample temperature identical to that of the reference holder provides a varying electrical signal equivalent to varying thermal behaviour of the sample. The DSC spectrum can give valuable information regarding the various thermodynamic processes happened to the material when it is subjected to heating. The DSC thermograms can be used to obtain the activation energy of crystallization, Avarami exponents and frequency factor.

3.5 Structural Analysis

3.5.1   X Ray Diffraction (XRD)

X-ray diffraction patterns have been widely used in materials research as a primary characterisation technique for obtaining information like crystal structure, crystallite size, lattice constants and strain.

In XRD a collimated beam of X-ray with a wavelength λ (In this study $\lambda = 1.5406$ Å) is incident on a specimen and is diffracted by the crystalline planes in the specimen according to the Bragg's law

$$n\lambda = 2d \sin\theta \qquad\qquad 3.1$$

Where λ is the wavelength of the X-radiation, n is an integer, d is the spacing between atomic planes in the crystalline planes and θ is known as diffraction angle. The intensity of the diffracted x-rays was measured and plotted as a function of diffraction angle 2θ. From the 2θ values of the peaks, the lattice spacing (d) values are calculated using the equation (3.1). The lattice parameter 'a' was then computed by assuming cubic symmetry and combining equations (3.1) and (3.2).

$$d_{hkl} = \frac{1}{\sqrt{\frac{h^2}{a^2} + \frac{k^2}{b^2} + \frac{l^2}{c^2}}} \qquad\qquad 3.2$$

When a=b=c, $\quad d_{hkl} = \frac{a}{\sqrt{h^2 + k^2 + l^2}} \qquad\qquad 3.3$

Sample identification can be easily done by comparing the experimental pattern to that in the International Centre for Diffraction Data (ICDD) file. Except for single crystalline particles, the randomly oriented crystals in polycrystalline samples/thin films cause broadening of the diffraction patterns. The effect becomes more pronounced, when the crystallite size is of the order of few nanometers. The simplest and most widely used method for estimating crystallite size is from the Full Width at Half Maximum (FWHM) of a diffraction peak using Scherrer formula, $D = \frac{0.9\lambda}{\beta \cos\theta}$, where 'D' is the crystallite size, λ is the wavelength of the X-radiation, β is the angular width (in radians) which is equal to the (FWHM). Rigaku Dmax–C, and Bruker Discover D8 X-ray Powder Diffractometers were used to obtain the X-ray diffraction pattern of the samples using Cu Kα lines.

3.5.2 Grazing Incidence X-Ray Diffraction (GIXRD)

It is sometimes very difficult to analyze thin films due to their small diffracting volumes (thickness), which result in low diffracted intensities

compared to the substrate and background. This combination of low diffracted signal and high background make it very difficult to identify the phases present. So special techniques must be employed when analyzing thin films. The most common technique for analyzing thin films as thin as 100 Å is to use a grazing incidence angle arrangement. Grazing angle diffraction techniques are used when the information needed lies within a thin top layer of the material. Figure 3.6 shows the Seemann-Bohlin parafocusing geometry which is commonly used in the study of thin films.
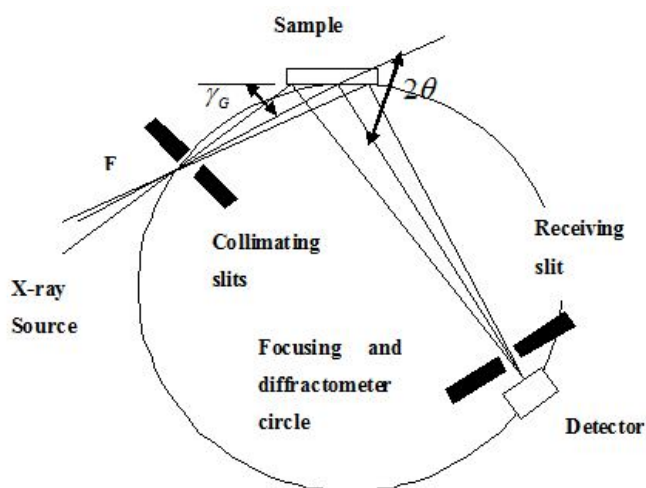

Fig.3.6 Seemann-Bohlin diffractometer. The point F is either the focal point of the x-ray tube or the focal point of a focusing monochromator.

For the Seemann-Bohlin geometry (Figure 3.6) the incident X rays impinge on a fixed specimen at a small angle, γ_G (typically 1^0 to 3^0) and the diffracted X rays are recorded by a detector that moves along the focusing circle. This method provides good sensitivity for thin films, due to para-focusing and the large diffracting volume, which results from γ_G being small and the X-ray path length in the film being large (proportional to $1/\sin(\gamma_G)$. By increasing the path length of the incident X-ray beam through the film, the intensity from the film can be increased, while at the same time, the diffracted intensity from the substrate can be reduced. Overall, there is a dramatic increase in the signal to the background ratio.

3.5.3   Transmission Electron Microscopy (TEM)

TEM is a technique based on the principle that an electron beam interacting and passing through a specimen causes atoms to eject/emit electrons/photons. The electrons emitted by the source are focused and magnified by a system of magnetic lenses. The geometry of TEM is shown in figure 3.7. The electron beam is confined by the two condenser lenses which also control the brightness of the beam, passes the condenser aperture and "hits" the sample surface. The electrons that are elastically scattered consist of the transmitted beams, which pass through the objective lens. The objective lens forms the image display and the following apertures, the objective and selected area aperture are used to choose the elastically scattered electrons that will form the image of the microscope. Finally, the beam goes to the magnifying system that consists of three lenses, the first and second intermediate lenses which control the magnification of the image and the projector lens. The formed image is shown either on a fluorescent screen or in monitor or both and is printed on a photographic film.

Operation

The operation of TEM requires an ultra-high vacuum and a high voltage. TEM offers two methods of specimen observation, diffraction mode and image mode. In diffraction mode, an electron diffraction pattern is obtained on the fluorescent screen, originating from the sample area illuminated by the electron beam. The diffraction pattern is entirely equivalent to an X-ray diffraction pattern: a single crystal will produce a spot pattern on the screen, a polycrystal will produce a powder or ring pattern (assuming the illuminated area includes a sufficient quantity of crystallites), and a glassy or amorphous material will produce a series of diffuse halos. The image mode produces an image of the illuminated sample area.

The image can contain contrast brought about by several mechanisms: mass contrast, due to spatial separations between distinct atomic constituents;

thickness contrast, due to non-uniformity in sample thickness; diffraction contrast, which in the case of crystalline materials results from scattering of the incident electron wave by structural defects; and phase contrast. If the unscattered beam is selected for image formation, one obtains the Bright Field Image. Dark Field Images are attained if diffracted beams are selected by the objective aperture. Also in TEM, analysis can be done with EDS (Energy Dispersive X-ray spectroscopy), EELS (Electron Energy Loss Spectrum) and EFTEM (Energy Filtered Transmission Electron Microscopy) data.
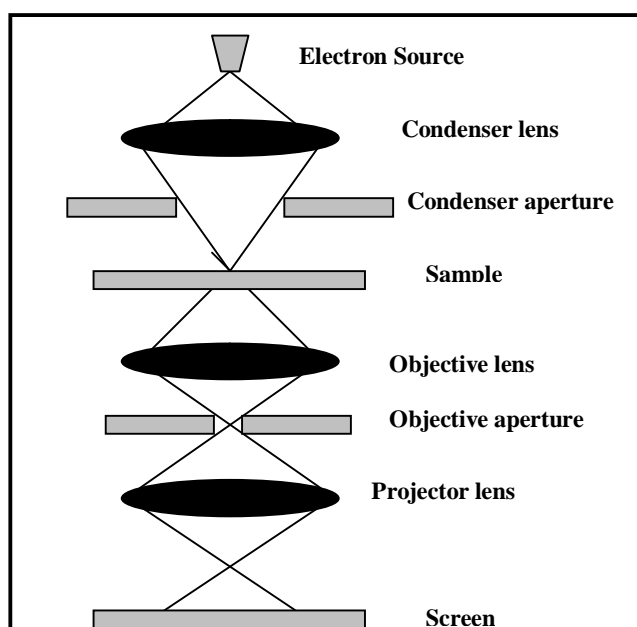
Figure 3.7: Transmission electron microscope with all of its components.

The greatest advantage that TEM offers are the high magnification ranging from 50 to 10^6 and its ability to provide both image and diffraction information from a single sample.

3.6 Surface Morphology Analysis

3.6.1 Scanning Electron Microscopy (SEM)

In SEM, a source of electrons is focused in vacuum into a fine probe that is rastered over the surface of the specimen using suitable arrangement of coils. As the electrons penetrate the surface, a number of interactions occur that can

result in the emission of electrons or photons from or through the surface. A reasonable fraction of the electrons emitted can be collected by appropriate detectors, and the output can be used to modulate the brightness of a cathode ray tube (CRT) whose x and y inputs are driven in synchronism with the x-y voltages rastering the electron beam. In this way an image is produced on the CRT; every point that the beam strikes on the sample is mapped directly onto a corresponding point on the screen. As a result, the magnification system is simple and linear magnification is calculated by the equation: M=L/l where L is the raster's length of the CRT monitor and l the raster's length on the surface of the sample.
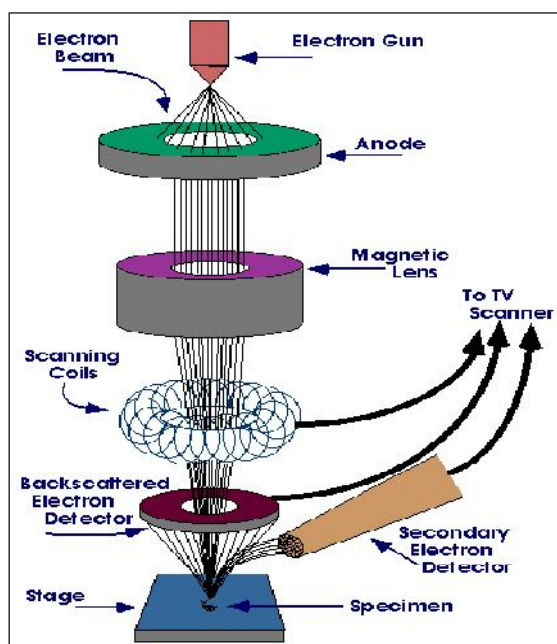

Figure 3.8: Geometry of SEM

SEM works on a voltage between 2 to 50 kV and its beam diameter that scans the specimen is 5 nm-2 μm. The principle images produced in SEM are of three types: secondary electron images, backscattered electron images and elemental X-ray maps. Secondary and backscattered electrons are conventionally separated according to their energies. When the energy of the emitted electron is less than about 50 eV, it is referred to as a secondary electron and backscattered

electrons are considered to be the electrons that exit the specimen with energy greater than 50 eV [73]. Detectors of each type of electrons are placed in the microscope in proper positions to collect them.

3.6.2   Atomic Force Microscopy (AFM)

The Atomic Force Microscope was developed to overcome a basic drawback of the STM (scanning tunnelling microscope) - that it can only image conducting or semi conducting surfaces. The AFM, however, has the advantage of imaging almost any type of surface, including polymers, ceramics, composites, glass, and biological samples. Binnig, Quate, and Gerber invented the Atomic Force Microscope in 1985 [4]. Since then a large number of scanning probe microscope (SPM) variants were developed based on the detection of forces between the probe tip and a sample. A variety of tip-surface interactions may be measured by an atomic force microscope (AFM), depending on the separation between tip and sample. At short distances the tip predominantly experiences inter-atomic forces: the very short range (≈ 0.1 nm) Born repulsive forces and the longer range (up to 10 nm) Van-der-Waals forces. Further away from the surface where the Van-der-Waals forces decay rapidly and become negligible (100-500 nm above the surface), long-range electric, magnetic and capillary forces are still significant and can be probed.

The underlying principle of AFM is that the interactions between the sample and the end of a probe tip that is mounted on a cantilever result in a response in the cantilever, notably a deflection. In continuous contact model, also known as repulsive mode, an AFM tip makes soft "physical contact" with the sample. The sharp probe tip, often a pyramidal-shaped etched silicon nitride tip, is attached to the end of a V-shaped spring cantilever with a low spring constant, typically between 0.06 N/m and 0.6 N/m. As the scanner gently traces the tip across the sample, the contact force causes the cantilever to deflect to accommodate changes in topography. In the standard constant force mode, a feedback system maintains the cantilever deflection at a constant level (which

corresponds to a constant force according to Hooke's law). The set point, a parameter, which is defined by the user, defines the force that will be exerted on the surface by the tip (which can be as low as ~ 0.1 nN).

A common way to measure the cantilever deflection is by utilizing a laser beam which is reflected off the back of the cantilever, *via* a mirror, onto a position-sensitive photo detector. The laser beam which bounces off the cantilever functions as an optical lever arm, amplifying the deflection. As the sample is scanned under the tip, the x, y and z position of the sample surface with respect to the tip is determined by a piezoelectric tube scanner. The movement of the sample in the z-direction, that is needed to keep the deflection at its constant set point level, is registered during x-y scanning, and a three dimensional map is constructed which is closely related to the topography of the surface.
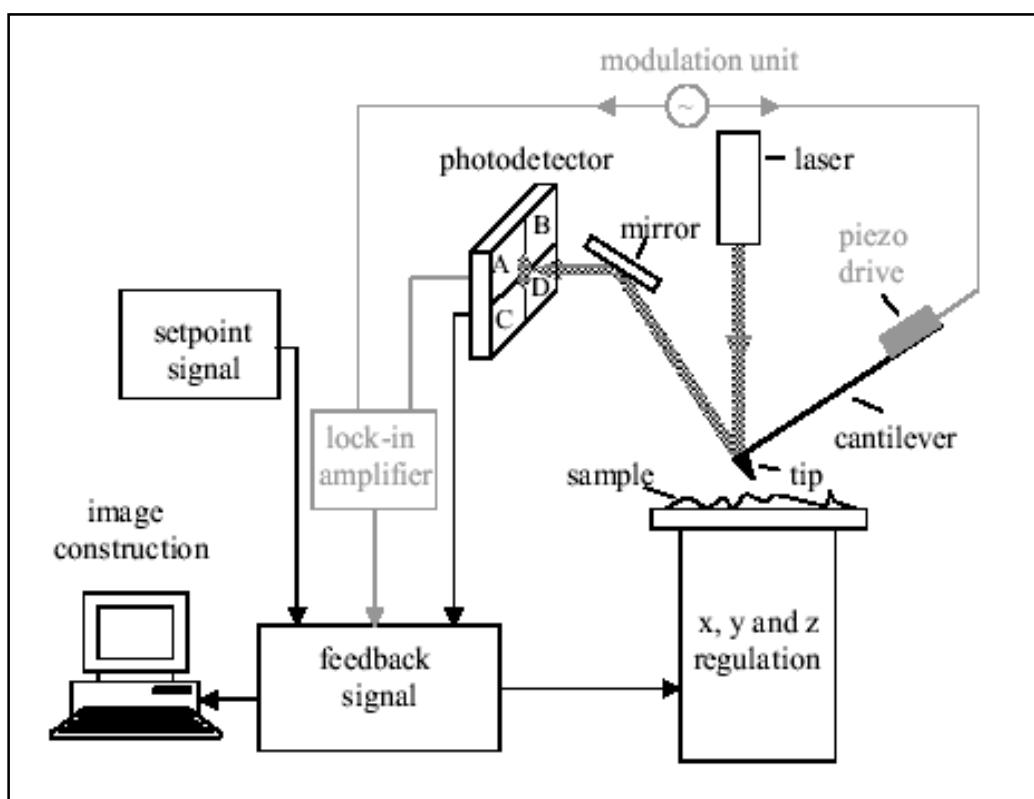

Figure 3.8: Block diagram of the essential components of the continuous contact and tapping mode AFM.

Tapping mode (TM) AFM successfully overcomes many drawbacks of the contact-mode. In tapping mode, to diminish lateral and normal forces exerted by the tip on the sample, the tip is brought only intermittently into contact with the surface during scanning. The basic idea is that the cantilever is brought into oscillation, and changes in oscillation amplitude or phase are detected as the vibrating tip sweeps across and interacts with the surface.

3.7 Magnetic Studies

3.7.1 Vibrating Sample Magnetometry (VSM)

The magnetic characterization of the samples was carried out using a Vibrating Sample Magnetometer (VSM), model: EG & G Par 4500 and DMS 1660 VSM. The main parts of a VSM and the simplified block diagram are given in Fig 3.9 and 3.10 .Saturation magnetization (M_s), Retentivity (M_r) and Coercivity (H_c) were evaluated from the hysteresis loops.
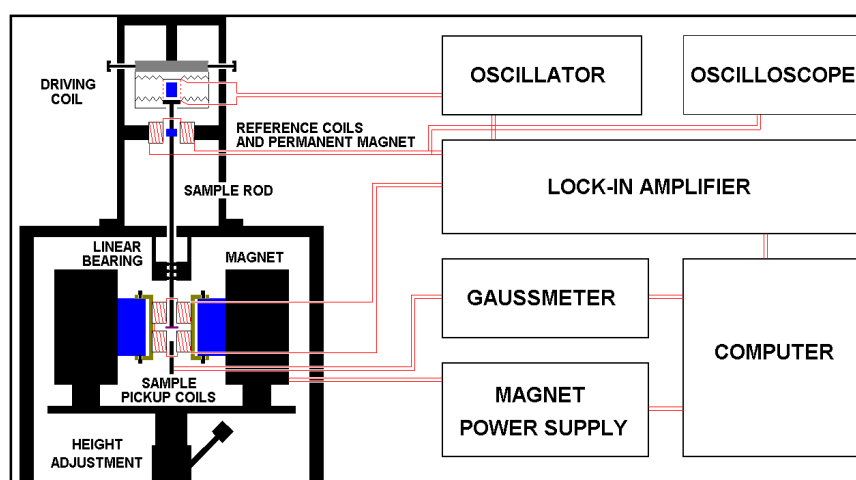

Figure 3.9: Schematics of VSM

The magnetic thin films are kept in the sample holder, which is centered in the region between the pole pieces of an electromagnet. A slender vertical sample rod connects the sample holder with a transducer assembly located above the magnet. The transducer converts a sinusoidal ac drive signal into a sinusoidal vertical vibration of the sample rod and the sample was thus made to undergo

sinusoidal motion in a uniform magnetic field. Coils mounted on the pole pieces of the magnet pick up the signal resulting from the sample motion.

However, vibration amplitude and frequency also will have some contributions to the induced emf. A servo mechanism is used to stabilize the amplitude and frequency of the drive so that the output accurately tracks the moment level without degradation due to variation in the amplitude and frequency of the oscillator. This servo technique uses a vibrating capacitor located beneath the transducer to generate an ac control signal that varies solely with the vibration amplitude and frequency. The signal, which is at the vibration frequency, is fed back to the oscillator where it is compared with the drive signal so as to maintain constant drive output. It is also phase adjusted and routed to the signal demodulator where it functions as the reference drive signal. The signal developed in the pickup coils is then buffered, amplified and applied to the demodulator. There it is synchronously demodulated with respect to the reference signal derived from the moving capacitor assembly. The resulting dc output is an analog signal, which depends only on the magnitude of the magnetic moment, and not influenced by the amplitude and frequency drift. The cryogenic setup attached to the sample assembly can be used to study the magnetization of samples at low temperatures.
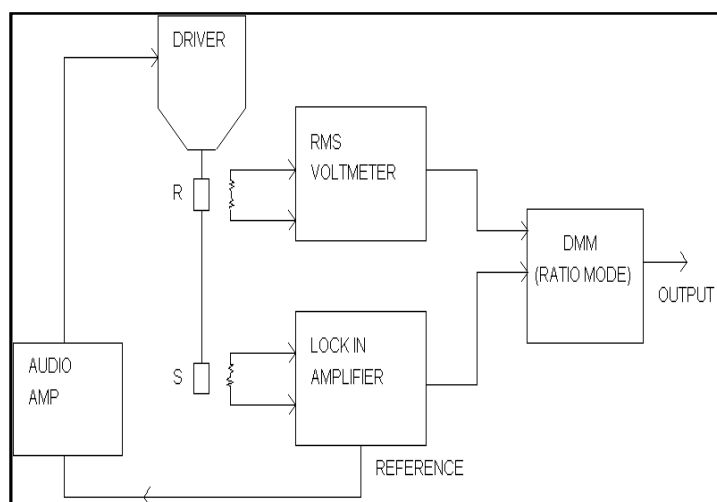

Figure 3.10: Block Diagram of VSM.

Principle & Theory Involved in VSM

When a sample is placed in a magnetizing field 'H', it will respond with a magnetic induction 'B'

$B_{sample} = \mu_0 (H+M)$

where 'M' is the magnetization in the sample. The magnetization and the magnetic moment 'm' and the volume 'v' to get:

$$B_{sample} = \mu_0 \left[H + \frac{m}{v} \right]$$

In free space, outside the sample, a magnetic induction 'B $_{by\ sample}$' is proportional to the magnetic moment 'm' of the sample present:

$$B_{by\ sample} = gm$$

where 'g' is a proportionality constant depending on the position of the point in space. The total magnetic induction at a point in space is:

$$B_{space} = B_{ext.} + B_{bysample} = B_{ext} + gm$$

where $B_{(ext.)}$ is the magnetic induction of free space due to the magnetizing field 'H'. Note that when the external field 'B$_{ext}$ is varied, the pickup coils do not pick up the change due to the fact that the coil pairs are wound in opposite directions. When the sample is moved near a pickup coil, a voltage is induced in the coil:

$$V = -NO\frac{dB_{space}}{dt} = -NO\frac{d}{dt}\left(B_{ext.d} + gm\right)$$

where N is the number of turns and O is a constant depending on the geometry of the coil. Note that only the components of the field normal to the area of the coil are included in this and all subsequent expressions. Since the magnetizing field H and consequently the magnetic induction B $_{ext}$ due to the field is constant, we can write:

$$V = -NO\frac{dg}{dt}m$$

Here g is not a constant and it depends on the position of the sample and is a function of time. If the sample is in a sinusoidal motion we can write:

$$V = -NOA\frac{de^{j\omega t}}{dt}m$$

89

–*NO* is substituted by a constant 'k' and taking the derivative we get:

$$V = k\omega jAe^{j\omega t}m$$

It can be seen that a voltage 'V' proportional to the magnetic moment 'm', is induced in the coil.

VSM uses an electromechanical driver (voice coil) to move a vertical drive rod with a small amplitude 'A', and frequency 'ω' mounted on the drive rod of the sample holder *S*, and a small permanent magnet or small coil with a constant dc excitation current of constant magnitude as reference magnetic moment *R*. Pick-up coils near *R* will have an induced voltage

$$V_R = jk_R\omega Ae^{\omega t}m_R$$

Where, 'k_R' is a constant depending on coil geometry, and 'm_R' is the constant magnetic moment of reference R. 'V_R' is in the milli volt range and easily measured by a rms voltmeter. Similarly, the sample pick-up coils will see a voltage $V_s = jk_s\omega Ae^{\omega t}m_s$ or more precisely $V_s = -k_s\omega Am_s\sin(\omega t)$, where, '$k_s$' is a constant depending on the sample coil geometry and 'm_s' is the magnetic moment of the sample coil S. An RMS-to-dc conversion is performed on both 'V_R' and 'V_S' by the RMS voltmeter and lock-in amplifier, respectively. The ratio of these two dc voltages is then taken by a digital multimeter (DMM) which has ratio capabilities. Taking the root-mean-square average of the previous two equations, it is seen that the dependence on frequency 'ω', and drive amplitude 'A', cancel and the DMM output is

$$V_{out} = \frac{\langle V_S \rangle_{rms}}{\langle V_R \rangle_{rms}} = km_S$$

where 'k' is the calibration constant which has absorbed 'k_R', 'k_S', 'm_R', as well as any amplifications of the reference signal and the sample signal by the lock-in amplifier. Since the magnetic moment 'm' is related to the magnetization 'M' and the volume 'v' of the sample we can write:

$$V_{out} = kvM_s$$

We can directly read off the magnetization of the sample 'M_s' by writing:

$$M_s = \frac{V_{out}}{kv}$$

3.8 Surface Magnetic Properties

3.8.1   Magneto Optic Kerr Effect (MOKE)

Magneto Optic Kerr effect (MOKE) discovered by reverend John Kerr in 1877, is a useful tool in studying the magnetic properties of thin films and surfaces. The effect stems from the interaction of electromagnetic radiation with electrons of the media through which they propagates.
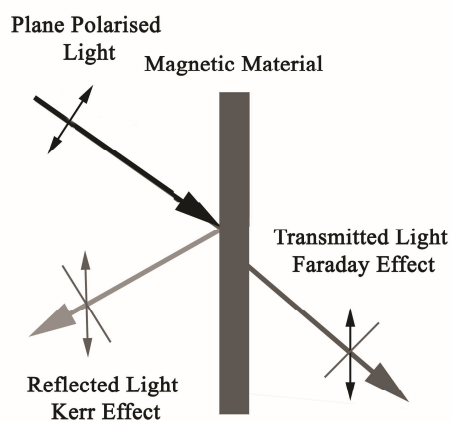

Figure.3.11: Magneto optic Kerr effect

When a plane polarized light interacts with a magnetic medium there is a proportional change on the state of polarisation of reflected/transmitted light. The effect in reflection geometry is called Kerr effect and in transmission geometry is called Faraday or Voight effect. When a linearly polarized light is reflected from a magnetic material the magneto optical Kerr effect manifests itself as an elliptical polarization and rotation of plane of polarization of the reflected beam. The magnitude of Kerr effect is proportional to the direction and magnitude of magnetisation of the sample surface and hence this technique can be used to measure the magnetic properties of a surface.

By measuring the Kerr rotation as a function of applied magnetic field the magnetic hysteresis can be obtained. The Kerr effect can be attributed to the off diagonal elements in the magnetic susceptibility tensor.
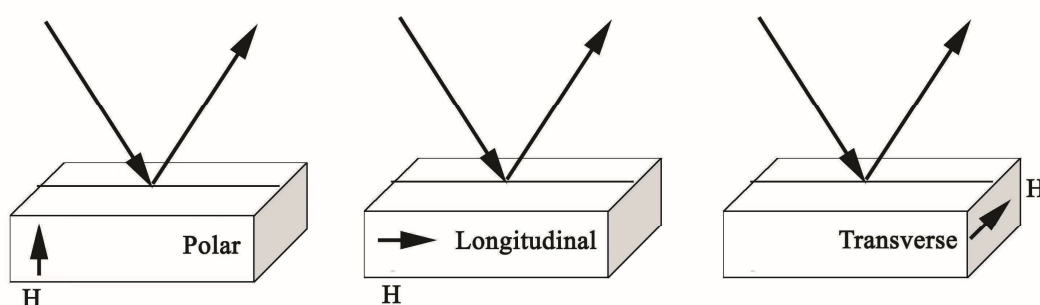

Figure 3.12: Three different configurations for measuring MOKE

Basically three are different geometrical configurations for using MOKE depending on the direction of magnetic moments and plane of polarization of incident light. In polar configuration as shown in figure 3.12 a the applied field is perpendicular to sample surface. In such a case the magneto optic effect is proportional to the magnetisation perpendicular to the surface. In longitudinal case the applied field is along the film plane and parallel to the plane of incidence. The MOKE signal is proportional to the magnetisation in the direction of the applied field. In transverse configuration the applied field is along the sample surface and perpendicular to the plane of incidence. The magneto optic signal is proportional to the component of magnetisation parallel to the surface but perpendicular to H.

The MOKE setup essentially consists of a He-Ne laser, polarizer, photo elastic modulator, electromagnet, analyser, and solid state detector with instrumentation and computer for automation. The instrument is automated using GW basic programme. Measurement is carried out using an intensity stabilized He-Ne Laser (1 mW, 632.8 nm) with a spot size of 1.5 mm with a divergence of approximately 1.8 mrad at the sample. The laser beam is plane polarized using the polariser and the beam incidence angle is kept at 45°. Glan-

Taylor prisms with antireflection coatings are used as analyser and polarizer. When a polarized beam of light falls on a nonmagnetic sample the reflected light will also be plane polarized. However if the polarized beam falls on a magnetic sample the reflected beam will consists of an s component (Es) and p component (Ep).

   To obtain information from MOKE measurement one has to measure the s component and eliminate the p component. This can be realized by keeping an analyser just before the detector with its axis in crossed position with respect to the polarizer. Thus if there is any change in the plane of polarization there will be an output from the analyser and the photo diode will detect the signal. The quality of polarisers and analysers are denoted by the extinction coefficient (In this case the value is $>10^{-5}$).
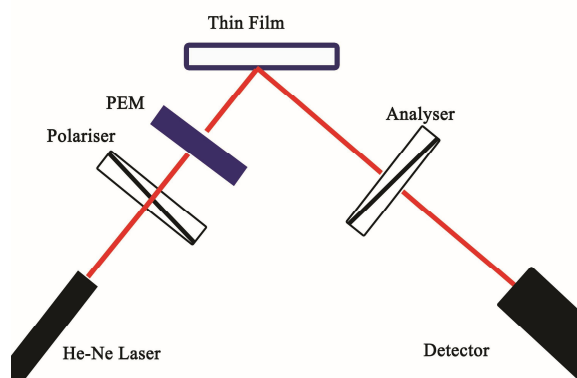

Figure 3.13: Schematics of a MOKE measurement system.

   Usually instead of keeping the analyser and polarizer in crossed position they are usually kept very near to extinction (in this experiments -2°). A standard electromagnet provides a magnetic field up to 1800 Oe in the plane of the sample. In order to avoid the noise in the measured signal a photo elastic modulator is used to modulate the state of polarization with a frequency 50 kHz and measure the output using the lock in amplifier. The frequency reference signal from the PEM is used to lock the signal from the output voltage. The data read from the lock in amplifier and gauss meter is fed to the computer and the

experiment is repeated for a whole set of field values ranging from 1800 to -1800 Oe to obtain sufficient data for plotting hysteresis loops.

3.8.2   Magnetic Force Microscopy (MFM)

Magnetic force microscopy detects the force (or force derivative) acting on a small magnetic probe in the stray field close to the specimen. MFM consists of a cantilever which is suspended on one side. On the free end a small volume of magnetic material, the tip, is mounted. When a magnetic surface is brought close to this tip they will interact by the magnetic stray field. Magnetic force microscopy is a non-contact technique and during scanning, the sample is kept at a distance of several nanometers from the tip. A computer assigns grey-or colour values to different strengths of interaction forming a microscopic image of interaction on the sample surface.

In a MFM two basic detection modes can be applied which are sensitive to two different types of interaction. The static (or DC) mode detects the magnetic force acting on the tip whereas the dynamic (or AC) mode measures the force derivative.

During the MFM measurements, there are two forces acting on the tip; magnetic and Van-der-Waals forces. Hence, in MFM, the signal contains both information of surface topography (called 'Topo signal') and surface magnetic property (called 'MFM signal'). The dominating force depends on the distance between the tip and the sample surface, because the inter-atomic magnetic force persists for greater tip-to-sample separations than the Van-der-Waals force. These Van-der-Waals forces vary according to the tip-sample distance and therefore are used to measure the surface topography. If the tip is close to the surface, in the region where standard non-contact AFM is operated, the image will be predominantly topographic. As one increase the separation between the tip and the sample, magnetic effects become apparent. Collecting a series of images at different tip heights is one way to separate magnetic from topographic effects.

The key to successful MFM imaging lies in separating the magnetic signal from the entire signal. In MFM, this is done by 'Two Pass' technique. In this MFM mode, sample is scanned twice to separate the signal. In the first scan, the tip scans the surface as in true non-contact AFM to obtain the topography of the sample. In the second scan, the tip-sample distance is increased and the biased tip is scanned along the topography line obtained from the first scan. The tip is only affected by the magnetic force and MFM image is obtained as a result.

References

[1]   I.M. Watt, The Principles and Practice of Electron Microscopy, Cambridge University Press, Cambridge, 1997.

[2]   B. David, M.P. Seah, Practical Surface Analysis by Auger and X-Ray Photoelectron Spectroscopy, John Wiley and Sons Ltd, Chichester, 1990.

[3]   D.J. O'Connor, B.A. Sexton, R.S.C. Smart, Surface Analysis Methods in Materials Science, Springer-Verlag, Berlin, 1992.

[4]   G. Binnig, C.F. Quate, C. Gerber, Physical Review Letters 56 (1986) 930.

Chapter 4

Effect of Thermal Annealing on $Fe_{40}Ni_{38}B_{18}Mo_4$ Films - Modified Herzer Model for Magnetic Evolution

4.1   Introduction

4.2   Experimental Methods

4.3   Results and Discussion

4.4   Conclusions

4.1 Introduction

Nano-crystalline alloys obtained from Fe rich metallic glasses by devitrification have been the subject matter of intense research ever since their discovery. Due to the unusual combination of various physical properties associated with these materials they are increasingly being sought after for various applications ranging from transformer cores to sensors [1].

Upon devitrification the microstructure of these materials changes to a soft magnetic nanocrystalline phase embedded in para/ferro magnetic amorphous matrix. The superior soft magnetic properties exhibited by these alloys are generally explained using the random anisotropy model (RAM) [2,3]. According to RAM when the structural correlation length is comparable to or smaller than the exchange correlation length, the anisotropies are averaged over several domains and the material exhibits low crystalline anisotropy. This is reflected in the low values of coercivity exhibited by such materials.

These materials are widely used for sensor applications and $Fe_{40}Ni_{38}B_{18}Mo_4$ alloy is known to have a large saturation magnetisation, low coercivity and low magnetostriction of ~12 ppm [4]. The magnetoelastic properties of these alloys are widely used for sensor applications. These alloys are commercially available in the form of thin ribbons with ~20 µm thickness and widths of several centimetres. Despite their ease of availability, METGLAS ribbons have several shortcomings for sensor applications. The as-cast material does not have superior magnetic properties, due to residual stress. Hence the material is subjected to stress relief and nanocrystallisation by techniques like thermal/current annealing in the presence or absence of magnetic field or stress to align the domains in particular directions and to induce nanocrystallisation.

In the past several years, researchers have tried to fabricate thin films using evaporation technique [5]. The resulting films were crystalline and they did

not report any magnetic and compositional studies. Liang *et.al.* reported fabrication of METGLAS films by co-sputtering process using Fe-Ni, Mo and B targets. They observed that the alloy film showed good soft magnetic properties compared to its bulk counterparts of the same composition [6]. There are few reports in the literature pertaining to the fabrication of thin films derived from these systems. Fabricating thin film forms of these types of soft magnetic materials will help integrating them to micro/nano electro mechanical systems. Also realisation of amorphous thin films and possible nanostructuring of such systems for superior magnetic properties is important from a fundamental point of view. Since nano-crystalline materials are widely used for sensor application [7], increasing the surface area would facilitate fabrication of thin film sensors that can be integrated with today's microelectronics. Also, when one or more of the sample dimensions is reduced to the order of domain wall width ($\delta \sim 40$ nm for iron based alloys) in the bulk material, they will serve as a good platform to investigate the applicability of Herzer's model in low dimensional systems. The above conditions can alternatively be realized by depositing ultra thin layers of metallic glasses on suitable substrates. In this study Fe-Ni-B films on glass substrates and the modification of their magnetic properties with thermal annealing is investigated. A modified model based on Herzer model for bulk ribbons is found to explain the observed evolution of soft magnetic property with thermal annealing in ultra-thin magnetic films.

4.2 Experimental Methods

METGLAS ribbons having the composition $Fe_{40}Ni_{38}B_{18}Mo_4$ were vacuum evaporated under high vacuum of 1×10^{-6} Torr using tungsten filaments on ultrasonically cleaned glass substrates. During evaporation, the pressure in the

chamber increased to 3x10^{-6} Torr. The thickness of the deposited films was determined using the Dektac 6M Stylus Profiler. XPS study of the films deposited on float glass substrates were performed with an Omicron Nanotechnology XPS system with a monochromatic Al Kα radiation (hν = 1486.6 eV) of source voltage 15 kV and emission current of 20 mA. All scans were carried out at an ultrahigh vacuum of 1.5× 10^{-10} Torr. The obtained XPS spectra were deconvoluted and quantified using Casa XPS program (Casa Software Ltd, UK), in which the background was simulated using the Shirley function and the peaks were fitted using a Gaussian Lorentzian function. The spectrum recorded was corrected using the binding energy of adventitious carbon at 284.6 eV and the accuracy of the measured binding energy values is estimated to be ± 0.2 eV. The elemental composition of the sample is extracted from the wide scan, while the individual element peaks were analyzed to obtain the chemical composition. As charging effects are unavoidable in the XPS study of thin films deposited on non conducting samples, charge compensation was performed by electron gun flooding. The deposited film is scratched to obtain the film material which was subsequently subjected to Differential Scanning Calorimetry (DSC) to determine their crystallization temperatures and thermal stability. Based on the DSC results, the thin film samples were also annealed at different temperatures ranging from 373-673 K under high vacuum conditions. The X-ray diffraction (XRD) spectra of the thin films samples, pristine as well as annealed were recorded using an X-ray diffractometer (Rigaku D-max-C) using Cu Kα radiation (λ =1.5405 Å). The average particle size is determined from the measured width of their diffraction curves using Scherrer formula $D = \left(\frac{0.9\lambda}{\beta \cos\theta} \right)$, where λ is the wavelength of Cu Kα radiation (λ =1.5405Å), β is FWHM, D the average grain size and θ the diffracting angle. The surface topography of the prepared thin

films was studied using a standard AFM (Digital Instruments Nanoscope V) with provisions for MFM imaging. AFM imaging is used to study the morphology and MFM imaging is used to study the magnetic domain characteristics. The hysteresis loop parameters of the Fe-Ni-B samples was evaluated using a VSM (model: EG & G PAR 4500) in the parallel and perpendicular fields (magnetic field parallel and perpendicular to the film plane) at room temperature for both pristine and annealed thin films. The MOKE study on the film samples was done using custom made equipment at UGC-CSR, Indore.

4.3 Results and Discussion

4.3.1. Compositional Analysis

The thicknesses of the deposited films measured using the Dektac 6M Stylus Profiler is found to be 36 nm. The wide scan XPS spectrum shown in figure 4.1 has signature peaks of Fe, Ni, B and unavoidable contaminants like carbon and oxygen. The contribution of oxygen from a native oxide layer on top of the film cannot be ruled out as we have not used any capping layer to avoid the same. The quantification of the XPS wide scan spectrum yielded Fe, Ni and B concentration of $Fe_{70}Ni_{24}B_6$ (the subscripts represents the elemental composition in at wt%) .

The slow scan spectrum of iron is shown in figure 4.2 a. The deconvolution of the main peak representing $2p_{3/2}$ shows two components. The peak at 706.5 eV corresponds to metallic iron whereas the peak at 710.7 eV corresponds to Fe^{3+} from Fe_2O_3. There is a small satellite peak at 719.1 eV further confirming the presence of trivalent iron in the oxide [8].
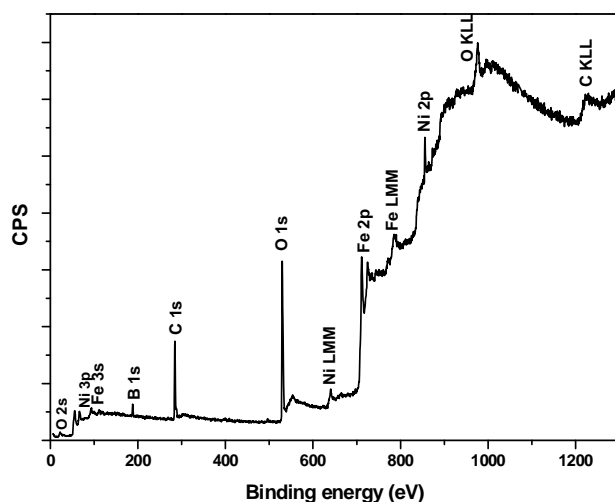
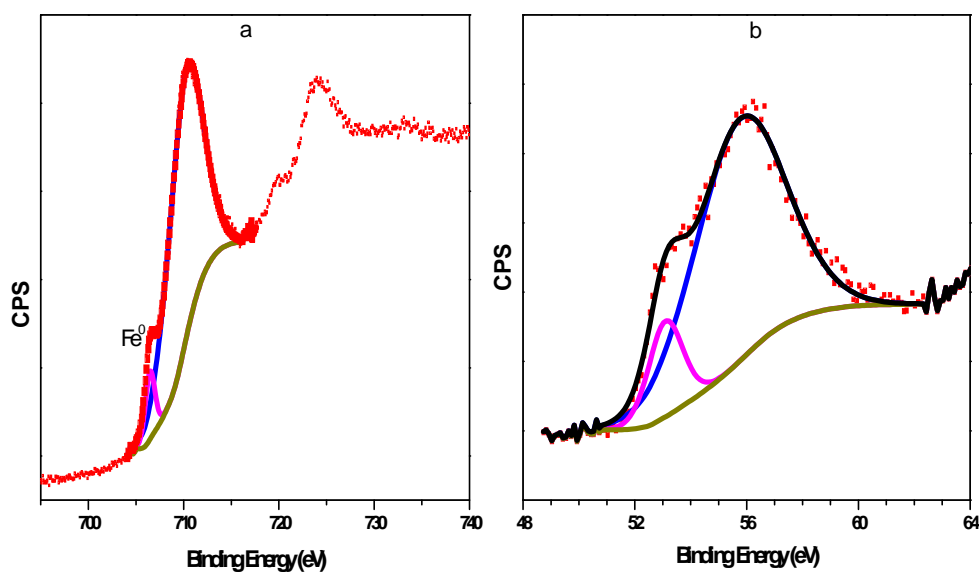**Figure 4.1: XPS spectrum of as deposited Fe-Ni-B thin films.**

Figure 4.2: Slow scan spectrum of a) Fe 2p and b) 3p core level transitions.

        The Fe 3p spectrum is also shown in figure 4.2 b. The Fe 3p peak can be convoluted to two small peaks. The peak at 53.0 could be attributed to the transition corresponding to metallic iron. The peak at 55.8 could be from α-Fe_2O_3 or γ-Fe_2O_3. Although the Fe 3p peak is a doublet consisting of both Fe $3p_{3/2}$ and Fe $3p_{1/2}$ only a single peak was observed in the XPS spectrum obtained from the present study. Theoretically the separation energy of the XPS peaks is

proportional to the spin–orbit coupling constant, which depends on the value $\frac{1}{r^2}$, where r is a radius of the particular orbit [9] and thus the peak separation becomes smaller towards the outer shell. It would appear that the resolution of the current instrument cannot separate these two peaks at 3p level for Fe [10]. The above results suggest that the thin film have a native oxide layer of iron on top of the film. Iron, when exposed to atmosphere will readily form a thin oxide layer on top and this will prevent further oxidation. In this study, since the XPS suggests the existence of Fe in metallic form within the probing depth ~3nm, it can be inferred that the oxide layer is less than 3 nm or metallic iron exists on the film surface. This latter is not possible due to the higher surface energies, iron on contact with atmosphere readily form a thin oxide layer on top of its native surface [11].
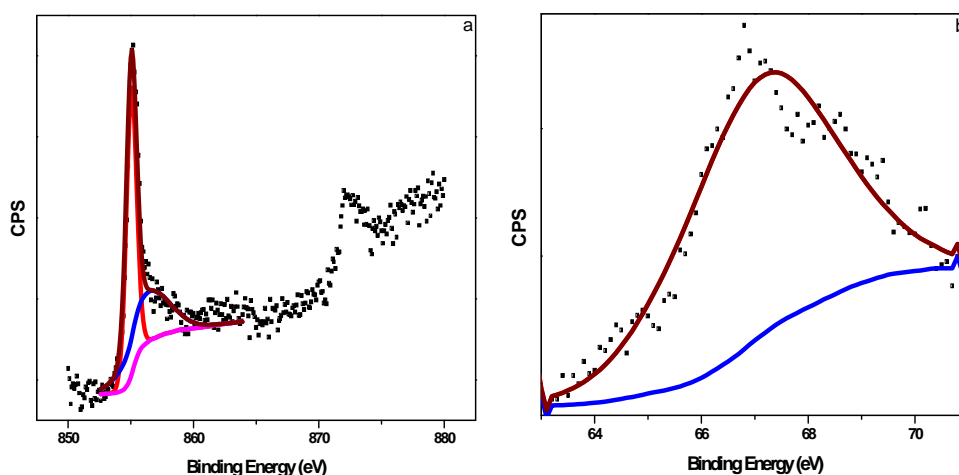

Figure 4.3: Slow scan spectrum of a) Ni 2p and b) 3p core level transitions

The 2p core level spectrum of Ni is shown in figure 4.3a. The spectrum is similar to the spectrum of metallic nickel. This is further reiterated from the 3p spectrum shown in figure 4.3b. The 3p spectrum is a convolution of $3p_{1/2}$ and $3p_{3/2}$. No other components corresponding to any other oxide is found. Thus it can be concluded that in the film, nickel exists in metallic form. This is understandable since nickel shows more corrosion resistance than iron [12] .
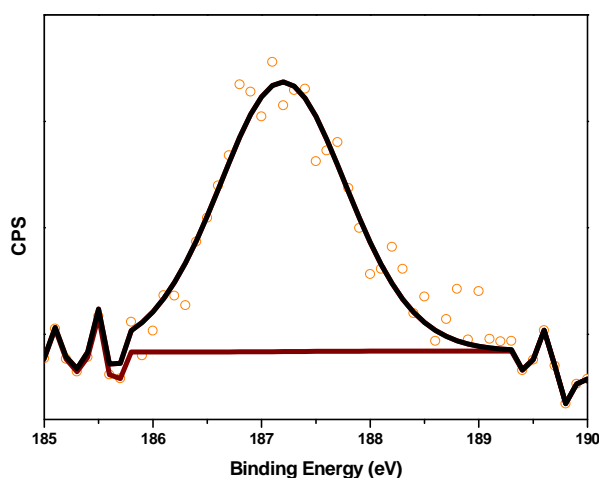
Figure 4.4: Slow scan spectrum of B 1s core level transition

Figure 4.4 shows the slow scan spectrum of Boron. The de-convolution of the slow scan spectra shows only one peak corresponding to elemental boron.
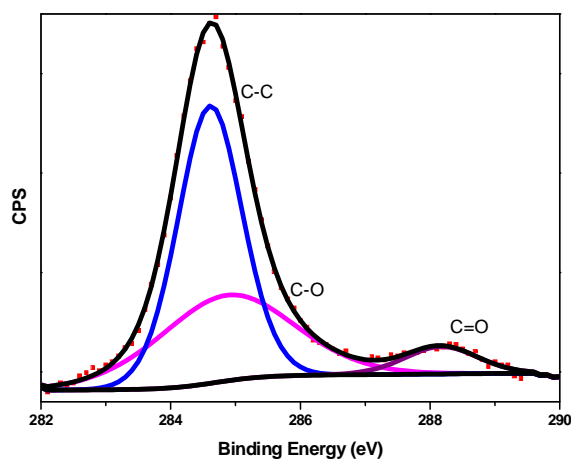

Figure 4.5: Slow scan spectrum C 1s core level transition

Figure 4.5 shows the slow scan spectrum of carbon. Carbon is ubiquitous and hence it is common practice in the XPS data analysis to use the carbon C 1s peak at 284.6 eV as a reference for charge correction. In routine XPS analyses of samples kept outside the vacuum chamber, relatively thick carbon layers are formed on the surfaces. The peak at 284.6 can be assigned to carbon single bond from carbon. The peak at 288.4 can be assigned to weak C=O bond. The peak at
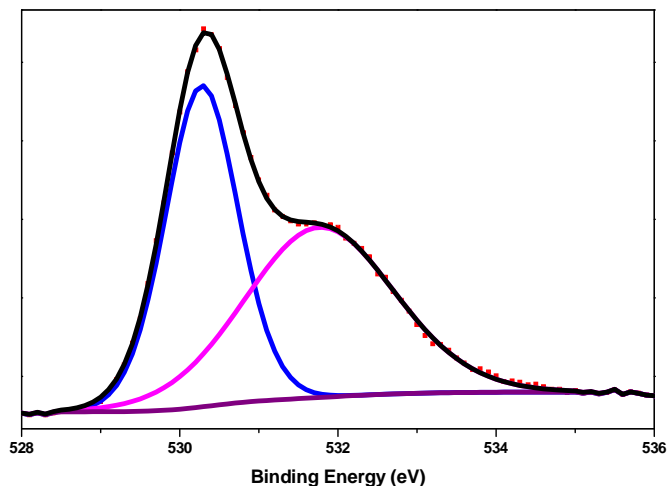
284.9 can be assigned to C-O bond.

Figure 4.6: Slow scan spectrum of O 1s core level transition

The oxygen slow scan spectrum shown in figure 4.6 can be de-convoluted to two peaks. The surface pollution is also evidenced by the presence, within the O 1s line, of a shoulder at (531.8) appearing at a binding energy 1.6 eV higher than the main O 1s peak. This shoulder corresponds to hydroxyl species on the surface [13]. The component peak at 529.8 can be ascribed to oxygen from metal oxide bond coming from native oxide of Fe.

The SNMS spectrum of the thin film is shown in the figure 4.7. The Fe, Ni concentrations maintain almost the same variation up to erosion time of around 800 s. Since SNMS is devoid of any matrix effects we can infer that the film has fairly same composition throughout the film.
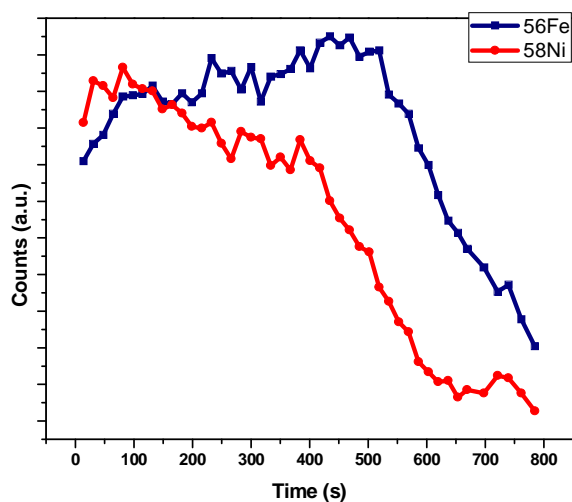
Figure 4.7: SNMS spectrum of Fe-Ni-B thin films.
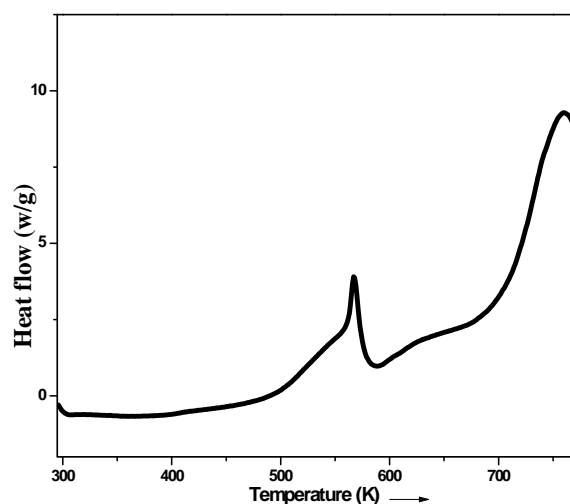
Figure 4.8.DSC thermogram of thin film for heating rate 10 K/min.

The DSC scan of the film material is shown in the figure 4.8. Due to the limitation regarding the maximum available temperature of the DSC apparatus we could not measure beyond 500^0C. From the two peaks in the DSC image it is evident that there are two crystallization events. The transition at $305\ ^0$C evidently corresponds to nanocrystallisation of fcc Fe-Ni. The second peak corresponds to the crystallization of boride phases.

4.3.2. Structural Analysis

From the XRD it is evident that the as prepared films are amorphous. Annealing the films at 473 K started the precipitation of nanocrystalline Fe-Ni which is evident from figure 4.9b suggesting that the Fe-Ni crystallization starts at a much lower annealing temperature. In bulk ribbons the presence of less diffusive molybdenum results in the precipitation of Fe-Ni-Mo at an annealing temperature of 693K. Compared with the 473K annealed film the films become more crystalline with thermal treatments at 673 K which is manifested as a narrow peak in the XRD. The x-ray diffraction pattern of the as deposited single layer films with thickness of 36 nm is shown in the (Figure 4.9a).
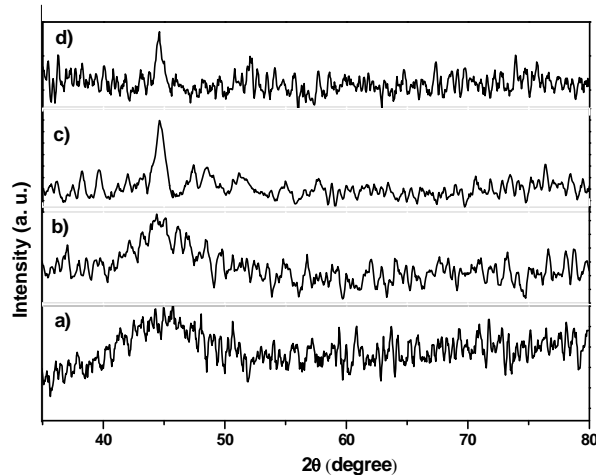
Figure 4.9: XRD pattern of a) pristine and annealed at b) 473K c) 573K d) 673K.

The pristine films show (figure 4.9) broad diffraction peaks, which indicate their amorphous nature. But interestingly this is in contradiction with the results reported by Menon *et. al.* [5], where they found that the as deposited films are crystalline. It must be borne in mind that we have employed vapour deposition technique rather than flash evaporation. In addition to these, our films contain boron which is a typical additive in metallic glass alloys to facilitate amorphisation. Moreover, since the films are ultra-thin, the number of planes contributing to the total x-ray intensity is very small compared with highly

107

crystalline bulk samples/thick films.

The film annealed at 473 K shows a broad diffraction peak. Since the film appears to be stress relaxed (as evidenced from the changes in magnetisation) the peak broadening may be attributed to the size broadening and the particle size is estimated to be 2nm. As the film is annealed at 573 and 673 K the particle size grows to 8.5 and 12.0 nm respectively.
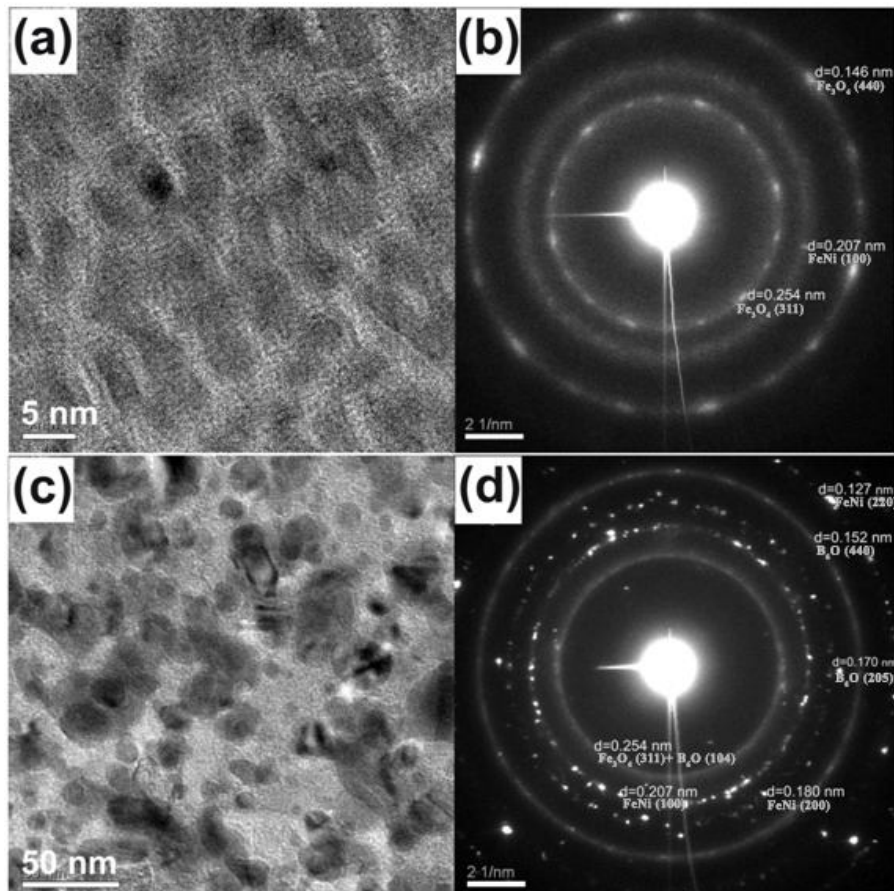
Figure.4.10: (a) HRTEM image, and (b) electron diffraction pattern of as-deposited Fe-Ni based metallic glass thin film (c) TEM bright field image and (d) electron diffraction pattern of Fe-Ni based metallic glass thin film after annealing at 673 K for 1 hr.

The TEM images of the as prepared (figure 4.10) and film annealed at 673 K is shown in figure 4.10c. The image of the as prepared film shows small contrast possibly arising from density fluctuations during vapour deposition. The SAED pattern of pristine film shows a diffused halo arising from (100) plane of

Fe-Ni at d = 0.207 nm suggesting short range ordering of Fe-Ni. The film also shows diffraction rings corresponding to planes (311) and (440) of Fe_3O_4 with d values 0.254 nm and 0.146 nm respectively, further corroborating the results of XPS analysis. As the film is annealed the Fe-Ni ring at d=0.207changes to polycrystalline structure manifested as a ring with well-defined spots. Complete rings were not observed as is the case of a perfect polycrystalline material since the film is thin; the total number of grains contributing to the overall diffraction pattern is small. The annealed sample also shows diffraction rings with d values 0.152 and 0.170 corresponding to (440) and (205) planes from B_6O. The annealed film also shows a diffraction ring from iron oxide. The film annealed at 673K shows large contrast typical of a nanocrystalline material with small grains embedded in an amorphous matrix. The particle size estimated from the size histogram (figure 4.11) turns out to be 11.1 nm close to the value of 12 nm obtained from XRD.
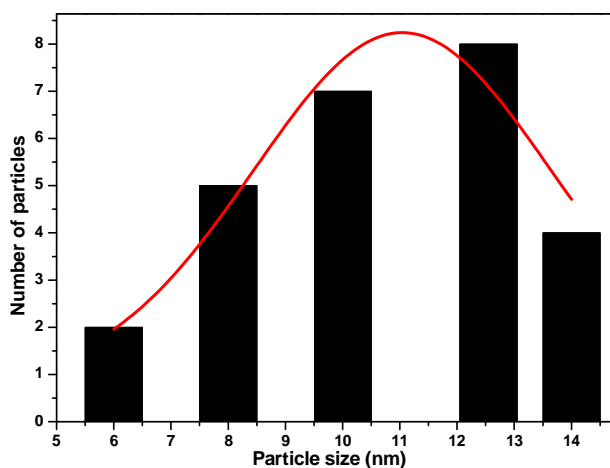
Figure 4.11: Particle size histogram from the TEM of 673K annealed sample.

4.3.3. Magnetic Studies

The   soft   magnetic   properties   are   strongly   dependent   on   the

microstructure of the thin films. The microstructure contribution to magnetism arises from morphology, properties such as magnetic anisotropy, magnetostriction, crystal size, crystal structure and the volume fraction of the precipitates.

Figure 4.12: Variation of coercivity with annealing temperature for Fe-Ni-B thin films. (The lines are guide to the eye)

Figure 4.13: Variation of retentivity with annealing temperature for Fe-Ni-B thin films. (The lines are guide to the eye)

Figure 4.12 and figure 4.13 depicts the variation of coercivity and retentivity with annealing temperature. The variation can be attributed to the structural changes occurring in the sample with heat treatments. The sharp drop

110

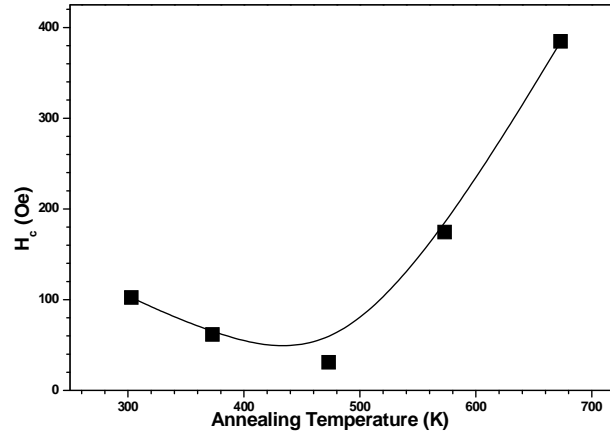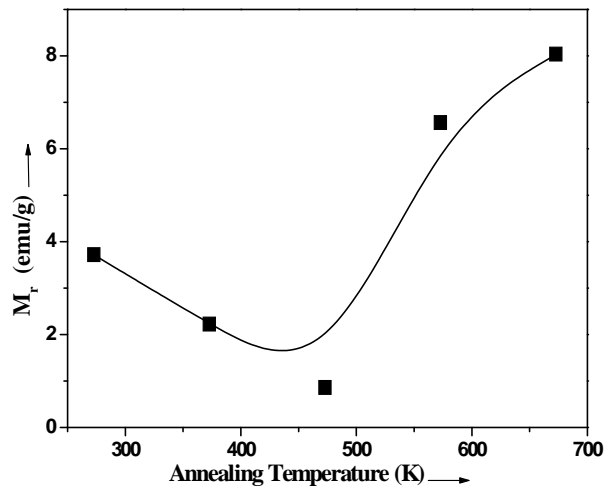of coercivity at 473 K represents the stress relaxation, onset of crystallization and exchange coupling between several grains. The grain sizes of the dispersed crystallites are rather small resulting in the averaging of magneto-crystalline anisotropies over several domains.

Typical hysteresis loops for Fe-Ni-B thin films in parallel field (applied external magnetic field parallel to the film plane) are shown in figure 4.14. The bulk material has a characteristic saturation magnetization of 90.5emu/g. But the prepared films have lower M_s values suggesting that the homogeneous precipitation of α-Fe-Ni-Mo cannot be realized by vapour deposition. Evidently vapour deposition has altered the stoichiometry and resulted in phase segregation.
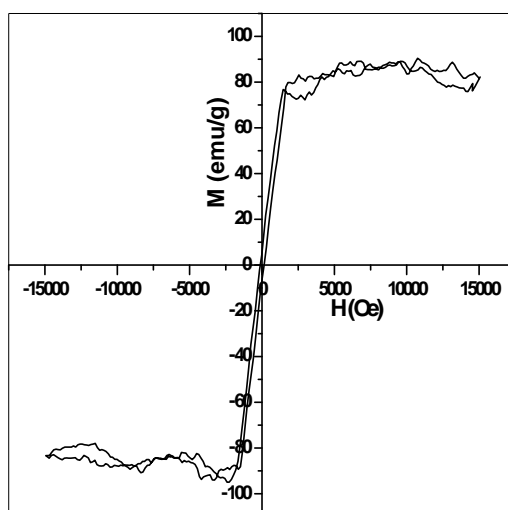
Figure 4.14: Typical hysteresis loop for Fe-Ni-B thin film in parallel field.

Based on the lowering of nano-crystallization temperature in the deposited thin films and considering the vapour pressures of the alloying elements and from the XPS analysis one can infer that the deposited film is devoid of molybdenum[14]. This can well account for the observed decrease in the crystallization temperatures since molybdenum is added to Fe-Ni-B to increase its crystallization temperature. However, at higher annealing temperatures small crystallite particles are precipitated increasing the number of

domain walls. The inclination of magnetization curve suggests that the major contribution of magnetization reversal is due to domain rotation. The relatively large coercivity of the thin films compared to bulk ribbons are due to the presence of localized stresses and roughness in the films which acts as pinning centers for domains. Annealing ribbons at 373 K results in the nucleation of Fe-Ni which is evident from the decrease of H_c after annealing at 373 K. The coercivity reaches a minimum at 473 K suggesting the onset of nano-crystallization and there after increases monotonically by orders of magnitude and reaches a maximum at around 673 K indicating grain growth with temperature. The coercivity minimum at 473 K suggests that the films undergo substantial stress relief and occurrence of nano-crystallization at that temperature. The slope of H_c after 473 K ensures that the size and volume fraction of the precipitates increase at a proportional rate. At 473 K Fe-Ni nano-grains become exchange coupled and magneto-crystalline anisotropies are averaged out resulting in very low coercivity. The increase in grain size and subsequent modification in the local stress accounts for the increase in coercivity at higher annealing temperatures. The second crystallization stage increases the volume fraction of boride phases whose presence is deleterious to the soft magnetic properties. This accounts for the increase in H_c values at higher annealing temperatures.

These variations can be explained by invoking the random anisotropy model originally suggested by Alben *et. al.* and modified by Herzer [3,15]. According to this model

$$H_c = \frac{p_c \langle K \rangle}{M_s} = p_c \frac{K_1^4 D^6}{M_s A^3}$$

4.1

In case of systems with thickness in the range of exchange correlation length,

$$H_c = \frac{p_c \langle K \rangle}{M_s} = p_c \frac{K_1^2 D^2}{M_s A}$$

4.2

This equation suggests that for ultra-thin films the Herzer's D^6 law has to

112

be replaced with a D^2 law [16,17]. The coercivity H_c is directly proportional to (D^2/M_s). The linear plot of D^2/M_s versus H_c is shown in figure 4.15 and confirms that the coercivity indeed obeys a D^2 behavior rather than a D^6 behavior.
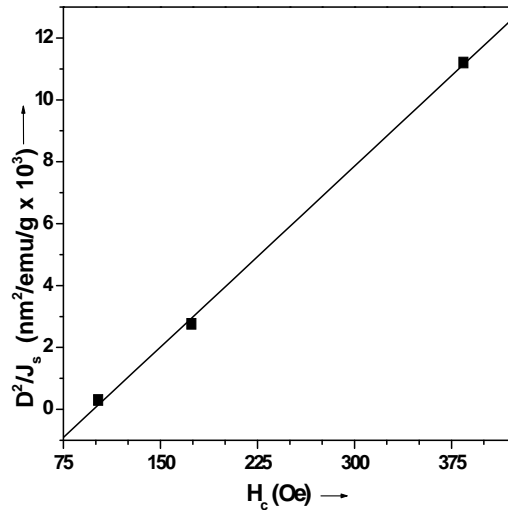
Figure 4.15: Verification of modified Herzer Law. Plot depicting variation of D^2/M_s Versus H_c.

4.3.4. Surface studies

The micro structural analysis carried on pristine and annealed samples is in good conformity with the results obtained from VSM studies. From XRD and TEM images it is clear that the as deposited films are amorphous. Clusters are found in the AFM image of pristine & annealed samples (figure 4.16). Obviously these are Fe-Ni clusters as evidenced from the XPS studies.

This clustering arises due to the variation in vapour pressures of the alloying components. Fe and Ni having low vapour pressures, compared to B and Mo, evaporate slowly in the beginning and later on when the melt is deficient in boron, the rate increases. This accounts for the clustering of Fe-Ni on the film surface. The 473 K annealed samples show crystallites-which show good magnetic response with well-defined grains arranged uniformly over the film. Hence it is evident that the vapour deposition of METGLAS has resulted in the decrease of the crystallization temperatures of Fe-Ni-B. The crystallization of first

phase occurs at 473 K and second crystallization occurs at 673 K.
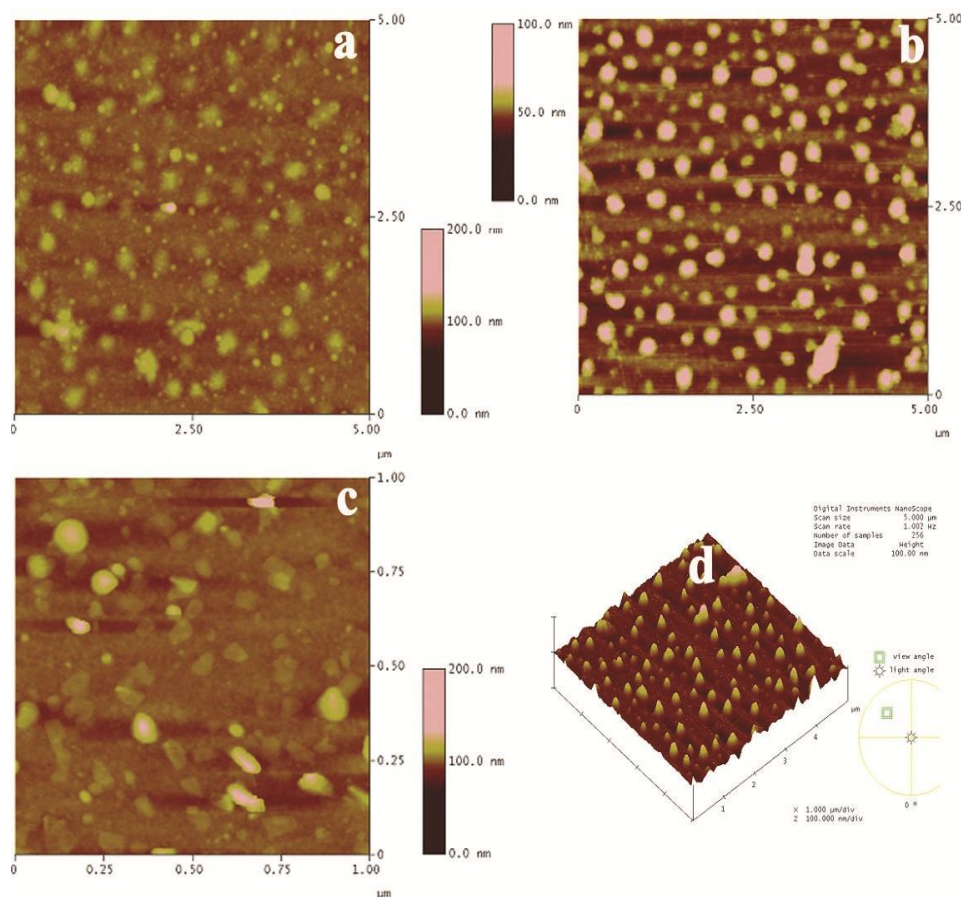
Figure 4.16 a)AFM image of pristine thin film. b) AFM Image of thin film annealed at 573 K c) AFM image of thin film annealed 673 K d) three dimensional MFM image of the thin film annealed at 573 K

4.3.5. MOKE Studies

The MOKE images of the pristine as well as annealed film are shown in figure 4.17. The pristine film has a coercivity of 72.5 Oe which is greater than the bulk coercivity of 10.2 Oe. This is understandable since bulk coercivity measures the coercivity of the whole material while the MOKE measures coercivity on a small area on top of the surface layer. Typically lasers used in MOKE measurements have a penetration depth < 10 nm. The coercivity measured by MOKE is a convolution of the surface and under layer. As revealed from XPS

114

the film surface has a native oxide layer of iron and this can contribute to the MOKE coercivity. As the film is further annealed VSM and MOKE measurement results generally follows similar trend
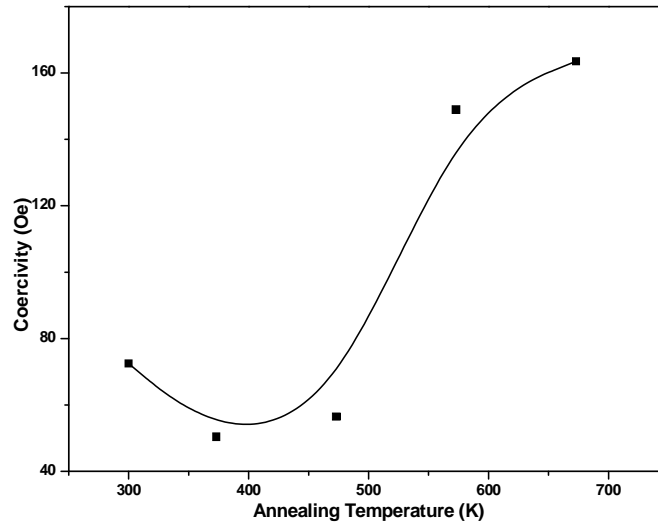
Figure 4.17: Variation of coercivity with annealing temperature from MOKE measurements.

Conclusions

It has been found that the temperature of annealing can modulate the magnetic properties of Fe-Ni-B thin films. Thin film samples annealed at 473 K show very low coercivity and large saturation magnetization suggesting that the critical condition predicted by Herzer model is attained at this temperature. The XRD spectrum of thin films annealed at 473 K shows that Fe-Ni nanostructures are embedded in the residual boron containing amorphous phase. Annealing films at higher temperatures resulted in monotonic increase of coercivity because of micro-structural changes. Finally an explanation is provided for the coercivity variation with annealing based on the modified Herzer model. There exists ample scope for modelling and simulation of the magnetic evolution of ultra-thin films using this new model. Thin films of these METGLAS ribbons can find many applications involving soft magnetic properties.

References

[1]   M.E. Mchenry, M.A. Willard, H. Iwanabe, R.A. Sutton, Z. Turgut, A. Hsiao, Bulletin of Material Science 22 (1999) 495.

[2]   R. Alben, J.J. Becker, M.C. Chi, Journal of Applied Physics 49 (1978) 1653.

[3]   G. Herzer, IEEE Transactions on Magnetics 26 (1990) 1397.

[4]   K.G. Ong, M. Paulose, C.A. Grimes, Sensors 3 (2003) 11.

[5]   M. Jyothi, C. Suryanarayana, Zeitschrift Für Metallkunde 76 (1985) 801.

[6]   C. Liang, C. Gooneratne, D. Cha, L. Chen, Y. Gianchandani, J. Kosel, Journal of Applied Physics 112 (2012) 113912.

[7]   E. Hristoforou, Journal of Optoelectronics and Advanced Materials 4 (2002) 245.

[8]   C.J.G. Peter, A.J.S. Marcel, Applied Surface Science 101 (1996) 36.

[9]   B. David, M.P. Seah, Practical Surface Analysis by Auger and X-Ray Photoelectron Spectroscopy, John Wiley and Sons Ltd, Chichester, 1990.

[10]   T. Yamashita, P. Hayes, Applied Surface Science 254 (2008) 2441.

[11]   B. Kolbeson, Symposium on Analytical Techniques for Semiconductor Materials and Process Characterization (Altech-2003), Electrochemical Society, Incorporated, France, 2003.

[12]   B.D. Cullity, C.D. Graham, Introduction to Magnetic Materials, 2nd ed., John Wiley and Sons Inc., 2008.

[13]   P. Babelon, A. Dequiedt, H. Mostéfa-Sba, S. Bourgeois, P. Sibillot, M. Sacilotti, Thin Solid Films 322 (1998) 63.

[14]   B. Seshu, A.K. Bhatnagar, D.G. Naugle, Journal of Materials Science Letters 16 (1996) 165.

[15]   G. Herzer, Journal of Magnetism and Magnetic Materials 294 (2005) 99.

[16]   T. Hysen, S. Deepa, S. Saravanan, R. V Ramanujan, D.K. Avasthi, P. A. Joy, S.D. Kulkarni, M.R. Anantharaman, Journal of Physics D: Applied Physics 39 (2006) 1993.

[17]   S. Thomas, S.H. Al-Harthi, D. Sakthikumar, I. Al-Omari, R. V Ramanujan, Y. Yoshida, M.R. Anantharaman, Journal of Physics D: Applied Physics 41 (2008) 155009.

Chapter 5

Annealing Induced Low Coercivity, Nanocrystalline Co-Fe-Si Thin Films Exhibiting Inverse Cosine Angular Variation

5.1 Introduction

Soft magnetic thin films are a hot topic of research due to their wide ranging applications in various fields such as magnetic recording, MEMS, sensors etc. [1–3]. Soft magnetic properties are related to various factors such as alloy composition, nature of magnetic phase, crystal structure, crystal size and annealing conditions. In this context, Co-Fe based materials assume importance, owing to their high saturation magnetisation and promising high frequency characteristics. The $Co_{70}Fe_{30}$ composition is thermodynamically stable in the bcc crystal structure [4]. This composition [4] is close to the maximum of spin polarization and possesses the maximum magnetic moment, as shown by the Slater Pauling curve [5]. Combination of these properties makes compositions near to $Co_{70}Fe_{30}$ suitable for various applications such as spin injection systems in spintronic devices [6].

Si can be added to Co-Fe alloys to facilitate amorphisation as well as to tune the magnetic properties. If the material can be tailored in to nanocrystalline thin films then they can be integrated in microelectronic devices. Co-Fe/Co-Fe-Si based metallic glasses are available commercially and these materials can be processed into nanocrystalline form by thermal annealing and they possess excellent soft magnetic properties, suitable for applications in transformer cores and magnetic shielding. Amorphous thin films of Fe-Ni/Fe-Ni-B which were subsequently processed into nanocrystalline form by annealing were recently reported [7–12]. However amorphous/nanocrystalline thin films of Co-Fe-Si have not been studied in detail or seldom reported. Hence a detailed investigation of the nanocrystallization and change of magnetic properties of Co-Fe-Si thin films with thermal annealing was conducted.

In the past, several researchers have reported soft magnetic Co/Co-Fe thin films by depositing them on an under layer or an over layer of CoO [13–16]. In the above mentioned investigations, the magnetic properties were explained

using the random anisotropy model (RAM) initially proposed by Alben *et. al.* and modified by Herzer [17–19]. According to Herzer, excellent soft magnetic properties can be realized, if the size of the individual magnetic domain is reduced to the exchange coupling length (L_{ex}). The subsequent exchange coupling results in very low local anisotropies and demagnetization effect. Hence for a large number of exchange coupled nanocrystalline grains, the local anisotropy K_1 is small, resulting in low coercivity. Thus, Co-Fe films can be prepared with very low coercivity by the deposition of an under layer or upper layer of an ultrathin oxide layer. Most of the earlier reports focus on the bulk magnetic property of films, probed using VSM. Hence, detailed investigations, comparing, the surface and bulk magnetic properties of Co-Fe-Si thin films is yet another motivation for this work.

There are several reports on the magnetisation reversal mechanism in Co-Fe thin films [6,16]. Stoner-Wolfarth model based on coherent rotation [20] and Kondorsky model based on domain wall motion/unpinning [21] are the two important models used for explaining the angular variation of coercivity. Even though one expects structures with sizes below the single domain size to obey the coherent rotation model, size dependent behaviour was also observed [22]. In most ferromagnetic materials magnetisation reversal is effected by domain nucleation and growth. In the coherent rotation model one assumes the magnetic vectors rotate collectively with the applied field before reaching saturation. In contrast, the Kondorsky model assumes that magnetisation reversal is primarily effected by nucleation and growth of reverse domains or the strong pinning of domains at local defects and in homogeneities and predicts a $1/\cos\theta$ dependence of coercivity, where θ is the angle between the easy axis direction and the applied magnetic field. The Herzer model predicts similar coercivity variations for magnetisation reversal by coherent rotation and domain wall pinning/motion models [19].

Even though the Kondorsky model was originally derived for explaining the angular variation of coercivity in hard magnetic materials [21], similar behaviour has been observed in many soft magnetic systems [23,24]. Thomson *et. al.* [25], reported that the magnetisation reversal of large soft magnetic islands of Co-Pt takes place by nucleation of a 180^0 reverse domain, followed by the spread of a domain wall throughout the islands. Delalande *et. al.* observed Kondorsky type angular variation of reduced coercivity in soft magnetic Co-Pt systems with perpendicular anisotropy [26]. Streubel *et. al.* modelled the angular variation of magnetisation reversal in Fe-Ni caps by the modified Kondorsky relation [27]. Spiridis *et. al.*, based on magnetic studies conducted on Co thin films of various thicknesses, reported that as film thickness decreases, the magnetisation reversal mechanism can change from coherent rotation to domain wall movement [28]. Liu *et. al.* reported Kondorsky type dependence in cobalt thin films [29]. The in plane easy axis coercivity of nanocrystalline[14–16] Co-Fe thin films was explained using the Herzer model. However no systematic investigation regarding the easy to hard axis magnetization reversal of Co-Fe-Si thin films has been reported in the literature. Hence investigations on the angular variation of magnetization reversal in Co-Fe-Si thin films assume significance.

We report the deposition of magnetic thin films of Co-Fe-Si on glass and NaCl substrates and the evolution of their magnetic properties with thermal annealing. The films exhibit onset of nanocrystallisation with annealing. Further the morphology shows a profound change with annealing which is reflected in the change in surface magnetic properties investigated using MOKE. The Herzer model is invoked to explain the observed soft magnetic properties of ultra-thin magnetic films. The angular variation of coercivity from in plane to out of plane shows an inverse cosine relationship exhibiting a Kondorsky type variation. The magnetization reversal is primarily governed by the pinning of domains at local defects.

5.2 Experimental Methods

Thin films were vacuum evaporated using tungsten filaments at a vacuum of 10^{-6}Torr on NaCl and chemically and ultrasonically cleaned glass substrates. A composite target with a composition corresponding to $Co_{69}Fe_4Ni_1Mo_2B_{12}Si_{12}$ was used for evaporation. Samples deposited on NaCl were used for TEM analysis. The thicknesses of the deposited films were determined using Dektac 6M Stylus Profiler. The thin film samples were annealed at 100, 300 and 400°C for one hour under a high vacuum of 10^{-6} Torr. GXRD measurements were carried out on the annealed and pristine samples using Bruker D8 Discover diffractometer with monochromatic Cu Kα X-rays at grazing incidence angle of 0.5^0 and wavelength 1.5414 Å. XPS study of the films deposited on float glass substrates were performed with an Omicron Nanotechnology XPS system with a monochromatic Al Kα radiation (hν= 1486.6 eV) of source voltage 15 kV and emission current of 20 mA. All scans were carried out at an ultrahigh vacuum of 1.5×10^{-10}Torr. The obtained XPS spectra were de-convoluted and quantified using Casa XPS program (Casa Software Ltd, UK), in which the background was simulated using the Shirley function and the peaks were fitted using a Gaussian Lorentzian function. The spectrum recorded was corrected using the binding energy of adventitious carbon at 284.6 eV and the accuracy of the measured binding energy values is estimated to be $\pm$ 0.2 eV. The elemental composition of the sample is extracted from the wide scan, while the individual element peaks were analyzed to obtain the chemical composition. As charging effects are unavoidable in the XPS study of thin films deposited on non conducting samples, charge compensation was performed by electron gun flooding. The nanoscale imaging was performed using atomic force microscopy (AFM) in tapping mode, using ultra high resolution cantilevers made of tungsten having radius of less than 1 nm and force

constant of 46 N/m. Room temperature magnetization measurements were carried out using VSM (DMS 1660 VSM) with field varying from -1 to $+1$ kOe. The angular variation of magnetization is recorded by measuring the magnetization with the sample positioned at different angles with respect to the applied field. When the field is along the plane of film the angle is 0° and out of plane, the angle is 90°. The surface magnetic properties were probed using a MOKE setup, operated using a red laser with 6328 Å wavelength from a He–Ne laser source. The loops were recorded with magnetic field applied along the in plane direction.

5.3 Results

5.3.1. Composition Analysis

The thickness of the films was measured to be 54 nm using stylus profilometer.
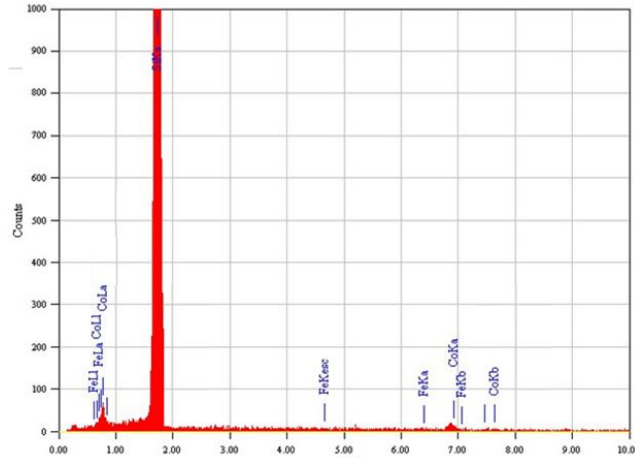

Figure 5.1: EDS spectra of Co-Fe-Si thin films.

The EDS spectra of the thin films showed that the sample consist of silicon, cobalt and iron. The peaks emanating from elements Co and Fe are masked by the huge peak from Si. This might be due to the reason that, since the sampling depth in EDS>500nm the major contribution to the signal is from the

122

Si substrate. To overcome this drawback XPS study was conducted on the samples with and without sputtering the sample surface with Ar ions.

The XPS wide scan of the as prepared thin films, as shown in figure 5.2a, clearly shows the presence of cobalt, iron, a small percentage of silicon and boron. The unavoidable adventitious carbon is also detected which is utilized to calibrate the XPS scan by assuming the aliphatic carbon peak position at 284.6eV. The wide scan also shows the presence of oxygen suggesting possible native oxide formation on film surface.
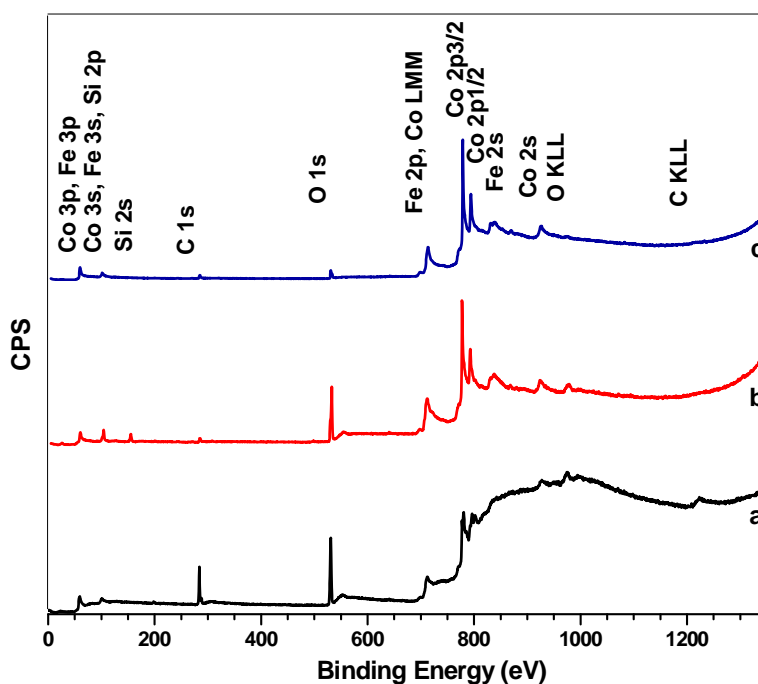
Figure 5.2: XPS wide scan of thin films: a) XPS spectra of as prepared Co-Fe-Si film b) XPS spectra of Co-Fe-Si film after sputtering with Ar⁺ ions for 15 minutes c) XPS spectra of Co-Fe-Si film after sputtering with Ar⁺ ions for 30 minutes

Quantification of spectra in figure 5.2a suggests that the surface is mostly covered with native oxide with a 43.84 wt. % Co, 24.50 wt. % Fe, 1.36 wt. % Si, 3.6 wt. % B and 26.70 wt. % O. However XPS spectra shown in figure 5.2b

123

which is recorded after the films were sputtered by Argon ions with energy 3keV for 15 minutes to obtain compositional information just beneath the surface shows 45.69 wt. % Co, 27.65 wt. % Fe, 10.45 wt. % Si, 0.20 wt. % B and16.27 wt. % O. The spectra shows reduction in oxygen content from 26.70 wt. % to 16.27 wt. % while the percentage of silicon is increased from 1.36 wt. % to 10.45 wt. % whereas significant reduction in boron content from 3.6 wt. % to 0.20 wt. % is also observed. XPS spectra shown in figure 5.2c, recorded after further sputtering by Argon ions with energy 3keV for 15 minutes shows 64.64 wt. % Co, 30.60 wt. % Fe, 0.34 wt. % Si, 0.02 wt. % B and 4.40 wt. % O and these values can be estimated as an estimate of the profile values for the entire thickness of thin films which is corroborated by the SIMS analysis shown in figure 5.3.

From the SIMS profile shown in figure 5.3, it is evident that upto 6 nm depth the concentration of silicon monotonically decreases and thereafter stabilizes. The profile of Co and Fe also show similar trends and the concentration of individual elements stabilize at around 6 nm. Thus it can be argued that sputtering the film surface with Ar ions at 3 keV for 30 minutes just resulted in the erosion of less than ~6 nm of the film. This is consistent with the well established existence of a 30 Å oxide film on iron surfaces cleaned in air [30]. The formation of native oxide layer in thin films of Co-Fe-Si is unavoidable and often demands the deposition of a protective ultra thin layer of Au or Ag on the as prepared surface. But the formation of an ultrathin oxide layer of Co/Fe and Si may act as a protective barrier against further oxidation and can reduce the coercivity in Co-Fe-Si thin films.
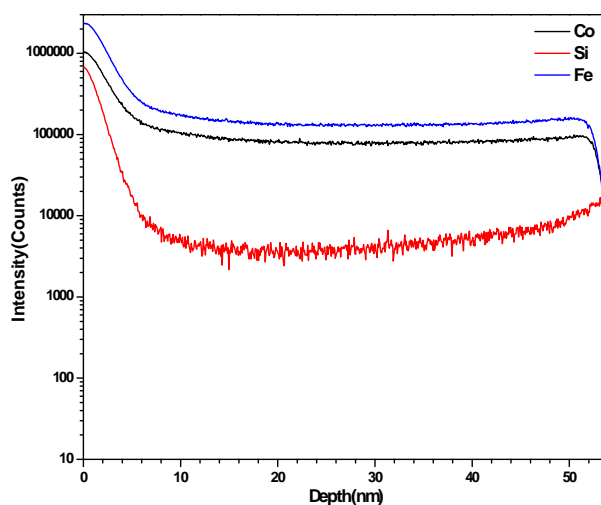
Figure 5.3: SIMS composition profile of Co-Fe-Si thin film. The x axis is transformed to depth scale by linear scaling of depth with sputtering time in order to qualitatively illustrate the composition profile along the entire thickness of the film.

The XPS slow scan spectra of the as prepared and sputtered samples for Co is shown in figure 5.4. The peak at 778.2 eV corresponds to metallic cobalt $2p_{3/2}$ [31]. However the prominent peak at 781.1eV can be assigned to Co^{2+} from CoO. This is further evidenced from the presence of shake up satellite present at 786.5 eV which is the characteristic signature of paramagnetic Co^{2+} present in octahedral sites of CoO [32]. Peak analysis has shown that 88% of Co is in oxide form and 12 percent is in elemental form. This is interesting since the penetration depth of XPS is ~3nm. This suggests that cobalt exists in elemental form within 3 nm from the film surface. Since cobalt cannot exist in elemental form on the film surface this observation suggests that the oxide layer might be even less than 6 nm. As the film is sputtered by 3keV Ar ions for 15 minutes (figure 5.4b) the contributions from CoO completely vanishes, since the satellite structure vanishes. The peak shape of Co $2p_{3/2}$ shows a sharp peak of metallic cobalt with an asymmetric tail extended on to the high binding energy side. Hence it can be

concluded safely that the surface native oxide layer have a thickness of <6 nm as evidenced from SIMS.

Figure 5.4: XPS slow scan spectrum of Cobalt from a) as prepared Co-Fe-Si film b) Co-Fe-Si film after sputtering with Ar⁺ ions for 15 minutes c) Co-Fe-Si film after sputtering with Ar⁺ ions for 30 minutes
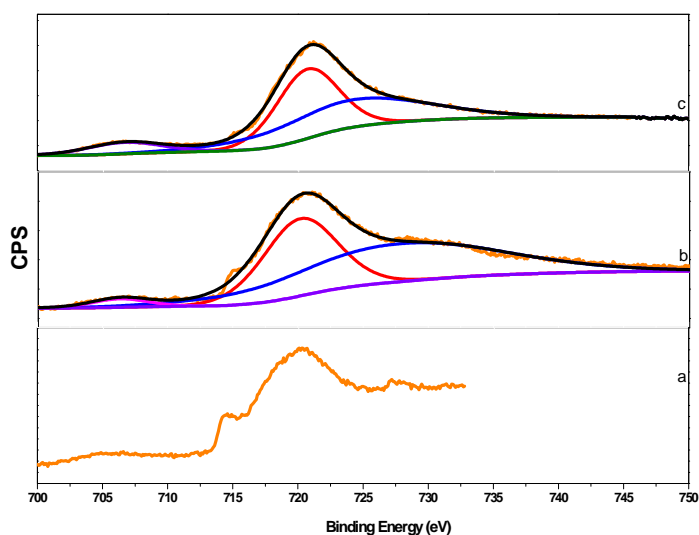
Figure 5.5: XPS slow scan spectra of Iron from a) as prepared Co-Fe-Si film b) Co-Fe-Si film after sputtering with Ar⁺ ions for 15 minutes c) Co-Fe-Si film after sputtering with Ar⁺ ions for 30 minutes

The slow scan iron 2p spectrum of the pristine film is shown in figure 5.5a. The spectrum being convolution of Fe 2p and Co LMM presents difficulty in de-convoluting the peaks exactly. However the peak at 707.2eV indicates the presence of metallic iron. On further sputtering the sample the pure iron content increases and reaches a maximum for sample sputtered for 30 minutes with 3keV Ar ions.

The XPS slow scan spectrum of silicon 2p is a convolution of Si 2p and Co 3s. The peak at 98.8eV corresponds to Si from Si-Si bond. The peak at 100.4eV arises from Si2p from Si-O bond indicating the presence of silicon oxide on the native surface of the film. This is rather beneficial since this oxide layer will also serves as a protective barrier against further oxidation of the film and prevents oxygen greedy iron and cobalt from being further oxidized. The peak at 101.4eV arises from Co 3s [33]. The unsputtered sample surface contains elemental Si and SiO_2 in wt % 30 and 70 respectively. However after sputtering for 30 minutes the oxide contribution almost vanishes. In the slow scan of oxygen from unsputtered sample only two components are present.
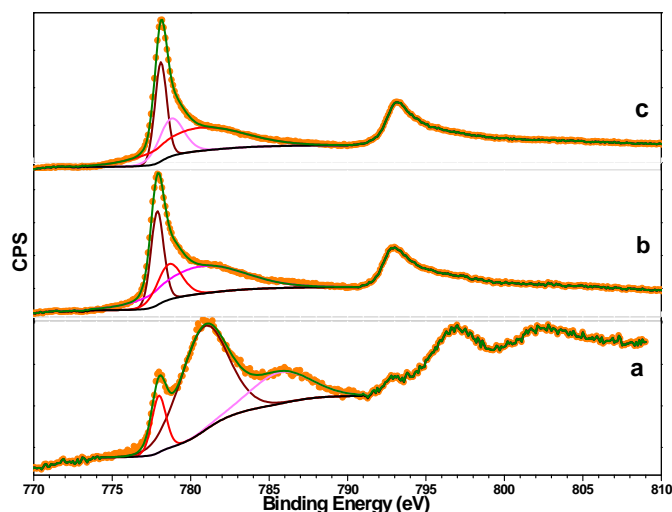

Figure 5.6: XPS slow scan spectra of Si from a) as prepared Co-Fe-Si film b) Co-Fe-Si film after sputtering with Ar⁺ ions for 15 minutes c) Co-Fe-Si film after sputtering with Ar⁺ ions for 30 minutes

The component peak at 529.8 eV can be ascribed to oxygen from metal oxide bond coming from native oxides of Co and Fe. The peak at 532.7 eV corresponds to oxygen from Si-O bond and B-O bond. This peak is a convolution of both peaks since both occur at an energy separation of just 0.4 eV. During the first erosion another peak appears which might be the oxygen from C-O bond. Even though the evaporation is done at high vacuum, contamination from the silicone based oils used in the diffusion pump may also be the source of Si and C. On second erosion the oxygen and carbon contents are negligible, which is evident from wide scan shown in figure 5.1c.
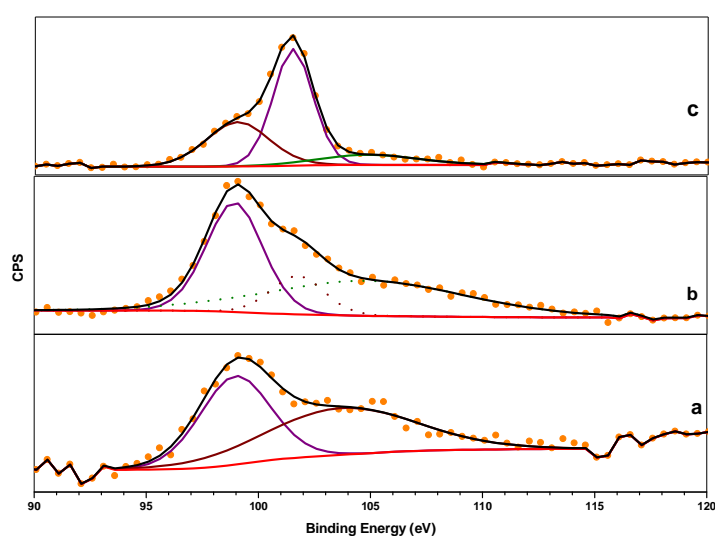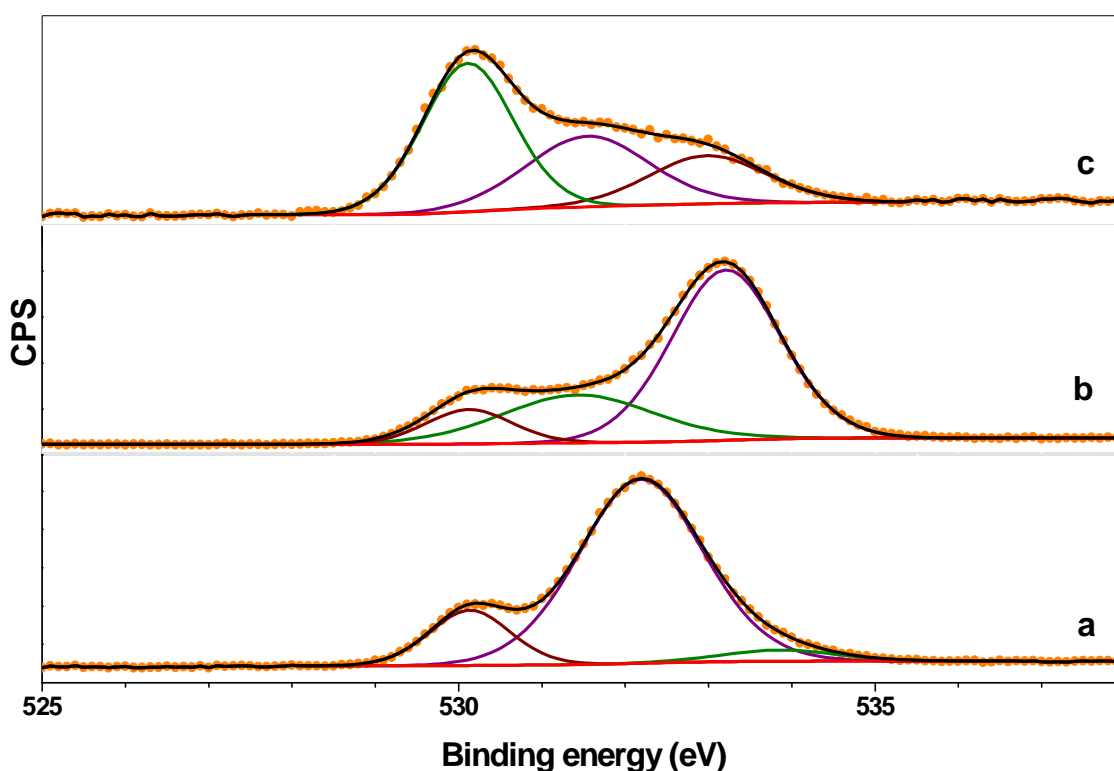

Figure 5.7: XPS slow scan spectra of Oxygen from a) as prepared Co-Fe-Si film b) Co-Fe-Si film after sputtering with Ar$^+$ ions for 15 minutes c) Co-Fe-Si film after sputtering with Ar$^+$ ions for 30 minutes

5.3.2. Structural Analysis

The GXRD pattern of the unannealed sample shows a broad peak at $44.32°$ indicating the amorphous nature of the film. This is unexpected since $Co_{100-x}Fe_x$ alloy is thoroughly researched and was reported to have good crystalline nature during the entire composition range. Our result can be explained by assuming that the films is composed of small nanocrystalline grains dispersed in an amorphous matrix [34].

However the samples show crystallinity with annealing which is evident from the figure 5.8b-d which corresponds to annealing at 100 $°C$, 300 $°C$ and 400 $°C$. The peak at $44.4°$ has a d spacing of 2.04 Å. The film annealed at 100 $°C$, 300 $°C$ and 400 $°C$ show crystallites with size 5.3 nm, 11 nm and 19.1 nm respectively. It is evident that there is progressive grain growth with annealing.
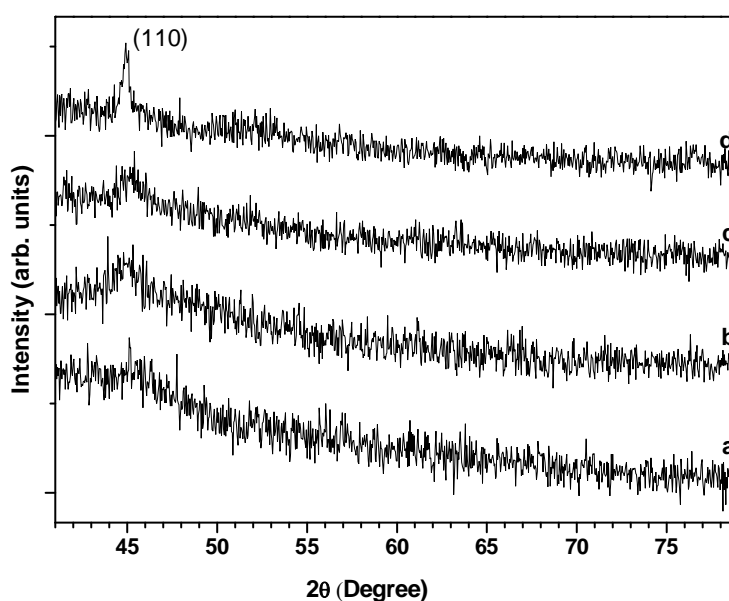
Figure 5.8: GXRD pattern of thin film a) as prepared and annealed at b) 100$°C$ c) 300$°C$ d) 400$°C$

The maximum intensity peak for fcc Co (PDF 150806) should occur at $44.26°$, bcc Fe (PDF 851410) at $44.39°$ and Cubic CoFe (PDF 491568) at $44.91°$. Further if the crystallites are that of Co there should have a peak with half intensity at $51.57°$. The HRTEM image shown in figure 5.9d reveals lattice fringes with

129

spacing 2.1 Å corresponding to Co-Fe phase. Hence it can be concluded that the crystallites are of Co-Fe.

The TEM of pristine sample shows more or less uniform contrast with few dark regions on the surface, which can be attributed to thickness variations resulting from vapour deposition. This type of structure is typical for metallic glasses which further validates the amorphous nature shown by the pristine sample in GXRD.
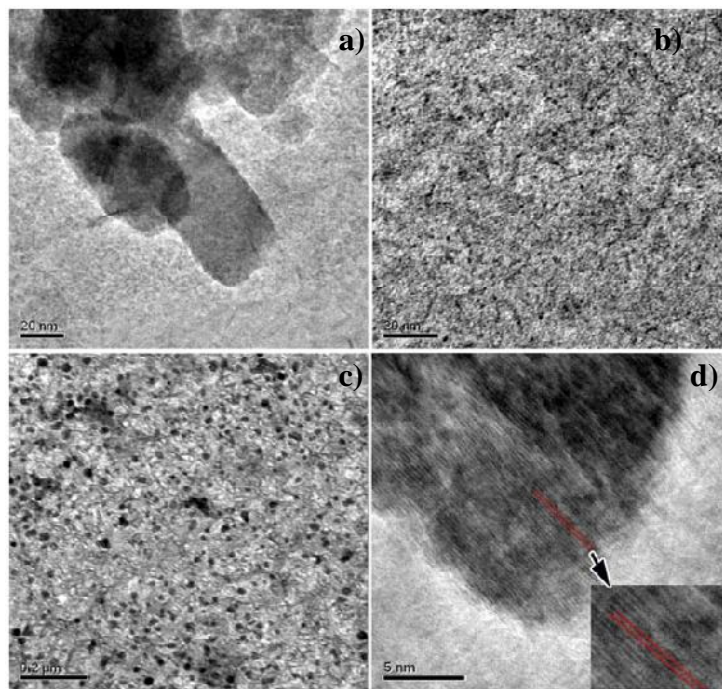
Figure 5.9: TEM Images of Co-Fe-Si Thin films a) Pristine b) annealed at 100ºC c) annealed at 400ºC d) HRTEM of film annealed at 400⁰C

However, on annealing the samples at 100 ºC the microstructure changes to a composite with nanocrystalline grains dispersed in an amorphous matrix. Fit of the size histogram yields an average grain size of 1.5 nm. The crystallite size extracted from TEM and GXRD does not match which is evident as GXRD probes the surface microstructure at a small grazing angle of less than 1º while TEM explores the 3 dimensional crystallite. The grains are visible as dark regions in an amorphous matrix appearing as gray regions. On further annealing at 400ºC

130

large crystallites gets precipitated which might have resulted from grain growth and Ostwald ripening process. The 400°C annealed sample shows crystallites with size ~22.14 nm.
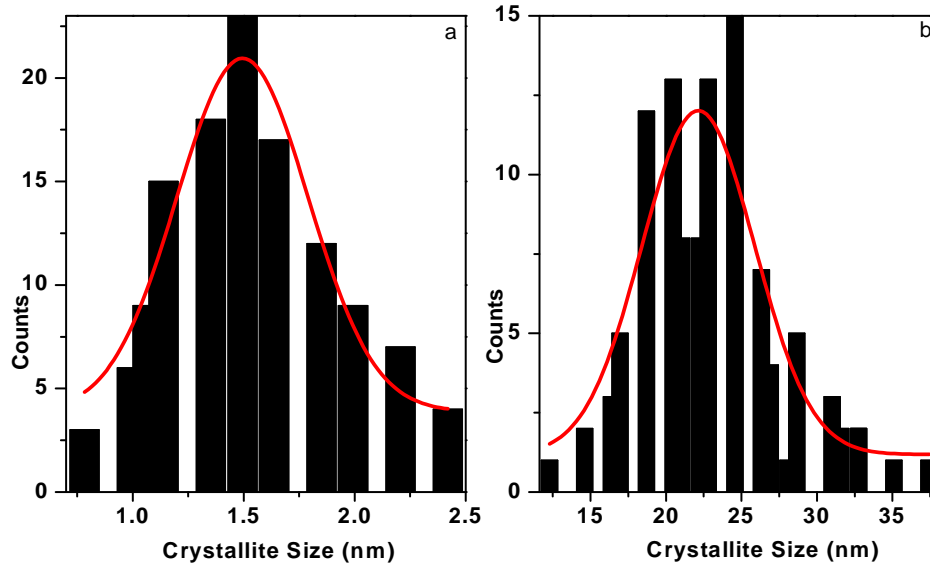
Figure 5.10: Crystallite size histogram of sample annealed at a)100°C and b) 400°C

5.3.3. Morphology Analysis

The magnetic properties of thin films are dependent on the morphology and AFM is a powerful tool for investigating this aspect. The recorded image was subjected to various analyses to obtain information regarding average roughness (R_a), root mean square roughness (R_q), skewness, and power spectral density (PSD). R_a represents the mean value of the surface height with respect to a centre plane whereas R_q is the standard deviation of the surface height within the given area. [35]. PSD can provide information regarding short and long wavelength ordering in the sample.

Table I: Roughness (R_a, R_q and S_{ku}) values derived from the AFM for the substrates and the pristine as well as annealed films.

Sample	R_q (nm)	R_a (nm)	Skewness(nm)
Glass Substrate	1.19	0.94	0.16
Pristine	3.46	2.76	0.56
Annealed at 100°C	2.68	1.95	1.29
Annealed at 300°C	2.21	1.59	1.72
Annealed at 400°C	1.11	0.748	2.39

The R_a, R_q and S_{ku} value derived from the AFM (figure 5.11&5.12) for the substrates and the pristine as well as annealed films are tabulated in Table 1. The substrate has some uneven surface features with an average roughness of 0.94 nm and root mean square roughness of 1.19 nm typical for float glass substrates. The as deposited films have R_a, R_q values of 2.76 and 3.46 nm respectively. This is possible since vapour deposition is known to produce thin films with relatively large roughness compared to films prepared by techniques like sputtering etc. The R_a and R_q values gradually reduce upon annealing. This is possible since the films are annealed in high vacuum, the native oxide layer may have smoothened out by diffusion and possibly reduced in thickness due to oxygen depletion. The S_{ku} value of glass substrate is nearly zero implying uniform distribution of surface features. As deposited film show S_{ku} value of 0.56 nm suggesting the presence of a wide distribution of small mounds/peaks on the surface. Annealed samples exhibited increase in S_{ku} value whereas the roughness decreases. This suggests the formation of larger flat structures on the film surface which can simultaneously reduce roughness and increase S_{ku}. The increase in the S_{ku} value with annealing indicates the presence of surface structures, perhaps due to grain coarsening and

surface diffusion resulting from annealing. Analysis of XPS spectra of the sample annealed at 300 $^{\circ}$C also showed that the wt. % of Co is 40.67, Fe is 39.9, O is 16.91, Si is 2.9 and B is 0.25 respectively. Compared to the unsputtered sample the annealed sample has 37% less oxygen and 60 % more iron on the surface. The surface also shows more silicon and less boron content. Thus it can be assumed that surface smoothening is driven by the increased presence of silicon and iron on the surface and oxygen depletion resulting from vacuum annealing.
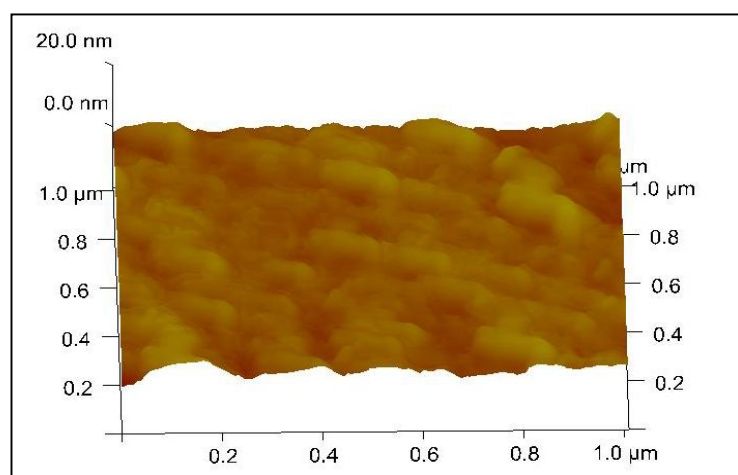
Figure 5.11: AFM Image of glass substrate

133
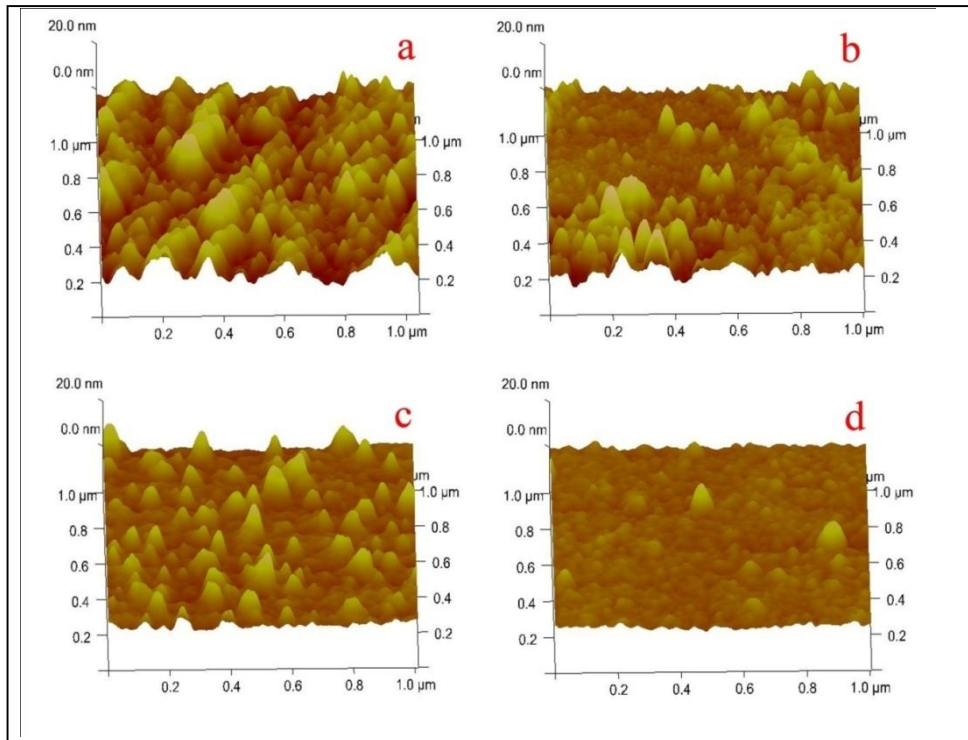
**Figure 5.12: 2D AFM Image Co-Fe-Si films a) Pristine b) annealed at 100°C
c) annealed at 300°C d) annealed at 400°C**

5.3.4. Bulk Magnetic Studies Using VSM

The magnetic properties of soft magnetic thin films depend on various properties such as morphology, magnetostriction, magnetic anisotropy, stress, volume fraction of the precipitates and composition. Figure 5.13 shows the variation of coercivity with annealing temperature, measured along the in plane direction. The variation in coercivity can be attributed to structural as well as morphological changes taking place in the sample with annealing. The coercivity of the pristine film is only 23 Oe. The coercivity shows an initial decrease to 20 Oe at 100°C annealing due to stress relaxation. As the film is annealed at 300°C and 400°C the coercivity shows a gradual increase from 40 to 69Oe. This can be explained in light of the crystal size increase observed from GXRD.
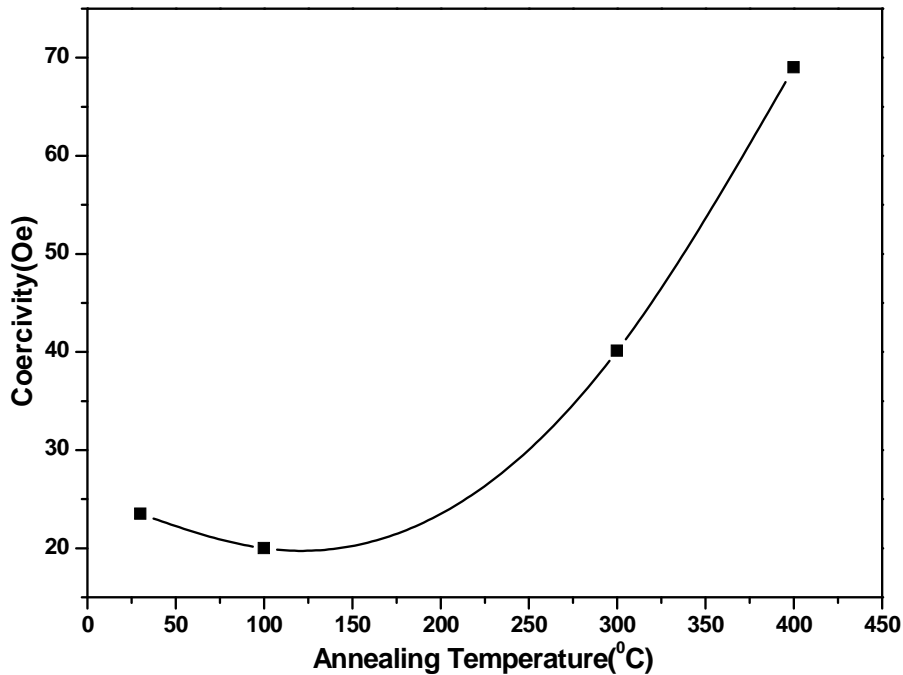
Figure 5.13: Variation of coercivity with annealing temperature for Co-Fe-Si films from VSM measurements

5.4 Discussion

5.4.1. Surface Evolution during annealing

The morphology of the as deposited films shows mound like structures which suggests the growth mode of films is Volmer Weber or island like. It is clear from the 2D AFM that, as the films are annealed from 100 °C to 400 °C the mound like structures progressively decreases, possibly due to surface smoothening resulting from surface diffusion of adatoms.

The 2D PSD of the bare glass substrates as well as pristine and annealed samples are shown in figure 5.14. The slopes of the PSD spectrum in the high frequency region obeys a power law with slopes corresponding to 4.42, 5.42, 5.38, 5.94, 6.02 for bare glass, pristine film and films annealed from 100 °C, 300 °C to 400 °C, respectively. The negative slope (δ) of the high frequency region   is

135

related to the roughness exponent α by the relation $\propto = \frac{\delta - d}{2}$, where d is the dimension from which PSD is extracted [36]. In this work d=2 which yields α values of 1.21, 1.71, 1.69, 1.97 and 2.01 for bare glass, pristine film and films annealed from 100ºC, 300ºC and 400ºC respectively. The values show a progressive increase except for the pristine film. The R_a and R_q values shows decreasing trend with annealing whereas the roughness exponents show the reverse trend.
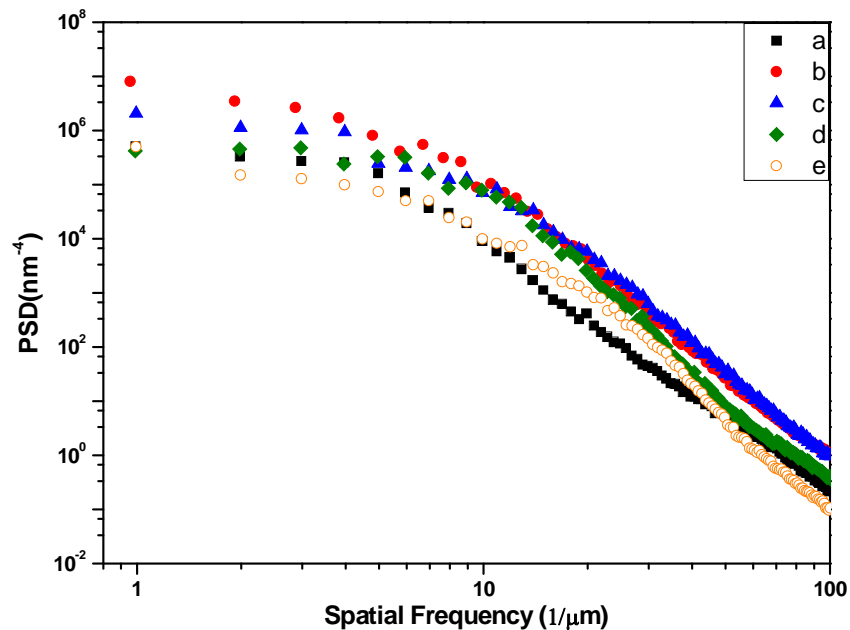
Figure 5.14: PSD spectra of a) bare glass substrate; Co-Fe-Si films b) pristine, c) annealed at 100ºC, d) annealed at 300ºC, e) annealed at 400ºC

The observed α values are quite different from the Kadar Parisi Zhang (KPZ) model which predict a value of α ~ 0.4 [37]. These exponents values can be interpreted using the Wolf-Villian linear diffusion model [38]. According to their model $\frac{\partial h}{\partial t} = R_D - \nu \nabla^4 h + \eta$ where the function $h(x,y)$ represents the surface height at point x and y. R_D is the deposition rate, representing the coalescence/diffusion rate at the surface, ν is a constant and η represents the roughening process with stochastic features. The above equation describes the

136

surface evolution as a competition between kinetic roughening, diffusion driven smoothening and grain coalescence. The term $\nu\nabla^4 h$ represents the surface smoothening by diffusion. This model gives a roughness exponent of $\alpha=1$. Values of α greater than 1 usually indicate the existence of nonlinear effects. Nonlinear diffusion effects can be incorporated into the equation by adding the nonlinear diffusion factor $\lambda\nabla^2(\nabla h^2)$, where λ is a constant related to the growth velocity [39]. This newly inserted nonlinear term takes care of particles that moved to overhangs at the sides of high steps. This new equation predicts roughness exponent values close to 1.5 which is close to the values observed by us in this study. This suggests the possible existence of nonlinear diffusion effects in the system during annealing. This also suggests that the diffusing atoms are preferentially deposited over the valleys, resulting in the film smoothening. As the films are annealed from 100 ^{0}C to 400 ^{o}C the roughness exponent increases from 1.69 to 2.71, suggesting the existence of nonlinear surface diffusion effects in the system, leading to surface smoothening. The PSD also show a small change in slope after spatial frequency (q) values of 100, which can be ascribed to the fact that the resolution of AFM tip corresponds to a q value of 100 and hence the change in slope after 100 may be due to possible tip artifacts.

5.4.2. Exchange Averaging and 2D-Herzer model for coercivity evolution in film plane.

Figure 5.13 is similar to the variation reported for the Random Anisotropy model (RAM). The low values of coercivity and anisotropy along the in plane direction suggests exchange averaging. The change in coercivity with crystal size can be modeled by RAM [17–19]. Fenineche reported that Co-Fe alloy films obey RAM [40]. According to RAM

$$H_c = \frac{p_c \langle K \rangle}{M_s} = p_c \frac{K_1^4 D^6}{M_s A^3}$$

(5.1)

In the above equation p_c acts as a fitting parameter and M_s is the saturation magnetization. These equations are derived by assuming a three

137

dimensional material of volume L^3_{ex}. Inserting typical values $K_u \approx 0.27$ kJ/m^{3}and $A \approx 9.11$x 10^{-14} J/ m^2 for Co-Fe in equation 1 gives $L_{ex} \approx 18.4$ nm [15]. Hence in such alloys, if the crystal separation is less than $L_{ex} \approx 18.4$ nm the anisotropies are averaged out over several crystals and the sample exhibits good soft magnetic properties. However, when one of the dimensions of the material is restricted to values comparable to this typical length scale the system can be approximated as a two dimensional system and the relevant equations are,

$$\langle K \rangle = \frac{K_1^2}{A} D^2$$

(5.2)

$$H_c = \frac{p_c \langle K \rangle}{M_s} = p_c \frac{K_1^2 D^2}{M_s A}$$

(5.3)

All the parameters refer to the same meaning discussed earlier, but they are now the two dimensional counter parts of the corresponding three dimensional values. This equation suggests that for ultra-thin films the D^2 law should be used instead of the D^6 law [7,8,41]

The above equation suggest that ln (H$_c$) is directly proportional to ln (D), under the assumption that saturation magnetization is the same for all the samples. The linear plot of ln(H$_c$) is directly proportional to ln(D) (figure 5.15) and confirms that coercivity indeed obeys a D^2 behavior rather than a D^6 behavior. The as prepared samples as well as samples annealed at 100 ^{o}C and 300 ^{o}C obey the Herzer relation. They have crystal sizes less than the exchange length of 18.4 nm. However the sample annealed at 400 ^{o}C has crystal size greater than the exchange length. This can account for the deviation of the data point for the 40 0°C annealed sample from the linear plot of ln (H$_c$) versus ln (D). Vopsaroiua *et. al.* also observed similar variation in Co-Fe thin films [15].
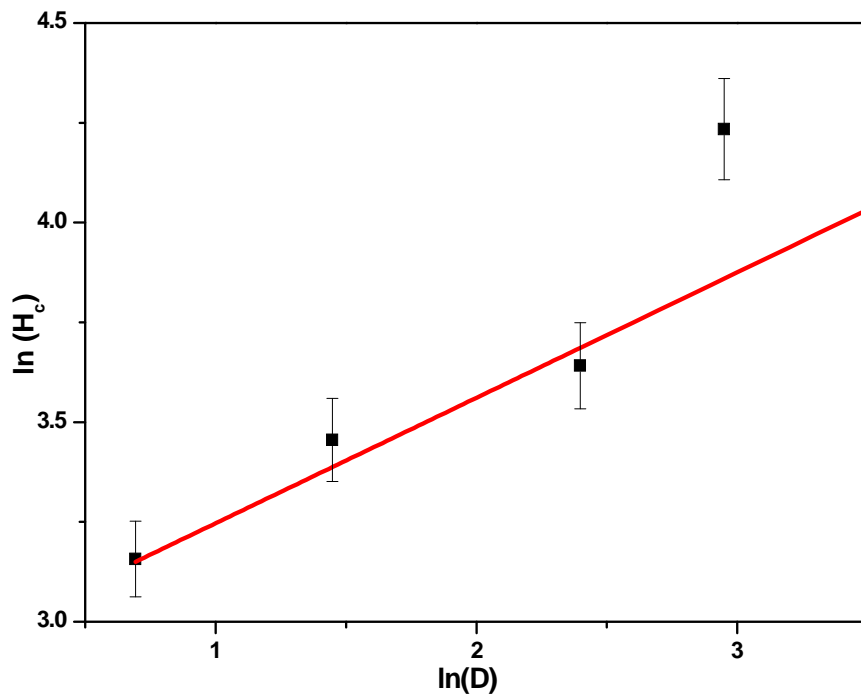
Figure 5.15: Plot of ln(H$_c$) versus ln(D)

5.4.3. Angular Dependence of Coercivity

The angular dependence of coercivity of the as prepared sample is measured by rotating the sample and recording the VSM loops at different angles. By convention it is measured in the angular range of 90º.

The in plane hysteresis loop is nearly square, suggesting that coherent rotation of domains or domain wall motion as the dominant mechanism for magnetization reversal. However as the angle changes to 10º and higher values, in addition to domain wall motion a domain rotation process is also operational as seen from the inclination of the magnetization curve before Ms is reached (figure 5.16). At 90º complete saturation cannot be achieved even at the highest fields, suggesting strong uniaxial anisotropy. This supports our use of the two dimensional RAM, which assumes exchange averaging only along the two dimensional surface of the film. It also suggests that magnetization reversal along in plane and out of plane may be due to different mechanisms. It is possible to

elucidate the magnetization reversal mechanisms from the angular plot of coercivity.
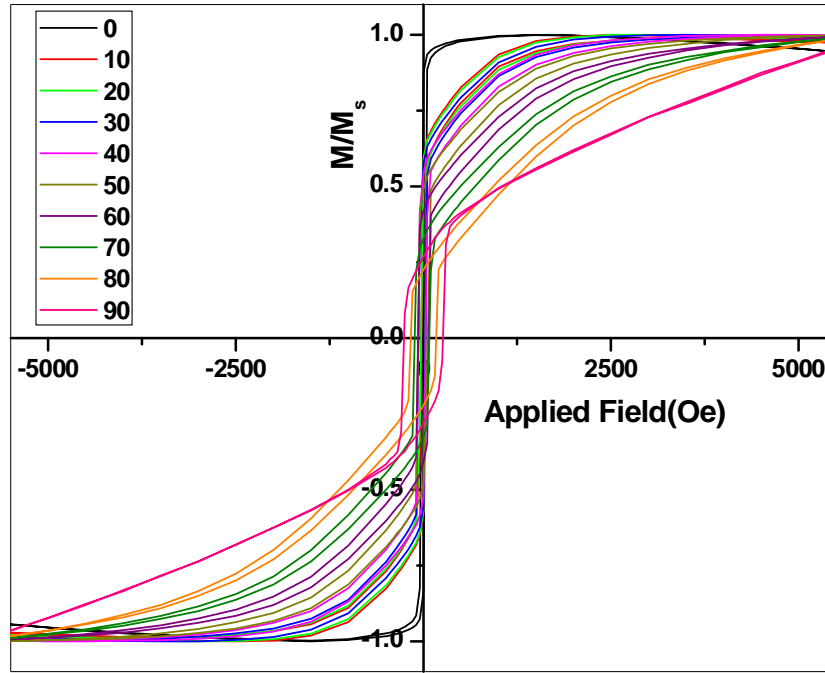
Figure 5.16: Hysteresis Loops of as prepared film for various angles

Generally there are two kinds of magnetization reversal mechanisms (1) coherent rotation, modeled by the Stoner- Wohlfarth (S-W) relation [20] and (2) domain wall motion, modeled by the Kondorsky relation [42]. The angular dependence can also give information about the isolation of crystals since the S-W relation assumes that the crystals are well isolated.

In the case of well isolated crystals, when the field is along the hard axis, the magnetization reversal is dominated by coherent rotation as per the S-W equation.

$$\frac{H_c(\theta)}{H_c(0)} = (\cos^{2/3}\theta + \sin^{2/3}\theta)^{-3/2} \text{ for angles } 0^\circ \leq \theta \leq 45^\circ$$

$$\frac{H_c(\theta)}{H_c(0)} = \sin(\theta)\cos(\theta) \text{ for angles } 45^\circ \leq \theta \leq 90^\circ$$

Where $h_c(\theta) = \frac{H_c(\theta)}{H_c(0)}$ is the coercivity scaled with the easy axis coercivity.

When the magnetization reversal is caused by domain wall motion/reverse domain nucleation, the coercivity follows the Kondorsky model.

$$h_c(\theta) = \frac{H_c(\theta)}{H_c(0)} = \sec(\theta) \text{ for } 0° \leq \theta \leq 90°$$

Here $H_c(0)$ is the intrinsic coercivity along the easy axis.

In uniaxial media if the effect of pinning sites have a prominent influence on magnetisation reversal a modified Kondorsky equation [27] can effectively model the reduced coercivity with angle as $h_c(\theta) = h + \frac{1-h}{cos(\theta)}$.
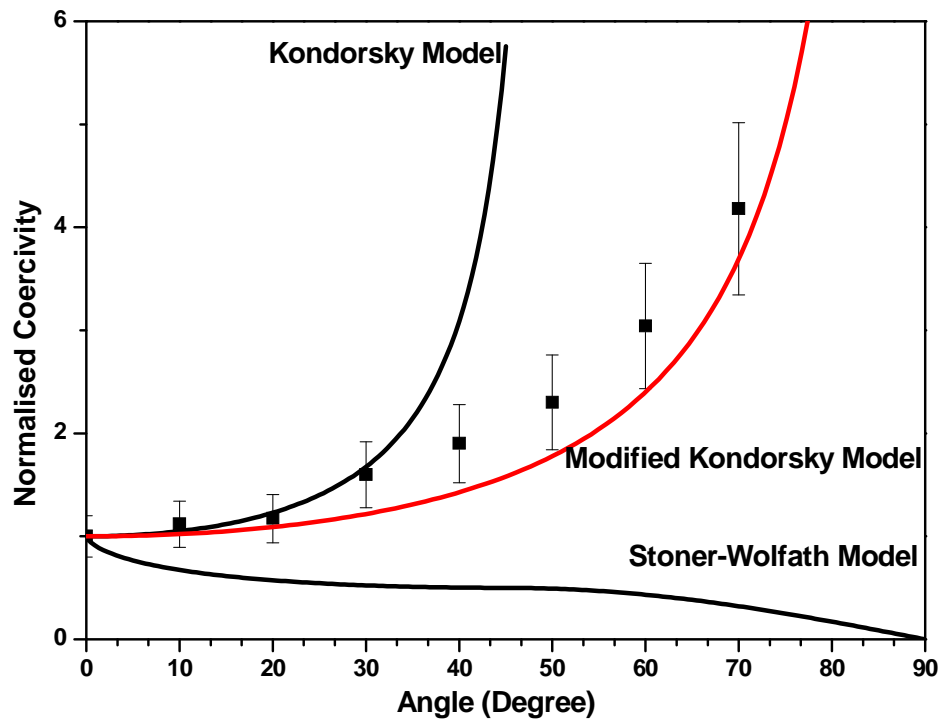
Figure 5.17: Plot of the coercivity versus angle for the as prepared film. The thick red line is fit to the data points using the modified Kondorsky model.

When the field is applied out of plane, in the as prepared sample, applied magnetic field of 6000 Oe is insufficient to overcome the magnetic anisotropy. The field reversal is a combination of domain wall motion/unpinning. Along the out of plane direction, the hysteresis loops towards the saturation end is inclined approximately $45°$ with coercivity of 260 Oe. This may be due to domain pinning

effects. The most probable origin of this domain pinning is the presence of a surface oxide layer on top as well as the large surface roughness of the film. The surface oxides can act as pining centers that drags domains from rotating with the applied field. This is manifested as the inclination of the hysteresis curve for the out of plane loops. When field is applied, the domain wall grows till further alignment along the magnetic field is not possible without domain rotation. According to the Kondorsky theory of domain-wall pinning at a local defect, the coercivity scales as the inverse of the cosine when domain walls grow around a local defect in the process of domain expansion [43].

Figure 5.17 shows the variation of coercivity with the angle that the applied field makes with the easy axis. The points suggest a sinusoidal behavior. The red line is the fit of the data points with the modified Kondorsky Model. Good fit of the data points indicates that the domain reversal mechanism is primarily Kondorsky type domain wall unpinning from a local defect. As discussed in the composition analysis section, the Co-Fe-Si films have a native oxide layer of Co, Fe and Si of thickness <6nm. The Co and Fe oxides can act as pinning centers for the Co-Fe domains residing underneath. Khan also observed similar behavior in Cu-capped ultrathin Co films [44].

Wei *et. al.* reports a mechanism to check the applicability of Kondorsky model [43]. If the hysteresis loops were plotted by scaling the x axis by H $\cos(\theta)$ for the loops taken at different angles, all the loops should coincide. In our case all loops (figure 5.18), except 0° and 90° coincide with the loop taken at other angles. This provides another proof for the dominance of domain wall motion/unpinning in magnetization reversal. However the in plane loop and out of plane loops do not fit into this category. As the direction of applied field changes from in plane, the magnetization, in addition to the dominant domain wall motion, has to rotate to reach saturation. This is visible by the presence of a small inclination of the loop after remanence. The modified Kondorsky model reproduces the angular dependence of coercivity. However the model is

142

developed on the assumption of a strongly pinned domain before magnetization switching.

The angular dependence of M-H loops and the reciprocal cosine angle dependence of coercivity clearly shows the role of domain wall motion/unpinning in magnetization reversal.
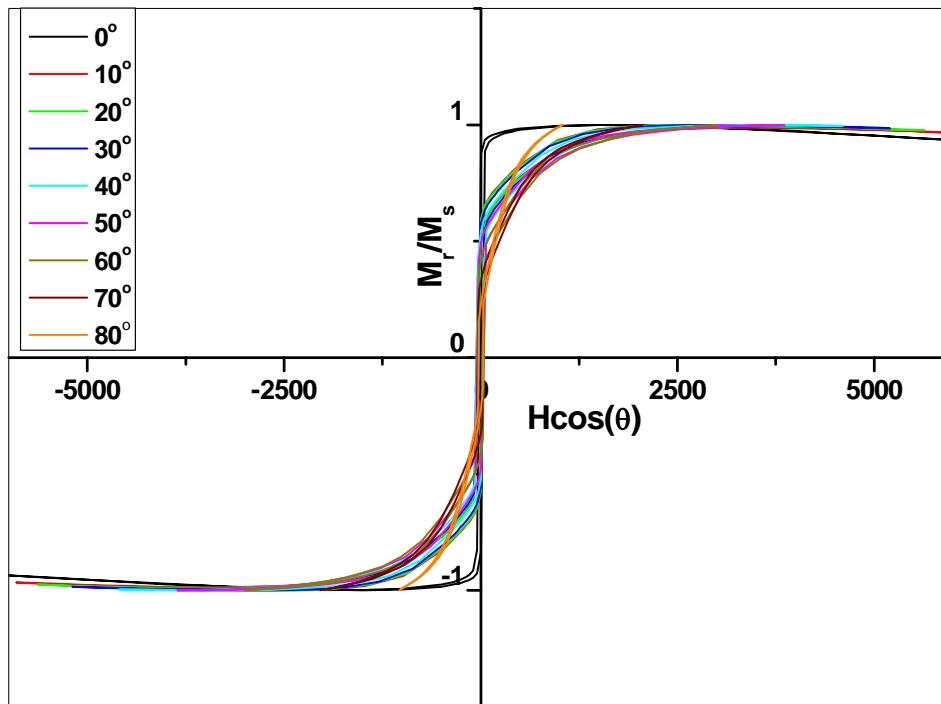
Figure 5.18: VSM loops re-plotted by scaling the H values of loops recorded at different angles with H cos(θ).

Rather than pinned domains, incoherent rotation of the domains is a more realistic description of the observed angular dependence. Further the Kondorsky model is generally valid for a continuous film whereas in this work the films, even though continuous, exhibit an island like growth behavior [26]. Uesaka *et. al.* earlier reported that a non uniform magnetic anisotropy across a particle can produce an asymmetric angular dependence of switching field [45]. Spiridis *et. al.* and Kisielewski *et. al.* reported the existence of domain wall motion in magnetisation reversal of ultrathin cobalt films [28,46]. Ji also reported the

contribution of domain wall motion to magnetisation reversal for 10 nm $Co_{70}Fe_{30}$ films along the (100) axis [16]. Chang *et. al.* reported that, Co when exposed to oxygen, can alter its electronic density of states, stress anisotropy and domain wall motion during magnetization reversal [47]. Thus the ultrathin oxide layer serves to pin the magnetic domains of Co-Fe forcing the magnetic reversal mechanism to be domain wall unpinning. This effect is prominent along the out of plane direction.

5.4.4. Surface Magnetic Properties
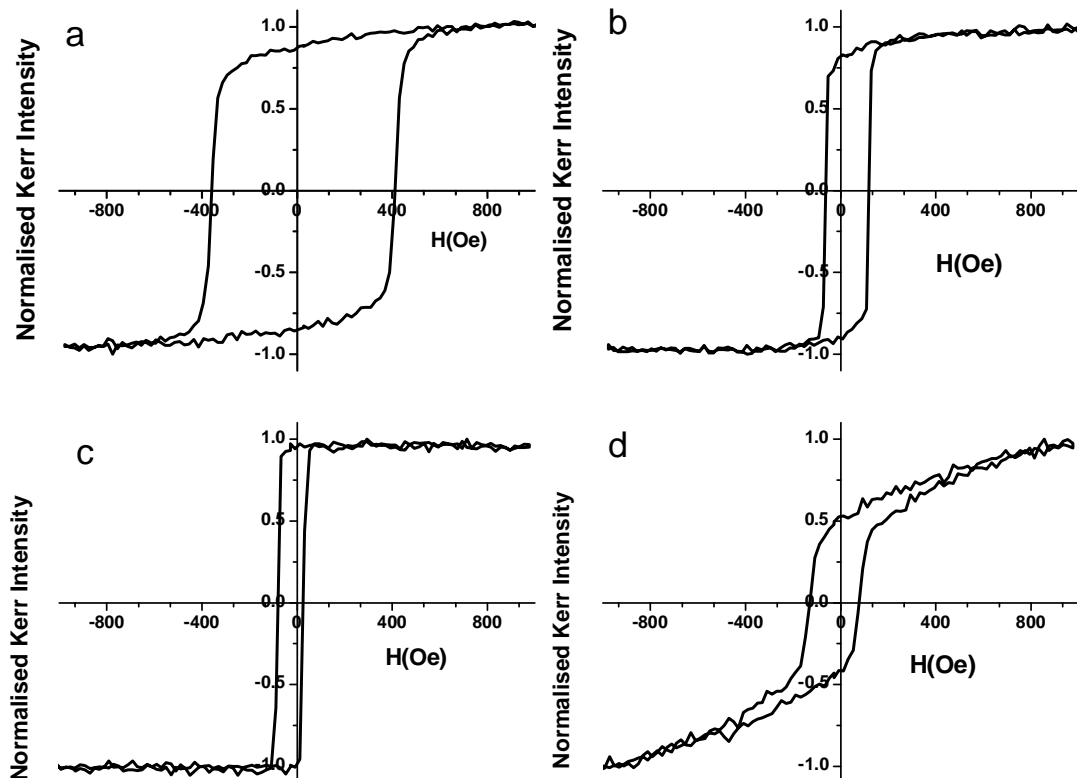
Figure 5.19: MOKE loops of films a) as prepared b) annealed at 100°C c) annealed at 300°C d) annealed at 400°C

The MOKE hysteresis loops (figure 5.19) show almost square loops with squareness nearly equal to one. However the coercivity evolution (figure 5.20)

144

with annealing temperature from MOKE shows a reverse trend as compared to the bulk VSM loops (figure 5.13). The XPS analysis shows that the films have a thin native oxide layer of iron and cobalt. This oxide layer with large roughness, offers very high resistance to domain rotation. The as prepared film has a roughness of 3.46 nm. As the film is annealed at 100°C and 300°C the roughness values changes from 2.68 nm and 2.21 nm respectively. This suggests possible surface smoothening, annealing out of pinning sites and decrease in thickness of the oxide layer. This can account for the decrease in coercivity.
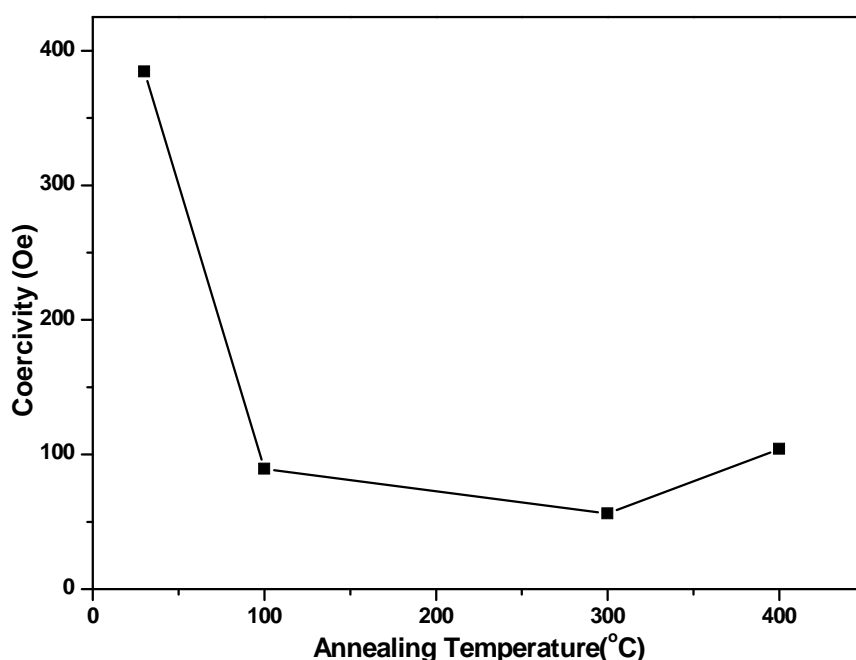
Figure 5.20: Variation of surface coercivity with annealing temperature.

However, the loop for 400°C annealed sample does not saturate even at 1000 Oe. Further, the shape of the loop suggests that in addition to domain wall motion, domain rotation is also operating. The anisotropy field is also very large. This increased coercivity may be due to the presence of elemental cobalt at the surface. The penetration depth of light is estimated to be <10 nm in metals [48]. Hence it can be expected that the MOKE signals carry magnetic polarisation information from the oxide layer as well as the Co-Fe-Si under layer. Since the

probing depth of XPS is ~3 nm we can conclude that elemental cobalt exists within 3 nm from the surface either as Co or as Co-Fe. Jergel reported such an increase in coercivity for cobalt thin films annealed at 400 ^{o}C and explained it by assuming the formation of hcp cobalt crystals [49].

5.5 Conclusions

Co-Fe-Si thin films prepared by employing thermal evaporation were found to have a native oxide layer on its surface. Annealed thin films were found to behave according to the Herzer model, except for the 400°C annealed sample. The samples annealed at 400°C have crystals with mean size greater than the exchange length; hence possess large coercivity due to the absence of exchange averaging. The angular dependence of coercivity shows that the dominant magnetization reversal mechanism is domain wall unpinning in accordance with the modified Kondorsky model. The MOKE measurements provide further evidence for domain wall pinning by showing a reverse trend compared to the VSM data. The bulk and surface magnetic properties were found to be different owing to the presence of a thin oxide layer on the film surface. There is further scope for a detailed investigation comparing the effect of nonmagnetic metallic layers on the surface and bulk magnetic properties of Co-Fe-Si thin films.

References

[1]   S. Ohnuma, H. Fujimori, T. Masumoto, X.Y. Xiong, D.H. Ping, K. Hono, Applied Physics Letters 82 (2003) 946.

[2]   Y. Kitamoto, H. Tagami, G. Kiyota, IEEE Transactions on Magnetics 41 (2005) 3295.

[3]   S.X. Wang, N.X. Sun, M. Yamaguchi, S. Yabukami, Nature 407 (2000) 150.

[4]   H. Kikuchi, M. Sato, K. Kobayashi, Journal of Applied Physics 87 (2000) 6055.

[5]   R.M. Bozorth, Ferromagnetism, Van Nostrand, Prinston, New Jersey, 1951.

[6]   A.T. Hindmarch, A.K. Suszka, M. MacKenzie, J.N. Chapman, M. Henini, D. Taylor, B.J. Hickey, C.H. Marrows, Journal of Applied Physics 105 (2009) 073907.

[7]   T. Hysen, S. Deepa, S. Saravanan, R. V Ramanujan, D.K. Avasthi, P. a Joy, S.D. Kulkarni, M.R. Anantharaman, Journal of Physics D: Applied Physics 39 (2006) 1993.

[8]   S. Thomas, S.H. Al-Harthi, D. Sakthikumar, I. Al-Omari, R. V Ramanujan, Y. Yoshida, M.R. Anantharaman, Journal of Physics D: Applied Physics 41 (2008) 155009.

[9]   S. Thomas, S.H. Al-Harthi, R. V. Ramanujan, Z. Bangchuan, L. Yan, W. Lan, M.R. Anantharaman, Applied Physics Letters 94 (2009) 063110.

[10]   S. Thomas, S.H. Al-Harthi, I. a Al-Omari, R. V Ramanujan, V. Swaminathan, M.R. Anantharaman, Journal of Physics D: Applied Physics 42 (2009) 215005.

[11]   S. Thomas, H. Thomas, D.K. Avasthi, a. Tripathi, R. V. Ramanujan, M.R. Anantharaman, Journal of Applied Physics 105 (2009) 033910.

[12]   H. Thomas, S. Thomas, R. V. Ramanujan, D.K. Avasthi, I. Al- Omari, S. Al-Harthi, M.R. Anantharaman, Nuclear Instruments and Methods in Physics Research Section B: Beam Interactions with Materials and Atoms 287 (2012) 85.

[13]   T. Thomson, P.C. Reidi, C.L. Platt, A.E. Berkowits, IEEE Transactions on Magnetics 34 (1998) 1045.

[14]   C.L. Platt, A.E. Berkowitz, D.J. Smith, M.R. McCartney, Journal of Applied Physics 88 (2000) 2058.

[15]   M. Vopsaroiu, M. Georgieva, P.J. Grundy, G. Vallejo Fernandez, S. Manzoor, M.J. Thwaites, K. O'Grady, Journal of Applied Physics 97 (2005) 10N303.

[16]   C.X. Ji, F. Lu, Y.A. Chang, J.J. Yang, M.S. Rzchowski, Applied Physics Letters 92 (2008) 022504.

[17]   R. Alben, J.J. Becker, M.C. Chi, Journal of Applied Physics 49 (1978) 1653.

[18]   G. Herzer, Physica Scripta 307 (1993) 307.

[19]   G. Herzer, IEEE Transactions on Magnetics 26 (1990) 1397.

[20]   E.C. Stoner, E.P. Wohlfarth, Philosophical Transactions of the Royal Society of London. Series A, Mathematical and Physical Sciences 240 (1948) 599.

[21]   L. Xiaoqi, Z. Haibao, K. Yukiko, W. Jian-Ping, Journal of Physics D: Applied Physics 41 (2008) 232002.

[22]   L. Sun, H. Xing, Journal of Applied Physics 104 (2008) 043904.

[23]   W.D. Doyle, J.E. Rudisill, S. Shtrikman, Journal of Applied Physics 32 (1961) 1785.

[24]   X. Fan, Y.S. Gui, a. Wirthmann, G. Williams, D. Xue, C.-M. Hu, Applied Physics Letters 95 (2009) 062511.

[25]   T. Thomson, G. Hu, B. Terris, Physical Review Letters 96 (2006) 257204.

[26]   M. Delalande, J. de Vries, L. Abelmann, J.C. Lodder, Journal of Magnetism and Magnetic Materials 324 (2012) 1277.

[27]   R. Streubel, D.J. Thurmer, D. Makarov, F. Kronast, T. Kosub, V. Kravchuk, D.D. Sheka, Y. Gaididei, R. Schäfer, O.G. Schmidt, Nano Letters 12 (2012) 3961.

[28]   N. Spiridis, T. Ślęzak, M. Zajac, J. Korecki, Surface Science 566-568 (2004) 272.

[29]   Z.Y. Liu, S. Adenwalla, IEEE Transactions on Magnetics 39 (2003) 2074.

[30]   S. Hufner, R.L. Cohen, G.K. Wertheim, Physica Scripta 5 (1972) 1972.

[31]   M.G. Mendez, F.F. Castillon, G.A. Hirata, M.H. Farıas, G. Beamson, Applied Surface Science 161 (2000) 61.

[32]   T.J. Chuang, C.R. Brundle, D.W. Rice, Surface Science 59 (1976) 413.

[33]   H.T. Yang, C.M. Shen, Y.G. Wang, Y.K. Su, T.Z. Yang, H.J. Gao, Nanotechnology 15 (2004) 70.

[34]   R. Sharif, S. Shamaila, M. Ma, L.D. Yao, R.C. Yu, X.F. Han, Y. Wang, M. Khaleeq-ur-Rahman, Journal of Magnetism and Magnetic Materials 320 (2008) 1512.

[35]   G. Yildirim, S. Bal, M. Gulen, a. Varilci, E. Budak, M. Akdogan, Crystal Research and Technology 47 (2012) 195.

[36]   J. Xu, L. Yu, I. Kojima, Journal of Applied Physics 94 (2003) 6827.

[37]   M. Kader, G. Parisi, Y. Zhang, Physical Review Letters 56 (n.d.) 889.

[38]   D.E. Wolf, J. Villain, Europhysics Letters 13 (1990) 389.

[39]   D. Aurongzeb, M. Holtz, L. Menon, Applied Physics Letters 89 (2006) 092501.

[40]   N.E. Fenineche, R. Hamzaoui, O. El Kedim, Materials Letters 57 (2003) 4165.

[41]   G. Herzer, Materials Science and Engineering A. 133 (1991) 1.

[42]   F. Schumacher, Journal of Applied Physics 70 (1991) 3184.

[43]   H. Wei, Q.F. Zhan, D.Y. Wang, L.J. Chen, Y. Sun, Z.H. Cheng, Chinese Physics 16 (2007) 3541.

[44]   R.A. Khan, A.S. Bhatti, Journal of Magnetism and Magnetic Materials 323 (2011) 340.

[45]   Y. Uesaka, Y. Nakatani, N. Hayashi, Japanese Journal of Applied Physics 34 (1995) 6056.

[46]   M. Kisielewski, Z. Kurant, A. Maziewski, M. Tekielak, N. Spiridis, J. Korecki, Physica Status Solidi (a) 189 (2002) 929.

[47]   H.W. Chang, J.S. Tsay, W.Y. Chang, K.T. Huang, Y.D. Yao, Journal of Magnetism and Magnetic Materials 321 (2009) 2398.

[48]   H. Oguchi, A. Zambano, M. Yu, J. Hattrick-Simpers, D. Banerjee, Y. Liu, Z.L. Wang, J.P. Liu, S.E. Lofland, D. Josell, I. Takeuchi, Journal of Applied Physics 105 (2009) 023912.

[49]   M. Jergel, I. Cheshko, Y. Halahovets, P. Šiffalovič, I. Maťko, R. Senderák, S. Protsenko, E. Majková, Š. Luby, Journal of Physics D: Applied Physics 42 (2009) 135406.

Chapter 6

Swift Heavy Ion Induced Surface and Micro-Structural Evolution in Fe-Ni-B Thin Films

6.1 Introduction

Metallic amorphous alloys are a class of materials that are widely investigated for plausible technological applications; owing to their enhanced structural, magnetic and electrical properties [1-4]. Most of these outstanding properties can be attributed to their random crystalline structure [3]. These materials can be synthesized by a variety of techniques like physical vapour deposition, solid-state reaction, ion beam irradiation, melt spinning, and mechanical alloying [3, 4], of which, ion beam irradiation seems to be a promising technique since it can induce a variety of changes in the material ranging from bulk structural to local magnetic properties. During irradiation, fast heavy ions passing through a material with velocities comparable to the Bohr velocity of electrons, loses energy mainly by two processes, namely, nuclear energy loss, and electronic energy loss. The former is dominant when the ion energy is in the keV range, and latter is dominant when the ion energy is in the MeV range.

Most of the effects associated with SHI irradiation occur in the electronic energy loss regime. This inelastic scattering assisted energy loss of fast heavy ions creates 1) latent tracks, 2) phase transitions, 3) amorphisation, 4) damage creation, 5) annealing effects, 6) dimensional changes, and 9) nanostructures. During irradiation, surface morphology also evolve resulting from the competition between dynamic roughening; which increase the surface roughness, and smoothening; which decrease the surface roughness. Recently, Kanjilal *et. al.* [5] reported surface roughening kinetics of 100 MeV Au beam irradiated $Si_{1-x}Ge_x$ alloy films for x = 0.5 and 0.7. The irradiation induced surface roughening behavior is demonstrated by studying the variation of surface roughness as a function of ion fluence. The composition dependent variation of surface morphology with increasing fluence is ascribed to the strain distribution along the

152

sample surface. Thomas *et. al.* [6] reported SHI irradiation induced coercivity changes in Fe-Ni based thin films and the observed changes were correlated with topographical evolution of the films with ion fluence. Dash *et. al.* [7] carried out quantitative roughness and microstructure analysis of as-deposited and SHI (107 MeV Ag and 58 MeV Ni) irradiated 10 and 20 nm thick Au films using AFM and its power spectral density analysis. They reported an increase in the root mean square (rms) roughness at low fluences and a decrease at higher fluences. The PSD analysis also showed similar variation of low frequency roughness with ion fluence. In the high frequency regime, surface morphology of irradiated samples was found to be governed by a combined effect of evaporation– re-condensation and diffusion dominated processes.

Gupta and Avasthi [8] reported sputtering in Au thin films, resulting from energy deposition in the films, owing to inelastic collision of SHI with electron clouds of target atoms. Gupta *et al.* [9] reported SHI induced surface smoothening, roughening and sputtering of thermally immiscible Fe/Bi bilayer system. The observed behavior of surface smoothing and roughening under SHI irradiation was explained on the basis of the thermal spike model. In general, magnetic properties of thin films are sensitively correlated to the surface roughness and hence it will be worthwhile to probe possible mechanisms by which roughness of thin films can be tailored. Further, rough films can act as templates for the growth of nanostructures using oblique angle deposition [10]. Pre-patterned substrates offer a suitable platform for growth of nanostructures by suitable deposition techniques.

There are also reports that electronic energy transfer to the amorphous alloys can lead to anisotropic growth, which means, shrinkage of alloy ribbons in the direction of the beam and expansion in the direction transverse to it [11]. In

thin films, this type of effects can create large stress in the film-substrate interfacial boundaries. The dense random arrangement of atoms in metallic glasses favours amorphous structure due to the increased liquid-solid interfacial energy. Any structural or morphological changes occurring in these materials are of great importance in determining the structural and magnetic properties. Hence, amorphous alloys can serve as ideal templates to investigate these varied effects.

Scanning probe microscopy (SPM) is a versatile technique to probe surface morphology of thin films in the nano range. In the case of magnetic thin films, surface morphology from AFM and magnetic morphology from magnetic force microscopy (if there is considerable out-of-plane stray field) can be extracted employing specific tips in SPM. The images can be further subjected to Fourier analysis using image analysis software to obtain PSD, roughness and auto correlation functions.

Most of the available literatures pertaining to the study of material modification by ion beams were based on bulk materials. Work on metallic glass thin films based on iron and nickel is seldom reported [12-16]. The authors group recently reported 108 MeV Ag^{8+} ions induced surface modification of Fe-Ni based metallic glass thin films in the as-deposited state [6]. In the present investigation, we focus on the influence of swift heavy ions on the microstructure and surface morphology of 673 K annealed metallic glass thin films, so as to study the impact of SHI on the crystalline nature of these films. The results are correlated with a view to gain insight into the structural and morphological evolution with SHI irradiation.

6.2 Experimental

6.2.1. Thin film preparation

Metglas thin films with nominal thickness of 100 nm were vacuum evaporated using tungsten filaments on chemically and ultrasonically cleaned glass substrates from a composite target having composition $Fe_{40}Ni_{38}B_{18}Mo_4$. The chamber pressure before deposition was $1x10^{-6}$ mbar, which increased to $3x10^{-5}$ mbar during deposition. Recently, microstructure and magnetic evolution of Fe-Ni based thin films with thermal annealing were reported in the literature by our group [12, 14]. From the TEM images it was found that, the microstructure of as-deposited films exhibits a contrast typical of an amorphous material [14]. The bright field TEM images of the films annealed at 473 K, 573 K and 673 K, revealed that the microstructure consisted of nanocrystallites embedded in an amorphous phase. Grain growth was also observed with an increase in the annealing temperature [12, 14]. Based on those results, the as-deposited Fe-Ni based metallic glass films were annealed at 673 K for 1 hour. Annealing was performed at $4x10^{-5}$ mbar for minimizing surface oxidation.

6.2.2. Swift heavy ion irradiation

As deposited as well as annealed films were irradiated with 103 MeV Au^{9+} ions at the 15 UD Pelletron accelerator at IUAC, New Delhi. The irradiations were performed at 0° angle of incidence with respect to the surface normal. Ion beam was raster scanned on the sample surface by a magnetic scanner for maintaining a uniform ion flux throughout the film. The fluences varied from $3x10^{11}$ to $3x10^{13}$ ions/cm^2. The irradiated sample area was 1 cm^2.
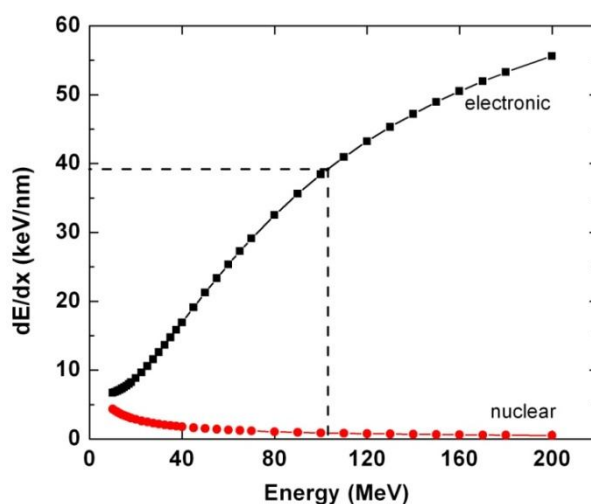
Figure 6.1: SRIM simulation showing electronic and nuclear energy loss versus ion energy. Dashed line shows the electronic energy loss corresponding to 103MeV energy

The Au ion is chosen due to its higher mass and the energy regime is selected after simulation using SRIM code [17]. For the chosen ion energy of 103 MeV, the lateral straggling is 5.87 μm, longitudinal straggling is 4.62 μm and the penetration depth is 6.98 μm. This value of penetration depth is two orders of magnitude greater than the thickness of the film. The energy of the Au^{9+} beams (103 MeV) was selected with a view to avoid the ion implantations in the film with maximum electronic loss (39 keV/nm) and minimum nuclear energy losses within the accelerator's maximum energy limit (see figure 6.1).

The samples were mounted on a massive copper block using carbon tape. The increase in sample temperature during ion irradiation can be estimated using the Fourier heat conduction equation, $j = -\lambda \frac{dT}{dz}$. The total heat carried into the system can be taken as the total energy carried by SHI, $E = \dot{\varphi} E_{shi}$, where $\dot{\varphi}$ is the ion flux and E_{shi} is the ion energy. In this study, a low ion flux of 6×10^9 cm^2/s was maintained with energy of 103 MeV per ions. The conductivity of float glass is nearly equal to 1 $Wm^{-1}K^{-1}$. However, even if we assume a still lower

conductivity for the system of film, glass substrate and carbon tape, the Fourier equation predicts a temperature rise of less than 10 K at the film surface [18, 19]. Thus the temperature rise due to ion irradiation is assumed to be small to effect any micro-structural changes in the film.
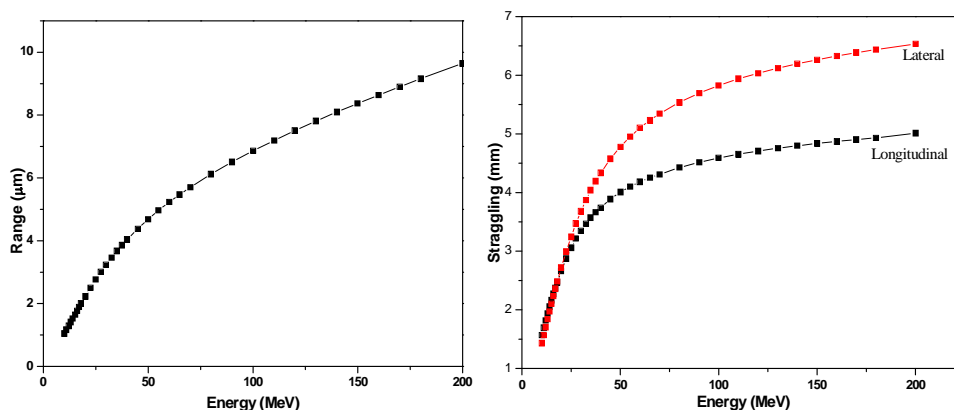
Figure 6.2 a) SRIM simulation of projected range versus energy for Ag^{+9} ions in the Fe-Ni-B thin film and glass substrate b) Longitudinal and lateral straggling for Ag^{+9} ions in Fe-Ni-B thin film and glass substrate.

6.2.3. Characterization

The XRD pattern of all samples were recorded using an X-ray diffractometer (Rigaku D-max-C) using Cu Kα radiation (λ=1.54 Å). The average particle size is estimated from measured width of the diffraction curves using Scherer formula. The surface topography of all thin films were analyzed using an AFM (Digital Instruments Nanoscope V). The AFM images were analysed using surface data analysis software SPIP (Image Metrology A/S, Hørsholm, Denmark) to obtain PSD, roughness and auto correlation functions. TEM measurements were performed in a 200 kV Philips CM 20 FEG TEM.

6.3 Results and Discussion

6.3.1. Microstructural evolution with SHI irradiation

Figure 6.3(a) shows XRD pattern of as-deposited Fe-Ni based metallic glass thin film. The film appears to be amorphous in XRD. In order to have a

deeper insight into the microstructure of the as-deposited films, high resolution transmission electron microscopy imaging was performed on this sample.
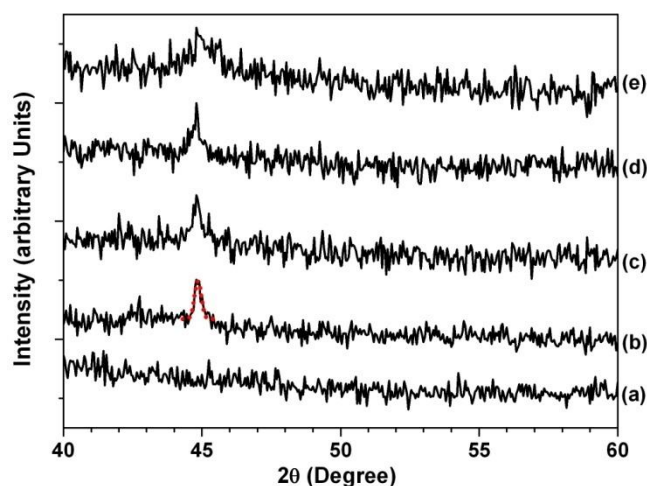
Figure 6.3: X-Ray diffraction pattern of Fe-Ni based thin films, (a) as-deposited, (b) annealed at 673K, the red dotted line shows a Gaussian fit to the peak to evaluate the crystallite size, (c) annealed at 673K and irradiated at fluence 3x10^{11} ions/ cm^2, (d) annealed at 673K and irradiated at fluence 3x10^{12} ions/cm^2, (e) annealed at 673K and irradiated at fluence 3x10^{13} ions/cm^2.

*(The TEM images of the as prepared and film annealed at 673 K is shown in figure 6.4c. The image of the as prepared film shows small contrast possibly arising from density fluctuations during vapour deposition. The SAED pattern of pristine film shows a diffuse halo arising from (100) plane of Fe-Ni at d = 0.207 nm suggesting short range ordering of Fe-Ni. The film also shows diffraction rings corresponding to planes (311) and (440) of Fe_3O_4 with d values 0.254 nm and 0.146 nm respectively, further corroborating the results of XPS analysis. As the film is annealed the Fe-Ni ring at d=0.207 changes to polycrystalline structure manifested as a ring with well defined spots. Complete rings are not observed as is the case of a perfect polycrystalline material since the film is thin; the total number of grains contributing to the overall diffraction pattern is small. The annealed sample also shows diffraction rings with d values 0.152 and 0.170 from planes (440) and (205) from B_6O.)

This paragraph and the TEM image are reproduced from chapter 4 for clarity.
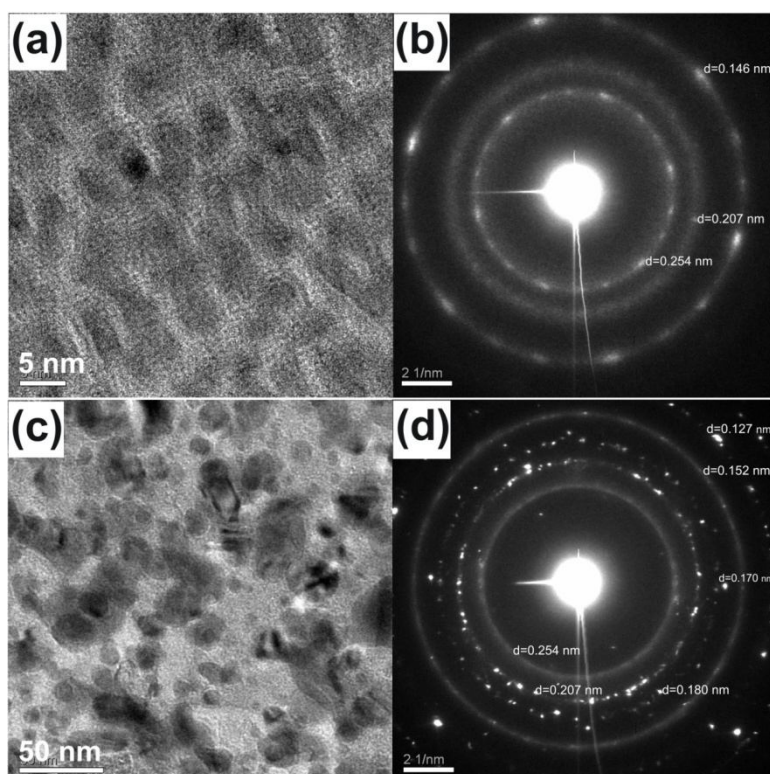
*Figure 6.4: (a) HRTEM image, and (b) electron diffraction pattern of as-deposited Fe-Ni based metallic glass thin film (c) TEM bright field image and (d) electron diffraction pattern of Fe-Ni based metallic glass thin film after annealing at 673 K for 1 hr.**

SHI irradiation on as-deposited films with fluences ranging from 3×10^{11} ions/cm^2 to 3×10^{13} ions/cm^2 did not produce any observable changes in the XRD pattern. The absence of any observable changes in the XRD pattern with irradiation can be attributed to the fact that the as-deposited films were already in a nanocrystalline state possessing a short range atomic order and the electronic energy loss of swift heavy ions in the material is stabilizing this short range order.

SHI irradiation on thermally annealed films with fluences ranging from 3×10^{11} ions/cm^2 to 3×10^{13} ions/cm^2 result in progressive line broadening of the XRD peak indicating fragmentation of crystallites with ion beam irradiation. The 673 K annealed sample already contains crystallites formed by nucleation and

growth due to thermal treatments. Irradiation of these films with higher fluences of SHI leads to size reduction of grains with multiple ion impacts and hence broadening of the peaks were observed (Figure 6.3(c), (d) and (e)). For an approximate estimate of the grain size, the full width at half maximum of the XRD peak was determined from a Gaussian fit. The 673 K annealed sample shows crystalline peak of Fe-Ni and the average crystallite size was estimated to be 28±3.6 nm. On irradiation of the sample with SHI at a fluence of 3×10^{11} ions/cm^2, the crystallite sizes reduced to 21±2.7 nm. The film irradiated at a fluence of 3×10^{12} ions/cm^2 showed crystallites with size 15±1.9 nm and at a higher fluence of 3×10^{13}ions/cm^2, the particle size is further reduced to 6±0.77 nm. The reduction in crystallite size as a result of SHI irradiation can be attributed to the strain induced fragmentation of crystallites. So far, thermal spike [20, 21] and Coulomb explosion models [22–24] have been successively used to describe the strain in the crystallites due to swift heavy ion irradiation. According to thermal spike model, the energy is deposited by the projectile ions in the electronic sub-system of the material. This energy is shared among the electrons by electron–electron coupling and is transferred subsequently to the lattice atoms via electron–lattice interactions. This results in a large increase in the temperature along and in the vicinity of the ion path. Because of the temperature spike, pressure waves develop and they cause strain in the crystallites. On the other hand, according to the Coulomb explosion model, a highly ionized zone of charged particles is created along the ion path. The ionization zone with positive charges may explode under electrostatic force and induce strain in the material. This strain may lead to the fragmentation of crystallites.

However, in addition to the crystallite size reduction, a partial contribution of the atom dislocations to the XRD line broadening also cannot be ruled out.

6.3.2. Surface evolution with ion beam irradiation

Figure 6.5 (a) shows AFM image of a Fe-Ni based metallic glass thin film annealed at 673 K. Lateral structures of sizes around 30 nm can be observed.
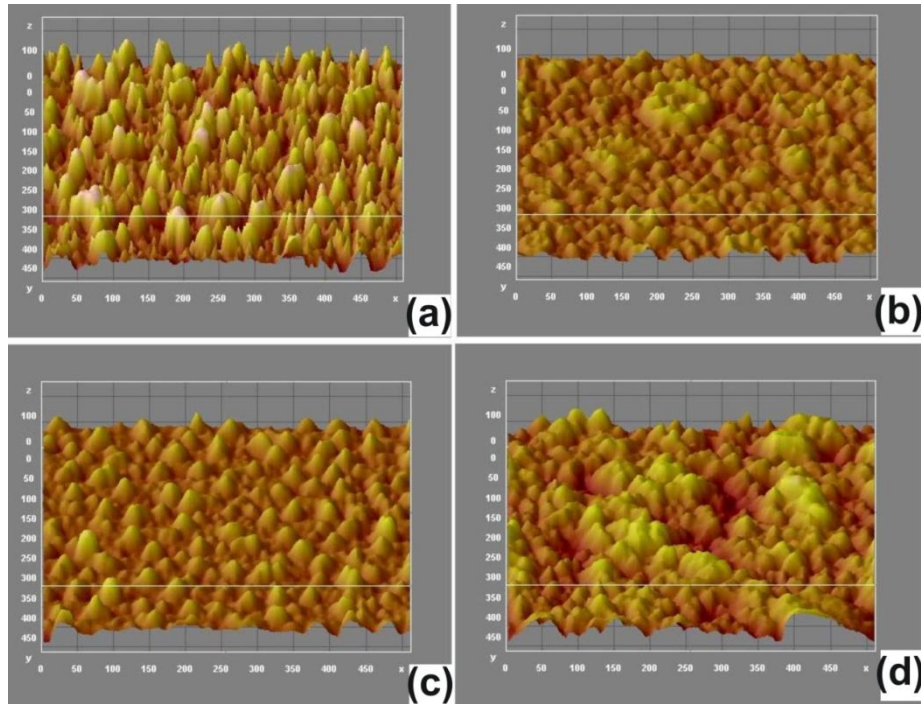
Figure 6.5: 3D AFM Images of Fe-Ni based metallic glass thin films (a) annealed at 673 K and subsequently irradiated with 103 MeV Au^{9+} ions of fluence (b) 3x10^{11} ions/cm^2, (c) 3x10^{12} ions/cm^2, (d) 3x10^{13} ions/cm^2. Image size is 500 nm^2 and z scale is 100 nm.

From the AFM images shown in figure 6.5(b)-(d), it is clear that irradiation of these annealed films, with 103 MeV Au^{9+} ions, changes the surface morphology, first at 3x10^{11} ions/cm^2, smoothing of the mesoscopic hill–like structures take place, and then, at 3x10^{12} ions/cm^2, new surface structures are created, and at still higher doses of 3x10^{13} ions/cm^2, an increase in the surface roughness is observed.

161

The evolution of surface roughness of the annealed films, irradiated at various fluences is shown in figure 6.6. The average roughness (*Ra*) of the 673 K annealed films is 27.05 nm and root mean square roughness (*Rq*) is 35.51 nm.
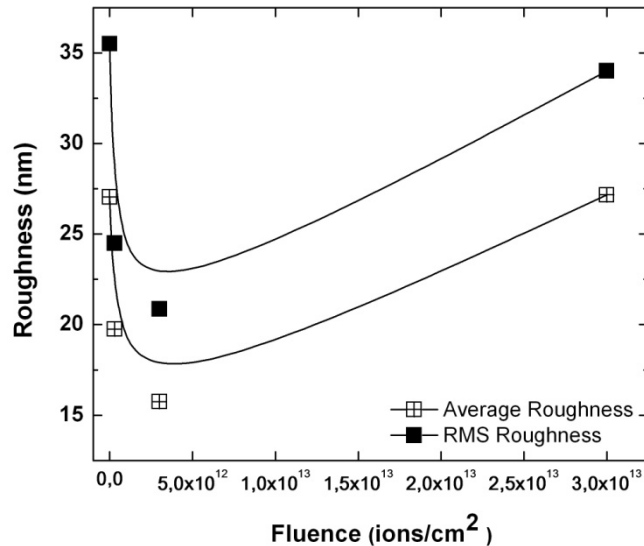
Figure 6.6: Variation of surface roughness with ion fluence. Solid line is drawn for a guide to eye

However, on SHI irradiation, roughness of the films reduces to value 19.75 nm, 24.49 nm (*Ra, Rq)* at fluences 3×10^{11} ions/cm^2 and 15.74 nm, 20.85 nm (*Ra, Rq)* at 3×10^{12} ions/cm^2 and thereafter monotonically increases to 27.16nm, 34.01nm (*Ra, Rq)*. The rapid initial decrease in surface roughness with ion fluence indicates that a surface smoothening process is taking place in the sample for the initial fluences. Plausible origins of this surface smoothening can be irradiation induced viscous flow, volume diffusion, or surface diffusion. Mayr and Averback [25] also observed surface smoothing in ion irradiated films. They identified smoothening process using stochastic rate equations for the evolution of the surface in Fourier space. In their example, they attributed the smoothing predominantly to irradiation-induced viscous flow. Goswami and Dev [26] observed a surface smoothening in silicon surfaces irradiated by a 2-MeV Si$^+$ ion beam. They explained the origin of irradiation induced surface smoothening as follows. The collision cascade as a result of ion-solid interaction can enable target

162

atoms to acquire a kinetic energy enough to escape from the solid surface (sputtering). However, if the energy (component normal to surface) of the displaced atoms is smaller than the surface binding energy, the atoms may reach the surface but cannot leave the surface. They can, however, drift parallel to the surface. Surface smoothening originates because of those atoms, which are ejected from the surface with too low energy to escape the energy barrier, but can translate parallel to the surface.

In order to have a deeper understanding of the initial surface smoothening mechanism with ion beam irradiation, power spectral density was obtained from the AFM images. The power spectral density of the films is shown in figure 6.7.
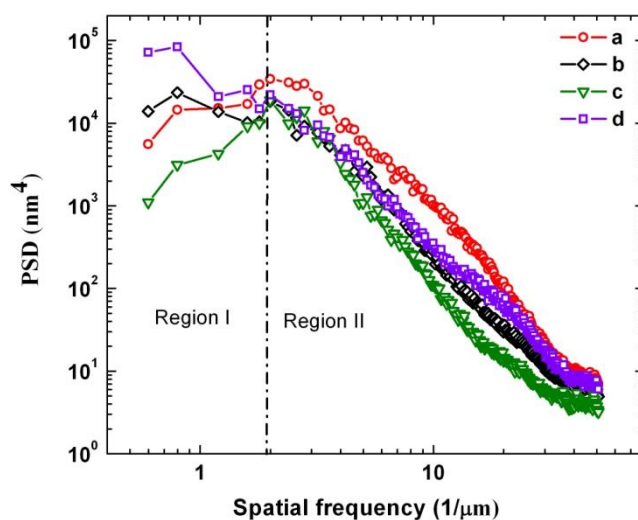
Fig. 6.7: Power spectral density plots of Fe-Ni based metallic glass thin films (a) annealed at 673 K and subsequently irradiated with 103 MeV Au^{9+} ions of fluence (b) 3×10^{11} ions/cm^2, (c) 3×10^{12} ions/cm^2, d) 3×10^{13} ions/cm^2.

From the log-log plot of PSD spectrum two different regions are visible. The low spatial frequency region (Region I) corresponds to the uncorrelated white noise and the high frequency region (Region II) represents correlated surface features. The PSD curves of the un-irradiated and irradiated films extracted from the AFM images essentially present the same characteristic

features consisting of a gradient in the high spatial frequency region and a low frequency region separated by a small cross over region
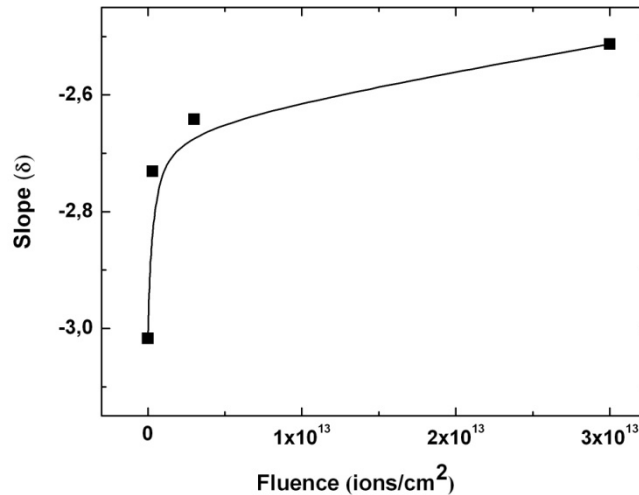
Figure 6.8: Dependence of the slope of the PSD spectrum (region II) with different ion fluences. Solid line is drawn for a guide to eye

The slope of the high frequency region of the PSD curves is intimately connected to the kinetics of surface evolution and hence can suggest the predominant mechanism responsible for the surface evolution of thin films with SHI. The variation in the slope of the high frequency region of the PSD curve is shown in figure 6.8.

It is clear that the slope, δ, gradually increases up to 3×10^{12} ions/cm^2 and thereafter the change in slope is relatively small. Earlier works by Herring and Mullins [27-29] established δ values of 1, 2, 3, and 4 to four different surface transport mechanisms i.e., plastic flow driven by surface tension, evaporation and recondensation of particles, volume diffusion, and surface diffusion, respectively. It is to be noted that, the evolution of surface morphology of solids during ion beam irradiation is governed by the interplay between the dynamics of surface roughening that occurs during sputtering and smoothening induced by the material transport. Form figure 6.8 and comparing δ with that suggested in the previous works, it is evident that as the irradiation fluence increases, the dominant materials transport mechanism changes from volume diffusion to

164

evaporation–condensation. This also explains the increased surface roughness at higher irradiation fluence. Surface roughening is assumed to be because of the evaporation of atoms from a hot surface heated by an inelastic thermal spike. The results indicate that at higher fluence 3×10^{13} ions/cm^2, the surface evaporation mechanism (sputtering) results in an increase in surface roughness and this is in line with our previous observations in 108 MeV Ag^{8+} ion irradiated as-deposited Fe-Ni based thin films [6].

From the combined XRD and AFM investigations it is seen that SHI is effective in surface modification of Fe-Ni based metallic glass thin films. However, further experiments are necessary to optimize these effects for specific applications.

6.4 Conclusions

Fe-Ni based metallic glass thin films were prepared by thermal evaporation. The films were annealed at 673 K and they showed more crystallinity than the as-deposited films. The as-deposited and annealed films were subjected to SHI irradiation at various fluences and their structural and morphological properties were investigated. The absence of any observable changes in the XRD of as-deposited films with ion beam irradiation can be attributed to the fact that the as-deposited films were already with a short range atomic order and the ion irradiation is stabilizing this short range order. For samples annealed at 673 K, upon irradiation, a significant reduction in grain size with ion fluence is observed. The grain fragmentation during ion beam irradiation is attributed to the strain transferred to the crystallites by the electronic energy loss. The irradiation of the sample rapidly changes the surface topography, first at 3×10^{11} ions/cm^2 smoothing of the mesoscopic hill–like structures, and then at 3×10^{12} ions/cm^2, creation of surface structures and at still higher doses of 3×10^{13} ions/cm^2 an increase in the roughness is observed. Volume diffusion was identified as the prominent surface smoothening mechanism at lower ion fluences and at higher fluences surface roughening was observed.   Further

165

investigations regarding the interplay between surface morphology and magnetic properties in these thin films are going on and there exists ample scope for probing the evolution of surface morphologies with magnetic properties in the case of magnetic films.

References

1. M. Telford, Materials Today 7 (2004) 36.

2. W. Klement Jr., R. H. Willens, P. Duwez, Nature 187 (1960) 869.

3. M. E. McHenry, M. A. Willard, D. E. Laughlin, Progress in Materials Science 44 (1999) 291.

4. T. R. Anantharaman, Metallic Glasses: production, properties and applications Trans Tech Publicatons, Switzerland, 1984.

5. A. Kanjilal, D. Kanjilal, Solid State Communications 139 (2006) 531.

6. S. Thomas, H. Thomas, D. K. Avasthi, A. Tripathi, R. V. Ramanujan, M. R. Anantharaman, Journal of Applied Physics105 (2009) 033910.

7. P. Dash, P. Mallick, H. Rath, A. Tripathi, Jai Prakash, D. K. Avasthi, S. Mazumder, S. Varma, P. V. Satyam, N. C. Mishra, Applied Surface Science 256 (2009) 558.

8. A. Gupta, D. K. Avasthi, Physical Review B: Condensed matter and materials Physics 64 (2001) 155407.

9. A. Gupta, R. S. Chauhan, D. C. Agarwal, S. Kumar, S. A. Khan, A. Tripathi, D. Kabiraj, S. Mohapatra, T. Som, D. K. Avasthi, Journal of Physics D: Applied Physics41 (2008) 215306.

10. M. M. Hawkeye,M. J. Brett, Journal ofVaccum Science and Technology A 25 (2007) 1317

11. Ming-dong Hou, S. Klaumünzer, G. Schumacher, Physical Review B:Condensed matter and materials Physics41 (1990) 1144.

12. T. Hysen , S. Deepa, S. Saravanan, R. V. Ramanujan, D. K. Avasthi, P. A. Joy, S. D. Kulkarni, M. R. Anantharaman, Journal of Physics D: Applied Physics39 (2006) 1993.

13. M. Jyothi, C.Suryanarayana, Z Metallkde 76 (1985) 802.

14. S. Thomas, S. H. Al-Harthi, D. Sakthikumar, I. A. Al-Omari, R. V. Ramanujan, Y. Yoshida, M. R. Anantharaman,Journalof Physics D: Applied Physics 41 (2008) 155009.

15. S. Thomas, S. H. Al-Harthi, R. V. Ramanujan, Zhao Bangchuan, Liu Yan, Wang Lan, M. R. Anantharaman, Applied Physics Letters 94 (2009) 063110.

16. S. Thomas, S. H. Al-Harthi, I. A. Al-Omari, R. V. Ramanujan, M. R. Anantharaman, Journal of Physics D: Applied Physics 42 (2009) 215005.

17. J. F. Ziegler, J. P. Biersack, and U. Littmark, The stopping and range of ions in solids, New York:Pergamon, 1985.

18. Tobias Roller, Wolfgang Bolse, Physical Review B: Condensed matter and materials Physics75 (2007) 054107

19. P. Mallick ,F, ChandanaRath , Jai Prakash , D.K. Mishra, R.J. Choudhary, D.M. Phase, A. Tripathi, D.K. Avasthi, D. Kanjilal, N.C. Mishra, Nuclear Instrumentsand Methods in Physics ResearchSection B: Beam Interaction with Materials and Atoms 268 (2010) 1613.

20. M. Toulemonde, C. Dufour, E. PaumierPhysical Review B: Condensed matter and materials Physics 46 (1992) 14362

21. Z G Wang, C Dufour, E Paumier and M Toulemonde, Journal of Physics: Condensed Matter 6 (1994) 6733

22. E. M. Bringa and R. E. Johnson, Physical Review Letters 88 (2002) 165501

23. R. L. Fleischer, P. B. Price, R. M. Walker and E. L. Hubbard, Physical Review 156 (1967) 353

24. R. L. Fleischer, P. B. Price, and R. M. Walker, Journal of Applied Physics 36 (1965) 3645

25. S. G. Mayr and R. S. Averback, Physical Review Letters 87 (2001) 196106.

26. D. K. Goswami and B. N. Dev, Physical Review B: Condensed matter and materials Physics 68 (2003) 033401

27. C. Herring, Journalof Applied Physics 21 (1950) 301.

28. William W. Mullins, Journalof Applied Physics 30 (1959) 77

29. William M. Tong and R. Stanley Williams, Annual Reviewof Physical Chemistry 45 (1994) 401

<div style="text-align: right;">**Chapter 7**</div>

On the Evolution of Surface Roughness Induced Magnetic Properties by Swift Heavy ion Irradiation on Co-Fe-Si Thin Films.

Work discussed in this chapter is under minor revision in the Journal of Magnetism and Magnetic Material.

7.1   Introduction

The increasing demand for miniaturisation of devices has fuelled intense research in fields of magnetic thin films owing to their applications in sensors, actuators, magnetic read write heads and MEMS [1-2]. A precise understanding of the magnetic evolution of thin magnetic films is essential for tailor making films for applications in diverse fields ranging from sensors to magnetic storage [3]. Co-Fe is one such widely studied soft magnetic material with potential applications in various fields. Co-Fe thin films are usually prepared on different seed layers to reduce coercivity [4-5]. M. Vopsaroiua *et. al.* reported the dependence of coercivity on grain size for 20 nm Co-Fe thin films prepared by sputtering. They observed a reduction in coercivity from 120 Oe for samples with a mean grain size larger than 17 nm down to 12 Oe for a sample with a mean grain size of 7.2 nm [6]. A detailed literature survey reveals that Co-Fe films can be made soft magnetic by depositing an under layer or upper layer of an ultra thin oxide layer [4-6].

It is also interesting to probe the magnetic properties of thin films of Co-Fe containing silicon, which is usually an alloying element used to prepare Co-Fe based metallic glasses. Also thin magnetic films assume importance in light of the ever increasing demand for miniaturisation of devices. The magnetic properties of thin films generally deviate from their bulk counterparts due to the increased surface area and consequently the surface morphology. Surface structures contributing to the roughness of films can quantitatively influence the magnetic properties. For example the presence of mound and valleys can act as pinning sites for domains thereby increasing the roughness. In addition, bulk and surface magnetic properties can differ appreciably due to the influence of surface morphology in determining magnetic properties. VSM measurements can extract the bulk magnetic properties of the thin films, whereas MOKE can be used to probe the surface specific magnetic properties. In the case of magnetic thin films, a relatively rough surface, with roughness of the order of nm, can be

prepared by vacuum evaporation. The film being rough, offers an ideal template to investigate the influence of roughness on magnetic properties. However, to elucidate the relationship between magnetic properties and roughness, it is imperative to tailor the roughness by suitable means. Annealing as well as irradiation with SHI can be used to alter the surface morphology. Thus there is ample scope for investigating the evolution of magnetic properties with changes in surface morphology of Co-Fe-Si thin films.

In the SHI process an energetic ion passing through a solid loose energy by two main mechanisms viz. nuclear energy loss and electronic energy loss. Seitz and Koehler in 1956 [7] proposed the Thermal spike model to explain the energy loss mechanism of swift heavy ions in a solid by suggesting the possibility of the existence of high energy electrons along the ion track in the wake of ion passage. The incoming ions is assumed to transfer energy to the electron clouds in a time scale less than 10^{-17} s, resulting in a region of hot electrons surrounded by a relatively unaffected cold lattice. The excited electrons achieve thermodynamic equilibrium in a short time span and transfer energy to the lattice via electron-phonon coupling. The temperature along the ion path can sometimes exceed the melting temperature of the material (depending on the energy of the ion and the target atom) and create ion tracks in the target [8-9]. This process is the main mechanism of material modification in metals and metallic alloys where the electron density is quite high.

AFM is a very powerful tool for probing the surface morphology of thin films. In this work all AFM images have a resolution of 512×512 pixels. The r.m.s roughness (Rθ)as defined in equation 7.1 parameterizes the surface roughness in to a single value and express the variation of the surface height function $h(r,t)$ over a two dimensional surface with linear size L

$$R\theta = \sqrt{\frac{1}{L^2}\sum\left(h(r,t)-\bar{h}(t)\right)^2}$$ 7.1

Where, r refers to the point where the height function is measured. The

average height is given by the expression $\bar{h}(t) = \frac{1}{L^2}\sum h(r,t)$. Even though this function gives an idea about the surface roughness it fails to account for surface morphological features like long wavelength and short wavelength periodicities. The same can be extracted by evaluating the square root of the square of the Fourier expansion of the surface spatial features. The resulting values are called Power Spectral Density (PSD) which is an expression that decomposes the surface profile into the r.m.s. amplitude of the components of the Fourier expansion of the AFM spatial image. In two dimensions the PSD is expressed as [9-10] $PSD(k) = \frac{1}{L}\left|\frac{1}{2\pi}\int h(r)e^{-ikr}dr\right|^2$, where $r = r(x,y)$ refers to the position over which the height is measured, k is the spatial frequency, $k = k(k_x, k_y)$ with wave vector $k = \frac{2\pi}{\lambda}$.

Recently we have reported the effect of SHI on the surface morphology and magnetic properties of Fe-Ni thin films [11,12] , wherein the variation of magnetic properties with ion fluence was correlated with the variation in surface morphology upon irradiation. In this work, thin films of Co-Fe-Si on float glass substrates were prepared by vacuum evaporation and they were subsequently subjected to SHI at different fluences. The films were deposited from a composite target and in order to obtain the exact compositional information of the films, they were subjected to XPS analysis before and after sputtering with Ar ions. The depth profiling was carried out using SIMS analysis. The evolution of magnetic properties with surface morphology was studied using AFM, VSM and MOKE and the results are correlated.

Surface morphology investigated using AFM revealed randomly distributed surface structures in pristine films, possibly resulting from the nonlinear evaporation of alloying components. On irradiation with SHI, the surface roughness initially decreases and thereafter when the fluence increases the

roughness also follows suit. The coercivity of films was found to progressively increase with fluence. The observed difference between the bulk and surface magnetisations are attributed to the presence of surface oxide layer of thickness <6 nm on the surface. The variation in surface magnetic properties correlates well with the surface morphology revealing the interrelation of surface morphology and surface magnetic properties.

7.2   Experimental

7.2.1   Thin Film Preparation

Thin films with a nominal composition of $Co_{65}Fe_{31}Si_{0.4}$ and thickness of 55 nm was vacuum evaporated using tungsten filaments on to chemically and ultrasonically cleaned glass substrates from a composite target. The chamber pressure before deposition was $1x10^{-6}$ mbar, which increased to $3x10^{-5}$ mbar during deposition. The as-deposited Co-Fe-Si based metallic glass films were annealed at 673 K for 1 hour. Annealing was performed at $4x10^{-5}$ mbar for minimizing surface oxidation. The preparation details are cited in chapter 5.

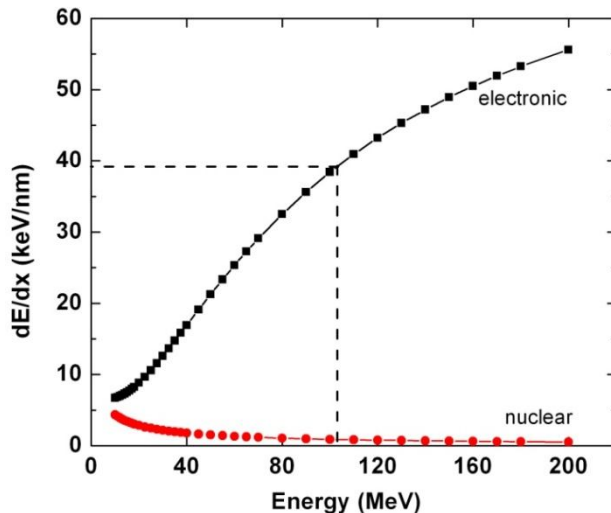### 7.2.2   Swift heavy ion irradiation

Figure 7.1: SRIM simulation showing electronic and nuclear energy loss versus ion energy. Dashed line shows the electronic energy loss corresponding to 100 MeV ion energy.

As deposited films were irradiated with 100 MeV Au^{7+} ions at the 15 UD Pelletron accelerator at IUAC, New Delhi, India. The irradiations were performed at 0° angle of incidence with respect to the surface normal. The ion beam was raster scanned on the sample surface by a magnetic scanner to maintain a uniform ion flux throughout the film. The samples were irradiated with SHI with fluences of 1×10^{11}, 1×10^{12} and 1×10^{13} ions/cm^2. The irradiated sample area was 1 cm^2. The energy regime for SHI irradiation was selected after simulation using Stopping and Range of Ions in Matter (SRIM)code [13]. For the chosen ion energy of 100 MeV, the lateral straggling is 5.87 μm, longitudinal straggling was 4.62 μm and the penetration depth was 6.98 μm. This value of penetration depth was two orders of magnitude greater than the thickness of the film. The energy of the Ag^{7+} beams (100 MeV) was selected with a view to avoiding ion implantations.

In this energy range a maximum electronic loss of 39 keV/nm will be transferred to the target system (see TRIM simulation results shown in Figure. 7.1).

7.2.3   Characterization

The XRD pattern of all samples were recorded using an X-ray diffractometer (Rigaku D-max-C) using Cu Kα radiation (λ=1.5414 Å). The average particle size was estimated from the measured width of the diffraction curves using the Debye Scherer formula, $D = \left(\dfrac{0.9\lambda}{\beta\cos\theta}\right)$ where β is full width at half maximum (FWHM) in radians, D the average grain size and θ the diffracting angle. The surface topography of all thin films were analysed using an AFM (Digital Instruments Nanoscope (V). The AFM images were analysed using surface data analysis software Nanoscope 7.2 (Vecco Scientific Ltd) to obtain PSD, roughness and depth analysis. TEM measurements were performed on a 200 kV Philips CM 20 FEG TEM. X-ray Photoelectron Spectroscopy (XPS) study of the thin films were carried out using an Omicron Nanotechnology XPS system with a monochromatic Al Kα radiation (hν= 1486.6 eV) of source

voltage 15 kV and emission current of 20 mA. All scans were carried out in an ultrahigh vacuum of 2×10^{-10} mbar. The elemental composition of the sample is extracted from the wide scan while the individual element peaks were analysed to obtain the chemical composition. As charging effects are unavoidable in the XPS study of thin films deposited on non conducting samples, charge compensation was performed by electron gun flooding. The obtained XPS spectra were deconvoluted using Casa XPS program (Casa Software Ltd, UK) in which the background was simulated using the Shirley/Touguard function and the peaks were fitted using a Gaussian Lorentzian function. The spectra recorded were corrected using the binding energy of adventitious carbon at 284.6eV and the accuracy of the measured binding energy values is estimated to be equal to $\pm$ 0.2eV. The composition analysis of the film was performed using Hiden Analytical SIMS Workstation using oxygen ion beam at 2 keV, 100 nA at a pressure of 8×10^{-8} Torr.

7.3   Results and Discussion

7.3.1   Surface Composition Analysis

The same thin film discussed in chapter 5 is used for the irradiation study. The XPS scan of the pristine sample bore signature peaks of cobalt, iron, small percentage of silicon and a small percentage of boron. The wide scan shows a peak of oxygen suggesting the existence of possible native oxide of Co, Fe or Si on the film surface. Quantification of XPS spectra in Figure 5.1 shows that the surface is composed of 43.84 wt. % Co, 24.50 wt. % Fe, 1.36 wt. % Si, 3.6 wt. % B and 26.70 wt. % O. However, to rule out the possibility of oxygen existing as an adsorbent on the film surface, XPS spectrum of the film (5.1) is recorded after the films were sputtered by Argon ions with energy 3keV for 30 minutes. Quantification of the spectrum gives a compositional profile of 64.64 wt. % Co, 30.60 wt. % Fe, 0.34 wt. % Si, 0.02 wt. % B & 4.40 wt. % O. These values can be taken as an estimate of the profile values for the entire thickness of thin films. Further from XPS and SIMS (figure 5.1 – 5.7) analysis it is found that the oxide

layer have an approximate thickness of <6nm.

7.3.2   Structural Analysis

7.3.2.a Films Deposited on glass substrates

The GXRD pattern of the pristine sample shows a broad peak at 44.32^o indicating the amorphous nature of the film. This is unexpected since $Co_{100-x}Fe_x$ alloys are thoroughly researched and reported to be crystalline in the entire composition range. Our result can be explained by assuming that the films are composed of small nanocrystalline grains dispersed in an amorphous matrix [14]. SHI irradiation on as-deposited films with fluences ranging from 1×10^{11} ions/cm^2 to 1×10^{13} ions/cm^2 did not produce any noticeable changes in the XRD pattern
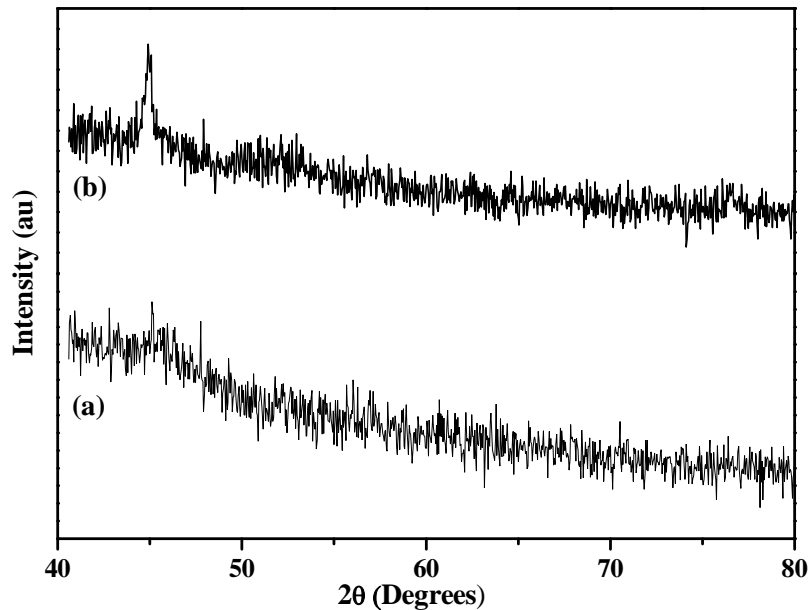

Figure 7.2: GXRD pattern of thin film deposited on glass substrate (a) pristine (b) annealed at 400ºC

176

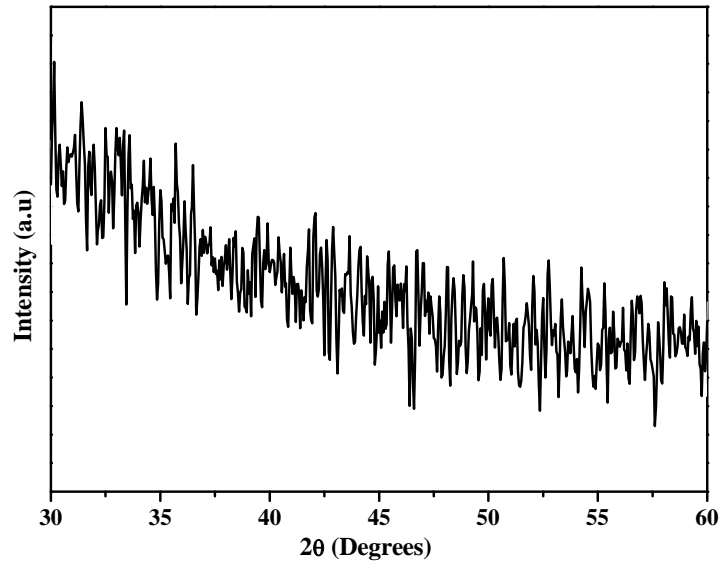**7.3.2.b Film deposited on silicon substrates**

Figure 7.3: GXRD pattern of thin film deposited on silicon substrate (a) pristine (b) annealed at 400ºC

The above figure shows the XRD pattern of film deposited on silicon substrates. The absence of any well defined peak suggests the amorphous nature of the deposited material. A small broad peak masked by the noise is visible near $2\theta=44^0$, which is a signature of the short range ordering in the film.

7.3.3   Surface analysis

When a collimated beam of low/high energy ions impinges on a surface, the morphology of the surface gets altered due to various factors. Interesting patterns e.g. hillock like structure can be produced by tuning the ion energy and incidence angle [15]. The ion induced surface evolution is usually modelled using the instability theory proposed by Bradley and Hooper [16] The surface evolution is a competition between the ion induced sputtering and adatom diffusion. Ion induced sputtering occurs when an atom gains enough energy from the thermal spike, resulting from the ion passage, to eject itself from the surface. However, if the energy gained is low the atom may overcome the energy barrier to translate

177

along the surface resulting in diffusion of atoms. The dominance of one mechanism over other is governed by a number of factors like the material, composition, crystallinity, ion energy thermal diffusivity etc.
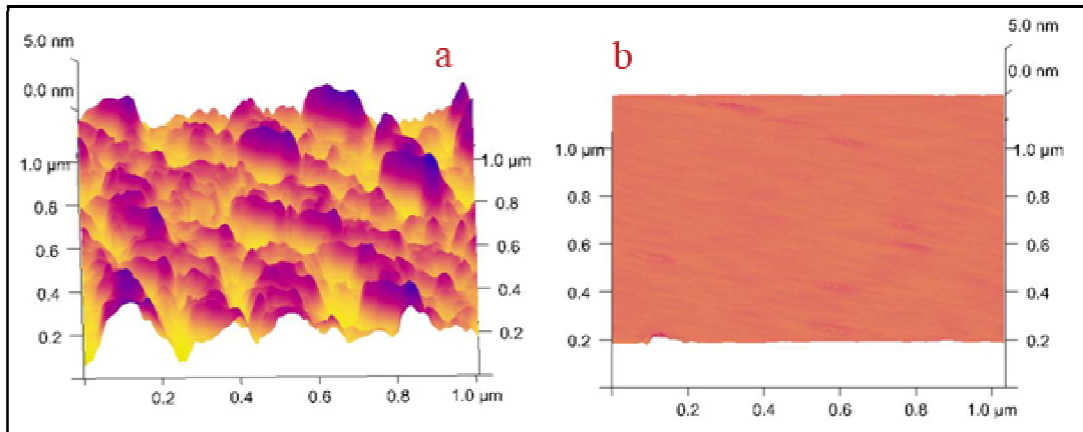

Figure 7.4: AFM image of a) glass substrate b) silicon substrate

The above images show the 3d AFM images of glass substrates as well as silicon substrates. From the above figure it is clear that the silicon surface is much smoother than the glass substrates. The silicon substrate has and R_q and R_a value of 0.92 1nd 0.25 nm where as the glass substrates exhibits R_q and R_a values of 1.07 and 0.845 respectively. Consequently one expects the films deposited on silicon substrates to have less roughness than the films deposited on glass substrates.

The 3D AFM images of the as deposited film on glass substrates (Fig. 7.5) show small structures suggesting island like growth mode of the films. The as deposited film is rough with a R_q 8.97 nm and R_a 5.68 nm. Large lateral structures of sizes ranging from ~290 nm to 90 nm can be seen scattered over the film surface. From AFM images shown in Figure 7.5(b)-7.5(d), it is evident that irradiation of the as deposited films, with 100 MeV Au^{7+} ions, changes the surface morphology. At 1×10^{11} ions/cm^2, smoothing of the mesoscopic hill–like structures take place. Then, at 1×10^{12} ions/cm^2, new surface structures are created.
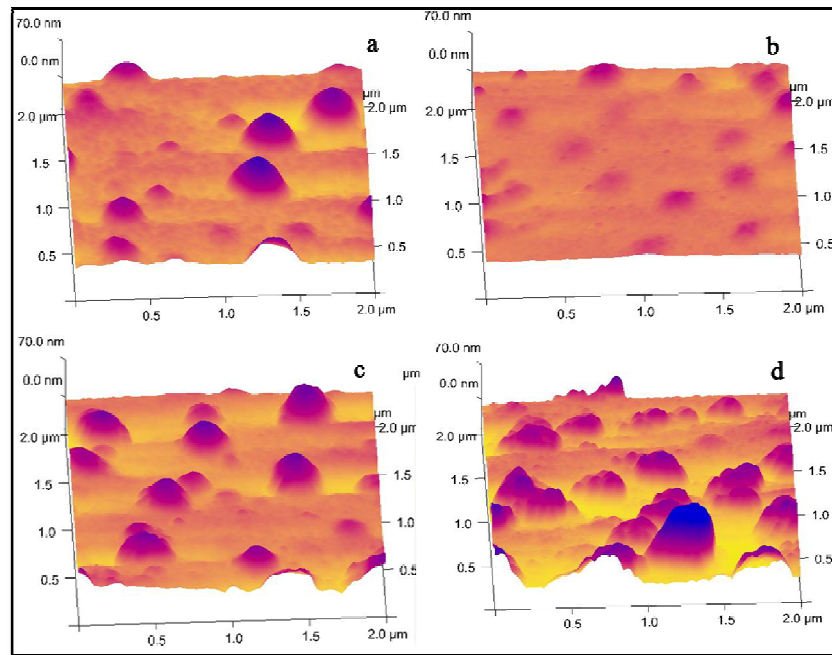
Figure 7.5: AFM images of thin films deposited on glass substrates (a) pristine (b) irradiated with fluence 1x10^{11} ions/cm^2(c) 1x10^{12} ions/cm^2 (d) 1x10^{13} ions/cm^2.

When the fluence is further increased to 1×10^{13} ions/cm^2, an increase in surface roughness is observed. When the film deposited on glass substrates is subjected to SHI at a fluence of 1x10^{11} ions/cm^2 the surface roughness decreases from 8.97 nm, 5.68 nm (R_q, R_a) to 3.47 nm, 2.34 nm (R_q, R_a) where as when the films deposited on silicon substrates were subjected to the same fluence the surface roughness decreases from 6.60 nm, 4.19 nm (R_q, R_a) to 1.69 nm, 1.13 nm (R_q, R_a) respectively. The decrease in surface roughness with ion fluence of 1x10^{11} ions /cm^2 suggests the existence of a surface smoothening process. This is because of the result of irradiation induced viscous flow, volume diffusion, or surface diffusion which can all result in smoothening of the surface. Mayr and Averback [17] also observed surface smoothening in ion irradiated films. They modelled the smoothening process using stochastic rate equations for the evolution of the surface in Fourier space and have attributed the smoothening process to irradiation induced viscous flow.
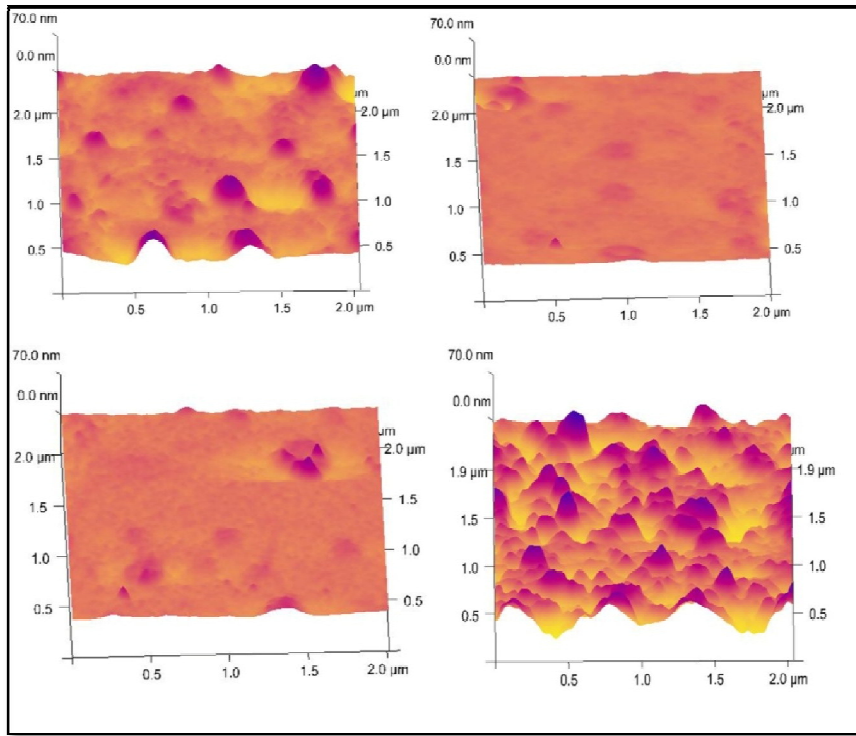
Figure 7.6: AFM images of thin films deposited on silicon substrates (a) pristine (b) irradiated with fluence 1x10^{11} ions/cm^2(c) 1x10^{12} ions/cm^2 (d) 1x10^{13} ions/cm^2.

Vauth and Mayr reported experimental and simulation results on Ion bombardment induced smoothening of amorphous metallic rough Zr$_{65}$Al$_{7.5}$Cu$_{27.5}$ thin films prepared using vacuum evaporation [18]. They compared the experimental results with a model incorporating stochastic rate equations of the Langevin type in combination with classical molecular dynamics simulations to simulate the surface smoothening across length and time scales. Their model effectively illustrates the role of ion induced viscous flow in irradiation induced surface smoothening in metallic glass films [18]. Goswami and Dev [19] observed a surface smoothening in silicon surfaces irradiated by a 2MeV Si$^+$ ion beam. According to them, the collision cascade resulting from ion-solid interactions will result in target atoms gaining energy and in some cases enough energy to eject out from the target (sputtering). However, if the component of the energy gained by the atom perpendicular to the surface is less than the surface binding energy,

180

the atom can effectively drift along the surface creating an adatom. Narayan *et.al.* also observed surface smoothening in $Co_{69}B_{12}Si_{12}Fe_4Mo_2Ni_1$ ribbons irradiated with 260 MeV (Ag) and 130 MeV (Si) ions and attributed the smoothening to shear induced viscous elastic flow [20].

On irradiating, the film deposited on glass with an ion fluence of $1x10^{12}$ ions/cm^2 the surface roughness increases to 9.59 nm, 6.68 nm (R_q, R_a) and at a fluence $1x10^{12}$ ions/cm^2 the surface roughness further increases to 16.9 nm, 11.9 nm. The samples deposited on silicon substrates when irradiated with an ion fluence of $1x10^{12}$ ions/cm^2 the surface roughness increases to 2.27 nm, 1.45 nm (R_q, R_a) and at a fluence $1x10^{13}$ ions/cm^2 the surface roughness further increases to 10.8 nm, 8.18 nm respectively. These results are consistent with the recent observations made by us in Fe-Ni thin films [11,12].
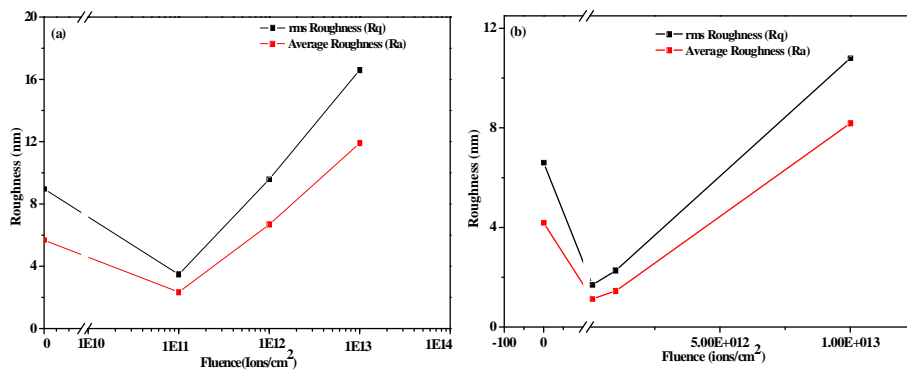
Figure 7.7: Variation of surface roughness with ion fluence for the thin film deposited on a) glass substrates b) silicon substrates.

The variation of surface roughness with ion fluence is shown in Figure 7.7. Recently Gupta *et. al.* observed similar variation of surface roughness in Fe/Bi bilayer system irradiated with 120 MeV Au ions. They observed smoothening of the surface with initial fluence and subsequent roughening at higher fluences and explained the results based on the positive heat of mixing of the elements which prevents interdiffusion across the interface during the thermal spike [21].

To investigate the possible mechanisms of surface smoothening at low

fluences and roughening at higher fluences the AFM images of the films were subjected to power spectral density analysis.

Figure 7.8: 2D ISO Power spectral density plots extracted from the AFM Images of thin films (a) pristine irradiated with fluence of (b) 1x10^{11} ions/cm^2(c) 1x10^{12} ions/cm^2 and (d) 1x10^{13} ions/cm^2.

The log-log plot of PSD (figure. 7.8) shows two regions separated by a cross over region. The high frequency region corresponds to the correlated surface features and the low frequen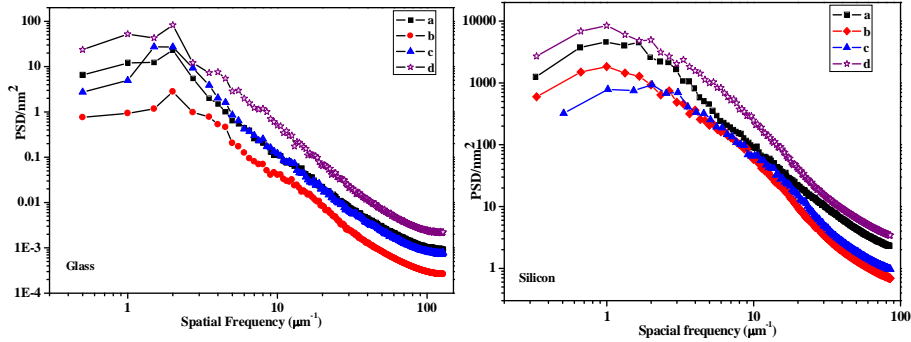cy regions correspond to uncorrelated white noise. The transition corresponds to the critical length scale below which the surface features are no longer correlated. The PSD curves of the pristine as well as irradiated films shows the same characteristic features consisting of a power law roll over in the high spatial frequency region and a low frequency region separated by a small cross over region. The slope of the PSD curve is related to the kinetics of surface evolution and hence can suggest the predominant mechanism affecting the surface morphology. The variation in the slope of the high frequency region of the PSD curve is shown in figure 7.9. Following a linear dimensional analysis, Herring has shown that 2, 3, and 4 represents four modes of surface transport viz. viscous flow, evaporation–condensation, volume diffusion, and surface diffusion, respectively [22-24]. In this study the slope values obtained for all the films are between 2 and 3.
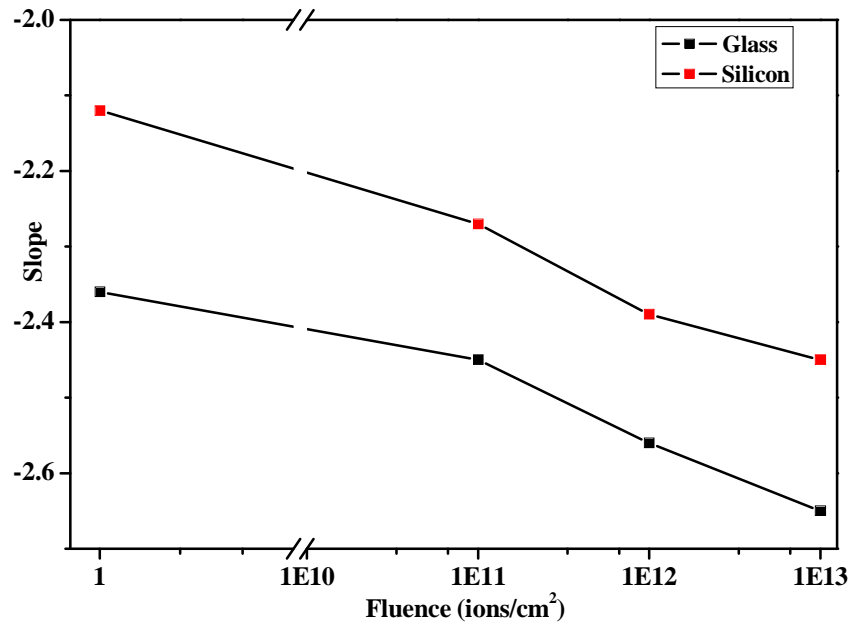
Figure 7.9: Variation of slope of power spectral density with ion fluence.

Following the arguments of Herring and Mullins the dominant surface transport mechanism seems to be a combination of evaporation, re-condensation and volume diffusion. For the film irradiated at a fluence of 1×10^{11} ions/cm^2 the dominant surface transport mechanism is evaporation - condensation and this explains the surface smoothening observed at that fluence. However, as the fluence increases to 1×10^{12} ions/cm^2 and still higher fluences of 1×10^{13} ions/cm^2, the dominant mechanism becomes volume diffusion or diffusion of adatoms. This explains the roughening observed in the films at these fluences. The drifting atoms choose to cling to the edges of prominent morphological features. The power law roll off has a typical exponent between 2.35 to 2.65 for samples deposited on glass and 2.1 to 2.45 for samples deposited on silicon substrates and is suggestive of the weak nonlinearity associated with ion irradiation effects [25].

The roughness exponent   is related to the negative of the slope of PSD curve by the relation $\alpha = \frac{\delta - 2}{2}$. For the pristine as well as films irradiated at 1×10^{10} ions/cm^2, 1×10^{12} ions/cm^2 and 1×10^{13} ions/cm^2 the α values obtained are 0.18, 0.23, 0.28 and 0.33 for glass substrates and 0.06, 0.14, 0.2, 0.23   for silicon

183

substrates respectively. Eklund *et.al.* reported α values between 0.2-0.4 consistent with the predictions of Kadar Parisi Zhang (KPZ) equation for the case of cleaved graphite sputtered with 5 keV argon ions [25]. From a quick look at the values of that roughness exponent it is clear that α increases with irradiation fluence. However, the roughness exponent (α) may not be be considered equivalent to surface roughness. According to Krim *et.al.* an increase in roughness exponent may or may not imply actual increase in surface roughness and hence it could only be considered as a term that quantifies how roughness changes with length scale [26]. In conjunction with the AFM images we conjecture that the increase in the value of α with irradiation fluence actually reflect the increase in surface roughness with fluence.

7.3.4 Magnetic Studies

As evidenced from the compositional analysis using XPS, the films had an ultrathin layer of oxide of cobalt, iron and silicon on its surface (*for detailed discussion see chapter 5).* However, considering the thickness of the sample (54nm) the oxide layer thickness is very small. This small layer can give distinctively different results for the surface and bulk magnetisation of the films. The penetration depth of light is estimated to be <10 nm in metals [27]. Hence it can be expected that the MOKE signals carries magnetic polarisation information from the oxide layer as well as the Co-Fe-Si underlayer. According to Bader, if the magnetic film over a nonmagnetic substrate is significantly thinner than the penetration depth of light, it is said to be ultrathin, and the entire film thickness is probed [28]. Extending this idea further, we assume that as the film thickness is more than one order of magnitude larger than the oxide layer thickness the dominant contribution to MOKE signal will be from the majority Co-Fe-Si film. However the small contribution from the oxide layer towards coercivity cannot be ruled out. Platt *et.al.* reported a coercivity of 12Oe for CoFe film deposited on CoO [5]. They showed that domain walls in the soft films have a relatively large mobility in response to changing magnetic fields below the nominal H_c. They also

attributed the observed low coercivity values to the averaging of the high anisotropy energy [5]. Vopsaroiua *et.al.* reported the dependence of coercivity on grain size for 20 nm Co-Fe thin films prepared by sputtering. They observed a reduction in the coercivity from 120 Oe for samples with a mean grain size larger than 17 nm down to 12 Oe for a sample with a mean grain size of 7.2 nm [6].
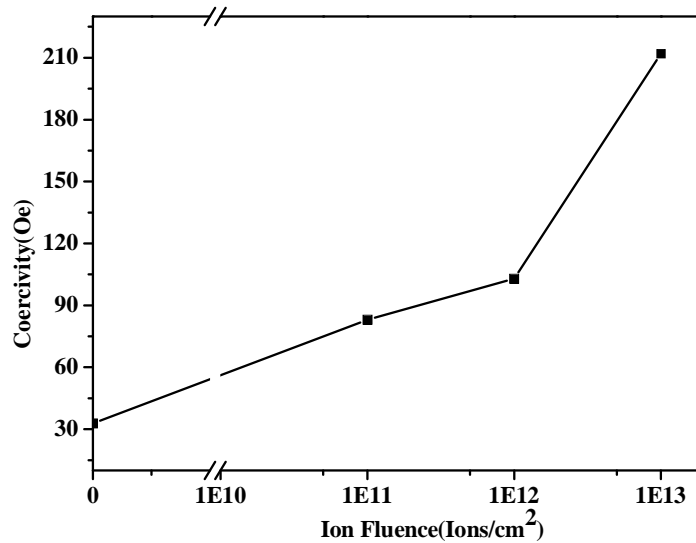
Figure 7.10: Variation of coercivity measured using MOKE as a function of irradiation fluence.

The low coercivity as measured by MOKE (figure 7.10) can be explained by the low film thickness and the presence of an ultra thin oxide layer similar to the results reported by Platt *et.al.* and Vopsaroiua*et.al.* [5, 6]. On the other hand VSM measures the bulk coercivity and the stress existing in the substrate sample interface might have contributed to the bulk coercivity. As the film is irradiated with a fluence of 1×10^{11} ions/cm^2, the coercivity measured by MOKE increases to 83Oe. The reason might be the disorder induced in the oxide layer by ions. The coercivity keeps on increasing from 100 Oe to 212 Oe as the films were irradiated with fluences of 1×10^{12} and 1×10^{13}ions/cm^2. The disorder induced in the oxide layer can increase the roughness. Further one should note that the roughness of the films were also increasing at these fluences, thereby creating new pinning sites, increasing the coercivity. The MOKE loop of the as prepared

185

film have a squareness ratio of 0.62 and as the film is irradiated with fluences $1x10^{11}$ions/cm^2, $1x10^{12}$ions/cm^2 and $1x10^{13}$ions/cm^2 the ratio changes to 0.76, 0.8 and 0.86 respectively. This enhancement in squareness ratio towards 1 is a typical feature when the exchange interaction starts to dominate the inherent anisotropies [29].
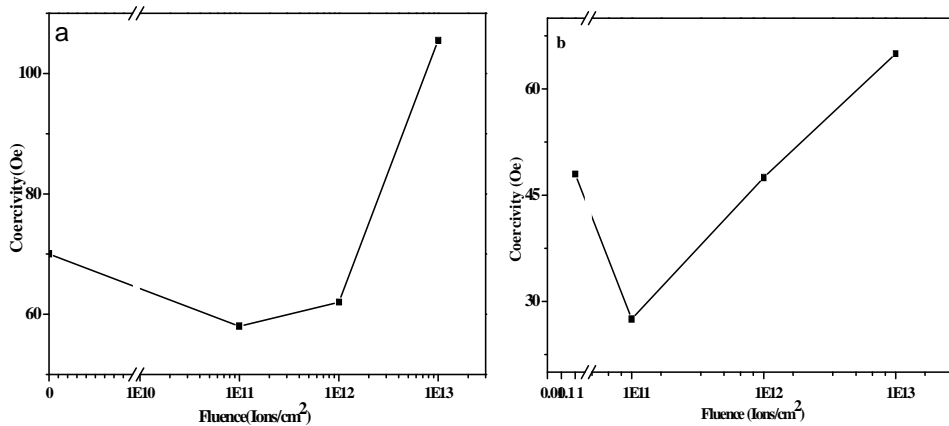
Figure 7.11: Variation of bulk coercivity measured using VSM as a function of irradiation fluence for films on a) glass and b) silicon substrates

The VSM loops of pristine films show coercivity (Fig.7.11a & b) of 70 Oe and 48 Oe for the films deposited on glass and silicon substrates respectively. The as prepared films are amorphous and rough providing surface pinning states for the magnetisation vectors of Co-Fe. As the films are irradiated with SHI, the energetic ions cause local atomic rearrangements resulting in local annealing effects and subsequent stress relief. This might be the reason for remanence enhancement observed in MOKE measurements. Also the energetic ions will cause disorder in the native oxide layer, reducing the available surface pinning sites. As the films are irradiated with fluence $1x10^{11}$ ions/cm^2 the surface coercivity at first shows a sharp decrease from 70 Oe to 58 Oe and 48 Oe to 27.5 Oe for the films deposited on glass and silicon substrates. This can be explained on the basis of the apparent decrease in r.m.s roughness of the irradiated film from 8.27 nm to 3.47 nm and 6.6 to 1.69 for samples deposited on glass and

silicon substrate respectively. The smoothening of the surface will evidently reduce the surface pinning sites for pinning of domain walls. The large coercivity of 70 Oe and 48 Oe in the pristine film also arises from the large number of pinning sites existing in the film, a fact which is evident from the AFM images and the r.m.s roughness of 8.27 nm and 6.6 nm corresponding to samples on glass and silicon substrates

The surface as well as bulk magnetisations of thin films are intricately related to the surface roughness. In amorphous films the domain walls are free to move and the magnetisation reversal mechanism is primarily dictated by domain wall motion. This process requires very low energy and consequently the hysteresis loops exhibits very low coercivity and large squareness ratio. The magnetisation loops generally show a switching type magnetisation reversal. Further, the loops get saturated at low fields. However, when the surface of thin films becomes rough then there is a possibility by which the domains can get pinned at positions of hillocks and valleys. These types of domains require greater energy to align along the field directions and further they move by the rotation of the domain. Loops from these types of materials require large applied fields to align them along the field direction. The hysteresis loops of as prepared films do not get saturated even at the highest applied field, suggesting the possibility of pinning sites. However as the film is irradiated with fluence 1×10^{11}ions/cm^2 the surface smoothens and the coercivity reduces. Further, the loops saturate at low fields suggesting a decrease in number of pinning sites.

Swift heavy ion induced stress relaxation also contributes to the reduction in coercivity [30]. When the films are irradiated at higher fluences (1×10^{12} ions/cm^2 and 1×10^{13}ions/cm^2) the roughness increases and hysteresis follows suit showing a progressively increasing coercivity. Kac *et. al.* recently observed a similar decrease in roughness at fluence 4×10^{11}ions/cm^2 and also an increase in squareness ratio with ion fluence in swift iodine ion irradiated in Fe/Cr bilayers [31]. They attributed it to the decrease in the fraction of antiferromagnetic

coupling in the bilayers. Hence we conjecture that SHI irradiation results in apparent reduction in the oxide upper layer and surface pinning sites. This is evidenced by the relative increase in the squareness ratio and decrease in coercivity with fluence [31]. Srivastava also reported an increase in the coercivity with irradiation fluence in Fe/Ni multilayers and attributed it to the increased concentration of defects after irradiation, which may act as pinning centres for domain wall motion [32]. Senoy *et.al.* made similar observations in Fe-Ni film and correlated the increase in coercivity with fluence to the corresponding increase in surface roughness [12].

7.4   Conclusions

Co-Fe-Si thin films of thickness 54 nm were vacuum evaporated to float glass and silicon substrates, respectively and subsequently subjected to SHI irradiation at fluences ranging from 1×10^{11} to 1×10^{13} ions/cm^2. The AFM images show randomly distributed surface features in the pristine film (both glass and silicon) itself resulting from the nonlinear evaporation of alloying components. On SHI irradiation the roughness initially decreases. Thereafter, when the fluence is increased to 1×10^{12} and 1×10^{13} ions/cm^2 with higher fluence the roughness increases. The slope of the power spectral density shows more or less linear behaviour. From the slope of the PSD the surface smoothening at 1×10^{11} ions/cm^2 can be attributed to evaporation-condensation and the roughening at 1×10^{12} and 1×10^{13} ions/cm^2 to adatom diffusion. The roughness exponents show progressively increasing values with increasing fluence suggesting roughening of the sample surface with fluence. The coercivity of thin films deposited on glass substrates measured by MOKE show a small decrease at fluence 1×10^{11} ions/cm^2 and thereafter the coercivity progressively increases with fluence. From the bulk magnetisation values measured by VSM it can be observed that the coercivity progressively increases with fluence. The observed difference between the bulk and surface magnetisations were attributed to the presence of the surface oxide layer of thickness <6nm nm. The variation in surface magnetic properties

correlates well with the surface morphology, further reiterating the effect of surface morphology on magnetic properties.

References

1.   F. Yongqing, D. Hejun, H. Weimin, Z. Sam, H. Min, Sensors and Actuators A: Physical 112, (2004) 395.

2. A.Spaldin Nicola, Magnetic Materials: Fundamentals and Applications, 2nd Edition, University of California, Santa Barbara, 2010.

3. J. K. Howard, Journal of Vaccum Science and Technology A 4, (1986)1.

4. T. Thomson, P. C. Riedi, C. L. Platt, A. E. Berkowitz, IEEE Transactions on Magnetics 34 (1998) 1045.

5. C. L. Platt, A. E. Berkowitz, D. J. Smith, M. R. McCartney, Journal of Applied Physics 88 (2000) 2058.

6. M. Vopsaroiu, M. Georgiev, P. J. Grundy, G. Vallejo Fernandez, S. Manzoor, M. J. Thwaites, K. O'Grady, Journal of Applied Physics 97 (2005) 10N303.

7. F. Seitz, J. S. Koehler, Solid State Physics2 (1956) 307.

8. E. Kuzmann, S. Stichleutner, K. Havancsák, M. R. El-Sharif, C. U. Chisholm, O. Doyle, V. Skuratov, K. Kellner, Gy. Dóra, Z. Homonnay, A. Vértes, Radiation Physics and Chemistry 75 (2006) 741.

9. A. Meftah , J. M. Costantini, M. Djebara, N. Khalfaoui, J. P. Stoquert, F. Studer, M. Toulemonde, Nuclear Instruments and Methods in Physics Research Section B: Beam Interactions with Materials and Atoms 122 (1997) 470.

10. A. Dolatshahi-Pirouz, M. B. Hovgaard, K. Rechendorff, J. Chevallier, M. Foss, F. Besenbacher, Physical Review B :Condensed matter and materials Physics 77 (2008) 115427.

11. Hysen Thomas, Senoy Thomas, R. V. Ramanujan, D.K. Avasthi, I.A. Al- Omari, Salim Al-Harthi, M.R. Anantharaman, Nuclear Instruments and Methods in Physics Research Section B: Beam Interactions with Materials and Atoms 287 (2012) 85.

12. Senoy Thomas, Hysen Thomas, D. K. Avasthi, A. Tripathi, R. V. Ramanujan, M. R. Anantharaman, Journal of Applied Physics 105

(2009) 033910.

13. J. F. Ziegler, J. P. Biersack, U. Littmark, The stopping and range of ions in solids, Pergamon, Oxford, 2003.

14. R. Sharif, S. Shamaila, M. Ma, L.D. Yao, R.C. Yu, X.F. Hana,Yong Wang, M. Khaleeq-ur-Rahman, Journal of Magnetism and Magnetic Materials 320 (2008) 1512.

15. S. Facsko,T. Dekorsy,C. Koerdt, C. Trappe, H. Kurz, A. Vogt and H. L. Hartnagel, Science 285 (1999) 1551.

16. R. M. Bradley, J. M. E. Harper, Journal of Vacuum Science and Technology 6 (1988) 2390.

17. S. G. Mayr, R. S. Averback, Physical Review Letters 87 (2001) 196106.

18. Sebastian Vauth, S. G. Mayr, Physical Review B : Condensed matter and materials Physics 77 (2008) 155406.

19. D. K. Goswami, B. N. Dev, Physical Review B : Condensed matter and materials Physics 68 (2003) 033401.

20. H. Narayan, H.M. Agrawal, R.P.S. Kushwaha, D. Kanjilal, S.K. Sharma, Nuclear Instruments and Methods in Physics Research Section B: Beam Interactions with Materials and Atoms 156 (1999) 217.

21. Ajay Gupta, R. S. Chauhan, D. C. Agarwal, S. Kumar, S. A. Khan, A. Tripathi, D. Kabiraj, S. Mohapatra, T. Som, D. K. Avasthi, Journal of Physics D: Applied Physics 41 (2008) 215306.

22. C. Herring,Journal of Applied Physics 21 (1950) 301.

23. William W. Mullins, Journal of Applied Physics 30 (1959) 77.

24. P. Dash, P. Mallick, H. Rath, A. Tripathi, Jai Prakash, D. K. Avasthi, S. Mazumder, S. Varma, P. V. Satyam, N. C. Mishra, Applied Surface Science 256(2009) 558.

25. E. A. Eklund, E. J. Snyder, R. Stanley Williams, Surface Science 285 (1993) 157.

26. J. Krim and J. O. Indekeu, Physical Review E: statistical, nonlinear and soft matter physics 48 (1993) 1576.

27. H. Oguchi, A. Zambano, M. Yu, J. Hattrick-Simpers, D. Banerjee, Y. Liu, Z. L. Wang, J. P. Liu, S. E. Lofland, D. Josell, I. Takeuchi, Journal

of Applied Physics 105 (2009) 023912.

28. S. D. Bader, Surface Science 500 (2002) 172.

29. G. Herzer; Journal of Magnetism and Magnetic Materials 294 (2005) 99.

30. RanuDubey, Ajay Gupta, Pooja Sharma, Nora Darowski, G. Schumacher, Journal of Magnetism and Magnetic Materials 310 (2007) 2491.

31. M. Kac, J. Z_Ukrowski, M. Toulemonde, R. Kruk, V. Tokman, A. Polit, Y. Zabila, A. Dobrowolska, O. Synashenko, M. Marszałek, Nuclear Instruments and Methods in Physics Research Section B: Beam Interactions with Materials and Atoms 267 (2009) 925.

32. S. K. Srivastava Ravi Kumar, A. Gupta, R. S. Patel, A. K. Majumdar, D. K.Avasthi, Nuclear Instruments and Methods in Physics Research Section B: Beam Interactions with Materials and Atoms 243 (2006) 304.

Chapter 8

Oblique Angle Deposition of Co-Fe-Si Thin Films for Tailoring Surface Roughness and Coercivity.

8.1 Introduction

Soft magnetic materials are nowadays increasingly sought after for application in various devices ranging from large electromagnets to NEMS/MEMS/ systems. For electromagnets bulk metallic glass ribbons offer an ideal choice owing to their low core loss and very low coercivity coupled with large permeabilities and inductions. However for NEMS/MEMS systems the soft magnetic films have to be realised in thin film form. A variety of techniques like sputtering, pulsed laser deposition, electron beam evaporation, thermal evaporation and other methods can be employed to prepare thin films. Co-Fe-Si thin films could easily be deposited on glass or silicon substrates by thermal evaporation. For certain applications, it is very much advantageous to use nano-sculptured films. Photolithography, ion beam mixing and other techniques could be used to realise the same. However, they are very much expensive, complicated and requires highly sophisticated machineries. Oblique angle deposition using physical vapour deposition offer a cheaper alternative for realising nano-sculptured thin films[1]. The vapour atoms impinging on the target will preferentially nucleate on surface irregularities and during growth will shadow the region behind it. This will result in the gradual growth of some columns leading to columnar microstructure. The resulting surface morphology is the competition between surface diffusion driven smoothening and shadowing driven surface roughening. The films generated by this type of process are usually self affine obeying certain scaling relations. One disadvantage of this technique is that since the nuclei are nucleated on surface features, which are randomly oriented, the distribution of nano-columns will be random. The same could be avoided by patterned substrates for depositing thin films.

To illustrate the technique of oblique angle deposition, consider a beam of collimated vapour beam impinging on a substrate at an incidence angle θ. If the vapour flux is denoted by V, then it will have components $V\cos\theta$ along the horizontal direction and $V\sin\theta$ along the vertical direction. $V\cos\theta$ is the term

responsible for shadowing effects. During the initial stages, some nuclei will be nucleated on surface features and as the time increases the tallest nuclei grows. As it grows in size the columns below it will be devoid of vapour flux due to its shadow. This process is termed shadowing effect. The height of the column has an effect on the shadowing distance. As the height increases the shadowing distance increases. During deposition at a particular angle the term $V_{\parallel}$ remains constant leading to a nano-columnar film with tilt angle β. The tilt angle β is different from the oblique angle θ and both are related by the relation $tan(\beta) = \frac{1}{2} tan(\theta)$ for small θ or the cosine rule $\beta = \theta - arcsin\left(\frac{1-cos(\theta)}{2}\right)$

Thin films deposited by oblique angle deposition are generally porous with nanostructures whose number, orientation and tilt angle depends on the oblique angle and deposition conditions. In the past years, significant work has been done on the oblique angle deposition of metallic thin films. A detailed understanding regarding the relationship between the surface morphology resulting from oblique angle deposition and magnetic properties is very essential for tailoring these materials for various applications.

In this work oblique angle deposition of Co-Fe-Si thin films and the relationship between the surface morphology on the magnetic properties is investigated as a function of deposition angle.

8.2 Experimental

Thin films were vacuum evaporated in 10^{-6} Torr using tungsten filaments, on chemically and ultrasonically cleaned glass from a composite target with composition corresponding to $Co_{69}Fe_4Ni_1Mo_2B_{12}Si_{12}$. The films were deposited at oblique angle geometry at angles 0, 45, 55, 65 and 75^0. The angles refer to the angle between the vapour beam direction and the substrate surface normal. In order to prepare nano-columnar structures by oblique angle deposition at different deposition angles, a substrate holder is designed with provisions for 5 projected portions whose surface normal were oriented at 5 different angles (45°,

55º, 65º, 75º and 85º) to the vertical normal. Each projected portions are 1cm apart and are fixed to a flat horizontal plate.
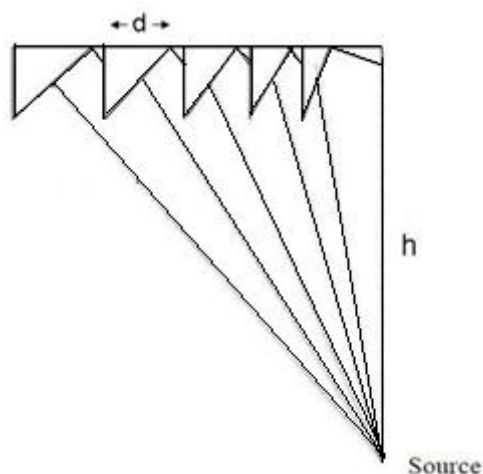

Figure 8.1: Geometry of oblique angle deposition process

Glancing angle X-ray diffraction (GXRD) measurements were carried out on the pristine samples to investigate their crystalline nature. XPS study of thin films deposited on float glass substrates were done with an Omicron Nanotechnology XPS system with a monochromatic Al Kα radiation (hν= 1486.6 eV) of source voltage 15 kV and emission current of 20 mA. All scans were carried out at ultrahigh vacuum of 2×10^{-10} mbar. The elemental composition of the sample is extracted from the wide scan while the individual element peaks were analyzed to obtain the chemical composition. As charging effects are unavoidable in the XPS study of thin films deposited on non conducting samples, charge compensation was performed by electron gun flooding. The nanoscale imaging presented were performed using atomic force microscopy (AFM) obtained in tapping mode using ultra high resolution cantilevers made of tungsten having radius of less than 1 nm and force constant of 46 N/m. Room temperature magnetization measurements were carried out using vibrating sample magnetometer (VSM) (DMS 1660 VSM) with field varying from −1 to +1 kOe

196

8.3 Results and Discussion

8.3.1   Composition analysis

The XPS wide scan of the as prepared thin films, as shown in figure 8.2a, clearly shows the presence of Cobalt, Iron, a small percentage of Silicon and Boron. The unavoidable adventitious carbon is also detected which is utilized to calibrate the XPS scan by assuming the carbon peak position at 284.6 eV.
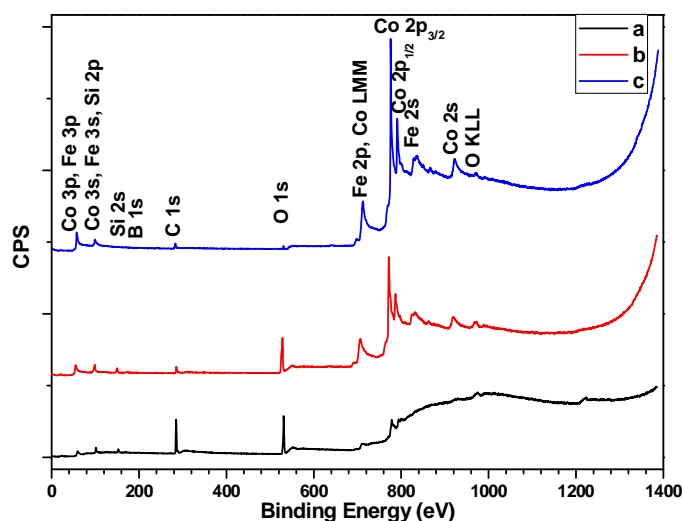

Figure 8.2: XPS wide scan of a) as prepared Co-Fe-Si film b) after sputtering with 4keV Ar⁺ ions for 15 minutes c) further sputtering for 15 minutes.

The wide scan also shows the presence of oxygen from metal oxygen bond suggesting possible native oxide formation on film surface. The wide scan also exhibits auger electron peaks of O KLL and Co LMM. This is possible since the surface is not passivated by deposition of Au or Pt. The quantification of the spectra in figure 8.2.a gives ~30 wt% Co ~10 wt% Fe ~60 Wt% Si and a very small percentage of Boron. XPS spectra of a film sputtered for 15 minutes with 4keV Ar ions at a pressure of 10^{-6} mbar shows 58 wt. % Co, 18 wt. % Fe, 24 wt. % Si. Further sputtering by Ar ions for 15 minutes gives 75 wt% Co 20 wt% Fe and 5 Wt % Si and these values can be estimated as an estimate of the profile values. This assumption is further corroborated by the fact that the percentage of oxygen is the lowest for the film sputtered by argon ions for 30 minutes.

197

8.3.2   Structural Analysis

The GXRD pattern of the unannealed sample shows a broad peak at 44° indicating the amorphous nature of the film. This result can be explained by assuming that the film is composed of small nanocrystalline clusters dispersed in an amorphous matrix [2].
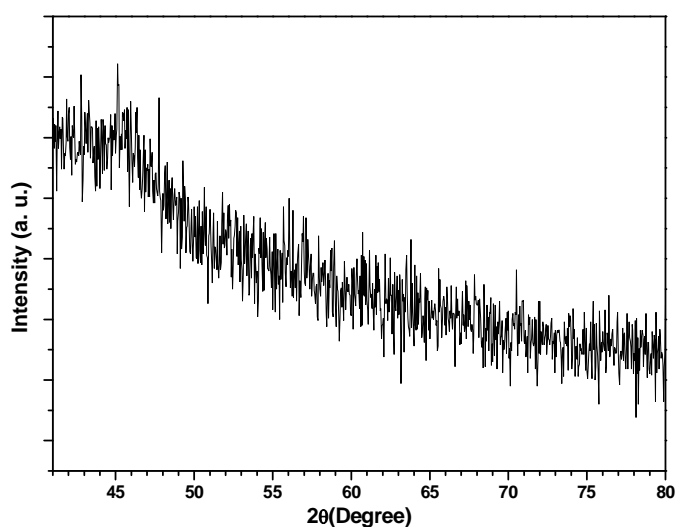

Figure 8.3: GXRD Pattern of Thin film

8.3.3   Surface Morphology Analysis

From the AFM images shown in figure 8.4, it is evident that oblique angle deposition has resulted in the growth of nanostructures. The growth favours island like growth due to the geometry of deposition process. The growth of nanostructures by vapour deposition is essentially a competition between self shadowing and adatom diffusion leading to surface smoothening. As the deposition process progress, the space in between the voids will fill up due to adatom diffusion leading to a layer plus island growth mode. The SEM images shown in figure 8.5 further corroborate this assertion. The analysis of the AFM images shows that the rms as well as average roughness progressively increases with deposition angle. This is possible since oblique angle deposition is known to lead to porous films and the porosity increases with deposition angle [3]. The

198

films deposited at normal incidence of the vapour beam at the substrate surface have an rms (Rq) and average roughness (Ra) of 3.4 ± 0.34 & 1.76 ± 0.18 respectively. However the film deposited at angles 45^0, 55^0, 65^0 and 75^0 have roughness values of 5.22 ± 0.52 & 3.25 ± 0.33, 5.84 ± 0.58 & 4.01 ± 0.40, 7.23 ± 0.72 & 5.15 ± 0.52, 7.65 ± 0.77 & 5.88 ± 0.59 respectively.
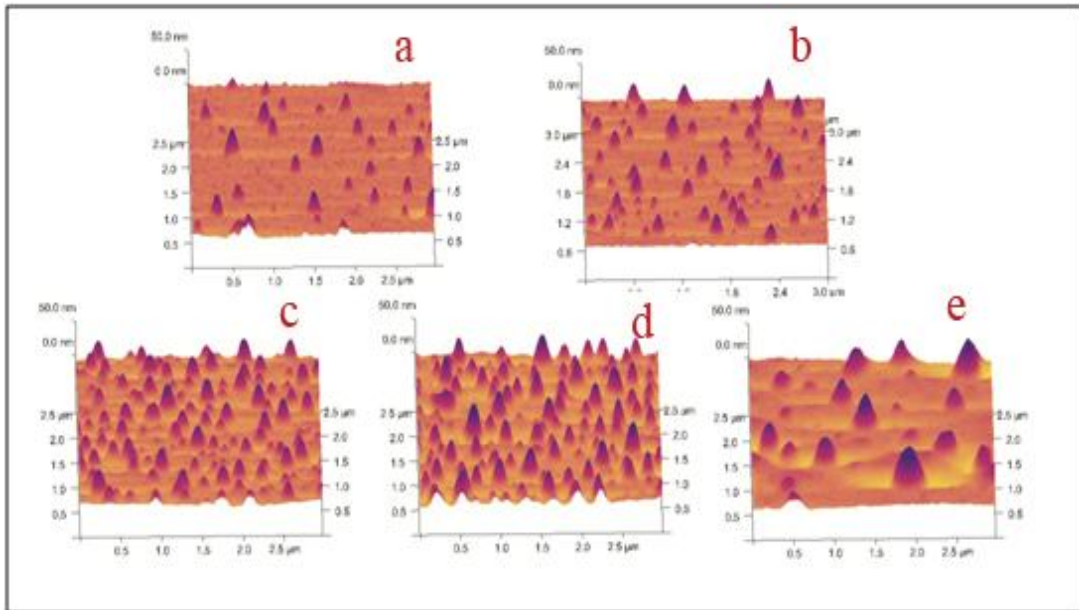
Figure 8.4: AFM Images of Co-Fe-Si thin films deposited at different oblique angles a)0^0 b) 45^0 c) 55^0 d) 65^0 e) 75^0.
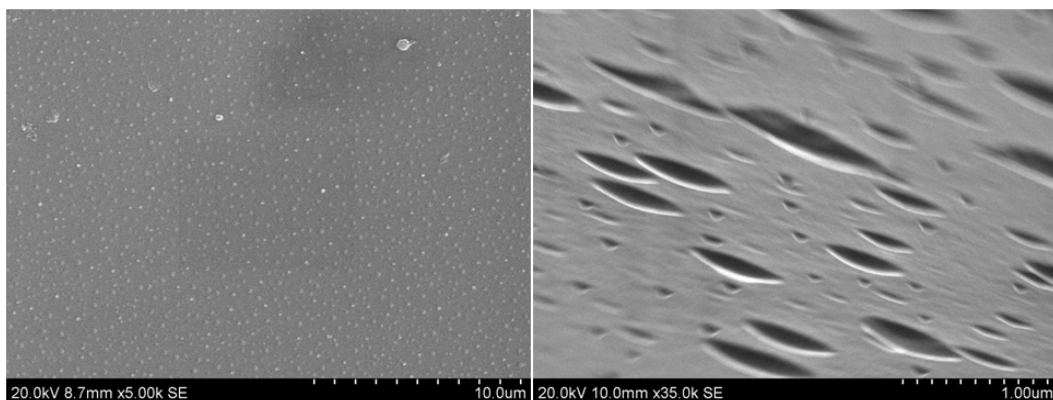
Figure 8.5: SEM images of thin film deposited at an angle 75^0.
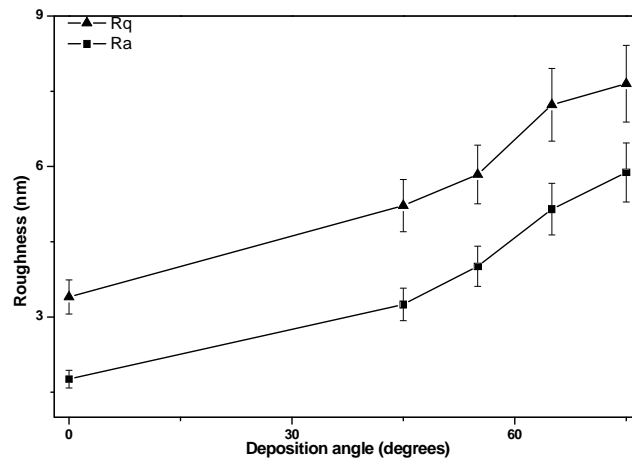
Figure 8.6: Variation of surface roughness with oblique angle.

Some nanostructures are visible in the thin film deposited at angle 0^0. Initially the nanostructures evolve from random nuclei nucleated on the surface.. As the deposition angle increases, the number of nuclei also increase resulting in more number of columns per deposited area. At higher deposition angles especially at 65^0 and 75^0 the surface smoothening due to adatom diffusion is also visible since the sizes of the nanostructures grow with angle.

Figure 8.7: Power spectral density plots of the thin films deposited at various oblique angle.

2D PSD were done on the AFM images to obtain information regarding periodicity of the surface structures. Figure 8.7 shows the log log plots of the PSD as a function of spatial frequency.

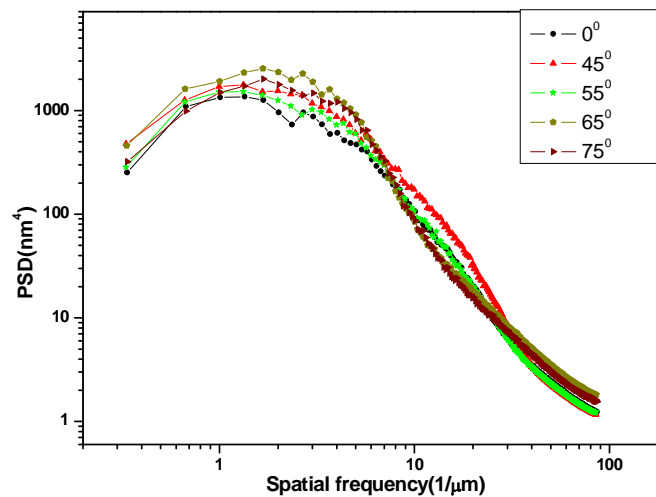The plot can be divided into two regions with the high frequency part obeying a power law roll off $\sim k^{-\delta}$ where k is the frequency and δ is the power. Fitting the high frequency part of the PSD spectrum with a straight line gives d values of   2.3, 2.51, 2.92, 3.04 and 3.14 respectively for the samples deposited at angles 0, 45, 55, 65 and 75 degrees. The d values are related to the roughness exponent by the relation $\alpha = \frac{\delta - d}{2}$. Here the scan dimension d=2,and hence the above equation yields roughness exponents of 0.15, 0.26, 0.46, 0.52, 0.57 for films deposited at angles 0, 45, 55, 65 and 75 degrees respectively. There are reports that surface diffusion effects resulting in surface smoothening will lower the exponents, whereas self shadowing will increase the roughness and result in higher values of roughness exponents [4]. The increase of the roughness exponents indicate that as the angle of deposition increases, the shadowing becomes more and more prominent leading to less surface diffusion effects. Island like structures are visible in the SEM images further corroborating the results of the AFM investigations.

The large surface features shadow a nearby region beneath it. All of the incident atoms that approach this region are captured by the taller surface object thereby resulting in further growth of the surface features. This is similar to the growth of islands by surface diffusion. In this growth mode the island will have a capture radius so that all impinging atoms falling within the area defined by the capture radius will become part of the island. The lateral distance shadowed by a surface object plays a similar role as the capturing length of an island in diffusion driven growth of islands. The capturing radius due to the shadowing increases with the height of the surface feature and for oblique angle deposition this shadowing length is $L_s = h_s \tan \theta$ where h is the height of the surface feature. Due to the randomness during deposition and film growth, some surface

columns can grow higher than the nearby ones and they get additional flux by the increase in shadowing length. As the thickness increases, this can give rise to a competition of columns that can lead to a reduction of the number of surviving columns. This can explain the large sizes of nanocoloumns observed for thin film deposited at 75^0.

8.3.4   Depth Analysis

Figure 8.8 shows the peak depth versus deposition angle plot for the samples deposited at various angles. From the figure 8.8 it is clear that the peak depth remains almost the same up to a deposition angle of 45^0 and thereafter increases with deposition angle. This also reiterates the fact that as the shadowing angle is larger and larger (nearing 90) the shadowing will lead to deeper valleys. This will lead to larger peak depth for samples deposited at higher oblique angles ($(45^0 < \theta > 90^0)$ films.
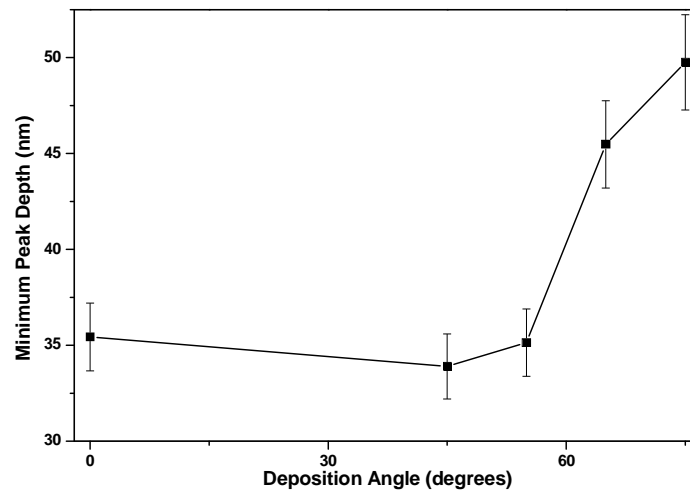

Figure 8.8: Minimum Peak depth versus deposition angle.

This is reiterated by the fact that the as deposited film has only peak depth of 35 nm resulting from the island plus layer growth mode whereas the oblique angle deposited film at 75^0 has peak depth of 49.7 nm.

8.3.5   Magnetic Properties-VSM

The VSM images of the samples deposited at various angles is shown in figure 8.9.The film deposited at normal incidence has a saturation magnetisation of 834 emu/cc. Conversion to emu/g is difficult since it would require accurate estimation of the porosity of the films. The films saturate at very low fields of 206 Oe and exhibit a low coercivity of 64 Oe. The magnetisation reversal is basically a switching type behaviour and also considering the magnetisation reversal along the out of plane direction suggests that the easy axis lies along the in plane directions. The film growth mode is primarily island plus layer mode and hence the as deposited film have thin layer of Co-Fe-Si with some local nano-coloumns. Hence they exhibit low coercivity along the in plane directions. The films deposited at 45° also exhibit a switching type magnetisation reversal with coercivity of 60 Oe. This is possible because of the fact that the as deposited and 45^0 deposited samples have similar number of nanostructures. However when the film is deposited at 55^0 the magnetisation exhibits a domain rotation in addition to magnetisation switching. This is possible since the 55^0 sample surface consists of a layer plus island mode with large number of nano-coloumns over the surface.

Also the size of the nano-coloumns increases. Shape anisotropy of the nano-columns could be the possible reason for the increased anisotropy exhibited by this sample, which means that, when the film surface have some dominant nano-coloumns, the magnetisation in the columns will prefer to stay along its length. Hence it will require some large fields to rotate the magnetisations in these domains to in plane direction and this might be the reason for the inclination of the magnetisation curve before saturation observed in samples deposited at and above 55^0. The 55^0 and 65^0 samples show similar behaviours. However as the films are deposited at higher and higher angles the total saturation magnetisation decreases progressively. This is possible since as the angle of incidence increases the possibility of scattering of impinging atoms

increases. Also there are existing reports that as the deposition angle increases the porosity of the films increases [5].
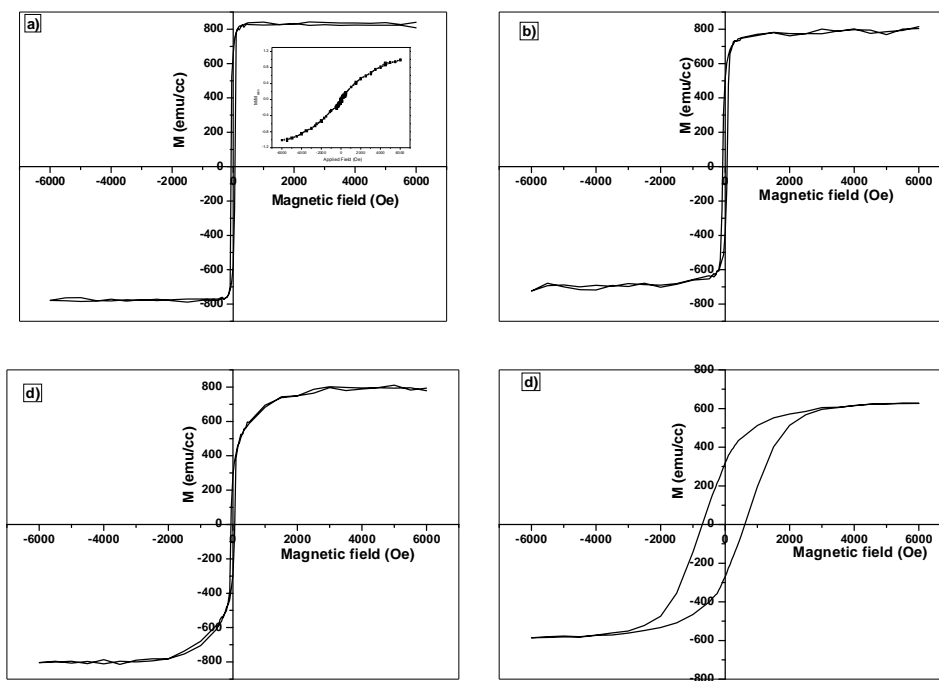

Figure 8.9: MH loops of films deposited at angles (a) 0° (b) 45° (c) 55° (d) 75°

8.4 Conclusions

In conclusion, Co-Fe-Si based amorphous structured thin films were grown on glass substrates by oblique angle deposition. The films were grown at oblique angles of 0^0, 45^0, 55^0, 65^0, and 75^0. AFM was used to investigate the surface morphology evolution with deposition at various deposition angles. Surface scaling analysis through roughness and PSD spectra showed that as the deposition angle increases, the growth mechanism is dominated by self shadowing. This situation resulted in the lateral growth of nanostructures at higher deposition angles. From an application point of view the method is promising since it offers a low cost method for tailoring the anisotropy of magnetic thin films. A precise control over the anisotropy direction could be obtained by depositing thin films on patterned substrates combined with substrate rotation.

References

[1]   B.S. Geoffrey, Proc. SPIE 4806 (2002) 207.

[2]   R. Sharif, S. Shamaila, M. Ma, L.D. Yao, R.C. Yu, X.F. Han, Y. Wang, M. Khaleeq-ur-Rahman, Journal of Magnetism and Magnetic Materials 320 (2008) 1512.

[3]   S. Vauth, C. Streng, S. Mayr, K. Samwer, Physical Review B 68 (2003) 205425.

[4]   J. Xu, L. Yu, I. Kojima, Journal of Applied Physics 94 (2003) 6827.

[5]   D.J. Poxson, F.W. Mont, M.F. Schubert, J.K. Kim, E.F. Schubert, Applied Physics Letters 93 (2008) 101914.

Chapter 9

Summary and Scope for Future Work

Magnetic amorphous alloys represent a new class of materials artificially synthesized by various techniques, and nowadays used for many technological applications ranging from golf rackets to implants in human body. Nanocrystalline alloys are a spinoff of amorphous alloys wherein the structure consists of finely dispersed nanocrystalline grains dispersed in an amorphous matrix. They became popular within a short period of time since the discovery of FINEMET alloy by Yozhizawa, Oguma and Yamauchi in 1988. The material is reported to have excellent permeability and very good soft magnetic properties. With the growing global concern for miniaturization of devices several researchers started to materialize thin film magnetic devices for various applications. In the past several attempts were reported in the literature using low tech techniques like thermal evaporation to hi-tech techniques like CVD. This has resulted in the application of thin film magnetic materials to various devices. However when a bulk material is transformed to thin film form many issues related with exchange correlation, grain size variation of coercivity, and dependence of surface morphology on magnetic properties etc needs to be addressed. This study was an attempt to answer such questions and this chapter reminiscence and concludes whether the proposed objectives have been achieved and what can be further done in this area.

Magnetic properties of nano-crystalline soft magnetic alloys have usually been correlated to the structural evolution with heat treatment. However, the literature is less abundant with reports pertaining to the study of nano-crystalline thin films. Thin films of Fe-Ni were deposited on glass substrates from a composite target of composition $Fe_{40}Ni_{38}B_{18}Mo_4$ under a high vacuum of $\approx 10^{-6}$ Torr by employing resistive heating. They were annealed at various temperatures

207

ranging from 373 – 673 K based on the DSC studies carried out on the film material. Thin film samples annealed at 473 K show very low coercivity and large saturation magnetization suggesting that the critical condition predicted by Herzer model is attained at this temperature. The XRD, TEM and SAED of thin films annealed at 473 K shows that Fe-Ni nanostructures are embedded in the residual boron containing amorphous phase. From DSC, XRD and TEM images it can be inferred that the crystallization temperature of the as prepared films are lower than their bulk counterparts. Also there is a progressive decrese of coercivity up to 473 K, which is an indication of the lowering of nano-crystallization temperature in thin films. The variation of coercivity with the structural evolution of the thin films with annealing is discussed and a plausible explanation is provided using the modified random anisotropy model.

Co-Fe-Si based films exhibit high magnetic moments and is highly sought after for applications like soft under layers in perpendicular recording media to magneto electro mechanical sensor applications. Thin films of Co-Fe-Si annealed at different temperatures and the effect of annealing on structural, morphological and magnetic properties were investigated. As prepared Co-Fe-Si thin films were found to have a native oxide layer on its surface. Annealed thin films were found to behave according to the Herzer model, except for the 400°C annealed sample. The samples annealed at 400°C have crystals with mean size greater than the exchange length; hence possess large coercivity due to the absence of exchange averaging. The angular dependence of coercivity from in plane to out of plane direction probed using VSM showed that the dominant magnetization reversal mechanism is domain wall unpinning in accordance with the modified Kondorsky model. The MOKE measurements provide further evidence for domain wall pinning by showing a reverse trend compared to the VSM data. The bulk and surface magnetic properties were found to be different owing to the presence of a thin oxide layer on the film surface.

Considering the prospects of fabricating thin films based on Fe-Ni from

metallic glass ribbons by simple vacuum evaporation techniques and the fact that amorphous alloys are not resistant to irradiation induced damages, a detailed investigation for probing the surface modification of amorphous thin films of Fe-Ni-B by SHI irradiation was undertaken. Fe-Ni-B based metallic glass thin films were prepared by thermal evaporation. The films annealed at 673 K showed more crystallinity than the as-deposited films. The as-deposited and annealed films were subjected to SHI irradiation at various fluences and their structural and morphological properties were investigated. The absence of any observable change in the XRD of as-deposited films with ion beam irradiation was attributed to the fact that the as-deposited films were already with a short range atomic order and the ion irradiation is stabilizing this short range order. For samples annealed at 673 K, upon irradiation, a significant reduction in grain size with ion fluence is observed. The grain fragmentation during ion beam irradiation is attributed to the strain transferred to the crystallites by the electronic energy loss. The irradiation of the sample rapidly changes the surface topography, first at 3×10^{11} ions/cm^2 smoothing of the mesoscopic hill–like structures, and then at 3×10^{12} ions/cm^2, creation of surface structures and at still higher doses of 3×10^{13} ions/cm^2 an increase in the roughness is observed. Volume diffusion was identified as the prominent surface smoothening mechanism at lower ion fluences and at higher fluences surface roughening was observed. Further investigations regarding the interplay between surface morphology and magnetic properties in these thin films are going on and there exists ample scope for probing the evolution of surface morphologies with magnetic properties in the case of magnetic films.

Co-Fe-Si thin films of thickness 54 nm were also vacuum evaporated to float glass and silicon substrates respectively and subsequently subjected to SHI irradiation at fluences ranging from 1×10^{11} to 1×10^{13}ions/cm^2. The AFM images show randomly distributed surface features in the pristine film (both glass and silicon) itself resulting from the nonlinear evaporation of alloying components.

On SHI irradiation the roughness initially decreases. Thereafter when the fluence is increased to 1×10^{12} and 1×10^{13}ions/cm^2 with higher fluence the roughness increases. The slope of the power spectral density shows more or less linear behaviour. From the slope of the PSD, the surface smoothening at 1×10^{11} ions/cm^2 can be attributed to evaporation-condensation and the roughening at 1×10^{12} and 1×10^{13} ions/cm^2 to adatom diffusion. The roughness exponents show progressively increasing values with increasing fluence suggesting roughening of the sample surface with fluence. The coercivity of thin films deposited on glass substrates measured by MOKE show a small decrease at fluence 1×10^{11} ions/cm^2 and thereafter the coercivity progressively increases with fluence. From the bulk magnetisation values measured by VSM it can be observed that the coercivity progressively increases with fluence. The observed difference between the bulk and surface magnetisations were attributed to the presence of the surface oxide layer of thickness <6nm.

The growth of nanostructures of amorphous magnetic materials by employing simple and cost effective methods is a hot topic of research and hence an alternative method starting from ribbon precursors was thought to be a viable one. In the present work a simple, cost effective and low technology technique was employed for creating soft magnetic nanostructures on thin films with a view to alter their magnetic anisotropies to tailor their magnetic properties. Fe-Ni based amorphous nano columns were grown on glass substrates by oblique angle deposition. Co-Fe-Si based amorphous structured thin films were grown on glass substrates by oblique angle deposition. The films were grown at oblique angles of 0^0, 45^0, 55^0, 65^0, and 75^0. AFM was used to investigate the surface morphology evolution with deposition at various deposition angles. Surface scaling analysis through roughness and PSD spectra showed that as the deposition angle increases, the growth mechanism is dominated by self shadowing. This situation resulted in the lateral growth of nanostructures at higher deposition angles. From an application point of view the method is promising since it offers a low cost

method for tailoring the anisotropy of magnetic thin films. A precise control over the anisotropy direction could be obtained by depositing thin films on patterned substrates combined with substrate rotation

In metallic glasses heat treatments produce profound changes in the microstructure of the materials and often results in a nanocrystalline material from an amorphous precursor. Also the nature of growth, size, dimension of growth and crystal structure affects the magneto-crystalline anisotropy, exchange interaction and thereby the magnetic properties of the material. Hence from the application point of view in addition to estimating activation energy, it is very important to probe the crystal growth mechanism. Kolmogorow Johnson Mehl Avarami (KJMA) equation is widely used for modeling the crystallization dynamics in metallic glasses. Using this model the three kinetic parameters viz, activation energy of crystallization, Avarami exponent and frequency factor could be successfully estimated. However, this is possible only if the system satisfies the fundamental assumptions made by the theory. If the system does not follow the KJMA kinetics then one should find a satisfactory model to describe the crystallization dynamics of the system. The kinetics of crystallization of $Fe_{40}Ni_{38}B_{18}Mo_4$ bulk amorphous alloy is investigated using isokinetic, isoconversion and model free isoconversion methods. The kinetic triplets estimated using the various models were compared and analysed. From the comparison of the prominent mathematical models used for estimating the kinetic triplets it can be concluded that isoconversional methods are superior in estimating the local activation energies, whereas isokinetic methods are superior in estimating the crystallization dynamics of the system. Also it is established that the variation of coercivity with grain size in Fe-Ni-Mo-B alloys follows the Herzer model.
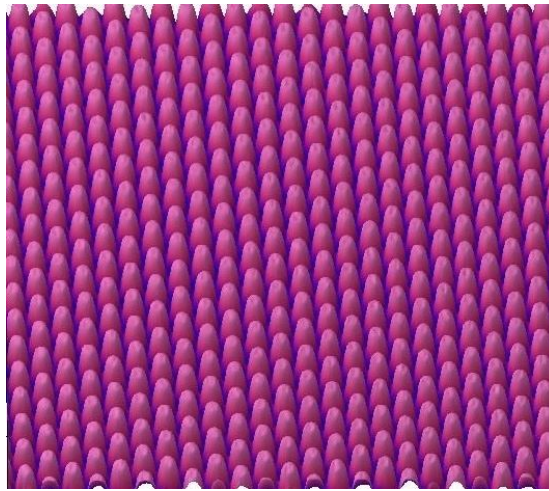
Figure 9.1: Patterned Silicon Substrates

The studies on columnar thin film preparation by OAD indicates that OAD on a patterned substrate can result in well separated nano columns which can be promising for future high density recording applications. Preliminary studies have already been carried out in this respect which can be extended to the future. The technique of OAD was successfully utilized for growing nano columns on glass and silicon substrates; however, there was no control over the inter-columnar separation or the height of the columnar structures. Patterned substrates (figure 9.1) with appropriately designed nanostructures can be used as templates for growing the nanostructures. Also when the substrate is kept at rest the nanostructures will grow in a slanted fashion. This can be avoided if the substrate is given a slow rotation with respect to a line going through the source and substrate. The rotation, speed direction, oblique angle and deposition rate will all affect the morphology of resulting nanostructures.

Since Fe-Ni-B are used for sensor applications due to their large magneto elastic effect there are ample scope for fabricating a thin film sensor utilizing the change in magneto elastic property of thin films with strain and loading. Since these films show good soft magnetic properties they could possibly be used as sensing layers in tunnel magneto resistance devices. One of the major problems while using thermal evaporation is the change in stoichiometry of film from the

212

target composition. This could be reduced to some extent by using flash evaporation. But if one is too much inclined to maintain stoichiometry then PLD is a good technique for realizing that goal. Multiple target sputtering (Fe,Ni, Mo and B) can also give the required stoichiometry, but it is a complicated process and one should do a lot of preliminary work to optimize the deposition conditions.

From this investigation it was found that Fe or Co based films, when exposed to ambient atmosphere, will form a thin oxide layer on top of it. It was found that this oxide layer can influence the magnetic properties of films beneath it. To investigate the exact magnetic properties of thin films one could utilize the penetration depth of laser in solid. Typically the penetration depth of laser used for in-situ measurement of MOKE is <10 nm. Hence while in-situ depositing a nonmagnetic material viz, Ag/Au/Cu, on the Fe-Ni-B or Co-Fe-Si thin film exposed to atmosphere, one could probe the surface magnetic properties of the upper layer from 10 nm beneath to the top layer. When there is no silver deposition the signal is from the oxide layer (>6nm) and the layer beneath it. When the silver layer thickness approaches the MOKE signal will be primarily from the top of the oxide layer. This oxide layer could be avoided by coating the film with a thin layer of Au (2nm) after the deposition of the magnetic layer.

Though this thesis took a look at the microstructure, morphology and magnetism related issues which are of fundamental in nature, not much could be gathered on the nature of interactions taking place on the surface. For example, the kind of studies that can be focussed on these amorphous alloys in the future may be the actual role of native oxide layer in changing the surface spins to behave in ways different than the atoms in the bulk.

<div style="text-align: right;">**Appendix A**</div>

Evaluation of Kinetic Triplets and the Evolution of Magnetic Properties with Micro-Structural Transformations in and Fe based Metallic Glass.

A.1 Introduction

A.2 Experimental Methods

A.3 Results and Discussion

A.4 Conclusions

.

A.1   Introduction

Recently there is renewed interest in metallic glasses due to their potential applications in soft magnetic devices [1]. The presence of short-range order combined with the absence of crystal defects such as grain boundaries and dislocations make them cheap alternatives for various applications. Metallic glasses are usually synthesized by rapid quenching techniques with cooling rates often exceeding 10^6 K/s. They can also be synthesized by viz, melt quenching, splat cooling, laser glazing, electro-deposition, ion implantation, swift heavy ion irradiation, and vapour deposition [2]. Synthesis of nano-crystalline materials, derived from amorphous metallic glasses through thermal treatments, have opened up new vistas for tailoring the properties of these classes of materials [3,4]. The extreme magnetic softness exhibited by many of these amorphous and nanocrystalline alloys can be attributed to the averaging of anisotropies over grains and the counterpoise between exchange correlation length and grain size. They exhibit ferromagnetism characterized by high saturation magnetization, vanishing macroscopic anisotropy, negligible magnetostriction and large magnetic permeability [3]. $Fe_{40}Ni_{38}B_{18}Mo_4$ is one such alloy that is widely used for sensor and soft magnetic applications. Boron and Molybdenum were added to Fe and Ni to improve the glass forming ability, increase thermal stability and to impede grain growth. The material is reported to have two-stage crystallization as is usually the case with most Fe based metallic glasses [5]. Its softness after nanocrystallization can be ascribed to its two phase nature consisting of an ultra-fine grained Fe-Ni phase embedded in the remaining boron rich amorphous matrix. The two phases has Curie temperatures of $\approx$ 760 K and $\approx$ 485 K, respectively and their contributions to the total saturation magnetisations are $\approx$46 emu/g and $\approx$ 49 emu/g respectively. It has room temperature saturation magnetization of 8.8 kG. Its increased curie temperature of 626 K and low saturation magnetostriction of 12 x 10^{-6} accounts for the good soft magnetic properties exhibited by this material. The material can be tailored by annealing to

216

induce nanocrystallization for inducing superior soft magnetic properties such as H_c= 7 mOe, M_r = 7.5 kG and a dc permeability of about 45000 [3].

      Activation energy of crystallization is an important parameter that decides the application potential of metallic glasses. Heat treatment of metallic glasses can induce crystallization in the material by supplying thermal energies to overcome the activation energy for crystallization. The material devitrifies into a supersaturated solid solution which consequently decays into a mixture of solid solution and crystalline phase or phases [6]. In any material, crystallization proceeds through nucleation, subsequent growth and Oswald ripening. Without losing generality one can combine the energy barriers for all these processes into a single activation energy E_c [7]. The approximation is warranted by the reasoning that for most of the materials these three stages have overlapping energy curves.

      There are discrepancies between the activation energies E_c of different crystallization stages of $Fe_{40}Ni_{38}B_{18}Mo_4$ alloy reported by various investigators. Antonione *et. al.* [8] was the first to report the crystallization dynamics of the material. Using non-isothermal calorimetric studies he had reported two-stage crystallization with activation energies 3.07 eV/atom and 3.46 eV/atom, respectively for the two phases. However Majumdar and Nigam [9] observed three stage crystallization in the material. Cubrera *et. al.* [10] had done a quantitative investigation on the crystallization kinetics and activation energies using both non-isothermal (2.984 and 3.678 eV/atom) and isothermal methods (2.984 and 4.673 eV/atom) using DSC, differential thermal analysis (DTA) and resistivity. Nicolai [11] has found five-step crystallization in the sample. Jen *et. al.*[12] reported the activation energy for α-Fe to be 2.92 eV/atom, and for (Fe, Ni) B to be 3.85 eV/atom. The above discussion suggests that reports on the crystallization dynamics of $Fe_{40}Ni_{38}B_{18}Mo_4$ are rather scanty and there exists diverse opinions about the activation energies for the nucleation and phase separation.

Metallic glasses are considered to exhibit structural and chemical disorder because of the high quenching rate involved in the fabrication process. In devitrification of metallic glasses, the nucleation rate sigmoidally increases from zero to an ultimate steady state value. Kolmogorow-Johnsen-Mehl-Avarami (KJMA) model replicate the crystallization rate with a sigmoidal curve and the model was widely used for evaluating Avarami exponent which signifies the dimensionality of crystal growth. Kurajica *et. al.* reported the *n* values for both the crystallization steps of $Fe_{40}Ni_{38}B_{18}Mo_4$ to be nearly equal to 2 [13]. However, according to Jen *et. al.* the first stage has an *n* value of 2.92, and for second stage *n* = 3.85 [14]. However, he reported the second stage to have two *n* values indicating the changes of kinetics of crystallization, with the former section with *n* = 3.5 signifies nucleation with constant nucleation rate, while the latter section with *n* = 1.2 signifies growth by diffusion without nucleation. From the above discussion it is evident that there have been diverse views about the kinetics of crystallization and crystallization stages of $Fe_{40}Ni_{38}B_{18}Mo_4$.

In the present work, we report the crystallization dynamics of $Fe_{40}Ni_{38}B_{18}Mo_4$ employing DSC, X-Ray Diffraction (XRD) and different analysis methods like isokinetic and isoconversional methods. A precise knowledge about the kinetics of crystallization is extremely important to determine the activation energy of crystal growth from DSC data. The present study employs techniques like DSC to establish the mechanism of crystallization and to evaluate the activation energy of crystallization and Avarami exponents.

A.2   Experimental

High purity alloy ribbons with composition $Fe_{40}Ni_{38}B_{18}Mo_4$ prepared by melt quenching technique were subjected to X-ray diffraction to confirm their amorphous nature. The ribbons were 20 μm in thickness and 25 mm in width. They were subjected to non-isothermal DSC studies for heating rates 5, 10, 20, 25 K/min. The activation energies were estimated employing the isokinetic and isoconversional techniques. Based on the results of DSC studies the samples were

subjected to thermal annealing at a high vacuum of $\approx 10^{-6}$ Torr at temperatures 100, 200, 300, 400 and 700 °C. The sample is heated to the annealing temperature at a heating rate of 5 K/min and is maintained at that temperature for one hour and subsequently cooled with the same ramp rate. The XRD pattern of the METGLAS samples, pristine as well as annealed were recorded with Rigaku D-max-C X-ray diffractometer using $Cu\,K\alpha$ radiation (λ=1.5405 Å). The average particle size is determined from the measured width of their respective diffraction curves using Scherrer formula. The hysteresis loop parameters namely saturation magnetisation (Ms), coercivity (Hc) and retentivity (Mr) of the METGLAS samples were evaluated using a vibrating sample magnetometer (VSM) (model: EG & G PAR 4500) in the parallel and perpendicular fields (magnetic field parallel and perpendicular to the film plane) at room temperature for both pristine and annealed ribbons.

A.3   Results and Discussion

A.3.1 Theoretical Models

KJMA kinetic equation is formulated based on different assumptions and is assumed to be valid when the growth rate of new randomly distributed nuclei is controlled by temperature and independent of time and the growth rate is linear [15]. Deviations from predictions of KJMA model happen if one or more of the above conditions are not satisfied. Phase transformations in glassy materials are modelled using the KJMA transformation rate equation derived for isothermal heating experiments. The equation is

$$\frac{d\alpha}{dt} = nk(1-\alpha)[-\ln(1-\alpha)]^{\frac{n-1}{n}} \qquad\qquad \text{A.1}$$

Where α is the degree of crystallite volume fraction transformed at time t, n the Avarami exponent and k the rate constant obeying an Arrhenius type relation

$$k = k_0 \exp(-\frac{E}{RT}) \qquad\qquad \text{A.2}$$

where k_0 the pre exponential factor, E the activation energy and R the universal gas constant.

The isoconversional techniques are based on the kinetic equation

$$\frac{d\alpha}{dt} = k(T)f(\alpha)$$ A.3

where k(T) is the rate constant given by equation A.2 and f(α) is the model used to simulate the reaction. The integral form of the above equatin can be obtained by substituting A.2 in A.3 and integrating by separation of variables

$$\int_0^\alpha \frac{d\alpha}{f(\alpha)} = \frac{k_0}{\beta} \int_0^{T_f} \exp(-\frac{E}{RT})\, dT = \frac{k_0 E}{\beta R} \int_{y_f}^\infty \frac{\exp(-y)}{y^2}\, dy$$ A.4

where, $y_f = \frac{E}{RT_f}$ and T_f is the temperature at a particular equivalent stage of crystalline transformation fraction (α) for different constant heating rates β. The integral in the above equation is called the temperature integral or Arrhenius integral. The equation can be extended to non isothermal conditions by scaling 't' with the equation $T = T_0 + \beta t$. However, according to Henderson, this is valid in certain special circumstances in which the growth proceeds from a system saturated with nuclei [16]. He also argued that the conversion factor α depends on the thermal history of the material. Model free isoconversional methods are widely used to give accurate values of activation energies. Isoconversion methods are generally categorized into two. One set of methods springs by approximating the temperature integral [17] using various approximations. This methods includes the Kissinger-Akahira-Sunose method, Flyn-Wall Ozawa Method and Starink models [15,18–21]. The other set of models-even though does not use any approximations- rely on the determination of reaction rate at an equivalent stage of the crystallization process for various heating rates. Friedman method falls into this category [15]. Starink has provided a review about the various isoconversional methods [15]. The aim of this work is to estimate the kinetic parameters for the alloy $Fe_{40}Ni_{38}Mo_4B_{18}$ from nonisothermal DSC data using the various isoconversional and isokinetic methods so as to have a comparative estimate of the values predicted by various models.

A.3.2 Discussion

The DSC of the as-prepared ribbon samples were conducted at constant heating rates of 5, 10, 20 & 25 °K min^{-1} to investigate the inherent thermodynamics governing the crystallization process (figure A.1.).
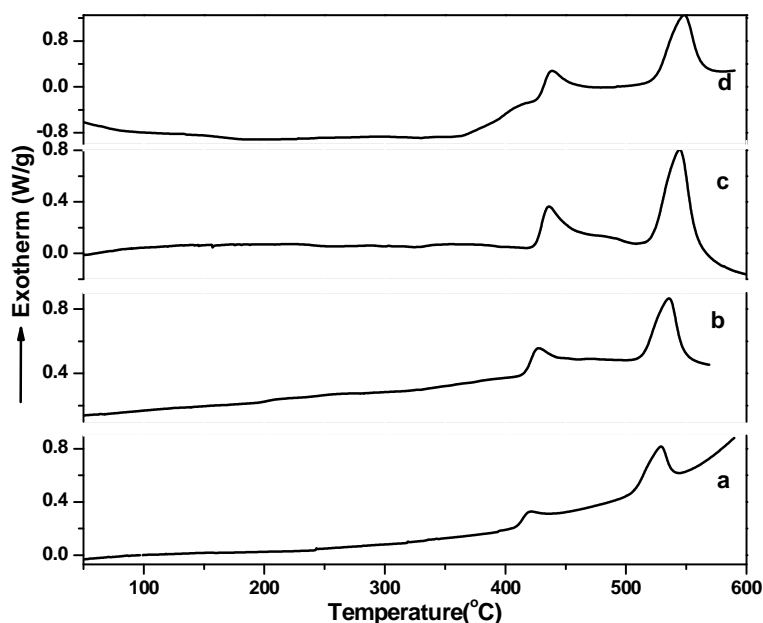

Figure A.1: DSC thermograms of METGLAS ribbon at different heating rates a) 5 K min^{-1} b) 10 K min^{-1} c) 20 K min^{-1} d) 25 K min^{-1}

The first crystallization peak inception occurs at T_1 = 699 K while the second one is at T_2 = 809 K (heating rate 15 K min^{-1}), and up to 900 K, on DSC trace, no other thermodynamic events were found which is the characteristic response showed by Fe rich amorphous alloy materials with low B content. However the small kink just before the first pertinent peak in the DSC trace at a heating rate 20 K min^{-1} can be ascribed to the structural relaxation, chemical ordering and glass transition in the material with thermal gradients. This type of thermal relaxation may be prominent near the glass transition temperature, which is revealed as an endothermic peak in the DSC spectrum due to fast change in specific heat. The total heat content for this thermodynamic event is 11.8 J/g.

The first peak, at low temperature, which is rather sharp, is due to the formation of crystallization phases including the metastable phases signifying spontaneous nucleation and grain growth and implies that the delay between nucleation and grain growth is very small. This can be ascribed to the relative ease of expulsion of highly diffusive boron from the vicinity of Fe-Ni-Mo clusters. The initial crystalline phase is responsible for the supreme magnetic properties exhibited by $Fe_{40}Ni_{38}B_{18}Mo_4$ [5]. The second phases with relatively low sharpness insist sluggish nucleation and growth of the second phase at the expense of the first phase. The second peak in DSC exotherm corresponds to redistribution and re-crystallization of metastable phases of the residual amorphous phase and the precipitation of $(FeNiMo)_{23}B_6$ which is deleterious to the soft magnetic properties [5]. The first exotherm with its asymmetric tail end extended on to the higher end of the spectrum can be attributed to the devitrification process giving a finely dispersed nano-phase embedded in an amorphous matrix. Further, it is evident that the first crystallization step extends up to the initial stage of the second crystallization with progressive grain growth of the initially nucleated crystallites. The deconvolution of the first peak using Gaussian curve fitting reveals two distinct Gaussian curves instructive of the biphasic transitions at that regime. The enthalpy change associated with crystallization, which corresponds to the maximum energy, associated with the phase transformations for the two peaks in the primary crystallization step are 13.9 J/g and 17.71 J/g respectively. From the prominence of the first peak and in comparison with the reported literature on this material it can be concluded that the first phase corresponds to α-Fe-Ni (result derived from xrd analysis). However, no other phases except Fe-Ni is found in samples annealed up to 690 K, henceforth the second associated peak we could not ascribe to any effect.

With progressive heating, the crystallization in the sample starts at around T_x = 695 K. Peak fitting of the small dip in the DSC referring to relaxation yields the glass transition temperature T_g= 648 K. In our investigation we have determined the onset temperature Tg as the characteristic temperature which can

be determined as the intersection of the tangents to the scan above and below the initial change in the baseline slope. Thus, super cooled liquid region $\Delta T_x == T_x - T_g$ is estimated to be 47 K. The relatively higher value of ΔT_x explains the improved thermal stability of $Fe_{40}Ni_{38}B_{18}Mo_4$, which stems from the larger atomic size and the negative heat of mixing of alloying elements. A duplex structure in Fe-base hypoeutectic alloys is possible as long as α-Fe nanoparticles expel a component that acts to raise the crystallization temperature of the remaining amorphous phase.

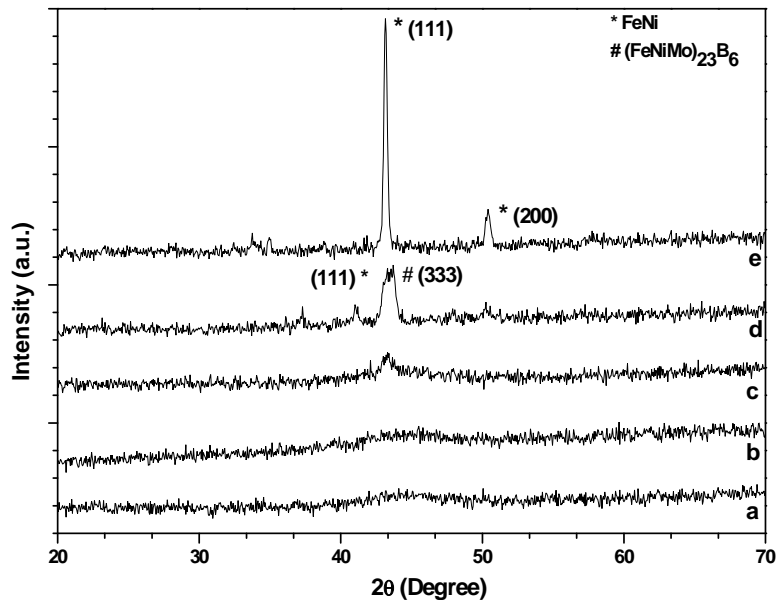## A.3.3 Structural Studies Using XRD

Figure A.2: XRD of metglas ribbon a) Pristine and annealed at b) 373 K c) 573 K d) annealed 673 K e) 973 K

The x-ray diffraction pattern of the unannealed metglas ribbons are shown in Fig A.2 The pristine films show broad diffraction peaks, which indicate their amorphous nature and the fine dispersion of Fe and Ni in the sample. The crests in as quenched samples are in harmony with the earlier reports on crystallization of metglas [9]. The amorphous peak in pristine sample can be attributed to FeNi solid solution [5]. Evidence of the earlier assumption of the

existence of a metastable state of metastable equilibrium for the quenched alloy is found in the x-ray diffraction pattern of the pristine alloy. The basic argument to support this assumption emerges from the fact that after annealing the glass at 373 K and 573 K, distinct Bragg peaks were noticeable at the position of the braod peak in the pristine sample.
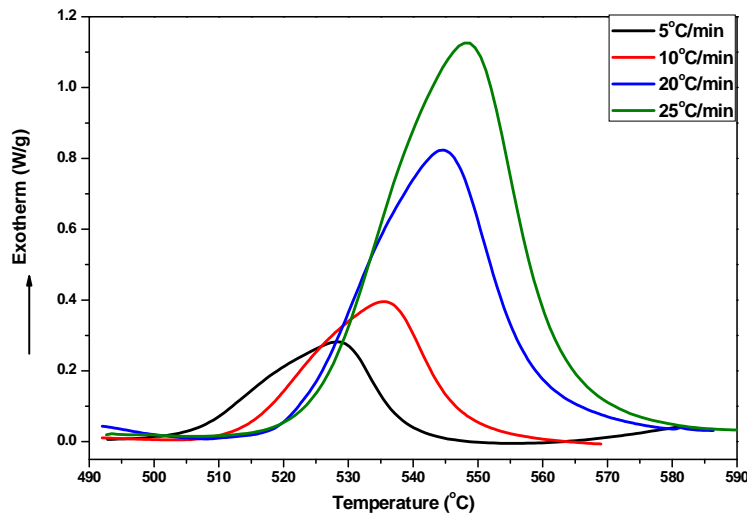

Figure A.3: DSC Peak of Fe-Ni-Mo-B corresponding to the first crystallization at different heating rates. The shift in peak position towards high temperature with increase in heating rate is clearly visible.

The ribbons annealed at 673 K in vacuum possess heterogeneous microstructure consisting of FeNi and $FeNiMo_{23}B_6$. At temperatures above the crystallization temperatures of the first phases (FeNi at 420°C) crystallites tends to grow to micrometric dimensions. Figure A.2e shows the XRD spectrum of ribbons annealed at 700 °C. There is progressive grain growth of FeNi phase with increase in annealing temperatures. Above 400 °C, $FeNiMo_{23}B_6$ phase starts to appear whose presence is reported to have been deleterious to the soft magnetic properties [22]. The intensity of boride phase increases with annealing temperature at the expense of the FeNiMo phase, while the FeNiMo crystallite size increases. At 400 °C anneal almost 55% of the crystalline volume fraction

were FeNiMo particles of size~13.37 nm, substantiating the classification of $Fe_{40}Ni_{38}B_{18}Mo_4$ as a nano-crystalline soft magnetic alloy
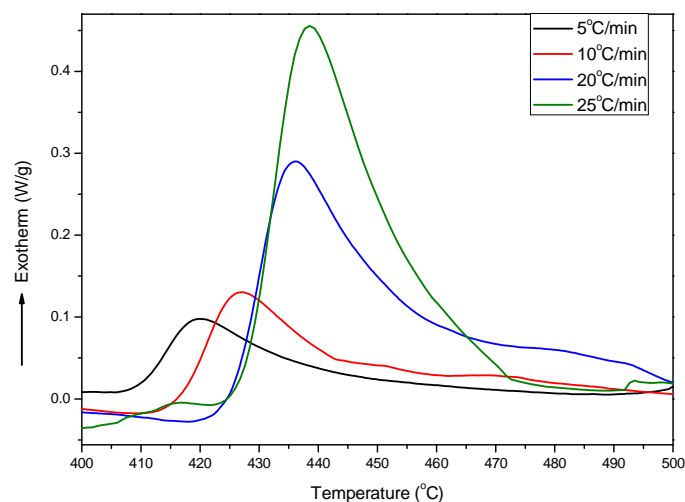

Figure A.4: DSC Peak of Fe-Ni-Mo-B corresponding to the second crystallization at different heating rates. The shift in peak position towards high temperature with increase in heating rate is clearly visible.
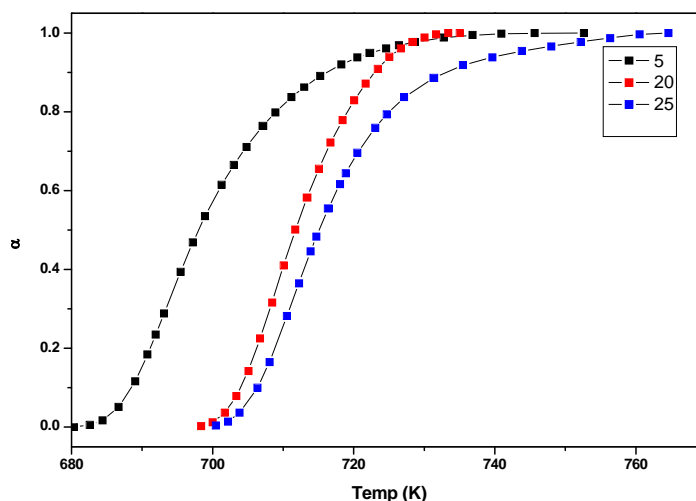
A.3.4 Applicability of KJMA model

Figure A.5: Crystalline volume fraction versus temperature for the first crystallization peak
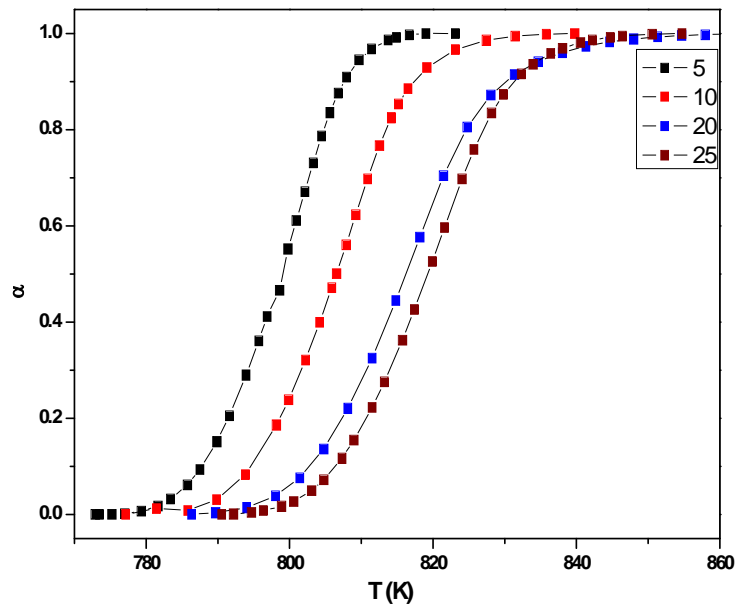
Figure A.6: Crystalline volume fraction versus temperature for the

second crystallization peak

The kinetics of phase transformations is usually modelled using the well-known KJMA equation [23]. The equation predicts an "S type sigmoidal curve" for the transformation with slow rate of transformation at the beginning which then accelerates and there after decelerates. The KJMA equation is erected on the basic assumption of random distribution of nuclei in the material. Figure A.5 and A.6 corresponding to the first and second crystallization steps show a sigmoid curve. However, that doesn't mean the KJMA model can readily simulate the crystallization event. Applicability of the KJMA equation to a transformation can be verified by the linearity of the plot of $\ln[-\ln(1-\alpha)]$ versus $\frac{1}{T}$. However this method is widely accepted to be unreliable. Another validity check given by Malek involves plot of the function $z(\alpha) = \frac{d\alpha}{dT}T^2$ versus α [24]. For the KJMA equation to be valid the maximum of this plot should fall within $0.62 < \alpha_p(z_{max}) < 0.64$. Another validity check for KJMA is to plot $y(\alpha) = \left(\frac{d\alpha}{dT}\right)\exp(\frac{E_c}{RT})$ versus α. The maximum of y(α) plot depends on the value of n

and it is equal to zero if n< 1 and greater than 0 if n>1 [25]. The plot of $z(\alpha)$ and y(α) versus α for both crystallization peaks are shown in figure A.7.
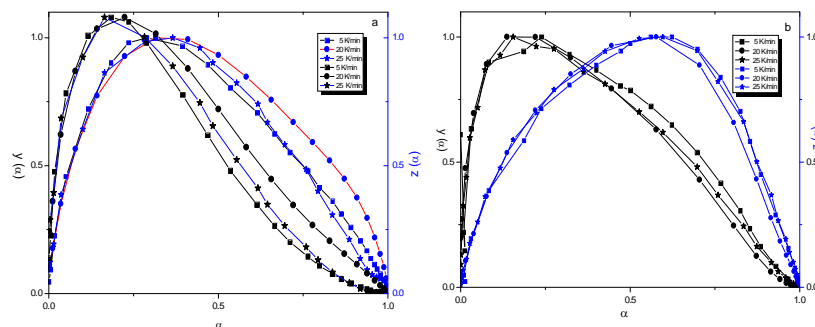

Figure A.7: Plot of y(α) and z(α) versus α for the a) first crystallization step and b) second crystallization step.

The above plot clearly shows that the first peak of crystallization does not follow the KJMA model. The maximum of y(α) = 0.21 and z(α) = 0.32 which is clearly different from the value for KJMA model. However, the second peak have y(α) = 0.132 and z(α) = 0.624 suggesting the applicability of KJMA model. Hence for evaluating the kinetic triplets for the first crystallization step it is required to apply other models.

A.3.5 Linear Integral Iso-conversional Techniques

A.3.5.1 Kissinger-Akahira-Sunose Method

This technique suggested by Kissinger, Akahira and Sunose use an approximation put forward by Coats and Redfern to modify the temperature integral. According to this method $ln\frac{\beta}{T^2} = \text{In}\left(\frac{k_0 R}{Eg(\alpha)}\right) - \frac{E}{RT}$ where T is the temperature corresponding to a particular conversion factor. From the slope of the plot of $ln\frac{\beta}{T^2}$ versus 1000/T gives $-\frac{E}{1000R}$ from which E value can be estimated. Special cases of this general model were also reported in literature based on choosing specific values of temperature based on certain conditions.

A.3.5.2 Kissinger Model

This model assumes maximum reaction rate as well as constant conversion factor at the peak crystallization temperature. $ln\frac{\beta}{T_p^2} = \ln\left(\frac{k_0 R}{E}\right) - \frac{E}{RT_p}$. A slope of the plot of $ln\frac{\beta}{T_p^2}$ versus 1000/T$_p$ gives $-\frac{E}{1000R}$ from which E can be evaluated. From the intercept the preexponential factor k can also be evaluated. The analysis gives an activation energy of 331 and 429 kJ/mol. The frequency factor is evaluated as 6.79×10^{22} and 6.40×10^{25} for the first and second crystallization event respectively.
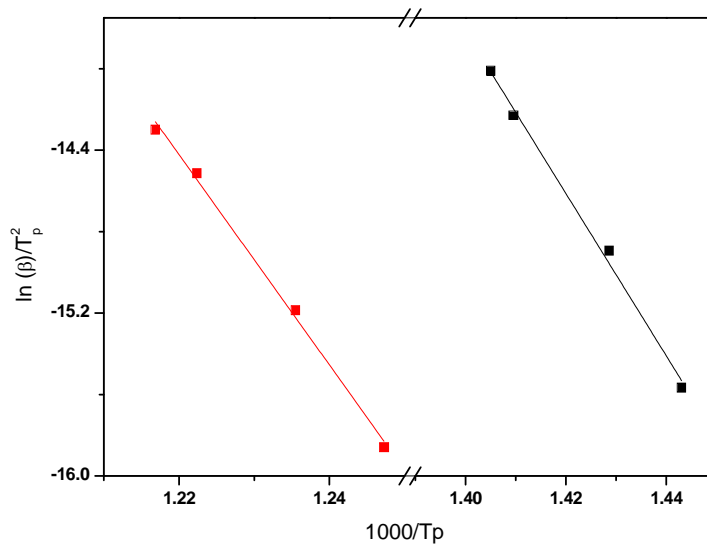

Figure A.8: Kissinger Plot corresponding to the first and second crystallization events.

A.3.5.3 Augis and Bennet Method

This method is a variant of Kissinger method and incorporates the onset temperature of crystallization also for the calculation of activation energy. This method is reported to be one of the most accurate methods for evaluating E. $ln\frac{\beta}{T_{p-T_0}} = \ln(k_0) - \frac{E}{RT_p}$. The values of E and k$_o$ can be estimated from the slope

and intercept of the straight line fit to the plots of $ln\frac{\beta}{T_p-T_0}$ versus 1000/Tp.

Further $n = 2.5\frac{T_p^2}{\Delta T E/R}$ where ΔT is the FWHM of the DSC peak. The kinetic triplets are [349 (E), 1.56 (n) and 7.75x10^{24} (k$_0$)] and [498, 1.28 and 5.1x10^{30}] for the first and second crystallization step respectively.
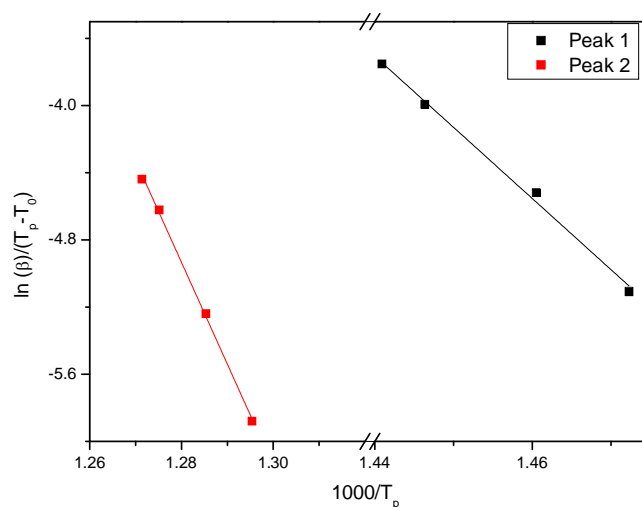

Figure A.9: Augis and Bennet Plot for the Two Crystallization Steps

A.3.5.4 Boswell method

Boswell method suggests an expression of the form

$$ln\frac{\beta}{T_p} = -\frac{E}{RT_p} + const.$$
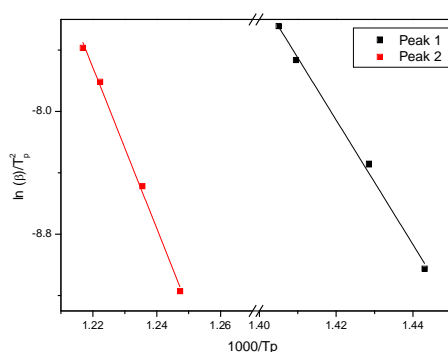

Figure A.10: Boswell plot for the two crystallization steps.

229

Plots of $ln\frac{\beta}{T_p}$ versus 1000/Tp can be used to estimate the activation energy. The activation energy calculated from the linear plots are 337 and 437 kJ/mol respectively for the first and second crystallization processes.

A.3.6 Ozawa-Flynn-Wall method

In this method, the temperature integral is modified using the Doyles Approximation and assumes the form $ln\beta = -1.0516\frac{E(\alpha)}{RT_p(\alpha)} + const.$ The plots of $ln\beta$ versus 1000/T_p for various crystallization rate fractions can be used to evaluate the local activation energies. At T(a) =T(p) the equation is called the Ozawa equation which is a special case of the Ozawa Flynn Wall equation.

A.3.7 Transformation Rate Isoconversion methods

These methods do not make any mathematical approximations, but rather needs the value of rate of transformation at $T_f(\beta)$. This method is also called liner rate isoconversion method.

Inserting equation A.2 in equation A.3 and taking the logarithm yields $\ln\left(\frac{d\alpha}{dt}\right)_f = -\frac{E}{RT_f} - lnf(\alpha)$. If in nonisothermal DSC measurements at different heating rates, T_f be the temperature where a particular fraction of crystalline volume fraction transformed (α) can be identified, then $f(\alpha)$ wll be a constant. For a particular transformed volume fraction, the straight line fit to the plot of $\ln\left(\frac{d\alpha}{dt}\right)_\alpha$ versus 1000/T$_a$ can be used to evaluate the activation energy of crystallization. However since it is easier to evaluate $\frac{d\alpha}{dT}$ than $\frac{d\alpha}{dt}$, the denominator of the RHS of the equation can be changed using the relation $T = T_0 + \beta t$ yielding $\ln\left(\beta\frac{d\alpha}{dT}\right)_f = -\frac{E}{RT_f} - lnf(\alpha)$. Hence a plot of $\ln\left(\beta\frac{d\alpha}{dT}\right)_f$ versus 1000/T$_f$ can be used to evaluate E. Since this method do not assume any functional form or approximation for $f(\alpha)$ it is called a model free method and is considered to be an accurate method for the estimation of activation energy. Special cases of this model are also reported in the literature

A.3.7.1 Gao and Wang model.

When $T_f = T_p$ the Friedman model reduces to the Gao and Want model and suggest an expression of the form $\ln\left(\beta \frac{d\alpha}{dT}\right)_p = -\frac{E}{RT_p} - lnf(\alpha)$. The model suggests a very low activation energy of 275 and 382 kJ/mol respectively for the two pahses.
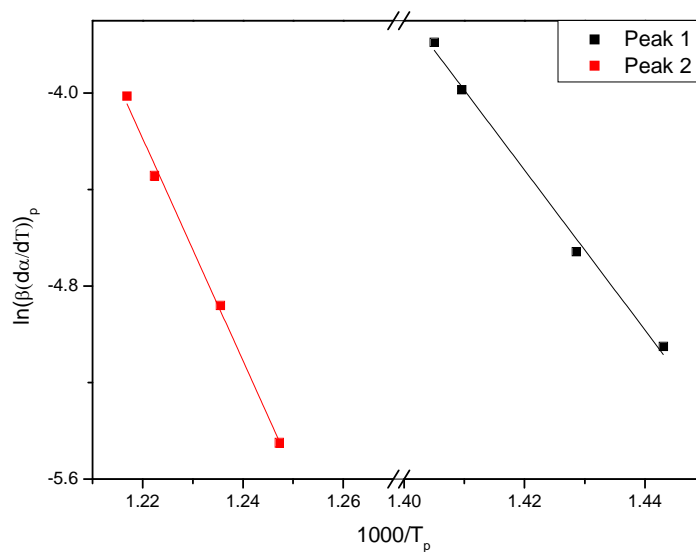

Figure A.11: Gao and Wang plot for the two crystallization steps.

A.3.8 Isokinetic Methods

A.3.8.1 Matusita and Saka Method

When a glass is heated to a higher temperature from room temperature, the crystal nucleation rate will be highest at a temperature above the glass transition temperature and will not be the same as the temperature where the transformation rate is the maximum. During heating, the nuclei are formed at a lower temperature and thereafter increase in size. Based on these assumptions Matusita and Saka derived an expression $\ln[-\ln(1-\alpha)] = -n\ln(\beta) - 1.052\frac{mE}{RT}$. Here n is the Avarami exponent and m is another parameter that is connected to the crystal growth. The slope of the straight line fit to the plot of

$\ln[-\ln(1-\alpha)]$ verus $\ln(\beta)$ at any particular temperature gives the value of n. A plot of $\ln[-\ln(1-\alpha)]$ versus 1000/T gives a straight line and the m value can be extracted from the slope.
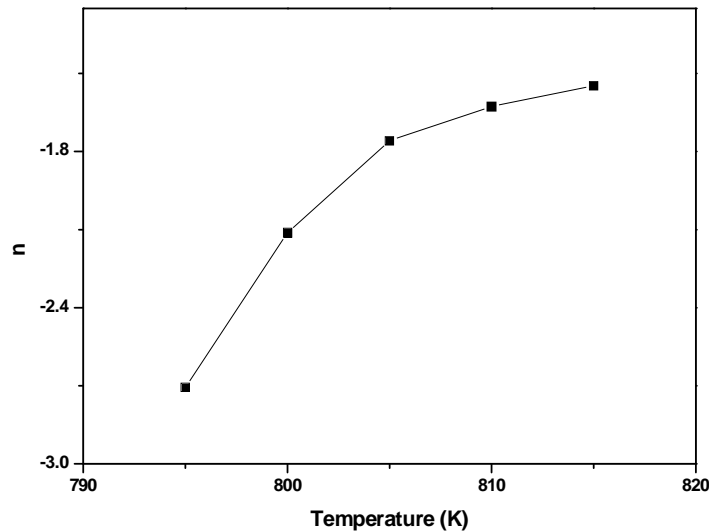

Figure A.12: Variation of Avarami exponent with transformation temperature estimated using Matusita and Saka method.

A.3.9 Alternative Method to Estimate Avarami Exponent

The KJMA equation is erected on the basic assumption of random distribution of nuclei in the material. The theory predicts that the volume fraction transformed is exponentially dependent on the absolute temperature.

$$x(t) = 1 - e^{[-(\kappa t)^n]}$$

A.5

Where n is an integer or half integer that reflects the dimensionality and mode of nucleation and growth of crystals. k is the thermally activated reaction rate constant with Arrhenian type temperature dependence.

$$k = k_o e^{\left[-\frac{E_a}{RT}\right]}$$

A.6

E_a denotes the activation energy and k_0 the frequency factor. At small times the equation reduces to:

$$X = \left(\kappa t\right)^n$$ and the derivative $\dfrac{d \ln X}{d \ln t}$, gives the exponent n.

Table I. Table depicting the Avarami exponent for the primary crystallization step for various heating rates

K/min	N
5	1.58
10	1.37
20	1.22

Table II. Table depicting the Avarami exponent for the secondary crystallization step for various heating rates

K/min	N
5	1.02
10	1.30
20	1.34

Table I & II lists the values of the Avarami index n for three different heating rates. The data elucidates a clear decreasing trend of Avarami index with increasing heating rate for the first peak and a reverse trend for the second peak. Slow heating rates were desirable for better completion of the crystallization process and stronger intergranular coupling. Avarami's analysis of nucleation and growth process leads to a value $n = 1.5$ if all the nuclei are present at time $t = 0$ and the subsequent growth of particles is parabolic. For the primary crystallization, heating rate of 5 K/min favors parabolic growth of crystallites and there is a clear trend for parabolic to circular growth of crystallites with increasing

heating rates. It is well known that the crystallization of metallic glasses is associated with the nucleation and growth process, and the extent of crystallization increases with an increase in heating rate. In other words it tends to its maximum value. The decreasing trend of *n*, therefore, shows the decrease in the nucleation rate due to nucleation saturation. The character of crystallization goes over from nucleation-driven in the beginning to a growth-driven regime by the end of the crystallization process. [26]

According to Christian [27], the Avarami exponent for the first phase with n = 3.5 signifies nucleation with constant nucleation rate, while the secondary phase with n = 1.2 signifies growth by diffusion without nucleation. This fact also agrees partially with investigation by other techniques that α-Fe-Ni-Mo crystallites first grow in size and number, but then nucleation stops at the later stage of crystallization. However, the assignment of $n = 3.5$ with the first stage of crystallization is fraught with error. This higher value for nucleation and growth in the alloy ribbon may be due to overlooking the presence of initial islands of compositional fluctuations in the alloy that can serve as nuclei for heterogeneous nucleation and growth during heating. During rapid quenching, some compositional fluctuation or even nuclei may be quenched in and a high quenching rate will reduce the size and number of such quenched-in nuclei reflecting in the Avarami exponent of the alloy [28]. For the second crystallization step the average value of *n* comes out to be 1.22, which shows that the crystallization mechanism in the present glasses has approximately one-dimensional growth during the secondary crystallisation event. The values of the Avarami exponent, $n = 1$, are consistent with diffusion-controlled growth with a nucleation rate close to 0. The values calculated using this method is close to the values obtained by Augis and Bennet method.

Table III: Local activation energies for the first and second crystallization peak corresponding to different conversion factors estimated using the KAS, Friedman and OFW methods.

| | Activation Energy (kJ/mol) | | | | | |
| | Peak 1 | | | Peak II | | |
α	KAS	FRIEDMAN	OFW	KAS	FRIEDMAN	OFW
0.1	371	373	344	-	402	463
0.2	379	389	351	-	396	448
0.3	404	407	359	-	394	437
0.4	412	421	364	450	391	430
0.5	-	-	-	435	390	430
0.6	419	468	395	424	373	413
0.7	351	471	403	416	354	407
0.8	358	467	416	416	342	388
0.9	-	-	-	399	337	363

A.3.10 Magnetic Studies on Fe-Ni-Mo-B Ribbons

The magnetic evolution of amorphous and nanocrystalline ribbons with grain size is generally modeled using random anisotropy model originally suggested by Alben *et. al.* and modified by Herzer [29,30]. According to the RAM coercivity is found to be related to the sixth power of grain size as

$$H_c = \frac{p_c \langle K \rangle}{M_s} = p_c \frac{K_1^4 D^6}{M_s A^3}$$

A.7

In the above equation p_c serves as a fitting parameter and M_s is the saturation magnetization. These equations serve well for the three dimensional cases. Typical values of (L_{ex}) for a metallic glass with $K_1 \approx 6$ kJ/m^3 and $A \approx 10^{-11}$ J/m^3 turns out to be ≈ 40 nm. In bulk metallic glasses if the nanocrystalline grain size is less than the exchange correlation lengths (≈ 40nm) the anisotropies are averaged out over several grains and the sample exhibits good soft magnetic properties.
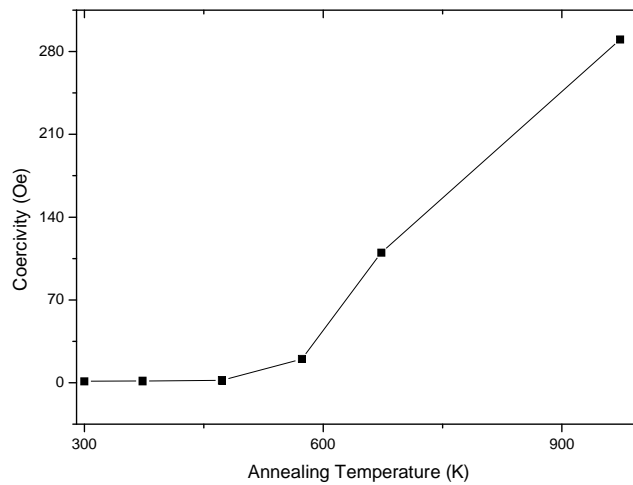
Figure A.14:The evolution of coercivity with annealing temperature in METGLAS 2826MB

The coercivity evolution of the alloy with annealing temperature is shown in figure A.14. The shape of the curve is similar to the coercivity-grain size curve for alloys obeying the Herzer law. This is understandable since for a constant annealing time the grain size is proportional to the annealing temperature. A plot of ln(Hc) versus ln(D) gives a straight line. However it should be noted that the scatter in the plots is rather large. A very large number of data points are required to validate the assumption of fitting such a graph with a straight line. However the slope of the fit doesn't give a value of 6 as was expected from the Herzer model. The anisotropy constant K1 was estimated from the slope of Hc versus D^2 plot. Substituting the values of Ms=112 emu/g A=10^{-11}J/m and assuming pc=1 yields a K1 value of 2.29 kJ/m^3 which is slightly greater than the reported values for bulk Fe-Ni with similar composition (1 kJ/m^3) [31].
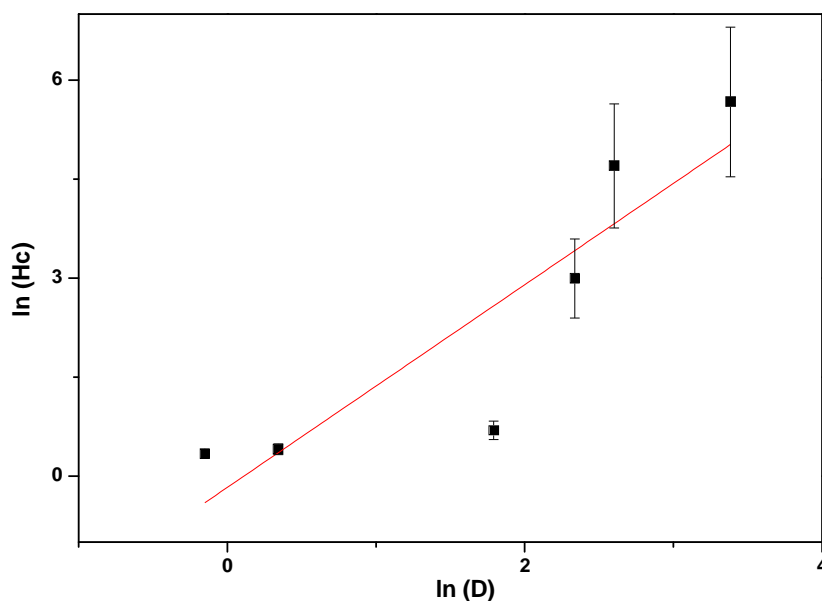
Figure A.15. Verification of Herzer relation connecting coercivity with grain size.

A.4   Conclusions

The analysis of DSC data to evaluate kinetic triplets employing the various analytical techniques, leads to the pertinent question 'which is the best model for evaluating these parameters?'

The isokinetic methods are widely used for the evaluation of activation energy of crystallization. This method gives single activation energy for the entire crystallization process. Also the choice of a suitable model for simulating the reaction process is also cumbersome in isokinetic analysis. On the other hand, isoconversional models give activation energies as a function of conversion factor- considering the fact that crystallization is a thermodynamic process and also the process of crystallization depending on the thermal history of the sample, the assignment of different activation energies for the different stages of crystallization can be justified. Thus isoconversional methods are superior as far as the evaluation of activation energies is concerned.

In metallic glasses heat treatments produce profound changes in the microstructure of the materials and often results in a nanocrystalline material from an amorphous precursor. Also the nature of growth, size, dimension of growth and crystal structure affects the magneto-crystalline anisotropy, exchange interaction and thereby the magnetic properties of the material. Hence from the application point of view it is very important to probe the dynamics of crystal growth mechanism. KJMA equation is widely used for modeling the crystallization dynamics in metallic glasses. Using this model the three kinetic parameters could be successfully estimated. However, this is possible only if the system satisfies the fundamental assumptions made by the theory. If the system does not follow the KJMA kinetics then one should find a satisfactory model to describe the crystallization dynamics of the system.

Hence, it can be concluded that isoconversional methods are superior in estimating the local activation energies, whereas isokinetic methods are superior in estimating the crystallization dynamics of the system.

Finally, it is established that the variation of coercivity with grain size in FeNiMoB alloys follows the Herzer model.

References

[1]   Y. Cao, Q. Wang, G. Li, J. Du, C. Wu, J. He, Journal of Magnetism and Magnetic Materials 332 (2013) 38.

[2]   Z.A. Chaudhury, C. Suryanarayana, Thin Solid Films 98 (1982) 233.

[3]   R. Hasegawa, R.C. O′Handley, Journal of Applied Physics 50 (1979) 1551.

[4]   K. Shirae, Journal of Applied Physics 50 (1979) 7618.

[5]   S.W. Du, R.V. Ramanujan, Journal of Non-Crystalline Solids 351 (2005) 3105.

[6]   J. Li, Z. Su, T.M. Wang, S. Hage, H. Hahn, Y.Shirai., Journal of Materials Science 34 (1999) 111.

[7]   S. Ram, Current Science 86 (2004) 832.

[8]   C. Antonione, L. Battezzati, A. Lucci, G. Riontino, G. Venturelo, Scripta Materialia 12 (1978) 1011.

[9]   A.K. Majumdar, A.K. Nigam, Journal of Applied Physics 51 (1980) 4218.

[10]   F.L. Cumbrera, H. Miranda, A. Conde, R. Marquez, P. Vigier, Journal of Materials Science 17 (1982) 2677.

[11]   H.P. Nicolai, G. Kopmann, G. Frommeyer, Zeitschrift Für Metallkunde 72 (1981) 558.

[12]   S.U. Jen, D.R. Huang, Chineese Journal of Physics 24 (1986) 239.

[13]   S. Kurajica, J. Schmauch, E. Tkal, Croatica Chemica Acta 75 (2002) 693.

[14]   S.U. Jen, Chineese Journal of Physics 24 (1986) 239.

[15]   M.. Starink, Thermochimica Acta 404 (2003) 163.

[16]   D.W. Henderson, Journal of Non-Crystalline Solids 30 (1979) 301.

[17]   G.R. Heal, Thermochmica Acta 340-341 (1999) 69.

[18]   H.E. Kissinger, Journal of Research of the National Bureau of Standards 57 (1956) 217.

[19]   A.T. Sunose, Report Chiba Inst Technol. 16 (1971) 22.

[20]   T. Ozawa, Bulletin of the Chemical Society of Japan 38 (1965) 1881.

[21]   J.H. Flynn, L.A. Wall, Journal of Research of the National Bureau of Standards. A Phys. Chem. 70A (1966) 487.

[22]   T. Hysen, S. Deepa, S. Saravanan, R. V Ramanujan, D.K. Avasthi, P. a Joy, S.D. Kulkarni, M.R. Anantharaman, Journal of Physics D: Applied Physics 39 (2006) 1993.

[23]   D.R. Dos Santos, D.S. Dos Santos, Materials Research 4 (2001) 47.

[24]   J. Malek, Thermochimica Acta 355 (2000) 239.

[25]   D.M. Minić, B. Adnađević, Thermochimica Acta 474 (2008) 41.

[26]   R.S. Tiwari, N. Mehta, A. Kumar, Chineese Journal of Physics 44 (2006) 467.

[27]   S. Christian, N. J.Wagner, B. Micheal, Materials Science and Engineering A 133 (1991) 26.

[28]   K. Lu, J.T. Wang, Scripta Metallurgica 21 (1987) 1185.

[29]   G. Herzer, IEEE Transactions on Magnetics 26 (1990) 1397.

[30]   G. Herzer, Journal of Magnetism and Magnetic Materials 294 (2005) 99.

[31]   S. Chikazumi, S.H. Charap, Physics of Magnetism, Krieger Pub Co, New York, 1978.